THE UNIVERSITY OF
SYDNEY

SCHOOL OF MOLECULAR BIOSCIENCE
DISCIPLINE OF MICROBIOLOGY

The role of the microtubule cytoskeleton in poxvirus replication and pathogenesis

Helena Lynn

A thesis submitted in fulfilment of requirements for the degree of
Doctor of Philosophy

University of Sydney
2015

TABLE OF CONTENTS

ACKNOWLEDGEMENTS

So, I have to be honest. This was harder than I was expecting (and I was not expecting it to be easy, let me tell you). So first I want to say: sorry! Sorry Tim for frustrating you so much and forcing you to think creatively about how to manage your students. But also thank you for giving me an opportunity to work in your lab and do some fascinating, exciting, cutting edge science over the years. Thank you also for your support in pushing me through this last period and being the supervisor I needed when the going got really tough. A special thank you to Shona for telling me I should keep going when I didn’t think I could.

Thank you to Dean, for being my buddy in both hope and bitterness. Thank you for being the hardworking, frantic whirlwind of amazing science wizardry that you are.

Thank you to Bish, Chris, Elissa, Mai Anh, Marj and Newsome lab members past and present, for being brilliant and hilarious and drinking so much tea and just generally making work a brighter place to be. I blame you all for how long I took! (But also sorry for setting such a bad example.)

Thank you to Jaime and Lingsi and Sam and all my other dear, darling friends who are the most amazing, loving people anyone could possibly hope to have in their life. You all sat through an infinite amount of crying exisistential crises and still weirdly want to spend time with me. What’s up with that?

Thank you to my mum, for everything.

DECLARATION

I declare that the research presented here is my own original work unless otherwise stated and has not been submitted to any other institution for the award of a degree.

Signed:

Date:

ABSTRACT

The subcellular space is a dense, complex environment that viral pathogens must efficiently navigate for their survival and dissemination. The prototypal poxvirus member, vaccinia virus (VACV) has been shown to subvert both host microtubule-based and actin-based transport mechanisms to this end. The utilisation of fluorescent protein technology has been at the crux of many of these discoveries, but addressing remaining questions is made difficult by the various morphological forms of VACV and the sheer number of viruses being transported at any one time in a single infected cell.

We have used the development of photoswitchable fluorescent protein Dendra2 to create a cutting edge imaging system that allows us to gain insight into the dynamics of subcellular virus dissemination. We have constructed recombinant viruses expressing core protein A3 and envelope proteins B5 and F13 fused to Dendra2 in both parental and deletion strains of the Western Reserve strain and have examined the envelopment at and egress from the trans-Golgi network.

Egress of wrapped virus to the cell periphery following vaccinia virus (VACV) replication is dependent on interactions with the microtubule motor complex kinesin-1 and is mediated by the viral envelope proteins A36 and F12. We have utilised a mouse-based infection model to validate the important role these transport events have during an *in vivo*, endemic infection.

Ectromelia virus, an orthopoxvirus and the causative agent of mousepox, encodes an A36 homologue (ECTV-Mos-142) that is highly conserved despite a large truncation at the C terminus. Deleting the ECTV A36R gene leads to a reduction in the number of extracellular viruses formed and to a reduced plaque size, consistent with a role in microtubule transport. We also observed a complete loss of virus-associated actin tails, another phenotype dependent on A36 expression during VACV infection.

ECTV ΔA36R was severely attenuated when used to infect the normally susceptible BALB/c mouse strain. ECTV ΔA36R replication and spread from the draining lymph nodes to the liver and spleen were significantly reduced in BALB/c mice and in Rag-1-deficient mice, which lack T and B lymphocytes. The dramatic reduction in ECTV ΔA36R titers early during the course of infection was not associated with an augmented immune response. Taken together, these findings demonstrate the critical role that subcellular transport pathways play not only in orthopoxvirus infection in an *in vitro* context but also during orthopoxvirus pathogenesis in a natural host.

LIST OF FIGURES

ABBREVIATIONS

AAV	Adeno-associated virus
ACMM	Australian Centre of Microscopy and Microanalysis
AcMNPV	*Autographa californica* multiple nucleopolyhedrovirus
ADP	Adenosine diphosphate
AdV	Adenovirus
Amp	Ampicillin
APh	Alexa-Phalloidin
APS	Ammonium persulphate
Arp2/3	Actin-related protein-2/*3* complex
ASFV	African swine fever virus
ATCC	American Type Culture Collection
ATP	Adenosine triphosphate
BSA	Bovine serum albumin
BFP	Blue fluorescent protein
CB	Cytoskeletal buffer
CDC	Center for Disease Control and Prevention
CEV	Cell-associated enveloped virus
CFP	Cyan fluorescent protein
CMC	Carboxymethylcellulose
CPXV	Cowpox
DAPI	4', 6-Diamidino-2-phenylindole dihydrochloride
DMEM	Dulbecco’s modified Eagle Medium
DMSO	Dimethylsulfoxide
DNA	Deoxyribonucleic acid
dsDNA	Double-stranded DNA
dsRNA	Double-stranded RNA
EBOV	Ebola virus
ECTV	Ectromelia virus
EDTA	Ethylene diamine tetraacetic acid
EEV	Extracellular enveloped virus
EFC	Entry fusion complex
EGF	Epidermal growth factor
EGTA	Ethylene glycol tetraacetic acid
EHEC	Enterohaemorrhagic *Escherichia coli*
EPEC	Enteropathogenic *Escherichia coli*
ER	Endovector reticulum
F-actin	Filamentous actin
FBS	Fetal bovine serum
FLIP	Fluorescence loss after photobleaching
FRAP	Fluorescence recovery after photobleaching
FRET	Fluorescence resonance energy transfer
G-actin	Monomeric actin
GFP	Green fluorescence protein
gDNA	Genomic DNA
GFP	Green fluorescent protein
gpt gene	Guanine phosphoribosyltransferase gene
Grb2	Growth factor receptor-bound protein 2
GTP	Guanosine triphosphate
GTPase	GTP hydrolase
HBV	Hepatitis B virus
HCMV	Human cytomegalovirus

HCV	Hepatitus C virus
HIV-1	Human immunodeficiency virus-1
HPV	Human papillomavirus
HRP	Horse Radish Peroxidase
HSV	Herpes simplex virus
HTLV-1	Human T-lymphotrophic virus-1
IEV	Intracellular enveloped virus
IFA	Immunofluorescence assay
IMV	Intracellular mature virus
IV	Immature virus
kDa	Kilodalton
KHC	Kinesin heavy chain
KLC	Kinesin light chain
KO	Knockout
KSHV	Karposi's Sarcoma-Associated herpesvirus
LASV	Lassa virus
LB	Luria Broth
MLV	Murine leukaemia virus
MEM	Minimum Essential Medium
MES	2-(N-morpholino)ethanesulfonic acid
MOI	Multiplicity Of Infection
Mos	ECTV strain Moscow
Mowiol	Polyvinyl Alcohol 4-88
MPA	Mycophenolic Acid
MPYV	Murine polyomavirus
MPXV	Monkeypox virus
MQ Water	Milli-Q® water
mRFP	Monomeric red fluorescent protein
mRNA	Messenger RNA
MTOC	Microtubule organising centre
MV	Mature virion
MVA	Modified virus Ankara
MYXV	Myxoma virus
Nav	ECTV strain Naval
Na-V	Na-orthovanadate
Nck	Nck adaptor protein
NIH	National Institutes of Health
NK cells	Natural killer cells
NPC	Nuclear pore complex
NPF	Nucleation promoting factor
N-WASP	Neural Wiskott-Aldrich syndrome protein
ORF	Open reading frame
PBS	Phosphate Buffered Saline
PBST	Phosphate Buffered Saline Tween-20 (0.1%)
PBST-milk	Phosphate Buffered Saline Tween-20 milk (5%)
PCR	Polymerase Chain reaction
pE/L	early/late promoter
PFA	Paraformaldehyde
PFU	Plaque forming units
PMSF	Phenylmethanesulphonylfluoride
PrV	Pseudorabies virus
RNA	Ribonucleic acid
RO Water	Reverse Osmosis water
SCV	*Salmonella*-containing vacuole

SeV	Sendai virus
SDS	Sodium Dodecyl Sulfate
SDS-PAGE	Sodium dodecyl sulfate polyacrylamide gel electrophoresis
SFM	Serum free medium
SV40	Simian virus 40
TDS	Transient dominant selection
TEMED	N,N,N,N -Tetramethyl-Ethylenediamine
TGF-α	Transforming growth factor alpha
TGN	Trans-Golgi network
TPR	Tetratricopeptide repeat
Tyrosine 112	Y112
Tyrosine 132	Y132
VACV	Vaccinia virus
VARV	Variola virus
VGF	Vaccinia growth factor
WH2	WASP homology 2 domain
WHO	World Health Organisation
WIP	(Wiskott Aldrich Sydrome Protein) Interacting Protein
WR	VACV strain Western Reserve
WV	Wrapped virion
Y2H	Yeast 2 Hybrid
YFP	Yellow fluorescent protein
YLDV	Yaba-like disease virus

CHAPTER 1: Introduction

1.1 CELLULAR TRANSPORT

1.1.1 Introduction

Pathogen subversion of essential host-cell functions is fundamental to survival and dissemination inside the host. Outside the cell, pathogens may spread by diffusion through extracellular fluids such as blood and lymph, although pathogenic mechanisms such as flagella [1] and type IV pili [2] are able to enhance this process. Inside the cell, pathogens must access specific host compartments to replicate and evade host innate and adaptive immune functions. Entry into and navigation of the intracellular space is critically important for viral pathogens, which are unable to complete their replicative cycles without host cell machinery.

The complexity and density of the subcellular environment present substantial barriers to pathogen motility. Host cells face the same cytoplasmic hurdles when transporting and organising cytosolic components and their own biological processes and have therefore evolved complex transport systems that pathogens themselves have evolved to exploit.

1.1.2 Transport through the cytoplasm

Eukaryotic cells are differentiated from their prokaryotic ancestors primarily by their highly compartmentalised organisation, such as the nucleus and other organelles. Organelles are membrane-delineated compartments where specific biochemical processes such as Adenosine triphosphate (ATP) generation (mitochondria, [3]), protein folding and lipid metabolism (endoplasmic reticulum, [4]), protein packaging and transport (the Golgi apparatus, [5]) and hydrolytic degradation (lysosomes, [6]) occur. Although organelles are present in some prokarya [7], they are definitive features of all eukaryotic cells that are believed to contribute to eukaryotic evolvability [8].

Movement of large macromolecular complexes and membrane traffic between organelles through the cytoplasm cannot be achieved efficiently through passive transport. High concentrations of dissolved macromolecules such as nucleic acids and proteins lead to an environment that impedes the diffusion of even relatively small objects to a degree that would disrupt effective metabolic functioning. For example, 80 nm synthetic microspheres have been shown to diffuse at a rate of approximately 0.5 µm/min, a diffusion coefficient 500 to 1000-fold lower than water [9]. With mammalian cells ranging from 8 to 130 µm in diameter, transport from the nucleus to the plasma membrane would take between 8 min and over 2 h [10].

The increased spatial complexity and size of eukaryotic cells, as well as the density of the cytoplasm necessitates sophisticated transport mechanisms to target cellular components to locations in the cell determined by need and independent of concentration. These cargos can be directed to different cellular compartments by signalling sequences that are hydrophobic membrane insertable peptides translated at the N-terminus of completed proteins [11]. In eukaryotic cells, two structures fulfil the bulk of the requirements to transport directed cargos: the microtubule cytoskeleton, and the actin cytoskeleton, which are jointly responsible for long-range and short-range transport respectively.

A third network of cytoskeletal filaments in eukaryotic cells is composed of intermediate filaments, although unlike the actin and microtubule cytoskeletons, intermediate filaments are only present in metazoans and insects [12]. Intermediate filaments are composed of a large and diverse group of proteins that differ depending on cell type. Over 50 members have been identified and include keratins, vimentin and lamins. Functionally, intermediate filaments have roles in cell shape determination, structural support against mechanical stressors, motility and signal transduction [13, 14]. Filaments composed of these proteins lack directionality (are not polar) and are therefore unsuited to fulfilling subcellular transport requirements; as such they are beyond the scope of this thesis.

1.1.3 The microtubule cytoskeleton

Beyond its function as a subcellular transport system, the microtubule cytoskeleton also plays key roles in cellular movement; maintenance of internal organisation; mitotic and meiotic cell division; signalling and sensing the extracellular environment; and the formation of flagellum and primary cilia [15, 16]. The microtubule cytoskeleton in non-dividing metazoan cells consists of a network of polar filaments predomininantly arranged radiating from the centre to the periphery of the cell. At this point of radiation, adjacent to the Golgi network, is a microtubule organising centre (MTOC) called the centrosome.

The centrosome consists of two centrioles surrounded by pericentriolar material (PCM) and it is proteins contained in the PCM, such as γ-tubulin, pericentrin and ninein that possess microtubule nucleation and anchoring activity [17]. γ-tubulin is present in a complex called the γ-tubulin-containing ring complex (γ-TuRC), a template upon which microtubules can form [15, 18, 19]. Microtubules also nucleate from secondary MTOCs to form non-centrosomal microtubule arrays such as those in epithelial cells, although γ-tubulin is essential in all cases [20].

The microtubule filaments comprise two proteins: α-tubulin and β-tubulin, that heterodimerise. These then generate a polarised protofilament through the successive binding of α-tubulin in each αβ dimer to the previous β-tubulin on the end of the protofilament. The end of more rapid growth is referred to as the positive or plus -end and the more static end being referred to as the negative or minus-end. Both tubulins are bound to a molecule of GTP, at a non-exchangable (N) site in α-tubulin and an exchangeable (E) site in β-tubulin [21]. The addition of a new heterodimer to the protofilament initiates the hydrolysis of the previous β-tubulin-bound GTP to GDP that can be exchanged for another GTP upon depolymerisation [22] [**Figure 1.1**]. A GTP cap forms when the rate of hydrolysis to GDP is slower than the addition of new heterodimers [23]. A number of these protofilaments, with 13 being typical in many cell types, will associate laterally to form a curved sheet that will then close into the metastable tubular structure of a single microtubule [**Figure 1.1**] [24]. This structure is a hollow tube with a diameter of 25 nm [25].

The growth of microtubules in the cell is not a static event, microtubules will cycle through phases of growth and rapid depolymerisation or collapse with resultant shrinking. This non-equilibrium process is called dynamic instability and allows for the rapid rearrangement of the microtubule cytoskeleton to cellular requirements [26]. This process is believed to occur stochastically, with the loss of the stabilising GTP-bound tubulin cap at the end of microtubules [**Figure 1.1**] [23, 27]. Dynamic instability may act to probe the subcellular environment and through the stabilisation of particular microtubules, can lead to a functional conformation of the microtubule network that connects important cellular structures/organelles and is responsive to changing cellular requirements [28].

A diverse group of unrelated proteins, collectively known as Microtubule-Associated Proteins (MAPs) have key roles in regulating microtubule dynamics. Activities include the binding and severing of microtubules (katanin [29]), influencing the rate of catastrophe (transitions from slow growth to rapid depolymerisation) (Op18/stathmin [30]), rescue (the reversal of catastrophe) (pVHL [31]) or stabilisation of microtubules (Tau [32]). A subset of MAPs are plus-end tracking proteins (+TIPs) that form complexes at the growing end of microtubules. EB1 is believed to play a key role in the formation and dynamics of these end complexes including promoting catastrophes and rescues, as well as nucleation, growth and closure of microtubule sheets into microtubules [33, 34].

Additionally, microtubules undergo a variety of post-translational modifications at either α- or β-tubulin that include the addition or removal of tyrosine, glycine, glutamate, acetate, phosphate and palmitoyl groups [35]. These have complex and wide ranging effects, many of which are mediated through recruitment of the aforementioned MAPs that in turn modulate microtubule dynamics. For example, the C-terminal tyrosine of α-tubulin is required for recruitment of CLIP170, a +TIP interaction partner of EB1 and mediator of microtubule dynamics [36, 37]. The function of another group of MAPs, the molecular motor complexes such as kinesins and dyneins, is also regulated by post-translational modifications and can affect their processivity (the distance a motor travels along a path before falling off) [38, 39], recruitment [39, 40] and subcellular targeting [41].

Microtubule motor complexes mediate the subcellular transport capabilities of microtubules by moving along their surface. These motors have specific directionalities that are made possible by the polarity of microtubules. Transport of cargoes can occur in an anterograde direction, from the minus to the plus end of microtubules, or in the opposite retrograde direction from the plus-end to the minus-end. In many cell types, the majority of filaments are oriented such that anterograde transport moves cargos from the MTOC to the cell periphery and retrograde transport the reverse, although this is not always the case in specialised cells such as neurons [42].

Families of molecular motors generally specialise in unidirectional transport, for example, the bulk of kinesin motor complexes carry out anterograde transport while dyneins carry out retrograde transport. It is the regulated packaging, binding and release of cargoes to and from specific motors that allow the cell to coordinate many of its complex transport needs.

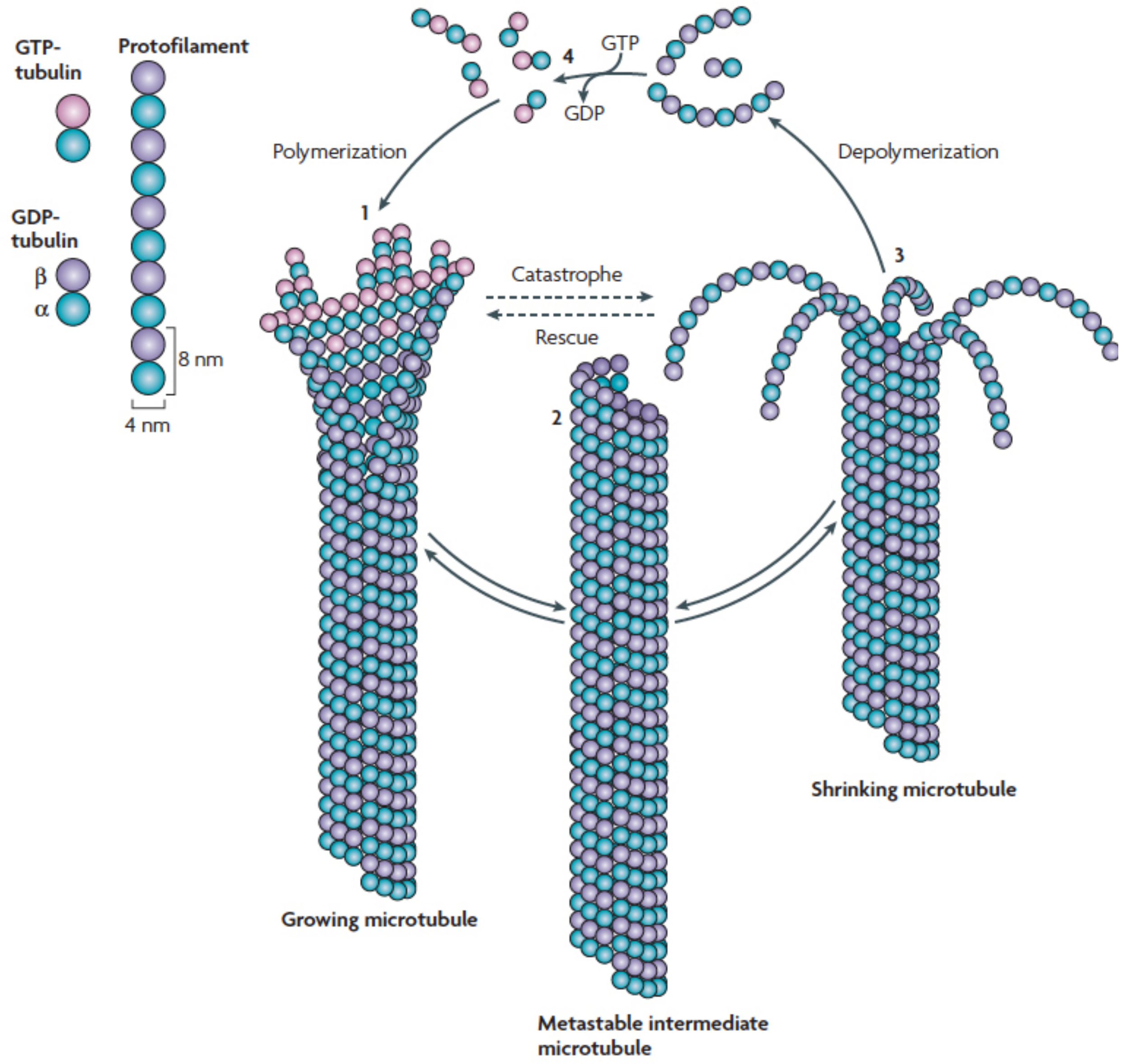

Figure 1.1: Microtubule subunits and dynamics

Dimers of α- and β- tubulin form into protofilaments, with sheets of 13 protofilaments associating laterally to form microtubules (a closing lattice seam is represented in the growing microtubule). Newly added dimers are bound to GTP that are hydrolysed to GDP over time; the tips of growing microtubules therefore have a GTP cap which is not present in the metastable intermediate microtubule. This lack of a stabilising GTP cap can result in catastrophe leading to the rapid dissociation and depolymerisation of the microtubule. Depolymerised tubulin dimers undergo GDP exchange for GTP ready for addition to protofilaments. From [43].

1.1.3.2 Kinesin

Kinesins represent a superfamily of molecular motors comprising 15 kinesin families from kinesin-1 to kinesin-14B and can be classified based on the relative position of the motor domain, which in turn has functional implications. N-terminal kinesins mediate plus-end directed (anterograde) movement (motor domain at the N-terminus), C-terminal kinesins mediate minus-end directed (retrograde) movement (motor domain at the C-terminus), and M-kinesins regulate the depolymerisation of microtubules [44] (motor domain at the middle of the protein).

Kinesins play specialised transport roles in axons and dendrites that are beyond the scope of this thesis but comprehensively reviewed in Hirokawa (2005) [45]. In non-neuronal cells, they are involved in bi-directional trafficking of cargos from the cis-Golgi network to the endoplasmic reticulum and anterograde transport from the trans-Golgi network to the cell periphery [46]. The correct positioning of the Golgi apparatus in the cytoplasm is itself dependent on the transport functionalities of motors of opposing directionalities; an anterograde kinesin 6 family member, KIF20A, retrograde kinesin 14B family member, KIFC3 and cytoplasmic dynein [47-49].

Conventional kinesin (kinesin-1) is the most abundant kinesin and has been shown to transport tubulin dimers [50], mitochondria [51], lysosomes containing LAMP2 [52] and synaptic vesicle and membrane precursors [53, 54]. It is an anterograde microtubule motor typically consisting of two kinesin heavy chains (KHCs) and two kinesin light chains (KLCs). There are 4 known KLC isoforms, and multiple splice forms for each isoform; KLC1 is ubiquitous, KLC2 is widely expressed and enriched in neuronal cells, KLC3 is testis-specific and the distribution of KLC4 has yet been characterised [55, 56]. However, KLCs are not essential to kinesin-1 function and various transport processes involving kinesin-1 do not have any association or involvement of KLCs, with recent estimates indicating that 14% of kinesin-1 complexes in tissue extracts lack KLC [44, 57, 58]. Together, the KHCs and KLCs form a structure with a N-terminal motor domain, a long stalk and a C-terminal cargo-binding domain [**Figure 1.2.**].

The motor domain of kinesin-1 is formed by the N-terminal of the KHCs and possesses both a microtubule binding site and an adenosine tri-phosphate (ATP) binding site on each chain. As the phosphatase activity of the motor domain converts ATP to adenosine di-phosphate (ADP), a conformational change occurs in the KHC that releases binding to the microtubule filament. When a new ATP is bound, the KHC undergoes a further conformational change and attaches once more to a filament. Each KHC of the kinesin will cycle through this ATPase activity, resulting in a step-wise progression [**Figure 1.2**].

Kinesin-1 can be composed of three KHC isoforms, KIF5A, KIF5B and KIF5C. KIF5B is the most significant of these isoforms and is expressed ubiquitously in tissues. The cargo-binding domain of these KHCs may act alone or in conjunction with KLCs and/or other adaptor proteins to bind cargo. A variety of C-terminal domains can be formed through alternative splicing of KIF transcripts and combined with the diversity of complexes formed with various KLCs/adaptor proteins, allows for a high degree of specificity in cargo recruitment [44, 59]. The best-characterised molecular features implicated in mediating interactions between kinesin-1 complex with respective cargos reside in KLC (although KHC complexes alone can also mediate cargo binding). KLC possesses a tetratricopeptide repeat (TPR) domain that interacts with tryptophan-aspartic acid or tryptophan-glutamic acid (WE or WD) motifs on cargos through a series of electrostatic interactions and sequence specific elements [60].

Kinesin-mediated transport requires tight regulation of the temporal-spatial dynamics for the delivery of cargoes to their intended destination (reviewed in [46]). This can be achieved through autoinhibition of kinesins by intramolecular association when cargoes are not bound, thereby preventing motor complexes from binding to microtubules [**Figure 1.2**] [61]. The binding of cargo and/or other adaptor proteins may relieve autoinhibition; for example, the binding of cargo Jun N-terminal Kinase (JNK) Interacting Protein (JIP1) and Fasciculation and Elongation Protein ζ1 (FEZ1) is necessary for complex formation between kinesin-1 and microtubules and subsequent activity [62].

Binding cargo and/or accessory proteins alone is insufficient in many cases to activate processive movement of a kinesin motor complex. Phosphorylation of kinesins and adaptor proteins by kinases plays varied roles in regulating kinesin motor activity, in addition to governing the association/dissociation of cargos [63, 64] as well as the strength of binding to microtubules [65, 66]. Binding of kinesins to adaptor proteins and cargos has also been shown to be modulated by Ca2+ signalling through Ca2+ responsive motifs in adaptor proteins [67] and by the GTP/GDP bound state of Rab GTPases that play intrinsic roles in organelle localisation [68, 69].

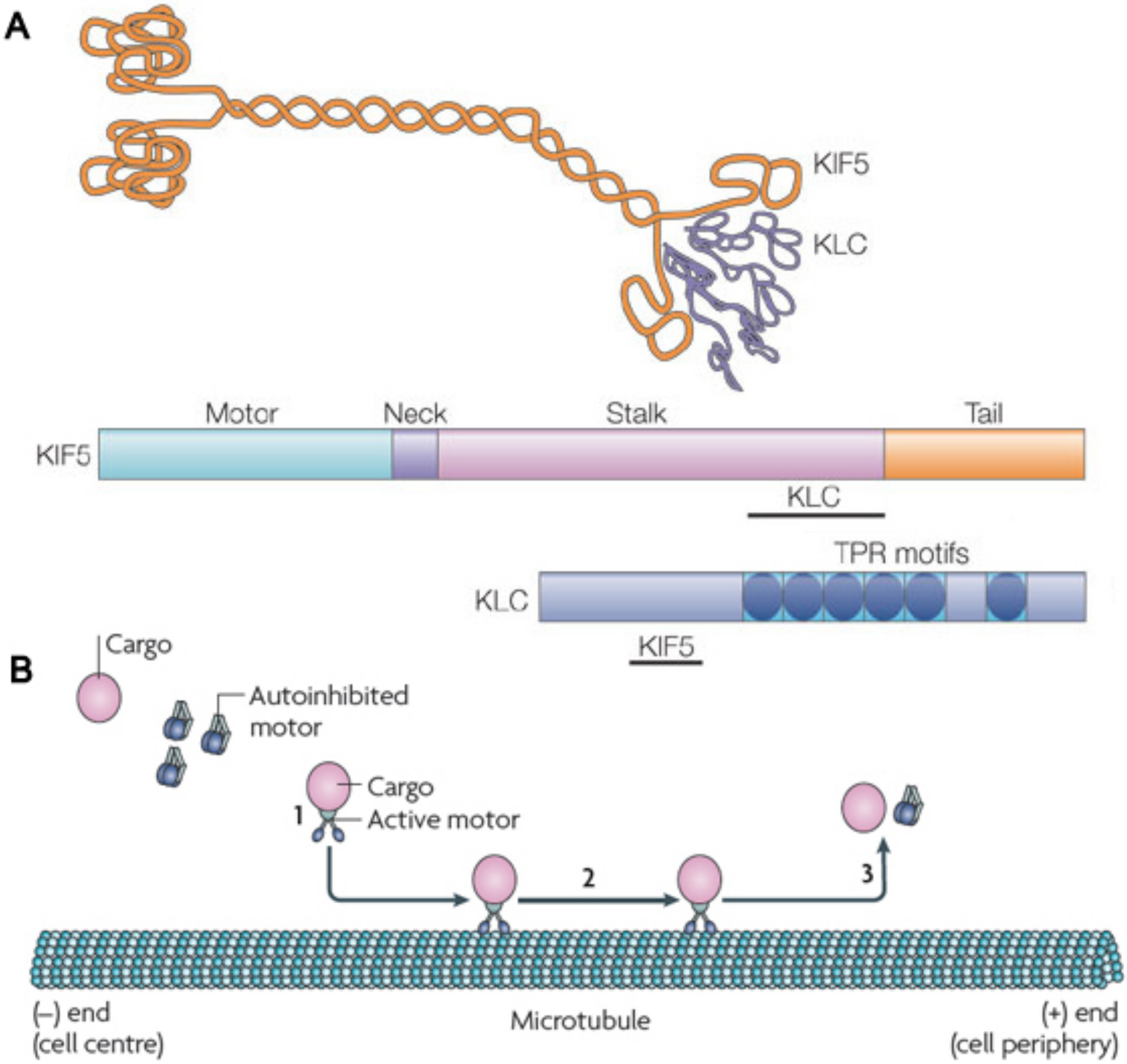

Figure 1.2: **Kinesin-1 and transport along microtubules**

(A) A diagrammatic representation of KIF5. Two kinesin-1 heavy chains form a heterotetramer with two KLC in their cargo binding tail regions, represented on the right. The motor domain is represented on the left. Black bars in the domain representations of KIF5 and KLC indicate regions of binding. From [45]. (B) Transport is initiated when cargos bind to autoinhibited kinesin motor complexes, which then associate with microtubules for processive movement from the minus end near the centre of the cell toward the plus end near the cell periphery. Upon reaching transport destinations, cargo binding is released, with the motor re-entering its autoinhibited state. Adapted from [61].

1.1.3.3 Dynein

Although dyneins represent a large family of proteins, a single member, cytoplasmic dynein is responsible for almost all retrograde microtubule transport in non-neuronal cells, with reported biological functions ranging from vesicular transport to maintaining the cytoplasmic localisation of organelles, such as the Golgi apparatus. Intraflagellar transport (IFT) dynein is the only other member in the family involved in cytoplasmic transport, with all others functioning in the axonemes that power cilia and flagella [70].

Cytoplasmic dynein consists of 9 polypeptides: two heavy chains (DYNC1H), two intermediate chains (DYNC1I), two light intermediate chains (DYNC1LI) and three light chains (TxTex1/DYNLT1, LC8/ DYNLL1, roadblock/LC7/DYNLRB1) [71] [**Figure 1.3**]. The dynein heavy chain houses the catalytic subunit of the cytoplasmic dynein complex; it is an AAA+ (ATPases Associated with cellular Activities) that at its C-terminus possesses a microtubule-binding domain and a motor domain. The motor domain is composed of six AAA+ modules that hydrolyse ATP eliciting processive movement along microtubules in a manner similar to kinesin [72]. The N-terminus of dynein is required for self-dimerisation and the docking of non-catalytic subunits to the complex, in addition to the mediation of cargo and dynein adaptor binding [72].

The functions of cytoplasmic dynein are governed by dynein adaptors such as dynactin, lissencephaly 1 (LIS1), nuclear distribution protein E (NUDE), NUDE-like (NUDEL), RZZ and Bicaudal D. Some of these adaptors mediate cargo binding, while others have dramatic effects on the mechanics of the motor domain [70]. Arguably the best characterised of these adaptors is dynactin, which is itself a large, multi-subunit protein complex consisting of $p150^{Glued}$, p62, dynamitin (p50), Arp1, Arp11, β-actin, CapZ α/β, p24, p27 and p25 [73].

One of the key effects of dynactin on cytoplasmic dynein is to enhance processivity, which allows for the transport of cargos over long distances within the cytoplasm [74-76]. In many eukaryotic systems dynactin modulates localisation of dynein to the plus-end of microtubules, where dynein complexes are recruited to bind to cargo for retrograde transport [70]. The requirement of dynactin for many aspects of dynein function is apparent by the functional abrogation of dynein from loss-of-function alleles of dynactin subunits, for example $p150^{Glued}$ [77, 78].

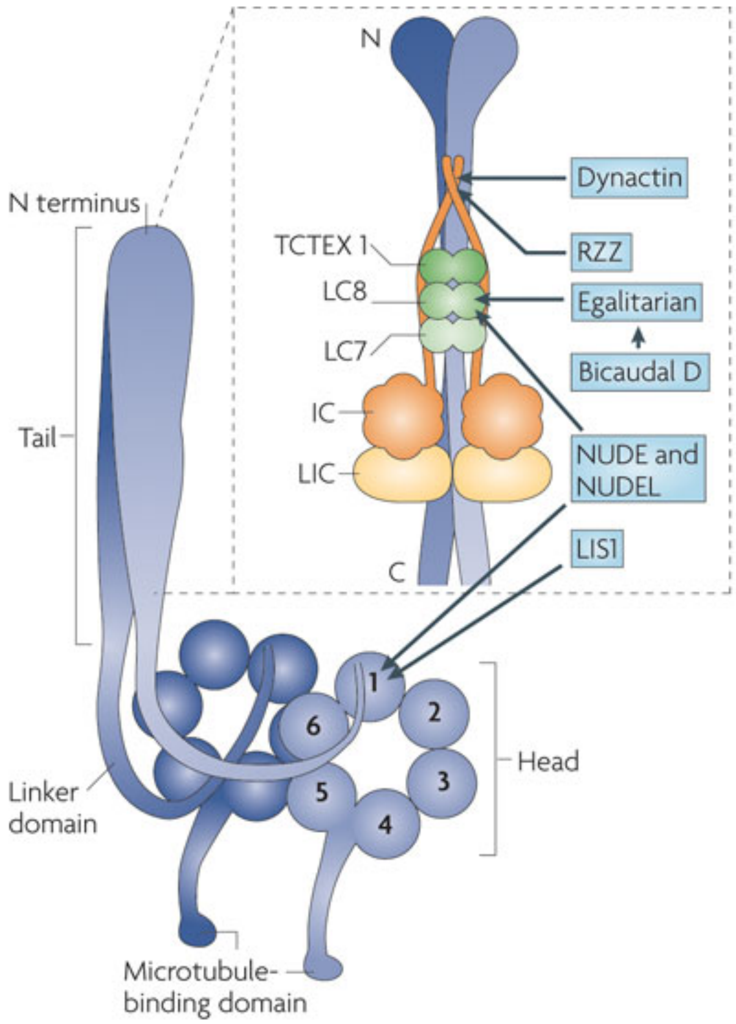

Figure 1.3: Dynein composition and binding of accessory proteins

The C-terminal domain of the dynein heavy chain (HC) is responsible for microtubule binding and ATPase activity for processive movement along microtubules. The N-terminal region mediates dimerisation, as well as binding to the intermediate (IC), light intermediate (LIC) and light chains (LC), with LC binding indirectly through the IC. Dynein adaptors Dynactin, RZZ, Bicaudal D (through interaction partner Egalitarian), NUDE, NUDEL and LIS1 then interact with dynein through various components of the complex or through direct interaction with HC. From [70].

1.1.4 The actin cytoskeleton

A primary role of the actin cytoskeleton in eukaryotic cells is a structural one, maintaining their three dimensional shape. Beyond this, it is involved in essentially all cellular processes, significantly cellular motility, the formation of cellular extensions, endocytosis, cytokinesis and intracellular transport [79]. The role of actin in intracellular transport is two-fold, as a propulsive force through polymerisation and the utilisation of actin filaments as tracts for mysosin motors [80]. Cellular actin is highly conserved between different species and is the most abundant protein in many cell types, making up as much of 5% of total cell protein, signifying its essentiality to cell function [81].

There are six actin isoforms in vertebrates, four of which form contractile tissues in muscle cells; α-skeletal and α-cardiac in striated muscle and α- and γ-isoforms in smooth muscle [82, 83]. The remaining two isoforms, β- and γ- cytoplasmic actin, are ubiquitous and together form the actin cytoskeleton in many cell types [84]. Although β- and γ- cytoplasmic isoforms are identical barring four conservative amino acid differences at their N-terminus, they have distinct but overlapping cellular localisations with discrete functional roles being the emerging paradigm from recent research [85]. The preferential localisation of β-actin to stress fibres, circular bundles and cell-cell contacts suggests a role in cell attachment and contraction, while the concentration of γ-actin at cortical and lamellipodial structures in moving cells is consistant with a role in cell motility [85].

The monomeric, G (globular)-actin form of β- and γ-isoforms polymerise to form F (filamentous)-actin. Actin filaments are polar and have a plus-ends and minus-ends (more commonly referred to as the “barbed” and “pointed” ends, respectively, owing to their appearance when decorated with myosin S1 fragments) [86]. Although G-actin monomers can be added on both ends, addition to the barbed end occurs at a much faster rate than at the pointed end [87].

Actin is also an ATPase; monomers bound to ATP are preferentially added to the filament and are subsequently hydrolysed to ADP.Pi over time [88]. As this process occurs at a slower rate than addition of monomers to the barbed end, a cap of ATP-bound actin forms at the barbed end, while ADP-bound actin dominates at the pointed end. The slight change in the structure of actin when bound to ATP or ADP results in the barbed and pointed end of the actin filament having different critical concentrations (the lowest concentration of monomers in the surrounding region required for their addition to the filament), which is 0.06 μM for the barbed end and 0.6 μM for the pointed end [89].

At steady state, when the overall length of filaments is stable, a process called treadmilling may occur. This is when elongation at the barbed end occurs at the same rate as depolymerisation at the pointed end, so that the filament appears to move forward while maintaining the same length [89]. The concentration of G-actin in the cell cytoplasm ranges between 20-100 µM, far above the critical concentrations (of both barbed and pointed ends) for native actin filaments; it is therefore necessary to sequester G-actin so that filament formation can be regulated. Sequestering of G-actin is achieved through the binding of accessory proteins such as thymosin β4 [90] or profilin [91] [**Figure 1.4: (11)**].

Polymerisation of F-actin from G-actin monomers and the subsequent controlled depolymerisation back to G-actin underlies the dynamic functionality of the actin cytoskeleton [92]. Although filaments may nucleate from single actin monomers, small actin oligomers are unstable and it is therefore the formation of new filaments that is the rate-limiting step in regulating the dynamics and function of the actin cytoskeleton [88]. Nucleation requires *de novo* synthesis of F-actin through actin nucleators such as the Arp2/3 complex, formins, Spire, cordon-bleu and leiomodin [93] [**Figure 1.5**].

Actin nucleators coordinate and orientate G-actin to the nascent F-actin filament to stimulate polymerisation in three main ways. Firstly, the Arp2/3 complex binds to the side of an existing actin filament and initiates the assembly of a new filament generating 70° branches [**Figure 1.4: (4)**]. The Arp2/3 complex forms a cap at the nascent filament's pointed end, while addition of actin monomers may continue at the barbed end [**Figure 1.4: (5)**] [94]. On its own, the Arp2/3 complex does not nucleate actin filaments efficiently and rates of nucleation are dramatically increased by the presence and binding of Nucleation Promoting Factors (NPFs) such as the Wiskott-Aldrich Syndrome Protein family proteins. Important members of this family are WASP (Wiskott-Aldritch Syndrome Protein) and N-WASP (Neural WASP) [95]. NPFs increase the nucleation efficiency of the Arp2/3 complex via their WH2 (WASP Homology 2) domains recruiting and orienting G-actin to the nascent F-actin seed [96].

Unlike the Arp2/3 complex, all other known actin nucleators generate unbranched filaments. Formins possess conserved formin homology (FH) domains that bind to the barbed ends of actin and act as a processive cap on the elongating filament. Similarly to formins, all other nucleators that have been identified contain G-actin-binding motifs that function in a similar manner as FH domains; these include WH2 domains in Spire that may introduce three or more actin monomers to the nascent actin filament simultaneously [93] [**Figure 1.5**].

Accessory proteins are critical to the regulation of actin polymerisation and dynamics [84]. These include the aforementioned proteins that sequester G-actin as well as proteins that prevent the further addition of G-actin to filaments (CapZ, [97]) [**Figure 1.4: (7)**]. Other accessory proteins stabilise (tropomodulins, [98]), depolymerise (actin depolymerising factor/cofilin, [99]) [**Figure 1.4: (9)**], sever (gelsolin, [100]) and bundle actin filaments (fascin-1, [101]). Many of these actin binding proteins are pleiotropic; profilin, for example, beyond its role in ADP:ATP exchange [**Figure 1.4: (10)**] and sequestering actin, can also inhibit nucleation while allowing filament extension [102].

The signalling cascades that regulate the dynamic remodelling of cellular actin are primarily through Rho GTPases, of which there are approximately 20 in humans, including Rho, Rac and Cdc42 [103]. Guanine nucleotide exchange factors (GEFs) or GTPase-activating proteins (GAPs) activate Rho GTPases that then bind to downstream effectors such as protein kinases, actin nucleators and NPFs, which can stimulate assembly and disassembly of F-actin [**Figure 1.4: (2)-(3)**] [104].

The polymerisation of G-actin into F-actin is not the only mechanism for actin-based motility in the cell cytoplasm. Like the microtubule network with kinesins and dyneins, ATP-driven molecular motors in the myosin family can traverse actin filaments to effect intracellular transport of cargoes.

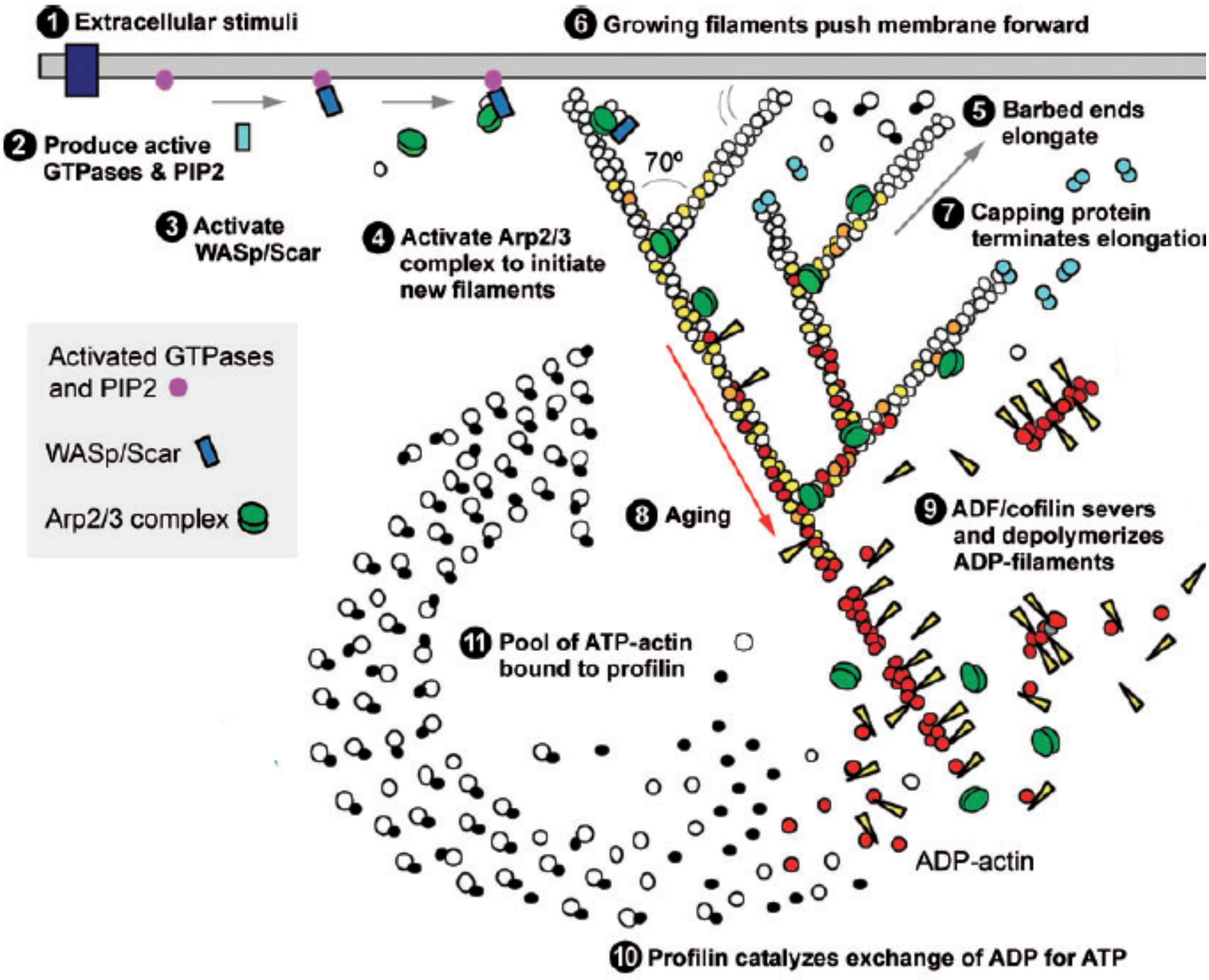

Figure 1.4: F-actin formation by Arp2/3 and interaction of adaptor proteins
Filaments are nucleated with Arp2/3; generating F-actin by addition of ATP-actin at the barbed end near the plasma membrane. This nucleation may occur in the cytoplasm or on already formed filaments, generating 70o branch points. Filaments can be capped by capping proteins or bundled by adaptors. At the pointed end (-) of the filament, depolymerisation of F-actin occurs, often with the aid of severing adaptors such as ADF/Cofilin. Monomers can then be sequestered, or bound to profilin for exchange of ADP to ATP. From [105].

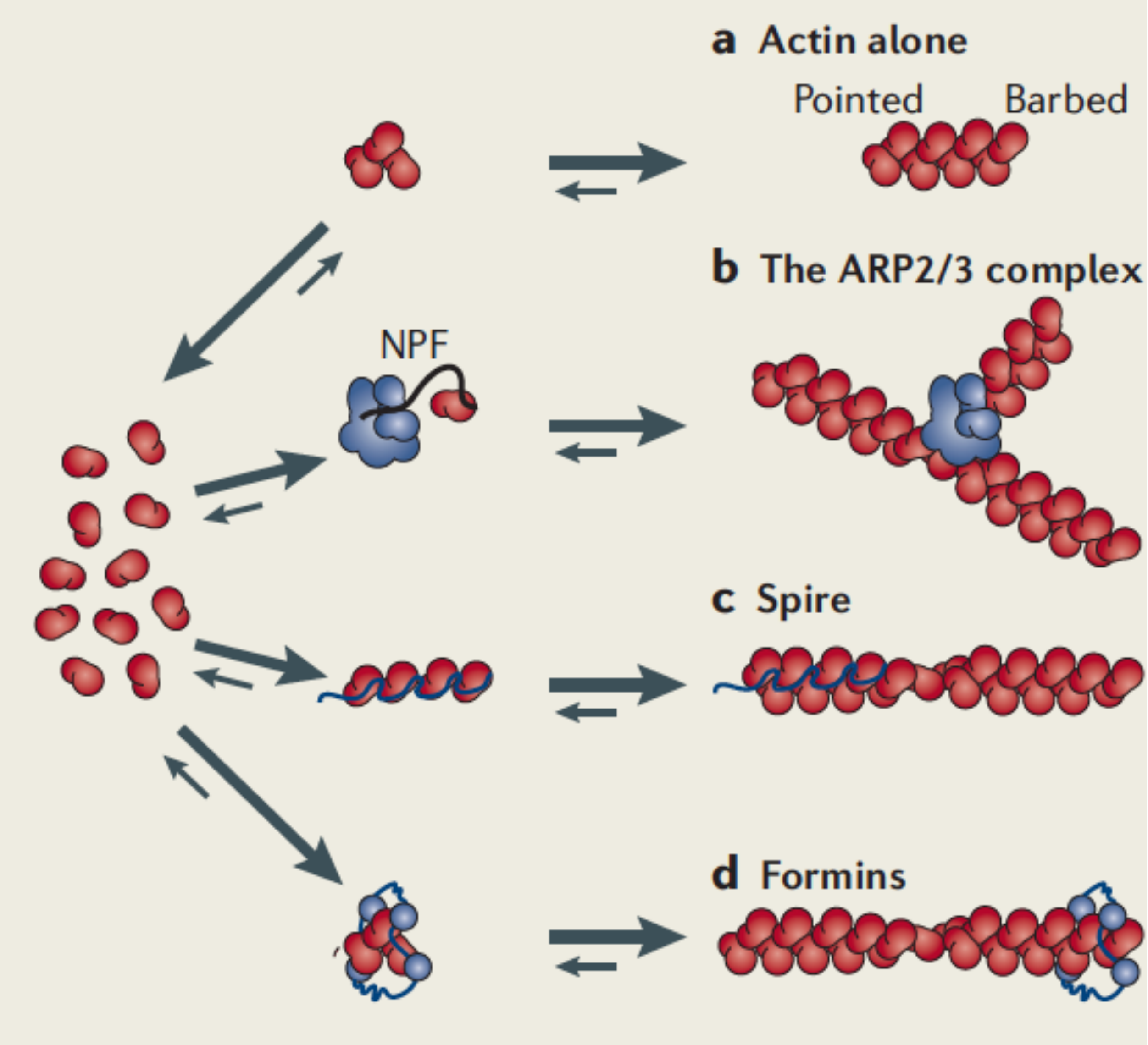

Figure 1.5: Different actin nucleators

While actin alone (a) is capable of nucleating and forming filaments, this is kinetically unfavourable and actin nucleators dramatically improve the efficiency of filament formation. Actin nucleators may form branched arrays such is the case with Arp2/3 (with the aid of NPFs) by binding along previously formed actin filaments and mimicking an actin dimer (b). Other nucleators form unbranched filaments, either with tandem WH2 domains forming a scaffold for addition of actin monomers such as the case of Spire (c) or with FH2 domains in formins stabilising actin dimers and extending along a growing filament to promote nucleation as a processive cap (d). From [106].

1.1.4.2 Myosin

Myosins represent a superfamily of F-actin motor proteins with more than 35 classes discovered. All classes characterised thus far, with the exception of class VI, are plus-end directed motors. The best understood member is muscle Myosin II that together with actin filaments forms the sarcomere that generates the force required for muscle contraction. Other myosins are involved in a broad range of biological processes, from cytokinesis to vesicle and organelle transport, as well as being implicated in the transport of RNA polymerases in the nucleus [107, 108].

Similar to kinesins, myosins have a N-terminal motor “head” domain, a variable “neck” domain and a C-terminal cargo-binding “tail” domain. The motor domain has an actin and ATP binding site. The motor generates movement through a swinging lever arm mechanism, in which the swinging lever arm is the distal part of the head not bound to the actin filament [109] [**Figure 1.6**]. The movement is driven by the innate ATPase activity of the myosin that hydrolyses ATP to ADP.Pi, which is subsequently released and exchanged for ATP. This reaction elicits the conformational changes in the head domain resulting in movement along the actin filament [110] [**Figure 1.6**].

Although myosins are able to function as monomers and oligomers (as in the sarcomere of muscles), the majority of those involved in cytoplasmic transport such as Myosin V are dimers with two motor domains complexed with multiple myosin light chains to form functional motor complexes [107]. These motors undergo step-wise processive movement along actin filaments, resembling the action of kinesin-1 along microtubules [111].

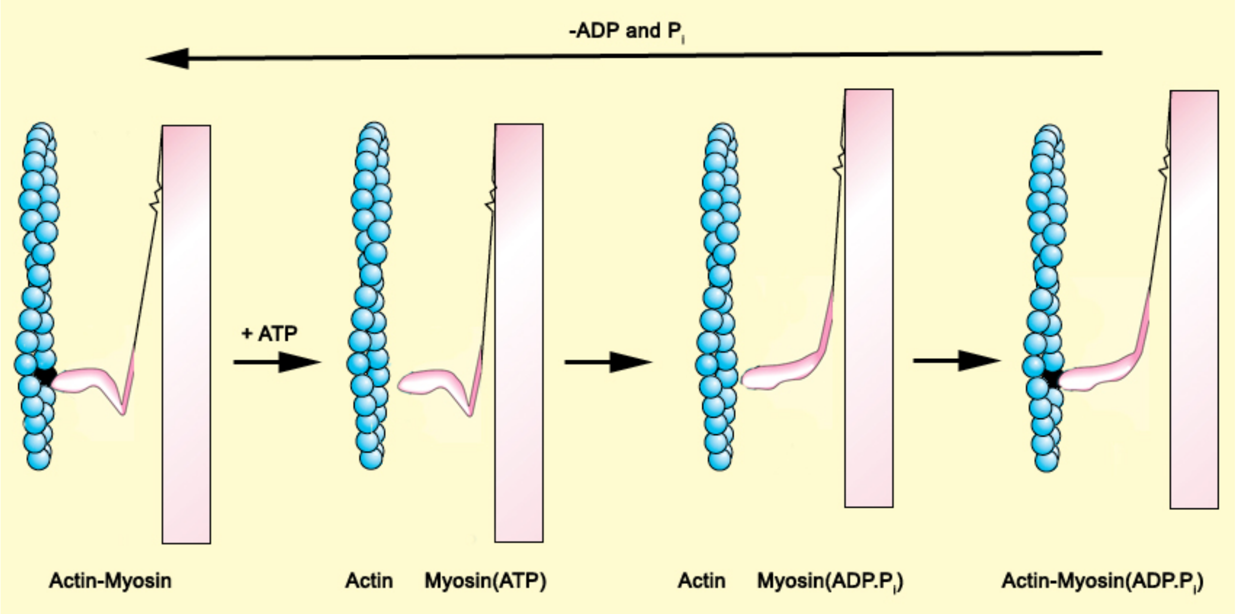

Figure 1.6: The swinging lever arm cross-bridge mechanism of myosin force generation

When actin and myosin are bound in their rigor state, the distal part of the myosin head is bent. Binding of ATP to myosin releases binding to the actin filament, with ATP hydrolysis to ADP.Pi allowing the binding to the actin filament again. This stimulates the release of ADP.Pi, which causes a conformational change in the distal part of the head, generating a pulling force along the filament. In myosin-based transport of cargo, each release allows binding further along the filament, with the other chain of the myosin dimer retaining an association to the filament and allowing processive movement. Adapted from [109].

1.2 PATHOGEN SUBVERSION OF HOST-CELL TRANSPORT MECHANISMS

1.2.1 Introduction

Pathogens encode a diverse range of factors that interact with the preexisting regulatory pathways of the host cell machinery to manipulate transport mechanisms including those based on the microtubule and actin cytoskeletons. Such pathogen-encoded factors are varied in their mode of action but all contribute to the intracellular motility and/or intercellular spread of the pathogen. In many cases, they are critical virulence factors that when absent, severely attenuate spread of the microbe.

1.2.2 Microtubule-based transport of intracellular pathogens

Pathogen utilisation of the microtubule network for subcellular transport is the major mechanism used by viruses for subcellular motility as they rely on host cell machinery for their often extremely complex replicative cycles. Viruses require well-regulated trafficking not only to enter the cell but also to transport viral components to their appropriate subcellular locations for virus assembly, organise viral replication organelles and additionally in the dispersal of mature progeny virus.

Many viruses display a reliance on microtubules for their replicative cycles; these range from relatively small retroviruses like human immunodeficiency virus-1 (HIV-1, ~100 nm) to large double stranded DNA viruses such as herpes simplex virus-1 (HSV-1, ~300 nm) and vaccinia virus (VACV, ~400 nm) [**Table 1.1**]. For most of these viruses, the utilisation of microtubules following cell entry has been well described [see **Table 1.1**, for references]. Although they are also likely to utilise microtubules for subsequent egress, this has been less widely characterised, being restricted to a few members of Adenoviridae, Asfaviridae, Retroviridae. Herpesviridae and Orthopoxviridae.

In most cases, the subversion of the microtubule network is dependent on molecular motors transporting viral cargos as it would transport cellular cargos. However, microtubules are often also manipulated in motor-independent ways, for example, human T cell leukaemia virus orientate the MTOC to cell-to-cell contacts where a virological synapse can form to promote dissemination [112, 113]. Both VACV and African swine fever virus (ASFV) disrupt centrosomes interfering with the nucleation of microtubules [114, 115]. VACV additionally affects microtubule dynamics through viral protein F11-mediated modulation of Ras family gene homology member A (RhoA) [116]. RhoA has diverse physiological roles in regulating microtubules, these include outgrowth for motility as well as intitial polarisation of the microtubule cytoskeleton [117]. How this aspect of viral-mediated microtubule remodelling aids in infection has yet to be elucidated.

The reliance of viruses on motor-dependent microtubule-based transport is not generally reflected in bacterial pathogens. A few species including *Citrobacter freundii*, *Serratia marcescens, Escherischia coli, Listeria* and *Salmonella* utilise the microtubule cytoskeleton to infect host-cells [118, 119] and while the mechanisms behind these processes are not well understood, they likely involve microtubule remodelling to permit invasion. There are however a few notable examples, namely *Wolbachia, Salmonella*, *Chlamydia trachomatis, Campylobacter jejuni* and *Orientia tsutsugamushi* that utilise motor-dependent microtubule-based subcellular transport in their replicative cycles [see **Table 1.1**].

For many of the aforementioned viral and bacterial pathogens, the motors involved in the particular motor-dependent transport processes have been elucidated, these are listed in **Table 1.1** and key examples will be discussed below.

Table 1.1. Microtubule-based motor-dependent transport of intracellular pathogens

FAMILY	PATHOGEN	MOTORS INVOLVED	REFERENCES
Viruses			
Adenoviridae	Adenovirus (AdV)	Dynein, kinesin-1	[120-123]
Parvoviridae	Adeno-associated virus (AAV)	?	[124]
	Canine parvovirus	Dynein	[125]
Asfarviridae	African swine fever virus (ASFV)	Dynein, kinesin-1	[126-128]
Herpesviridae	HSV-1	Dynein, kinesin-1, kinesin-3	[129-134]
	Pseudorabies virus (PrV)	Dynein, kinesin-3	[135-137]
	Human cytomegalovirus (HCMV)	?	[138]
	Karposi's Sarcoma-associated herpesvirus (KSHV)	Kinesin-2	[139]
	Rhesus rhadinovirus	Dynein	[140]
	Equine herpesvirus type 1	Dynein	[141]
Rhabdoviridae	Rabies virus 1	Dynein	[142]
	Mokola virus 3	Dynein	[142]
Retroviridae	Human foamy virus	?	[143]
	HIV-1	Dynein, kinesin-2, kinesin-4	[144-148]
	Bovine immunodeficiency virus	Dynein	[149]
Hepadnaviridae	Hepatitis B (HBV)	?	[150]
	Hepatitis C (HCV)	Dynein	[151]
Papillomaviridae	Human papillomavirus (HPV)	Dynein	[152, 153]
Polyomaviridae	Simian virus 40 (SV40)	Dynein	[154, 155]
	Murine polyomavirus (MPYV)	?	[156]

Reoviridae	Mammalian orthoreovirus	Dynein	[153, 157]
Paramyxoviridae	Sendai Virus (SeV)	?	[158]
Orthomyxoviridae	Influenza virus	Dynein	[159]
Picornaviridae	Poliovirus	Dynein	[160]
Arenaviridae	Lassa virus (LASV)	Kinesin-3	[161]
Filoviridae	Ebola virus (EBOV)	Dynein	[162]
Orthopoxviridae	VACV	Dynein, kinesin-1	[114, 163]
Flaviviridae	Dengue virus	Dynein	[164]
	West Nile virus	Dynein	[164]
Bacteria			
	Wolbachia	Dynein, kinesin-1	[165, 166]
	Salmonella	Dynein, kinesin-1	[167, 168]
	Chlamydia trachomatis	Dynein	[169]
	Campylobacter jejuni	Dynein	[170]
	Orientia tsutsugamushi	Dynein	[171]

1.2.2.1 Dynein

As obligate parasites, viral pathogens replicate within susceptible, living host cells. Many DNA viruses establish replication centres within the nucleus where host cell DNA replication machinery resides [172]. Viruses that replicate in the cytoplasm, including DNA viruses that encode their own replication machinery (such as members of Poxviridae) and many RNA viruses that utilise host cell machinery, form replication centres in peri-nuclear locations proximal to the centrosome [173] [**Figure 1.7**].

Upon entry into the cell, which may occur via fusogenic or endocytotic pathways, viruses commonly undergo retrograde transport along microtubules to establish sites of replication. For a number of viruses, an interaction with a molecular motor has yet to be characterised (Adeno-associated virus [AAV], Pseudorabies virus [PrV], Human cytomegalovirus [HCMV], Murine polyomavirus [MPYV] and Sendai virus [SeV]) and in these instances, microtubule dependent retrograde transport has been verified in three main ways [124, 135, 138, 156, 158]. Firstly, immunofluorescence assays (IFA) have demonstrated viral particle colocalisation with microtubules. Secondly, live cell microscopy revealed directional saltatory transport with speeds consistent with microtubule-based motility. Finally, treatment with the microtubule destabilising agent nocodazole has been demonstrated to inhibit viral replication or movement into the perinuclear region.

For many viruses that undergo retrograde transport, the specific involvement of dynein has been validated [**Table 1.1**], either through direct protein interaction studies, IFA colocalisation with dynein or the abrogration of retrograde transport following treatment of cells with anti-dynein antibodies or dominant negative expression of dynein and dynein adaptor subunits [**Table 1.1**]. Furthermore, the specific viral proteins that mediate interactions with dynein have been eludicated in several cases. In adenovirus, the capsid hexon subunit interacts directly with dynein intermediate chains and light intermediate chains in a pH-dependent manner (requiring a pH <5.5 for activation of the interaction). This reflects the pathophysiology of adenovirus, which enters the cell via an endocytotic vesicle with a final pH estimated to be ≤ 5.5 before being transported to the nucleus [122] [**Figure 1.7**].

In many cases the identification of viral protein/s involved in dynein recruitment has proved more elusive. HSV-1 is a prime example where multiple protein interactions between dynein components and viral proteins have been elucidated through biochemical assays, yet remain to be functionally validated [136]. Currently, the leading candidates include inner tegument proteins UL36 (VP1/2) and UL37 [174]. Inner tegument has been shown to bind to dynein and dynactin components in cytosolic cell extracts and capsids deficient of inner tegument are unable to be transported through the cytoplasm [174]. Conversely, deletions of UL37 in closely related PrV has demonstrated a delay in retrograde transport rather than complete abrogation, perhaps indicating a degree of functional redundancy between proteins mediating dynein interaction [175, 176].

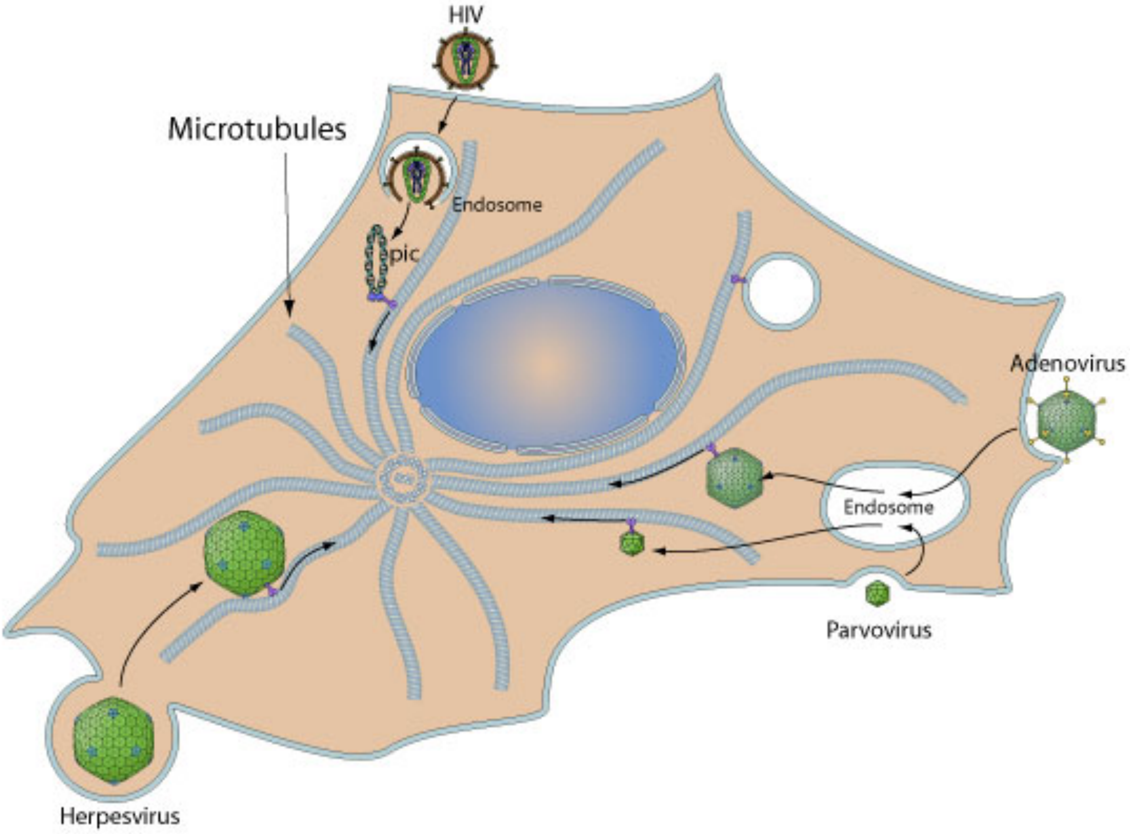

Figure 1.7: Viral entry and transport to the centrosome
Diverse families of viruses undergo dynein-mediated retrograde transport along microtubules to perinuclear locations. Herpesvirus enters the cell through membrane fusion and nucleocapsids are transported to the centrosome before entering the nucleus. Adenovirus and parvovirus enter via endosomes before being transported. HIV also enters via an endosome, but fuses with the endosomal membrane for uncoating, so only its preintergration complex (PIC) is trafficked to the perinuclear region. From http://viralzone.expasy.org/all_by_protein/983.html, accessed 30/09/2013.

1.2.2.2 Kinesin

Viral particles that egress to the cell periphery following replication and morphogenesis face similar challenges as incoming viruses, but in reverse. While in some instances, anterograde microtubule transport has been reported without an elucidated motor (Hepatitus B [HBV], [177]), in better-characterised viruses kinesin-1, kinesin-2, kinesin-3 and kinesin-4 have all been implicated in viral transport.

For Adenovirus [AdV] (kinesin-1, [123]), ASFV (kinesin-1, [128]), VACV (kinesin-1, [163]), Karposi's Sarcoma-associated herpesvirus [KSHV] (kinesin-2, [139]), Pseudorabies virus [PrV] (kinesin-3, [137]) and Lassa virus [LASV] (kinesin-3, [161]), a single kinesin motor has been reported as essential for efficient virus dissemination. With the exception of AdV, a simple transport paradigm exists where viral proteins such as ORF45 (KSHV) interact with kinesin subunits such as KIF3A for anterograde transport to the cell periphery [139]. Conversely, in the case of AdV, kinesin-1 is involved in viral entry into the nucleus through the nuclear pore complex (NPC); this process involves the simultaneous binding of NPC proteins and kinesin-1 subunits to the capsid, which leads to increased nuclear envelope permeability and viral uncoating resulting in entry of the viral genome to the nucleus [123].

For HSV-1, three (kinesin-1, kinesin-2, kinesin-3) kinesin motors are implicated in virus transport [132-134]. The kinesin-1 interaction follows the egress transport paradigm outlined previously, with US11 interacting with the heptad repeat binding region of KIF5B to transport non-enveloped HSV-1 nucleocapsids through the cytoplasm [132]. The kinesin-2 interaction on the other hand mediates anterograde transport of envelope glycoproteins for virion assembly, rather than the transport of virus particles themselves [133].

For HIV-1, two (kinesin-2, kinesin 4) kinesin motors are implicated in virus transport [146, 147]. The kinesin-2 interaction in HIV-1 follows the classical egress transport paradigm like HSV-1 and KIF5B, with KIF3A transporting HIV-1 containing compartments in macrophages for viral release [147]. The remaining kinesin interaction with kinesin-4 motor KIF4 mediates anterograde transport of viral component Gag for virion assembly [146].

Salmonella replicates in a compartment called the *Salmonella*-containing vacuole (SCV) that displays a perinuclear localisation for most of the infectious cycle, but subsequently relocates to the cell periphery to aid bacterial dissemination. This movement is microtubule and kinesin-1 dependent. PipB2 and SifA localise to the surface of SCV and *Salmonella*-induced filaments [Sifs]) and recruit inactive kinesin-1 and SKIP (SifA and kinesin-interacting protein) respectively [178, 179]. SKIP then interacts with the TPR domain of KLC and activates kinesin-1 to mediate anterograde transport [168].

1.2.2.3 Bidirectional transport

Cytoplasmic transport of viral cargos is not as simple as retrograde transport occurring during entry and anterograde transport during egress. In fact, HSV-1 and PrV undergo bidirectional transport during their entry and egress, AdV during its entry and VACV during its egress [120, 180, 181]. Bidirectional saltatory transport of endosomes, vesicles and mitochondria is typical in cellular contexts and although the purpose of this movement is unclear, it may facilitate roaming over larger regions of the cell, effective distribution, circumventing of obstacles and erroneous transport correction, all of which are qualities that would also be pertinent in a viral context [131, 182]. In HSV-1, the simultaneous binding of both retrograde (dynein) and anterograde (kinesin-1) motors has been demonstrated, although how directionality is determined and regulated remains to be clarified [134].

1.2.3 Actin-based motility

Pathogens manipulate the actin cytoskeleton in a variety of ways to aid their replicative cycles and infection of neighbouring cells. These include restructuring or bypassing the dense actin cortex to infect cells (for example, the internalisation of SV40 into caveolae, [183]), activating cell signalling pathways that remodel actin and induce cell motility (for example, Human T-lymphotrophic virus-1 [HTLV-1], [184]), myosin-based mechanisms that induce so-called 'surfing' along filopodia towards the cell body prior for infection (MLV, [185]), myosin-based exocytotic release of infectious progeny (HSV-1, [186]), virus-tipped filopodial formation (HIV-1, [187]) and Arp2/3 complex-based actin nucleation.

Of these, Arp2/3 complex-based actin nucleation is one of the best-understood mechanisms of actin-based motility. Many pathogens that have been found to utilise this actin based motility are intracellular bacterial species. They include *Listeria monocytogenes*, *Shigella flexineri*, *Rickettsia coronii, Rickettsia rickettsii, Mycobacterium marinum* and *Burkholderia psuedomallei* [see **Table 1.2** for references]. All these bacterial species utilise varying yet overlapping set of regulatory components to manipulate host pathways for their motility, ultimately leading to modulation of the activity of the Arp2/3 complex. Poxviruses and baculovirus are the only known viral pathogens demonstrated to use actin-based motility.

Enterohaemorrhagic and enteropathogenic *Escherichia coli* (EHEC and EPEC) do not grow intracellularly but are nonetheless able to mediate cellular actin polymerisation [188, 189]. This manifests as the formation of actin 'pedestals' directly under the cell surface where extracellular bacteria come into contact with the cell. While pathogen-mediated actin polymerisation generally aids in intracellular spread, in EHEC and EPEC it promotes adherence of bacteria to the gut epithelium.

Table 1.2. Actin-based transport of intracellular pathogens

FAMILY	PATHOGEN	NUCLEATOR/MOTOR INVOLVED (MICROBIAL FACTOR)	REFERENCES
Viruses			
Poxviridae	VACV	Arp2/3 complex (A36)	[190, 191]
	Variola virus (VARV)	Arp2/3 complex	[192]
	Monkeypox virus (MPXV)	Arp2/3 complex	[192]
Baculoviridae	*Autographa californica* multiple nucleopolyhedrovirus (AcMNPV)	Arp2/3 complex (P78/83)	[193]
Flaviviridae	HCV	Myosin 18A – endocytotic pathways	[194]
Herpesviridae	HSV-1	Myosin Va	[186]
	KSHV	c-Cbl-myosin IIA	[195, 196]
Lentiviridae	HIV-1	Myosin II	[197]
	HIV-1	Diaphanous 2	[187]
Bacteria			
	Listeria monocytogenes	Arp2/3 complex (ActA)	[198-201]
	Shigella flexineri	Arp2/3 complex (IcsA)	[202]
	Rickettsia coronii	Arp2/3 complex (RickA)	[81]
	Rickettsia rickettsii	Arp2/3 complex (RickA)	[203]
	Mycobacterium marinum	Arp2/3 complex (unknown)	[204, 205]
	Burkholderia pseudomallei	? (BimA)	[206, 207]
	Enteropathogenic or Enterohaemorraghic Escherichia coli (EPEC)	Arp2/3 complex (Tir)	[188, 189]

1.2.3.1 Nucleation

Almost all actin-nucleating pathogens identified thus far utilise the Arp2/3 complex for their motility (with the exception of *B. pseudomallei*). As previously mentioned, the Arp2/3 complex is an actin nucleator that generates branching arrays due to the formation of new actin filments attached at 70^{o} angle branch points from previously formed actin filaments [94] [**Figure 1.4**]. The Arp2/3 complex is composed of seven polypeptides; two of these, Arp2 and Arp3, are actin-related proteins (ARPs) that share structural similarities and amino acid identity to cellular actin isoforms. Upon activation, they provide a template upon which G-actin can be oriented [92]. *De novo* filament formation increases total levels of actin polymerisation and is able to provide a propulsive force to facilitate cellular processes such as rocketing vesicles and migration of the leading edge during cellular motility.

The NPFs such as WASP and N-WASP are able to dramatically increase rates of Arp2/3 complex-based nucleation. These NPFs possess a VCA domain at their C-terminus containing two verprolin homology (V) domains, also known as WASP homology 2 (WH2) domains, a cofilin homology (C) domain and an acidic (A) domain, which together provides a binding site for monomeric actin and the Arp2/3 complex [208]. NPFs increase nucleation efficiency of the Arp2/3 complex via their WH2 domains recruiting and orienting G-actin to the nascent F-actin seed [96], while the CA domains are thought to bind and induce conformational changes within the complex [209].

The inactive form of N-WASP has its Arp2/3 complex binding site occluded by autoregulatory elements at the amino terminal end of the protein [81]. Upon activation by the Rho GTPase Cdc42, a conformational change is induced in the N-WASP and the autoinhibition relieved [210].

Pathogens that nucleate actin can be grouped into two categories, those that encode NPF mimics (*L. monocytogenes, R. rickettsii/coronni, B. pseudomallei*) and those that recruit cellular NPFs (*S. flexineri, M. marinarum,* EPEC/EHEC and poxviruses) [211]. Each pathogen is able to generate F-actin structures with characteristic morphologies (ranging from short, highly cross-linked filaments to long, parallel bundled filaments) and associated characteristic rates of actin polymerisation [207]. These structures are generally referred to as actin comets or tails, with the bacterial cell or virus particle localising to the polymerising face of the structure. Through enhancing intracellular spread, potentially while avoiding immune detection, actin polymerisation has been demonstrated to play an important role in virulence for many of these pathogens [199, 212-215].

L. monocytogenes encodes a WASP family mimic ActA that is essential for motility. ActA possesses a VCA domain for G-actin and Arp2/3 complex binding [199, 201] [**Figure 1.8**]. The central region of ActA has an Enabled-vasodilator stimulated phosphoprotein (Ena-VASP) binding site that recruits profilin to the growing end of actin filaments, enhancing the rate of actin polymerisation [216]. This effect is responsible for increasing rates of dissociation between ActA and the Arp2/3 complex, effectively allowing the bacteria be pushed rapidly from Arp2/3 complex branch points by growing actin filaments [217]. Unlike the cellular homologue WASP, ActA lacks autoinhibitory domains and constitutively enhances actin nucleation [81].

The importance of ActA to *L. monocytogenes* virulence goes further than the stimulation of actin-based motility for cell-to-cell spread protected from host immune defenses [92], with recruitment of ActA to the bacterial cell surface having been found to prevent ubiquitinylation-mediated autophagic destruction of the bacterium [218]. It has also been found to be critical for bacterial aggregation and biofilm formation, which improves persistence of the bacteria in the intestines of mice, as well leading to increased shedding of bacteria in faeces, aiding transmission to other hosts [219].

S. flexineri induces Arp2/3 complex-dependent actin nucleation but recruits host NPFs rather than encoding functional NPF mimics. *S. flexineri* encodes IcsA, a protein that localises to the bacterial cell surface and is essential for actin-based propulsion and recruits N-WASP through a region of glycine rich repeats [**Figure 1.8**]. IcsA is thought to act as a functional mimic of Rho GTPase Cdc42 by disrupting the autoinhibited state of N-WASP [202, 207, 220]. Similarly to *L. monocytogenes*, growing actin filaments push against the surface of intracellular bacteria and propelling them through the cytoplasm and subsequently into neighbouring cells.

All of the pathogens described so far that utilise actin polymerisation utilise the Arp2/3 complex with the exception of *B. pseudomallei,* which encodes the protein BimA. While, the Arp2/3 complex has been shown to colocalise with *B. pseudomallei* induced F-actin strcutures [221], dominant negative experiments that sequester Arp2/3 complex components have no effect on *B. pseudomallei* tails [222]. BimA appears to be a NPF mimic with similar biochemical characteristics to WASP (including 2 WH2 domains) [**Figure 1.8**], yet evidence suggests that the Arp2/3 complex may be unnecessary for polymerisation, with BimA itself serving directly as a nucleator [222].

Interestingly, the nucleocapsids of *Autographa californica* multiple nucleopolyhedrovirus (AcMNPV), a baculovirus that stimulates actin-based motility, undergo motility during two stages of its replicative cycle. First, during the early stage of infection when virus transits to the nucleus and translocates through the nuclear pore complex; and second, for transport and accumulation of nucleocapsids at the cell periphery following the onset of viral gene expression. Both stages of movement require the ability of nucleocapsid protein P78/83 to stimulate actin nucleation with the host Arp2/3 complex. The exact mechanism of this stimulation, whether the Arp2/3 complex is directly or indirectly recruited through an NPF has yet to be determined [193]. The accelerated passage of virus through infected insect tissues that is enabled by actin polymerisation is vital to evasion of host defense mechanisms.

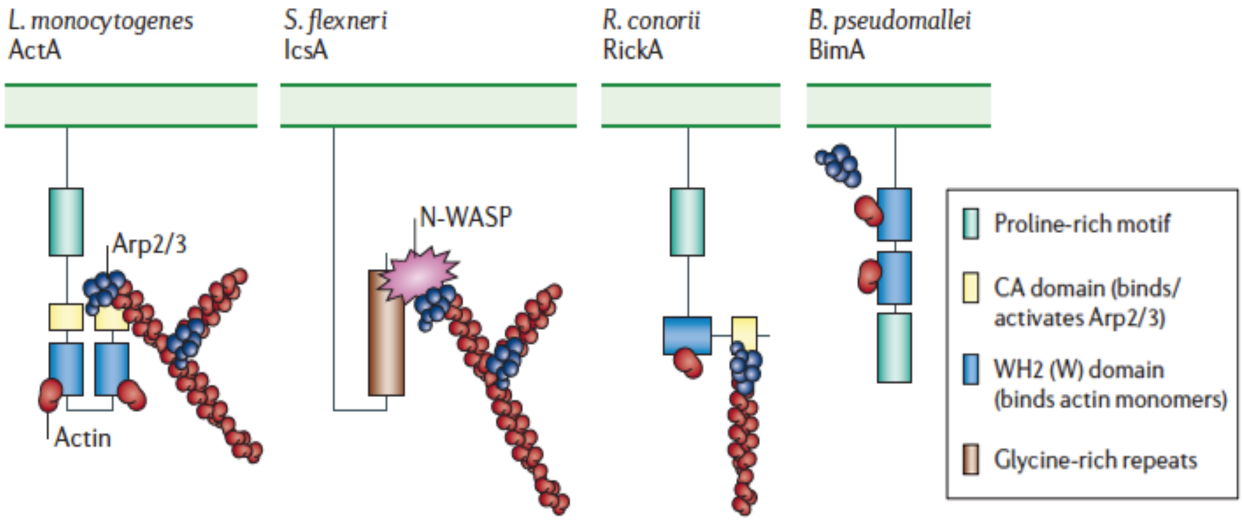

Figure 1.8: Intracellular bacterial actin polymerisation

The membrane of the bacteria *L. monocytogenes, S. flexineri, R. cornorii and B. pseudomallei* are shown in green. Each encodes a transmembrane protein essential for actin-based motility, ActA, IcsA, RickA and BimA respectively. Two of these, ActA, and RickA, are NPF mimics with WH2 domains for actin monomer binding and CA domains that directly recruit and activate Arp2/3. Conversely, IcsA recruits host cell N-WASP that in turn recruits Arp2/3 for polymerisation. The pathway of BimA directed actin polymerisation is unclear, with Arp2/3 potentially not required for nucleation. From [207].

1.3 POXVIRUSES

Poxviridae are a family of large, double stranded DNA viruses that includes many important human, animal and insect pathogens. The family is divided into two subfamilies, Chordopoxvirinae and Entomopoxvidinae that infect vertebrates and insects respectively. These two subfamilies are further divided into 11 recognised genera [**Table 1.3**] with additional species such as yoka virus and cotia virus currently unclassified and potentially representing new genera [223, 224].

Structurally, poxviruses are unlike many other viruses in that they do not display any helical or icosohedral symmetry, instead virions measuring approximately 320 x 250 x 130 nm are brick-shaped or ovoid, with a “dumbbell”-shaped core containing the viral genome [225-228]. Poxvirus genomes are as large as 360kb and encode hundreds of genes, of which 49 are conserved across all poxviruses [229] [230]. This core set of genes includes genes functioning in morphogenesis (H3L/intracellular mature virus morphogenesis viral protein/VP55), transcription (A5R/RNA polymerase subunit 19) and replication (E9L/DNA polymerase) [229]. It is these genes that allow poxviruses to replicate in the host cell cytoplasm, an uncommon feature of DNA viruses, shared by certain members of the nucleocytoplasmic large DNA virus clade (NCLDV) that also includes iridoviruses, asfarviruses and mimiviruses [231].

Table 1.3. Members of Poxviridae

SUBFAMILY	GENUS	EXAMPLE VIRUSES
Chordopoxvirinae	*Avipoxvirus*	Fowlpox virus
	Capripoxvirus	Sheeppox virus
	Leporipoxvirus	Myxoma virus
	Molluscipoxvirus	Molluscum contagiosum virus
	Orthopoxvirus	Variola virus, cowpox virus, vaccinia virus
	Parapoxvirus	Orf virus
	Suipoxvirus	Swinepox virus
	Yatapoxvirus	Yaba monkey tumour virus
Entomopoxvirinae	*Alphaentomopoxvirus*	Melolontha melolontha virus
	Betaentomopoxvirus	Amsacta moorei virus
	Gammaentomopoxvirus	Chironomus luridus virus

The most well-known member of poxviridae is variola virus (VARV), the causative agent of smallpox, one of the most devastating human diseases in history. It is an ancient disease, with evidence of its characteristic pus-filled lesions present on the preserved remains of ancient Egyptian mummies dating to approximately 1200 BC [232]. In the 20th century alone, smallpox is believed to have caused in the realm of 300-500 million deaths, with an overall mortality rate of 30%. A global vaccination program led by the World Health Organisation (WHO) eradicated the disease in 1979, with the last recorded natural case in Somalia in 1977 [232].

Smallpox was the first disease documented for which preventative innoculation was attempted. A practice developed in India before 1000 AD where dried scabs from smallpox victims were ground and administered to healthy individuals in an attempt to introduce small amounts of live virus to stimulate an immune response but not fatal disease [233]. This process, called variolation, existed throughout the world in various forms, with variable success in producing protective immunity due to the uncontrolled dosage and virulence of virus administered (variolation could also produce fatal disease).

In 1796, Edward Jenner, a British physician, observed that people infected with cowpox were subsequently protected from smallpox. He inoculated virus from cowpox lesions into the skin of healthy individuals and demonstrated protective immunity against smallpox, effectively practising the first vaccination [234]. Cowpox virus (CPXV) was subsequently used globally against smallpox. In the 1960s, in an attempt to obtain a purified vaccine strain for use in the WHO's global eradication attempt, it was discovered that the virus being used for vaccination was not CPXV, but a closely related virus that was subsequently named vaccinia virus (VACV) [235].

Various aspects of VACV biology have since been widely studied, including its replication, interactions with the host cell and the immunological response to infection. VACV is the prototypal poxvirus, with research able to be broadly extrapolated to other viruses in the family due to substantial similarities existing in the pathogenesis and replication between members of this group [228].

1.3.1 Vaccinia virus

> **Some of the reviewed information below was published in an earlier form:** TP Newsome, AJ Marty, **H Lynn**, & DJ Procter [2009]. *Navigating the subcellular space: Lessons from vaccinia virus* in **Viral Transport, Assembly and Egress**, edited by RJ Diefenbach & AL Cunningham (Research Signpost, Kerala, India, 2011)

VACV is a member of the orthopoxviridae genus of the poxviridae family. It infects a wide range of vertebrates, including cows, rodents and humans, although none of these are the natural reservoir host [236]. The origins of VACV remain controversial; while there is the possibility that the natural host is extinct, it has also been speculated that the natural host are cows or horses, although the virus may no longer exist in these hosts in the wild [235, 237, 238].

To date, there are 35 VACV strain genome sequences collated at The Viral Bioinformatics Resource Centre (http://athena.bioc.uvic.ca/), of which Western Reserve (WR) and Copenhagen (Cop) are the most widely utilised laboratory strains. Both possess genomes of approximately 200kb and contain greater than 200 open reading frames ([239], http://www.poxvirus.org/). These numbers are typical of most VACV strains, with Modified Vaccinia Ankara (MVA), a severely attenuated vaccine strain generated through over 500 passages through chicken embryo fibroblasts being a notable exception with only 163 intact open reading frames [240].

VACV genes are annotated with a capital letter, a number, and then either L or R. The first capital letter corresponds to the fragment of the VACV-Cop genome digested with HindIII restriction nuclease that the gene is located in, with the fragments designated alphabetically from the largest fragment A to the smallest, P [239, 241]. The number represents the gene's sequential position within that fragment from the 5' to the 3' end of the genome. The L or R indicates the transcription direction of the open reading frame (left or right) and as such, is omitted from protein names (for example, the E9L locus encodes for the E9 protein) [242].

The VACV replicative cycle is complex and involves the production of distinct morphological forms with characteristic transport steps [**Figure 1.9**]. The replicative cycle can be divided into three main phases; entry, morphogenesis and egress. Entry involves the viral membrane fusing with the host cell plasma membrane or an endosomal membrane and release of the core into the cytoplasm [243-245]. This process is mediated by a complex of up to 12 viral proteins called the entry fusion complex (EFC) [246, 247]

The released viral core is transported along microtubules to a perinuclear location while early mRNA and protein synthesis is initiated, with DNA replication following soon after [248-250]. The viral enzymes necessary for transcription of early genes are present in infecting particles [251] and early mRNAs can therefore be detected 20 min after infection of HeLa cells [252]. Intermediate and late genes are regulated by the products of earlier gene transcription and protein synthesis, so are not detected until 100 and 140 min post infection respectively [252]. The cascade of early gene products regulating intermediate gene transcription and intermediate gene products regulating late gene transcription is dependent on specific promoter sequences that coordinates the tight temporal regulation of gene expression [253-257].

At 2 hpi (hours post infection), sites of DNA replication begin to be surrounded by membranes of the endoplasmic reticulum (ER) that coalesce to form a viral replication and morphogenesis compartment called the virus factory (VF) [250, 258]. Replicated viral DNA is packaged into membrane crescents containing lipid and virally-encoded proteins to form immature virus (IV). These then undergo proteolytic cleavage of several core proteins to generate the characteristic brick-shaped intracellular mature virus (IMV) [259]. IMV are infectious and their formation is thought to be the end-point of morphogenesis for the majority of virus particles, which are then released upon cell lysis.

However, a small subset (5-20%) of IMVs are transported along microtubules to the *trans*-Golgi network (TGN) where they are wrapped by an additional two lipid membranes to become intracellular enveloped virus (IEV) [260], a process regulated by viral gene A27L [163] (which is discussed further below) [**Figure 1.10**]. While there is dispute in the field about the number and origin of the IMV membrane(s), which may be derived from the membranes of the intermediate compartment or otherwise synthesised de novo [261], the IEV membranes that wrap IMV are known to be derived from endosomal or trans-Golgi cisterna [260, 262].

After being wrapped, IEV will undergo egress with a final microtubule-based transport step to move virus from the TGN to the cell periphery [263]. At the cell periphery, the outermost membrane fuses with the plasma membrane to generate cell-associated enveloped virus (CEV). CEV may stimulate actin-based motility that generates a propulsive force to push CEV into the extracellular space, where they become extracellular enveloped virus (EEV). As virus particles are large, actin-based motility of CEV can be directly visualised by fluorescent light microscopy revealing movement in association with thick actin bundles at speeds of approximately 0.2 µm/sec [264]. The formation of EEV is believed to play roles in mediating long-range spread of virus within a host [265, 266] as the additional membrane has been demonstrated to aid evasion of host defense mechanisms such as complement [267].

Although there are substantial structural differences between IV and IMV, the key difference between all other morphological forms is the number of membranes present (alternate nomenclature which differentiates IMV, called mature virus [MV] from all the enveloped forms of the virus known collectively as wrapped virus [WV] acknowledges this), which in turn alters the protein composition of virions [**Figure 1.10**]. The IMV form contains all proteins necessary for replication, including structural proteins, the proteins of the aforementioned EFC and enzymes such as DNA polymerases and endonucleases [268].

Eight proteins; A33, A34, A56, B5, F13, A36, F12 and E2 are integral to or associated with the IEV membranes and absent from IMV, with A36, F12 and E2 specifically associated exclusively with outer of the two membranes, and are therefore are absent from EEV [**Figure 1.10**] [266]. These proteins have a range of functions associated with viral egress or infectivity, including efficient wrapping of IEV, formation and release of EEV and microtubule-based transport of IEV [269-273]. Those proteins responsible for microtubule-based transport of IEV, A36, E2 and F12 are of particular interest and are discussed further below.

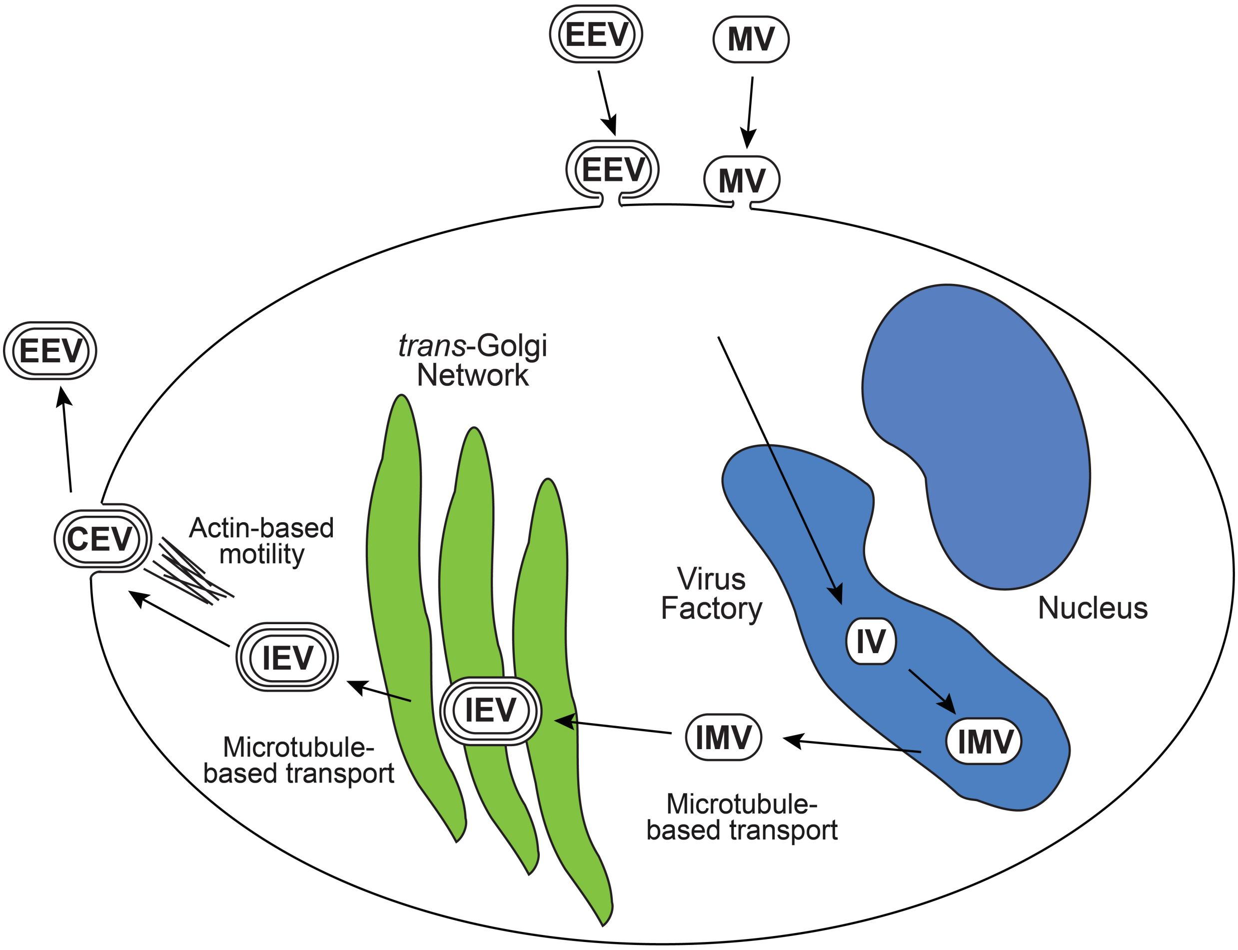

Figure 1.9: The VACV replicative cycle

Upon fusing with the plasma membrane of the host cell, the viral core is released into the cytoplasm to be transported along microtubules to a perinuclear location where it generates a viral replication centre called the virus factory (VF). DNA is packaged into immature virus (IV) that undergo cleavage to become intracellular mature virus (IMV). A subset of IMVs are transported along microtubules to the *trans*-Golgi network (TGN) where they are wrapped by two lipid membranes to become intracellular enveloped virus (IEV). A final microtubule-based transport step occurs to transport IEV to the cell periphery, where the outer most membrane fuses with the plasma membrane to generate cell-associated enveloped virus (CEV). These may stimulate actin-based motility that generates a propulsive force to push CEV into the extracellular space, where they are referred to as extracellular enveloped virus (EEV).

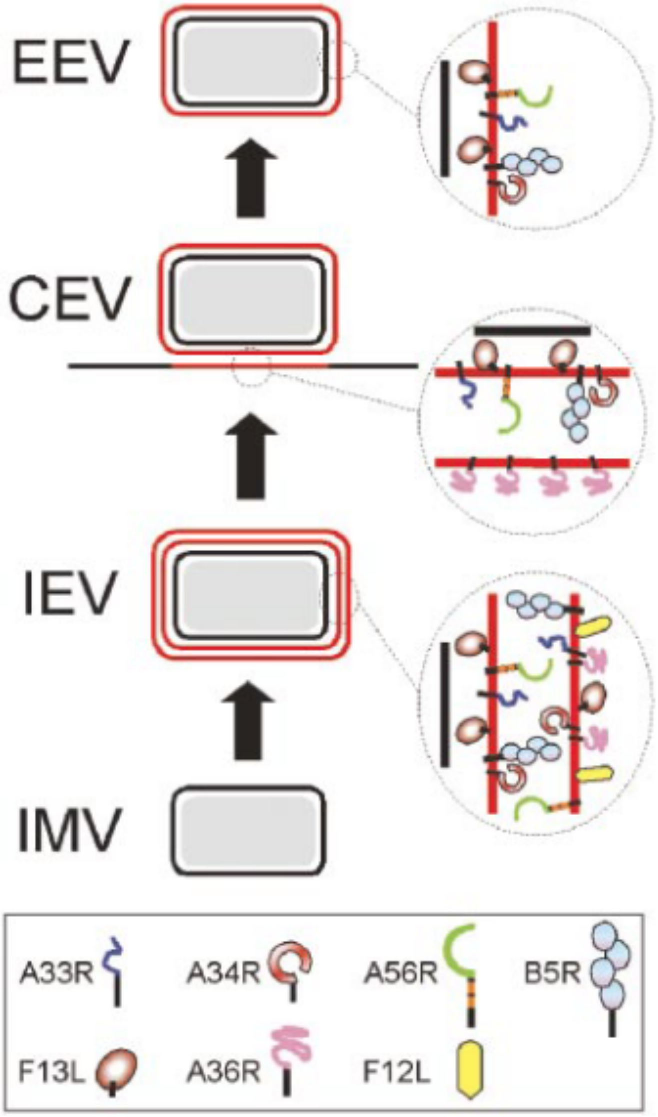

Figure 1.10: Localisation of envelope proteins
Schematics of IMV, IEV, CEV and EEV are shown indicating the different localisation of various intergral membrane and membrane-associated proteins. A36 and F12 (and E2, which is associated with F12 but not represented) are located on the outer IEV membrane only, but are not present in CEV and EEV as formation of CEV leads to dissociation of F12 and redistribution of A36 beneath the CEV particle on the plasma membrane. A33, A34, A56 (only in two thirds of EEV particles), and B5 are on the outer surface of CEV/EEV and F13 is present between the IMV surface and IEV membranes. From [266].

1.3.1.2 A27L

A27L encodes a 14kDa protein referred to as A27 that is resides on the surface of IMV (or MV, when released from the cell) [274]. Acting in concert with H3, D8 and A26, A27 mediates attachment of MV to the host cell through binding to glycosaminoglycans and laminin on the cell surface [275]. Both A25 and A26 are involved in the endocytotic entry pathway of VACV into the cell and require A27 to mediate their association with the MV [276, 277]. A27 itself is bereft of transmembrane domains and is anchored to IMV though its interaction with A17 [274]. In addition to facilitating the association of A25 and A26, A27 also plays a direct role in membrane fusion during entry [278, 279], although the exact nature of this role has been contentious [247]. A27 is not one of the 12 proteins identified as a component of the EFC that mediates membrane fusion [247].

A27 plays diverse roles in the VACV replicative cycle and has also been found to be essential in the microtubule-based viral egress of progeny virus particles. Deletion of A27 leads to a greatly reduced-size plaque phenotype, with minimal effects on virus production in a one-step growth curve. This indicates that deletion of A27 does not disrupt IMV production while nonetheless abrogating EEV production [280]. The underlying mechanism that manifests this phenotype is unclear; it has been reported that disruption of A27 leads to inhibition of microtubule-based movement of IMV to the TGN for wrapping in addition to defects in wrapping [163]. Conversely, imaging of a fluorescently tagged ΔA27L virus reveal IMV undergoing bidirectional microtubule-based motility to and from the VF, with reductions in EEV production being attributed solely to aberrant wrapping [280].

1.3.1.3 A36R

A36 is a type Ib transmembrane protein that contains a ~190 residue surface in contact with the cytoplasm [191, 281]. It is localised to the trans-Golgi network and acquired by virus particles during the wrapping of IMV to form IEV at this compartment. As previously mentioned, it is integral to the outer of two IEV membranes that fuses to the plasma membrane upon formation of CEV and is therefore absent from EEV particles. Viruses deleted for A36R display a reduction in transport of IEV to the cell surface, a phenotype reminiscent of cells treated with the microtubule destabilising drug nocodazole [282-286] [**Figure 4.1**]. In immunofluorescence assays, this presents phenotypically as a loss of formation of CEV/EEV, except in regions where the TGN lies in proximity to the cell membrane [**Figure 1.11**].

A key role for A36 is to direct the recruitment of the kinesin-1 anterograde motor complex. Expressing dominant negative constructs that interfere with kinesin-1 function also inhibit IEV egress from the trans-Golgi network [282, 287]. This interaction appears to be via a direct interaction with kinesin-1 light chain (KLC), with yeast-2-hybrid assays and fluorescence resonance energy transfer approaches confirming an interaction between A36 and the TPRs of KLC2 [181] [288].

This interaction between A36 and kinesin-1 has been mapped to a bipartite tryptophan motif in A36 at residues 64/65 ($A36^{W64E65}$) and 97/98 ($A36^{W97D98}$) [181, 282, 286]. When both these sites are mutated to AA, egress of virus to the cell periphery is retarded to the same extent as in complete loss of A36, and recruitment of kinesin-1 is abolished. The $A36^{W97D98}$ site plays the dominant role in this interaction and $A36^{W64E65}$ an ancilliary role; with a $A36^{WDAA}$ mutant (both residues of the $A36^{W97D98}$ tryptophan motif mutated to AA) generating plaques approximately 33% the size of parental plaques, compared to approximately 95% of a $A36^{WEAA}$ mutant [286].

A simple paradigm that emerges from these findings suggests that A36 on the surface of IEV presents an interaction site for kinesin-1 resulting in transport to the cell periphery. Confounding this paradigm is the viral protein F12 that is also been implicated in the microtubule transport of IEV, but the exact function of this protein and its mechanism of action remains to be resolved [285, 289-291] [**Section 1.3.1.4**].

A36 also directs a second transport event following delivery of IEV to the cell periphery. Upon fusion of the outer IEV membrane to the plasma membrane, A36 localises directly beneath CEV [281]. Two tyrosine residues, $A36^{Y112}$ and $A36^{Y132}$ are phosphorylated by Src and Abl family kinases leading to the initiation of signalling cascades involving Nck (recruited by $A36^{Y112}$), Grb2 (recruited $A36^{Y132}$), WIP, N-WASP and finally the Arp2/3 complex [292-298]. This leads to the rapid nucleation of actin filaments that propel CEV across the surface of the cell thereby facilitating cell-to-cell spread [299, 300] [**Figure 1.11**].

Mutation of these two critical tyrosine residues to phenylalanine ($A36^{Y112F}$ and $A36^{Y112F}$, together referred to as $A36^{YdF}$) prevents tyrosine phosphorylation and completely abolishes viral actin-based motility [300, 301] [**Figure 1.11**]. It is the $A36^{Y112}$ that is the critical tyrosine, with the $A36^{Y112F}$ mutant leading to an approximately 10-fold reduction in actin tail formation [301]. In the absence of $A36^{Y132}$ phosphorylation, the effects on motility are more subtle; there is a modest reduction in the initiation efficiency of actin-based motility (the chance that an infected cell will have actin tails), although infected cells have on average fewer numbers of CEV-associated actin tails [293].

This nucleation of actin by A36 has also been recently demonstrated to aid in EEV release. Cells infected with the $A36^{YdF}$ virus deficient in localised actin nucleation, displayed a 10-fold reduction in virus release with transmission electron microscopy and 3D-SIM super-resolution microscopy demonstrating CEV trapped in small invaginations/pits at the plasma membrane [302]. These results indicate that the propulsive force generated by actin polymerisation promoted the disengagement of CEV attachment sites with the plasma membrane and facilitating the release of EEV into the extracellular space [302].

The early expression of VACV A36 is believed to be important in repulsion of super-infecting virions, a process that allows viral spread to occur at a rate beyond the speed of its replicative cycle. Through cell surface signalling involving B5 on the virus surface and A36 and A33 on the host membrane, viral entry into early-stage infected cells yet to manufacture infectious virus is blocked. Super-infecting virions are directed toward uninfected cells, allowing plaques to expand at a rate that outpaces the rate of replication [299].

1.3.1.4 F12L

F12 is a 65-kDa protein that lacks transmembrane domains [303]. It is recruited to the virus upon membrane wrapping at the trans-Golgi network and is therefore present on IEV particles but absent from IV and IMV [289]. It is also absent from CEV and EEV, indicating that like A36, it is lost from the virus upon fusion with the plasma membrane. While A36 is present in the cell membrane beneath CEV however, F12 is not detectable. This transient recruitment to IEV during egress to the cell periphery strongly indicates involvement of F12 in microtubule-based transport [285].

A VACV deletion mutant of F12L produces a small plaque phenotype [**Figure 1.11**]. While the effect of the deletion on IMV production is fairly minor, production of CEV and EEV production was affected dramatically, with a seven-fold reduction in infectious EEV released from infected cells [303]. Immunofluorescence and electron microscopy (EM) revealed large numbers of IEV clustered in the centre of the cell, indicating deficient dispersal of virions [283, 289]. With reduced transport to the cell periphery, there is a concurrent reduction in actin-tail formation (by 99.5%), unlike ΔA36R however, actin tails can still be formed [303].

The transient nature of the F12 interaction suggests protein–protein interactions may be involved in recruiting the protein to IEV. Yeast 2-hybrid screens between F12 and IEV proteins A33, A34, A36 and B5 demonstrated interaction between F12$^{351\text{-}458}$ and A36$^{91\text{-}111}$ [291, 304]. Deletion of the A36 interaction site in a recombinant virus (B5R-GFP/F12L$^{\Delta 351–458}$) abrogates association with IEV and subsequent viral egress, effectively reproducing the ΔF12L phenotype [291, 304]. A caveat to this study was that there was no evidence that F12L$^{\Delta 351–458}$ retained any functionality or indeed was correctly folded.

The precise role of F12 in IEV transport is yet to be definitively determined. Kinesin-1 is not recruited to IEV in the absence of F12, with A36 alone being insufficient for the recruitment of kinesin-1 [290]. This suggests that F12 may potentially stabilise interactions between A36 and kinesin-1 or that F12 could fulfil a regulatory role. If, however, F12 acts through A36, an apparent paradox is how loss of F12 leads to a stronger phenotype than loss of A36. Fewer IEV reach the cell surface in the absence of F12L than A36, and plaque growth is more dramatically retarded [283, 303] [**Figure 1.11**]. This paradox and observations of IMV accumulation in the virus factory in the ΔF12L strain [291] has led to conflict in the field regarding the existence of additional non-transport roles of F12 such as in IEV wrapping, as well as exploration of additional F12 interaction partners that may be disrupted by deletion of F12L.

Using a recombinant virus in which F12 was fused to affinity tag Glutathione S-Transferase (GST), the viral protein E2 was identified as a co-purifying protein [285]. Like F12, E2 colocalises with IEV in transit along microtubules and deletion of E2L results in a reduction in IEV egress and a small plaque phenotype, effectively mimicking loss of F12L [285, 305]. There is interdependence between these two proteins in recruitment to IEV, with loss of either leading to abrogation of IEV localisation of the other partner [285]. Wrapping defects are also apparent with loss of either E2 and F12, with examination of EM images revealing excess layers of membrane and other forms of aberrant wrapping [285, 305]. Quantitative measurements in a later study utilising serial section and tilt series analyses of EM images contradicted previous findings by showing both F12 and E2 deletion viruses wrap normally, with no difference in the number of IMV or partially wrapped IEV relative to wild type [290].

Complicating the elucidation of F12 function, it has been proposed that F12 may be a KLC mimic, possessing 14 TPR-like sequences that make up 80% of the protein. Structural modeling of TPR-like repeats 1-6 and 7-12 of F12 demonstrates substantial similarity to the TPR domain of KLC2 [290]. TPR domains mediate protein-protein interactions, including those between KLC and WD/WE motifs in cargo proteins [**Section 1.1.3.2**]. The structural similarity to TPR domains has subsequently been contested in a report suggesting that F12 is an inactivated DNA polymerase [306].

Additionally, F12 possesses a critical WD motif, that when mutated blocks the recruitment of F12 and KHC to IEV and preventing egress to the cell periphery [290]. Together, these results imply a role for F12 as a mediator of binding of kinesin-1 to IEV, however, while protein-protein interactions have been found between F12 and IEV protein A36, there is so far no evidence of direct interaction with either KHC or KLC [181, 290, 291].

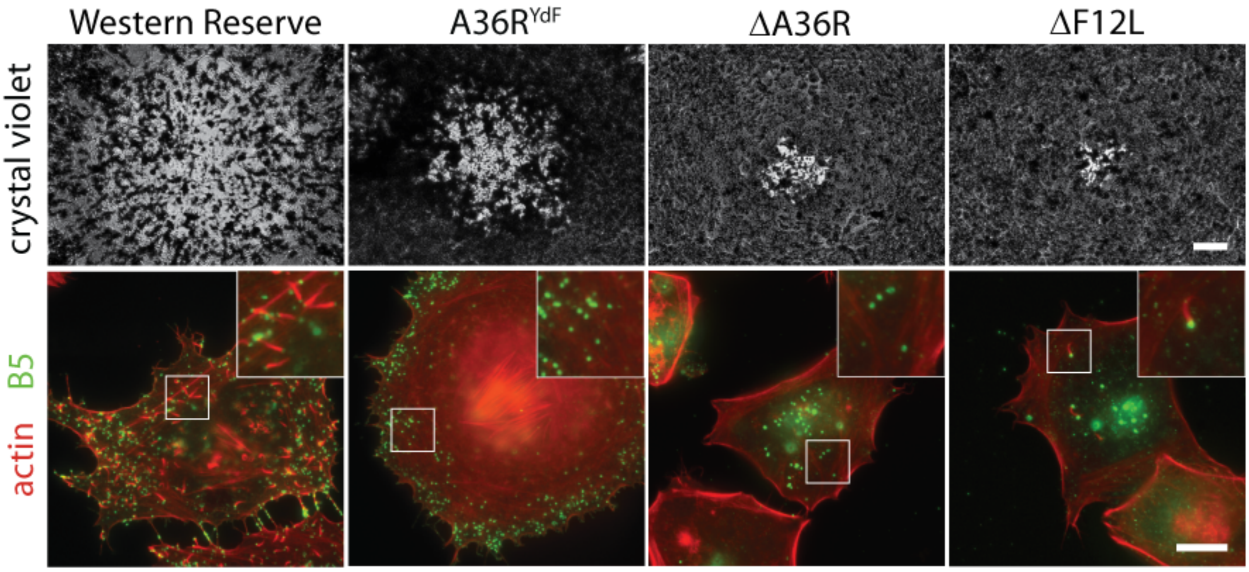

Figure 1.11: Effect of gene mutations and deletions on phenotype
The plaque phenotype of WR, A36R^{YdF}, ΔA36R and ΔF12L are represented in the upper panels and immunofluorescence images with cell-associated virus (CEV) in green (anti-B5R, non-permeabilised cells) and F-actin in red are displayed in the lower panels. While all enveloped form of virus are B5-positive, CEV are differentiated from IEV in IFA by applying α-B5 antibodies to cells that have not been permeabilised. As antibodies are too large to diffuse through intact cell membranes, only IEV that have reached the cell periphery and fused with the cell membrane to become CEV will be detected. Disruption of A36 tyrosine phosphorylation (A36R^{YdF} strain) completely abrogates actin-based motility, but does not inhibit the appearance of CEV in the cell periphery indicating intact microtubule-based motility. Correspondingly, there is a limited reduction in plaque size relative to WR. Disruption of microtubule-based transport (ΔA36R, ΔF12L) on the other hand strongly attenuates both plaque size and CEV dispersal. Unlike ΔA36R, ΔF12L has intact actin-based motility, and the reduced numbers of enveloped viruses that reach the cell surface are capable of forming actin tails. Scale bar is 100 μm in the upper panels and 10 μm in the lower panels. From [307].

1.4 PROJECT AIMS AND HYPOTHESES

A speculative model of regulation [**Figure 1.12**] of VACV motility generated from current research in the field suggests that during motility, a small stretch of residues on the cytoplasmic surface of A36 is able to interact with multiple partners thereby enabling motility. Egress of IEV to the cell periphery occurs when a complex of kinesin-1, F12 and E2 binds to A36, mediated by a bipartite tryptophan motif in A36 at residues 64/65 (WE) and 97/98 (WD). Upon reaching the cell periphery, the outer IEV membrane fuses with the plasma membrane and phosphorylation of $A36^{Y112}$ and $A36^{Y132}$ promotes kinesin-1 release and the recruitment of the actin nucleation machinery. Stimulation of actin-polymerisation propels EEV into the extracellular space by breaking cellular–viral membrane contacts.

This speculative model highlights A36 as the critical mediator of all virus motility, with F12/E2 playing an ancillary role, possibly in stabilising kinesin-1 recruitment. The suggested role of F12 is however inconsistent with mutant plaque phenotypes which demonstrate stronger attenuation in the absence of F12 than A36 (which may or may not be due to a role in IEV morphogenesis). This project therefore broadly aims to elucidate and clarify the contributions of proteins A36 and F12 to microtubule-based egress of IEV. To achieve this, this we aimed to generate a novel viral imaging system utilising photoactivatable fluorescent proteins to track the trajectories of viruses in different mutant backgrounds. While appearing to play important roles in microtubule-based egress of VACV, the contentious role of A27 was not dissected in this thesis.

Lastly, we aimed to investigate the contribution of cytoskeletal-based motility to virulence in an animal model of smallpox. To do this, we aimed to characterise microtubule- and actin-based motility in ECTV, the causative agent of mousepox, which is a smallpox-like disease in mice. Due to the substantial genomic similarities between the two viruses, we hypothesised they would share similar characteristics in their microtubule- and actin-based motility and we aimed to generate a deletion mutant of an A36R homolog to test virulence in mice.

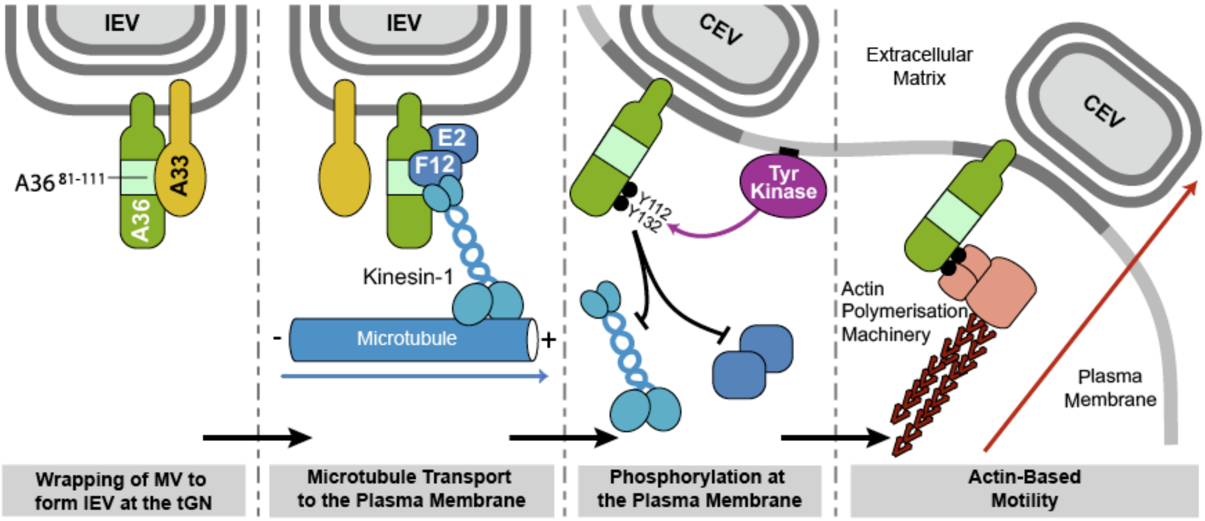

Figure 1.12: Speculative model of IEV regulation

While IEV are formed at the TGN, A33 potentially occlude kinesin-1 access to A36 and inhibits premature transport. A complex of kinesin-1, F12 and E2 is then recruited to A36 and transports virions to the cell periphery. Phosphorylation of Y112 and Y132 residues in A36 by tyrosine kinase promotes kinesin-1 release and initiates recruitment of the actin polymerisation machinery. From [307].

CHAPTER 2: Materials and Methods

2.1 MOLECULAR BIOLOGY AND BIOCHEMISTRY

2.1.1 Chemicals and reagents

Chemicals, reagents and commercial kits used and mentioned in this thesis are listed below, along with their suppliers and catalogue number in brackets.

- 30% Acrylamide/Bis Solution, 37.5:1 (2.6% C) (Bio-Rad Laborarോties) (Cat: # 161-0158)
- 35mm Glass Bottom Dishes (MatTek) (Cat: #P35G-0-10-C)
- µ-Dishes 3cm No. 1.5 glass (Ibidi) (Cat: #81151)
- Agarose (Bioline) (Cat: # Bio41025)
- Alexa Fluor® 568 Phalloidin (Invitrogen) (Cat: # A12380)
- Amersham ECL Westertn Blotting Detection Reagent (GE Health)(Cat: # RPN3243)
- Amersham Hyperfilm ECL (GE Health)(Cat: # 28-9068-37)
- Ammonium Persulphate for electrophoresis (APS) (Sigma-Aldrich) (Cat: # A3678)
- Ampicillin (Astral Scientific) (Cat: # AM0339)
- 3',3",5',5"-tetrabromophenolsulfonphthalein (bromophenol blue) (Sigma-Aldrich) (Cat: # B8026)
- Boric Acid (Astral Scientific) (Cat: # AM0588)
- Bovine Serum Albumin, Nuclease free (Fisher Biotec) (Cat: # BSA-50)
- Carboxymethylcellulose sodium salts, medium viscosity (Sigma-Aldrich) (Cat: # C9481)
- Chloramphenicol Crystalline (Sigma-Aldrich) (Cat: # C0378)
- 4', 6-Diamidino-2-phenylindole dihydrochloride (DAPI) (Sigma-Aldrich) (Cat: # D9542)
- D-Glucose (Astral Scientific) (Cat: # AM0188)
- Dimethylsulfoxide (DMSO) (Sigma-Aldrich) (Cat: # D2650)
- Disodium hydrogen Orthophosphate (Merck) (Cat: # 10248)
- dNTP Set (Bioline) (Cat: # Bio39026)
- Dulbecco's Modified Eagle Medium (D-MEM) (1X), liquid (High Glucose) (Invitrogen) (Cat: #11995073)
- ECL Western Blotting Reagent (GE Health) (Cat: # RPN2106)
- Ethidium Bromide (Amresco) (Cat: # X328)
- Ethylenediaminetetraacetic Acid (EDTA) Disodium Salt Dihydrate (Astral Scientific) (Cat: # AM0105)
- Fetal Bovine Serum (FBS) (Diethelm Keller Siber Hegner, DKSH) (Cat: # SFBS)
- Fibronectin from bovine plasma (Sigma-Aldrich) (Cat: #F1141-1MG)
- Frosted l End 1 Side, 1.0-1.2mm (Livingstone) (Cat: # 7105-1A)
- GelRed™ Nucleic Acid Gel Stain (Biotium) (Cat: # 41003)
- Glycerol, minimum 99% GC (Sigma-Aldrich) (Cat: # G5150)
- Glycine (Astral Scientific) (Cat: # AM0167)
- GPT Selection Reagent, 500X Mycophenolic Acid; 100X Aminopterin (Millipore) (Cat: # TR-1001)
- Hybond-C Extra (Amersham Biosciences, GE) (Cat: # RPN203E)
- Hyperladder I (Bioline) (Cat: # Bio33026)
- Hypoxanthine Cell Culture Tested (Sigma-Aldrich) (Cat: # H9636)
- Immersion Oil (Olympus) (Cat: # AV239000)
- Immersion Oil (Olympus) (Cat: # AV9602)
- Lens Paper (Olympus) (Cat: # AX6476)
- Lipofectin Reagent (Invitrogen) (Cat: # 18292-001)
- Lipofectamine 2000 Transfection Reagent (Invitrogen) (Cat: # 11668027)
- Magnesium Acetate Tetrahydrate (Sigma-Aldrich) (Cat: # M5661)
- Magnesium Chloride (APS Chemical) (Cat: # 296)
- β-Mercaptoethanol (Sigma-Aldrich) (Cat: # M3148)
- 2-(N-Morpholino)ethanesulfonic acid hydrate (MES) (Sigma-Aldrich) (Cat: # M8250)
- Microscope Coverslips No.1 Thickness Circular, 12mm (Livingstone) (Cat: # CS12RD)
- Minimum Essential Medium Eagle, with EAR (MEM) (Sigma-Aldrich) (Cat: # M2279)
- Modified Eagle Medium (MEM) (2X), liquid (Invitrogen) (Cat: # 11935046)
- Mycophenolic Acid (Sigma-Aldrich) (Cat: # M5255)
- Paraformaldehyde (PFA) (Sigma-Aldrich) (Cat: # P6148)
- Penicillin-Streptomycin-Glutamine (100X) (Cat: # 10378-016)
- Phenol Buffer Saturated (pH 6.7/8.0) (Astral Scientific) (Cat: # 0945)
- Phenol:Chloroform (pH6.7/8.0) premixed with isoamyl (25:24:1) (Astral Scientific) (Cat: # 0883)
- Phosphate Buffered Saline Tablet (Astral Scientific) (Cat: # AME404)
- Polyvinyl Alcohol 4-88 (Mowial) (Sigma-Aldrich) (Cat: # 81381)
- Polyoxyethylene Sorbitan Monolaurate (Tween-20) (Sigma-Aldrich) (Cat: # p2287)

- P-Phenylenediamine Free Base (Sigma-Aldrich) (Cat: # P6001)
- QiaexII Gel Extraction Kit (Qiagen) (Cat: # P20021)
- Qiaprep Spin Minikit (Qiagen) (Cat: # P27106)
- 0.25% Trypsin-EDTA 1X (Invitrogen) (Cat: # 25200114)
- Rubidium Chloride (Sigma-Aldrich) (Cat: # 215260)
- 5mL Serological Pipets (Beckon Dickinson) (Cat: # 357543)
- 10mL Serological Pipets (Beckon Dickinson) (Cat: # 357551)
- 25mL Serological Pipets (Beckon Dickinson) (Cat: # 357525)
- Skim Milk Powder (Oxoid) (Cat: # LP0031)
- Snap Strip II PCR tubes 8-Strip Standard Tube & with Individual Attached Flat Caps (Astral Scientific) (Cat: # I324500)
- Sodium Chloride (Astral Scientific) (Cat: # AMX190)
- Sodium Dihydrogen Orthophosphate (APS Chemicals) (Cat: # 471)
- Sodium Dodecyl Sulfate (SDS) (Astral Scientific) (Cat: # AM0227)
- Sodium Orthovanadate (Sigma-Aldrich) (Cat: # S6508)
- 60X15mm Standard Dishes (Beckon Dickinson) (Cat: # 353002)
- 100X20mm Standard Dishes (Beckon Dickinson) (Cat: # 353003)
- STrEP-Tactin Superflow resin suspension (Qiagen) (Cat: # 30001)
- Syringe Filter (Diethelm Keller Siber Hegner, DKSH) (Cat: # 431227)
- Tetracycline Hydrochloride Crystalline (Sigma-Aldrich) (Cat: # T3383)
- Tris-hydroxymethyl-aminomethane (Tris Base) (Astral Scientific) (Cat: # AM0479)
- 6-Well Flat-Bottom with Lid (Beckon Dickinson) (Cat: # 353046)
- Wizard® SV Gel and PCR Clean-Up System (250 preps) (Promega) (Cat: # A9282)
- Wizard® Plus SV Miniprep DNA Purification System + Vaccum Adaptors (250 preps) (Promega) (Cat: # A1470)
- Xanthine (Sigma-Aldrich) (Cat: # X4002)

2.1.2 Polymerase Chain Reaction (PCR) and Cloning

PCR was carried out according to standard methods using primers listed in **Table 2.1** below. PCR product cleaned with Wizard SV PCR Clean-Up Kit (Promega) and vectors (1μg) were digested with suitable restriction enzymes (5U) (all restriction enzymes from NEB) in corresponding buffer provided by manufacturer for 5min at 37ºC. DNA loading dye (2.5% Ficoll 400, 11mM EDTA, 3.3mM Tris-HCl, 0.017% SDS and 0.015% bromophenol blue) was mixed with digested sample and separated on 1% agarose gel in TBE buffer (10.781g/L Tris-base, 0.744g/L EDTA and 5.5g/L Boric acid). PCR products and gel slices containing digested vector backbone or insert were purified with Wizard SV Gel Extraction Kit (Promega) or QiaexII Gel Extraction Kit (Qiagen). Purified products were used for DNA ligation. DNA ligations were set up according to manufacturer's instructions (T4 DNA ligase, NEB) and performed either overnight at 4 ºC or 2 hours at room temperature.

Ligations were transformed into XL10-Gold® Ultracompetent Cells (Stratagene, La Jolla, CA, USA, Cat: # 200314) and plated onto Luria Broth (LB) agar plates (10g/L NaCl, 10g/L Tryptone, 5g/L Yeast Extract, 15g/L Bacteriological Agar) supplemented with ampicillin (50μg/mL). Successful ligations colonies were amplified and prepared with Qiaprep Spin Minikit (Qiagen) before being subjected to diagnostic digests and sequencing. All successfully cloned PCR products were sequenced at Australian Genome Research Facility Ltd. The vectors constructed and used in this study are detailed in **Table 2.2**.

2.1.2.1 Construction of vectors for VACV

All vectors used and constructed for this thesis are detailed in **Table 2.2**, including primers and restriction sites used. All primers used are listed in **Table 2.1**. All viral DNA was originally amplified from VACV WR (ATCC VR-1354) genomic extraction [**Section 2.3.4**]. Vectors constructed and used in VACV experiments were either for transient expression of fusion proteins or for homologous recombination to generate recombinant viruses [**Section 2.4**], with constructs used for homologous recombination bolded in **Table 2.2**.

With the exception of commercial vectors purchased or received as gifts, three main types of vectors were used, the first were CB6 vectors with protein expression, either fluorescent proteins or fusions between viral proteins and fluorescent proteins, under the control of a constitutive CMV promoter [**Figure 2.1**]. The second were pE/L vectors with protein expression, again of fluorescent or fluorescent fusion proteins under the control of a synthetic viral early/late promoter (pE/L) [282, 308] [**Figure 2.1**]. The third type were GPT selection vectors which contained an *Escherichia coli gpt* gene that encodes guanine-hypoxanthine phosphribosyltransferase (GPT, [309]) and screenable marker gene monomeric Red Fluorescent Protein (mRFP, [310]). GPT acts as a selection marker by allowing growth of VACV in the presence of mycophenolic acid (MPA; an inhibitor of purine metabolism), xanthine and hypoxanthine [311].

To generate pE/L LA-PSCFP2-A3L(500) and pE/L LA-Dendra2-A3L(500)GPT, homologous recombination cassettes for generation of viruses with fusions between viral proteins and PSCFP2 and Dendra2 [312] [see **Section 2.4.1.2** and **3.1.2.4**], a two step fusion PCR was carried out to create the LA-PSCFP2 and LA-Dendra2 fragment to then be cloned into vectors [see **Table 2.2**]. For pE/L LA-PSCFP2-A3L(500), primers A3L.LA.CFPsew1/A3L.LA.CFPsew2 were used to amplify the region 500 bp upstream of A3L (the left arm; LA) from VACV genomic DNA and primers A3L.LA.CFPsew3/PSCFP2 were used to amplify the PSCFP2 gene without a stop codon from the PSCFP2-N vector. These PCR products from the first two reactions were cleaned with Wizard SV PCR Clean-Up Kit (Promega), then diluted and combined in the PCR reaction to be used as template for a second step of amplification with A3L.LA.CFPsew1/PSCFP2 resulting in a full-length fusion product incorporating the two first-step fragments.

The same process with differering primers and template was used for generation of pE/L LA-Dendra2-A3L(500)GPT. The LA of A3L was amplified from VACV genomic DNA with A3L.LA.Dendrasew1/A3L.LA.Dendrasew2 and the Dendra2 gene was amplified from the Dendra2-N vector with A3L.LA.Dendrasew3/Dendra2 primers. The second step of the fusion PCR utilised these two first step products as the template with A3L.LA.Dendrasew1/Dendra2 to generate a full-length product.

A slightly different modular approach was used for construction of F13L-Dendra2 and F13L-GFP viruses [313] to enable transient dominant selection of recombinant viruses [**Section 2.4**]. A 300 bp fragment spanning 150 bp of the end of the F13L ORF (LA) and 150 bp of the sequence immediately downstream of the ORF (RA) were synthesised with NotI and BamHI sites between them and flanked by HindIII/SalI restriction sites. This fragment was cloned HindIII/SalI into a variation of the GPT Selection Vector [314] which has mCherry in place of mRFP, and lacks the represented BglII/NotI/BamHI MCS [**Figure 2.1D**]. Fluorescent protein gene inserts Dendra2 and GFP were then shuttled from other vectors between the LA and RA in the construct with NotI/BamHI.

2.1.2.2 Construction of vectors for ECTV

Vectors used for ECTV experiments were similar to those used for VACV and are detailed in **Table 2.2**. One construct, pE/L ECTV 137.5 Y112F, required a two-step fusion PCR to introduce a point mutation into the A36R gene, as opposed to fusing a viral sequence and fluorescent protein sequence together, as described for VACV constructs above. The first step involved amplification of ECTV genomic DNA with primer pairs a36r.for/a36r.mutrev and a36r.mutfor/a36r.rev which each amplified half of A36R. These PCR products from the first two reactions were diluted and combined to be used as template for a second step of amplification with a36r.for/a36r.rev, resulting in a full-length A36R gene product incorporating a Tyr to Phe mutation at site 112.

A vector which encoded Lifeact (pE/L Lifeact-GFP), a 17 amino acid peptide that binds to filamentous actin [315], fused to the 5’ end of GFP under the control of pE/L was constructed with PCR-based methods. However, as Lifeact was so short, the sequence of Lifeact was able to be directly added to the synthesised primer LifeactGFP.for, which was used with the GFPrev primer on a vector template of GFP to generate a PCR product spanning all of the GFP sequence. This PCR product was digested with BglII and NotI purified with and ligated in to a pE/L GFP vector.

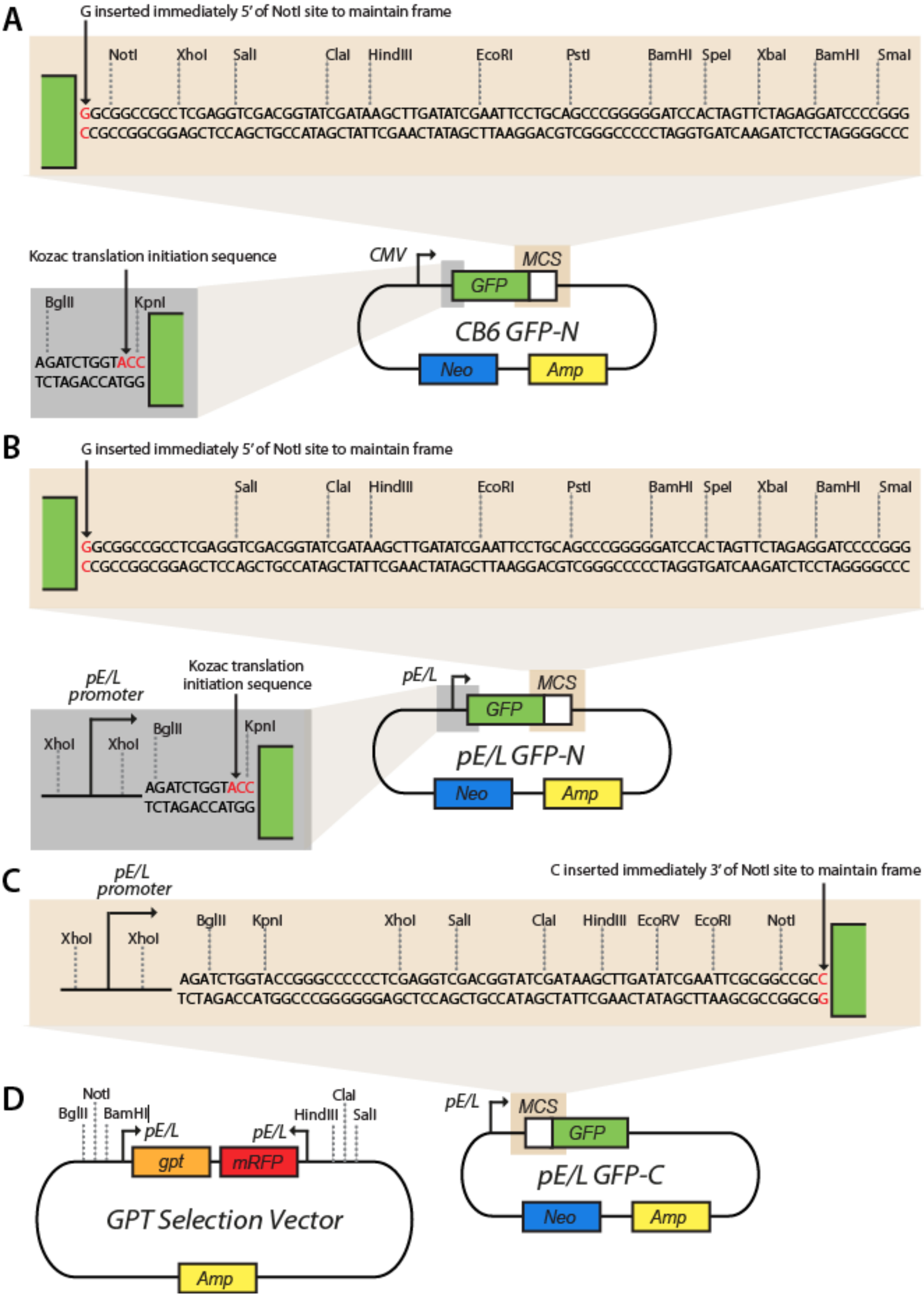

Figure 2.1: CB6 and pE/L GFP fusion protein vector restriction maps

Restriction maps of CB6 GFP, pE/L GFP-N and pE/L GFP-C vector maps used to generate the majority of expression constructs used in this project. MCS is the multiple cloning site, all vectors have neomycin (Neo) and ampicillin (Amp) resistance genes.

Table 2.1. Primers used for amplification of DNA

Gene	Name	Sequence (restriction site in blue, kozac sequence in orange, base insertion to maintain correct reading frame in red, stop codon in green)
For VACV, Chapter 3 and Chapter 4		
PSCFP2	PSCFP1	AAAGATCTACCATGAGCAAGGGCGCCGAGC
PSCFP2	PSCFP2	TTGCGGCCGCCCTTGTACAGCTCATCCATGC
PSCFP2	PSCFP3	AAGCGGCCGCCAGCAAGGGCGCCGAGCTG
PSCFP2	PSCFP4	TTGGATCCTTACTTGTACAGCTCATCCATGC
A3L	A3L1	AAGGCGGCCGCGAAGCCGTGGTCAATAGCG
A3L	A3L2	TTGGATCCCGAGAATGAATAAGTACTAAAGG
A3L	A3L.LA.CFPsew1	AAAGATCTCGTTGACGCCGAGCAATGC
A3L	A3L.LA.CFPsew2	GGCGCCCTTGCTCATTATTTATATTCGTAG
A3L	A3L.LA.CFPsew3	CTACGAATATAAATAATGAGCAAGGGCGCC
A3L	A3L.TDSfor.LA	AAGTCGACCGTTGACGCCGAGCAATGC
A3L	A3L.TDSrev.A3L500	TTAAGCTTCGAGAATGAATAAGTACTAAAGG
Dendra2	Dendra1	AAAGATCTACCATGAACACCCCGGGAATTAAC
Dendra2	Dendra2	TTGCGGCCGCCCCACACCTGGCTGGGCAGGGG
Dendra2	Dendra3	AAGCGGCCGCCAACACCCCGGGAATTAACCTG
Dendra2	Dendra4	TTGGATCCTTACCACACCTGGCTGGGCAG
A3L	A3L.LA.Dendrasew1	AAAGATCTGTCGACCGTTGACGCCGAGCAATGC
A3L	A3L.LA.Dendrasew2	GTTAATTCCCGGGGTGTTCATTATTTATATTCGTAGTTTTTAC
A3L	A3L.LA.Dendrasew3	GTAAAAACTACGAATATAAATAATGAACACCCCGGGAATTAAC
B5R	B5R(end).for	GTTCCATAAATTGCTACCG
B5R	B5R.RA.rev	AAAGGATCCTATACCATTAAGTGTATCCATCACC
F13L	F13L.for	AAAGATCTACCATGTGGCCATTTGCATCG
F13L	F13L.rev	TTGCGGCCGCCAATTTTTAACGATTTACTGTG
For ECTV, Chapter 5 and Chapter 6		
A36R-RA	a36r.rafor	ACCGCGGCCGCCAGATAATGCAGTTTATCAGTGTCG
A36R-RA	a36r.rarev	ACAGGATCCGCTCAATATACGTACTACTAGTTC
A36R-LA	a36r.lafor	AAAAAGCTTCTGTTGAAGTACTTAATGAAGATACC
A36R-LA	a36r.larev	AAAGTCGACCGGATGCTCGAGGTTACAAACATGG
A36R	a36r.for	GGGAGATCTACCATGATGCTGGTACCACTTATCACG

A36R	a36r.rev	TTTGCGGCCGCCGAAAGGATTGGATGAAAGTTAGG
A36R^{Y112F}	a36r.mutfor	AGCACGGAACATATTTTCGATAGTGTTGCCGGA
A36R^{Y112F}	a36r.mutrev	TCCGGCAACACTATCGAAAATATGTTCCGTGCT
Lifeact	LifeactGFP.for	AAAGATCTACCATGGGTGTCGCAGATTTGATCAAGAAATTCGAAAGCATCTCAAAGGAAGAAGCGGCCGCCAGCAAGGGC
Lifeact	GFPrev	TTTGGATCCAACTCCAGCAGGACCATGTGA

Table 2.2. Vector constructs made and used

VECTOR	DESCRIPTION	CREATED BY
For VACV, Chapter 3 and Chapter 4		
CB6 GFP-N	For constitutive expression of GFP, **Figure 2.1**	T. P. Newsome
pE/L GFP-N	For expression of GFP [316] under a viral promoter and generation of N-terminal GFP fusion proteins by cloning viral genes in, **Figure 2.1**	T. P. Newsome
pE/L GFP-C	For generation of C-terminal fusion proteins by cloning viral genes in, **Figure 2.1**	T. P. Newsome
pE/L LA-B5R-YFP-RA	Used as a source of LA and RA for construction of pE/L LA-B5R-PSCFP2-RA and pE/L LA-B5R-Dendra2-RA rescue constructs [see below]	T. P. Newsome, [285]
GPT Selection Vector	Used as vector for GPT selection, **Figure 2.1**	T. P. Newsome
PSCFP2-N	Used as template to amplify PSCFP2	Evrogen (FP802)
PSCFP2-C	Used as template to amplify PSCFP2	Evrogen (FP801)
pE/L PSCFP2-N	Primers PSCFP1/PSCFP2 used to amplify PSCFP2 gene from PSCFP2-N vector and cloned into pE/L GFP-N with BglII/Not1 in place of GFP	H. Lynn
pE/L PSCFP2-C	Primers PSCFP3/PSCFP4 used to amplify PSCFP2 gene from PSCFP2-C vector and cloned into pE/L GFP-C Not1/BamH1 in place of GFP	H. Lynn
CB6 PSCFP2-N	PSCFP2 was cloned in the place of GFP in the CB6 GFP-N vector with BglII/Not1 to use for constitutive expression of PSCFP2	H. Lynn
pE/L B5R-PSCFP2	B5R from pE/L B5R-GFP cloned BglII/Not1 into pE/L PSCFP2-C, for transient expression of B5R-PSCFP2 to check localisation	H. Lynn
pE/L PSCFP2-RA(B5R)	The region downstream of B5R (the right arm [RA]) was cloned from pE/L LA-B5R-YFP-RA into pE/L PSCFP2-C with BamH1 in the first step in construction of a recombination cassette to generate a B5R-PSCFP2 virus	H. Lynn

pE/L LA-B5R-PSCFP2-RA	A fragment spanning the region upsteam of B5R (the left arm [LA]) and B5R were cloned from pE/L LA-B5R-YFP-RA into pE/L PSCFP2-RA(B5R) as the second step in the contruction of a recombination cassette to generate a B5R-PSCFP2 virus [see **2.4.1.2**]	H. Lynn
pE/L PSCFP2-A3L(500)	Primers A3L1/A3L2 were used to amplify an approximately 500 bp fragment of A3L from the VACV WR genome and cloned into pE/L PSCFP2-N with Not1/BamH1 in the first step in construction of a recombination cassette to generate a PSCFP2-A3L virus	H. Lynn
pE/L LA-PSCFP2-A3L(500)	A fusion PCR was performed to generate a fragment spanning a 500 bp LA of A3L and PSCFP2 [see **2.1.2.1** for more details] which was cloned BglII/Not1 into pE/L PSCFP2-A3L(500) in the second step in construction of a recombination cassette to generate a PSCFP2-A3L virus	H. Lynn
pE/L LA-PSCFP2-A3L(500)GPT	A PCR was performed using primers A3L.TDSfor.LA/A3L.TDSrev.A3L500 with the LA-PSCFP2-A3L(500) vector to introduce SalI/HindIII restriction sites and cloned SalI/HindIII into the GPT selection vector as a recombination cassette to generate a PSCFP2-A3L virus [see **2.4.1.2**]	H. Lynn
Dendra2-N	Used as template to amplify Dendra2	Evrogen (FP822), Gift from K. Lukyanov
Dendra2-C	Used as template to amplify Dendra2	Evrogen (FP821), Gift from K. Lukyanov
pE/L Dendra2-N	Primers Dendra1/Dendra2 used to amplify Dendra2 gene from Dendra2-N vector and cloned into pE/L GFP-N with BglII/Not1 in place of GFP	H. Lynn

pE/L Dendra2-C	Primers Dendra3/Dendra4 used to amplify Dendra2 gene from Dendra2-C vector and cloned into pE/L GFP-C Not1/BamH1 in place of GFP	H. Lynn
pE/L Dendra2-RA(B5R)	The RA of B5R was cloned from pE/L LA-B5R-YFP-RA into pE/L Dendra2-C with BamH1 in the first step in construction of a recombination cassette to generate B5R-Dendra2 virus	H. Lynn
pE/L LA-B5R-Dendra2-RA	A fragment spanning the LA of B5R and B5R were cloned from pE/L LA-B5R-YFP-RA into pE/L Dendra2-RA(B5R) as the second step in the contruction of a recombination cassette to generate B5R-Dendra2 virus [see **2.4.1.2**]	H. Lynn
CB6 GFP-A3L(500)	A3L(500) was cloned Not1/HindIII from pE/L LA-Dendra2-A3L(500)GPT vector into the CB6 GFP vector in the first step in construction of a recombination cassette to generate Dendra2-A3L virus	H. Lynn
pE/L LA-Dendra2-A3L(500)GPT	A fusion PCR was performed to generate a fragment spanning a 500 bp LA of A3L and Dendra2 [see **2.1.2.1** for more details] which was cloned SalI/HindIII into the GPT selection vector as a recombination cassette to generate a PSCFP2-A3L virus [see **2.4.1.2**]	H. Lynn
pE/L LA-RA (F13L-fluorion)	Generated as the first step in the construction of a homologous recombination cassette to generate both both F13L-Dendra2 and F13L-GFP viruses [see **2.1.2.1** for more details]	J. Horsington
pE/L LA-Dendra2-RA (F13L-fluorion)	Recombination cassette used to generate F13L-Dendra2 virus [see **2.1.2.1** for more details]	H. Lynn
pE/L LA-GFP-RA (F13L-fluorion)	Recombination cassette used to generate F13L-GFP virus [see **2.1.2.1** for more details]	H. Lynn
For ECTV, Chapter 5 and Chapter 6		
pE/L VACV LA-A36R-GFP	Used for transient expression of VACV A36R	T. P. Newsome, [317]

pE/L VACV A36R-YdF-	Used for transient expression of VACV A36R^{YdF}	T. P. Newsome, [317]
pE/L ECTV 137.5-GFP	Used for transient expression of ECTV A36R (137.5), the A36R gene was amplified from ECTV Mos genomic DNA with primer pair a36r.for/a36r.rev and cloned BglII/NotI into pE/L GFP-C	S. Y. Han
pE/L ECTV 137.5 Y112F	Used for transient expression of ECTV A36R^{Y112F} [see **2.1.2.2** for more details]	S. Y. Han
pE/L ECTV 137.5 Knockout construct	Regions of approximately 900 bp of ECTV Mos genomic DNA flanking the gene locus A36R were amplified with primer pairs a36r.ra.for/a36r.ra.rev for RA and a36r.la.for/a36r.la.rev for the LA and cloned into the GPT selection vector HindIII/SalI and NotI/BamH1 respectively	C. O'Sullivan
pE/L Lifeact-GFP	Used for the transient expression of Lifeact-GFP [see **2.1.2.2** for more details].	H. Lynn

2.1.3 SDS-PAGE

SDS sample buffer

62.5mM Tris-HCl

0.25M glycerol

2% (w/v) SDS

0.01% (w/v) bromophenol blue

12.5% (v/v) β-mercaptoethanol

Resolving gel

10% Acrylamide/Bis Solution, 37.5:1

0.375M Tris-HCl, pH 8.8

0.1% (w/v) SDS

0.1% APS

0.1% TEMED

Stacking gel

4% Acrylamide/Bis Solution, 37.5:1

0.375M Tris-HCl, pH 6.8

0.1% (w/v) SDS

0.1% APS

0.1% TEMED

Mammalian cells, generally BSC-1 [**Section 2.2**] which were either uninfected controls, or had been infected with the appropriate virus [**Section 2.3.2**] were harvested in sodium dodecyl sulphate (SDS)-reducing sample buffer. Samples were then heated at 95°C for 3 min and cooled for 3 min on ice. This cycle was repeated three times to degrade genetic material, then protein samples were loaded into 10% SDS-polyacrylamide gels and were separated by gel electrophoresis (SDS-PAGE) in a Mini-Protean Tetra Cell (BioRad).

2.1.4 Immunoblot

Resolved proteins from SDS-PAGE were transferred to nitrocellulose membranes (Amersham Hybond-C Extra, GE Health) with a Mini Trans-Blot (BioRad) using buffers compatible with equipment (manufacturers instructions). Membranes were then probed with primary antibodies [**Table 2.3**] diluted in PBST-milk (5% [w/v] skim milk in PBS with 0.1% Tween 20) for 30 min. The membrane was washed three times in PBST-milk and probed with secondary antibodies conjugated with horseradish peroxidase (HRP) [**Table 2.4**] for 30 min. Immunoreactive protein bands were visualised by applying Amersham enhanced chemiluminescence (ECL) Western blotting reagent (GE Health) on top of PBS washed membranes and exposing Amersham Hyperfilm ECL photographic film (GE Health) before development with a CP1000 photographic film developer.

Table 2.3. Primary antibodies used for immunoblot

ANTIBODY	SPECIES	DILUTION	ORIGIN
α-A36	Rabbit	1 in 1000	[191]
α-B5	Rat	1 in 2000	[264]
α-β-actin (AC-74)	Mouse	1 in 2000	Sigma-Aldrich
α-β-tubulin (236-10501)	Mouse	1 in 2000	Invitrogen
α-mRFP (Ab-2)	Rabbit	1 in 2000	Chemicon
α-GFP (4E12)	Mouse	1 in 2000	Cancer Research UK
α-Dendra2 (1G6)	Mouse	1 in 1000	Origene

Table 2.4. Secondary antibodies used for immunoblot

ANTIGEN	LABEL	SPECIES	DILUTION	ORIGIN
α-mouse	HRP	Goat	1 in 1000	Pierce
α-rat	HRP	Goat	1 in 1000	Pierce
α-rabbit	HRP	Goat	1 in 1000	Pierce

2.2 TISSUE CULTURE

2.2.1 Cell lines

Cells lines, unless otherwise noted, were cultured in Dulbecco's Modified Eagle Medium (DMEM, Invitrogen) supplemented with 5% fetal bovine serum (FBS, DKSH), 292 µg/mL L-Glutamine, 100 Units/mL penicillin and 100 µg/mL streptomycin (Invitrogen) and incubated at 37ºC with 5% CO_2 atmosphere in a Heraeus BB 15 Function Line cell culture incubator (Thermo-Scientific). Details of all the cell lines used in this thesis are listed in **Table 2.5**. Cells were obtained from collaborators or the American Type Culture Collection (ATCC).

Table 2.5. Cell lines and media

CELL LINE	SPECIES	MEDIA	SOURCE
HeLa	Human	DMEM	M. Way (ATCC, CCL-2)
BSC-1	Monkey	DMEM	M. Way (ATCC, CCL-26)
NIH3T3	Mouse	DMEM	M. Way (ATCC, CRL-1658)
MEFs	Mouse	DMEM	[318]
N-WASP null MEFs	Mouse	DMEM	[318]
P-815	Mouse	RPMI	ATCC, H-2d
YAC-1	Mouse	RPMI	ATCC, TIB-160

2.2.2 Transfection

Two different transfection protocols were used over the course of this thesis to transfect cells, generally HeLa. Lipofectin (Invitrogen) was used first, and then Lipofectamine 2000 (Invitrogen) when it was demonstrated to lead to higher transfection efficiencies. Both types of transfections were carried out according to manufacturer's instructions.

2.3 VIRUS CULTURE TECHNIQUES

2.3.1 Viruses

The VACV WR strain (ATCC VR-1354) was a gift from Michael Way, Cancer Research UK, and was used as the parental strain for all VACV lines used in or generated in this study. These strains and their origin are listed in **Table 2.6** and the process used for generation of recombinant viruses are detailed in **Section 2.4** below. ECTV-Moscow strain (ECTV-Mos; ATCC VR1374) was a gift from Professor RM Buller, St. Louis University School of Medicine.

Table 2.6. Virus strains generated or used in this study

VIRUS STRAIN	VIRUS	GENERATED BY
WR	VACV	ATCC VR-1354
ΔA36R	VACV	[215]
ΔF12L	VACV	[303]
ΔB5R	VACV	[272]
B5R-CFP	VACV	T. Newsome
B5R-PSCFP2	VACV	H. Lynn
PSCFP2-A3L	VACV	H. Lynn
B5R-Dendra2	VACV	H. Lynn
B5R-Dendra2/ΔF12L	VACV	H. Lynn
F13L-GFP	VACV	H. Lynn
F13L-Dendra2	VACV	H. Lynn
F13L-Dendra2/ΔA36R	VACV	H. Lynn
Dendra2-A3L	VACV	H. Lynn
Dendra2-A3L/B5R-CFP	VACV	H. Lynn
Mos	ECTV	ATCC VR1374
ΔA36R	ECTV	S. Han

2.3.2 Infection

For all infections, growth medium was removed from cells and the cells washed once in PBS. Virus at a specified MOI was diluted in DMEM not supplemented with FBS (serum free medium; SFM) and applied to washed cells. Cells were incubated at 37ºC with 5% CO_2 atmosphere for 1 hour before SFM with virus was aspirated and the cells recovered with fresh growth medium appropriate for the cell line.

2.3.3 Plaque assays

For plaque assays, confluent BSC-1 monolayers were infected as described, but instead of recovery with fresh growth medium, were overlaid with GIBCO Modified Eagle Medium (MEM; Invitrogen) supplemented with 292 µg/mL L-Glutamine, 100 Units/mL penicillin, 100 µg/mL streptomycin and 0.45% Ultra Pure Agarose (Invitrogen) for purification or 1.5% carboxy-methyl cellulose (CMC) for purification or plaque visualisation/staining. Plaques were allowed to form for 3-5 days before examination as specified.

If plaque assays were for purification, plaques were picked by using a P1000 pipette tip to collect an agarose plug and the infected cells immediately beneath the plug. These were resuspended in SFM, frozen and thawed for three cycles before being placed onto a confluent monolayer of BSC-1 in a well of a 24-well plate for amplification. One hour post infection (hpi), an equal volume of DMEM with 10% FBS was added to the well for a final FBS concentration of 5%.

For plaque assays to visualise plaque morphologies, the MEM/CMC overlay was aspirated and cells were washed three times with PBS before the plaques were imaged individually on an Olympus BX51 Microscope [see **Section 2.5.5**] or the cell monolayer was stained with crystal violet (0.5% (w/v) in 20% methanol solution) for 10 min and then washed again three times with PBS. Individual plaques are formed by the lysis or cytopathic effects caused by viral infection and generate visible clearings in the stained cell monolayer. Stained monolayers were scanned with a high-resolution gel scanner (BioRad GS-800).

2.3.3.1 Measuring plaque size

Plaque size was measured in pixels using ImageJ (ver. 1.4.4, a public domain imaging processing program developed by the National Instutes of Health [NIH]) to draw a line across the diameter of the plaque (always horizontally) and then converted to mm with a ruler placed for scale.

2.3.4 Preparation of viral genomic DNA

PCR-based methods were used to check or confirm virus genotypes. This required the extraction of genomic DNA (gDNA) from virus-infected cells. Virus-infected cells were scraped into 1ml of SFM and centrifuged for 10 min (16100 rcf, 4˚C) in a refrigerated centrifuge (Eppendorf Microcentrifuge 5415R) to pellet cells. The cell pellet was resuspended in 500 µl TE, 0.1% SDS and the microcentrifuge tube vortexed to lyse cells. 500 µl of phenol-chloroform-isoamylacohol (25:24:1, Astral Scientific) was added to the lysed cells and inverted to mix. This mixture was centrifuged for 4 min (16100 rcf, 4˚C) and the top (aqueous) layer was transferred to a new microcentrifuge tube. This step was repeated a second time before 1 ml 100% chilled ethanol and

50 µl 3M NaAcetate was added to the aqueous layer and inverted to mix. This was cooled to -20˚C overnight or -80˚C for 1 hr to precipitate gDNA before a final centrifuge for 30 min (16100 rcf, 4˚C). The supernatant was removed and the gDNA pellet was allowed to dry (on bench or 50˚C for 10 min).

The pellet was resuspended in Milli-Q H_2O or 10 mM Tris 1 mM EDTA (pH 8.0) solution (TE). DNA was then used (1 µl per 50 µl PCR) as a template for PCR using appropriate primers to confirm or identify the genotype based on the generation of a specific amplicon. Furthermore, in certain instances these successful PCR amplicons were used for DNA sequencing (all sequencing performed by the Australian Genome Research Facility Ltd.).

2.4 MAKING RECOMBINANT VIRUSES

2.4.1 Fluorescent recombinant VACV

Three conceptual methods were used to generate fluorescent recombinant VACV (used throughout Chapters 3 and 4), the first is homologous recombination and involved the introduction of DNA into the virus through a double crossover event between homologous regions of viral genomic DNA and vector DNA [319, 320]. The second method, called transient dominant selection (TDS), instead introduced genetic material into the virus through a single crossover event between homologous regions of viral and vector DNA [321]. This generates an unstable intermediate that integrates the entirety of the vector into the viral genome, which possesses both screenable and selectable markers as well as the gene fusion of interest. Upon removal of a selective pressure, a second recombination event occurs through regions of homology within the newly recombinant viral genomic DNA, removing the screenable and selectable markers, but leaving the gene fusion of interest [**Figure 2.2**]. TDS can therefore be used to generate virus strains with gene insertion/deletion but which do not encode selection genes [313]. The third method involves the coinfection of cells with two different recombinant viruses and allowing intergenomic recombination to occur by a single strand-annealing model involving viral DNA polymerase [322-324]. Resulting progeny viruses that contain both genes of interest are then selected and purified.

2.4.1.1 Homologous recombination

Non-TDS recombination was used to generate B5R (VACV-WR-187, Genbank accession: YP_233069) and A3L (VACV-WR-122, Genbank accession: YP_233004) fusions. For B5R, regions of homology flanking B5R (the left arm and right arm) were cloned into a vector, along with a genetic fusion between B5R and the fluorescent marker, PSCFP2 or Dendra2 [see **Section 2.1.2.1** and **Table 2.2**]. These vectors (pE/L LA-B5R-PSCFP2-RA and pE/L LA-B5R-Dendra2-RA) were then introduced into cells infected with ΔB5R through Lipofectin (Invitrogen) or Lipofectamine 2000 (Invitrogen) transfection according to manufacturer's instructions. Homologous recombination was allowed to occur between genomic DNA and vector for 24 hpi before the cells were scraped into SFM and virus was released from cells by freeze-thawing 3 times in liquid nitrogen.

Plaque assays were performed to select for successful recombinants that displayed both fluorescent markers and restored plaque size (the ΔB5R mutant has an attenuated small plaque phenotype [325]) on an Olympus BX51 Microscope [**Section 2.5.5**]. PSCFP2 displayed blue fluorescence and was imaged with a DAPI filter, while Dendra2 displayed green fluorescene and was imaged with a FITC filter [**Section 3.1.2.4**]. Three rounds of plaque assays were performed to purify the recombinant virus.

2.4.1.2 Transient Dominant Selection

The process for generating A3L fusions was similar to B5R fusions [**Section 2.4.1.1**], but as ΔA3L is unviable, the construction of the recombination cassette and the homologous recombination differs (as we cannot select for restored plaque size). Instead of regions of interest flanking the gene of interest being cloned into the recombination cassette, the fluorescent protein gene (PSCFP2 or Dendra2) was fused with overlap extension PCR to the first 500bp of A3L (to form an N-terminal fluorescent fusion protein) and 500bp upstream of A3L (left arm) were cloned into a GPT selection vector for TDS (pE/L LA-Dendra2-A3L(500)GPT) [see **Section 2.1.2.1**, **Table 2.2**].

Recombinations were carried out in the same way as non-TDS homologous recombination, then plaque assays were carried out with the addition of GPT selection medium (25 µg/ml mycophenolic acid [MPA], 250 µg/ml xanthine, 15 µg/ml hypoxanthine) in the overlay [**Section 2.1.2.1]**. Plaques able to grow under GPT selection that displayed red fluorescence imaged with the TxRed filter of an Olympus BX51 Microscope [**Section 2.5.5**] were picked and purified three times by plaque assay with GPT selection throughout. These intermediate viruses [**Figure 2.2**] were then allowed to intra-genomically recombine in a GPT selection negative infection, 24 hpi virus was collected and a plaque assay was performed to isolate the desired fluorescent recombinant which displayed green fluorescence imaged with a FITC filter [**Section 3.1.2.4**]. Two additional rounds of plaque purification was performed without GPT selection before the integrity of viruses was checked with PCR and immunoblot [**Section 2.1.2, 2.1.3**].

TDS was also used to generate F13L-Dendra2 and F13L-GFP as described above, utilising vectors pE/L LA-Dendra2-RA (F13L-fluorion) and pE/L LA-GFP-RA (F13L-fluorion) [see **Section 2.1.2.1**, **Table 2.2**]. As regions of homology were shorter than in pE/L LA-Dendra2-A3L(500)GPT, recombination occurred at a lower efficiency, but still high enough for recombinant viruses to be isolated [313, 326].

2.4.1.3 Recombinations between viruses

Recombinant viruses were generated in a third way, which unlike the aforementioned methods involves the recombination between two strands of viral genomic DNA rather than between genomic DNA and a transfected vector. This method was used to generate viruses with two observable phenotypes/screenable markers, such as two fluorescent proteins

(Dendra2-A3L/B5R-CFP), or otherwise a fluorescent protein and a mutation that created a small plaque phenotype (B5R-Dendra2/ΔF12L and F13L-Dendra2/ΔA36R).

Two viruses, each encoding one of the two observable phenotypes were used to coinfect cells. 24hpi, cells were lysed and the first of three plaque assays was conducted to select both phenotypes/markers in single plaques. For Dendra2-A3L/B5R-CFP, these were plaques that displayed green fluorescence as imaged with a FITC filter and blue fluorescence as imaged with a CFP filter [**Section 3.1.2.4**]. For both B5R-Dendra2/ΔF12L and F13L-Dendra2/ΔA36R, small plaques compared to a B5R-Dendra2 or F13L-Dendra2 control that also displayed green fluorescence as imaged with a FITC filter were picked.

2.4.2 ECTV deletion virus construction

To construct an ECTV ΔA36R mutant, non-TDS homologous recombination was carried out with both selectable (GPT) and screenable (mRFP) markers [**Section 2.1.2**]. HeLa cells grown to 70% confluency were infected with ECTV Mos at an MOI of 1 and transfected with the recombination cassette (pE/L ECTV 137.5 Knockout construct, **Figure 2.2**, **Table 2.2**) using Lipofectamine 2000 (Invitrogen), according to manufacturers instructions. Cells were scraped 24 hpi and lysed by freeze thawing. Plaque assays were performed with GPT selection medium in the overlay. Plaques formed in the presence of GPT selection that also displayed mRFP fluorescence were purified and verified as ΔA36R with sequencing.

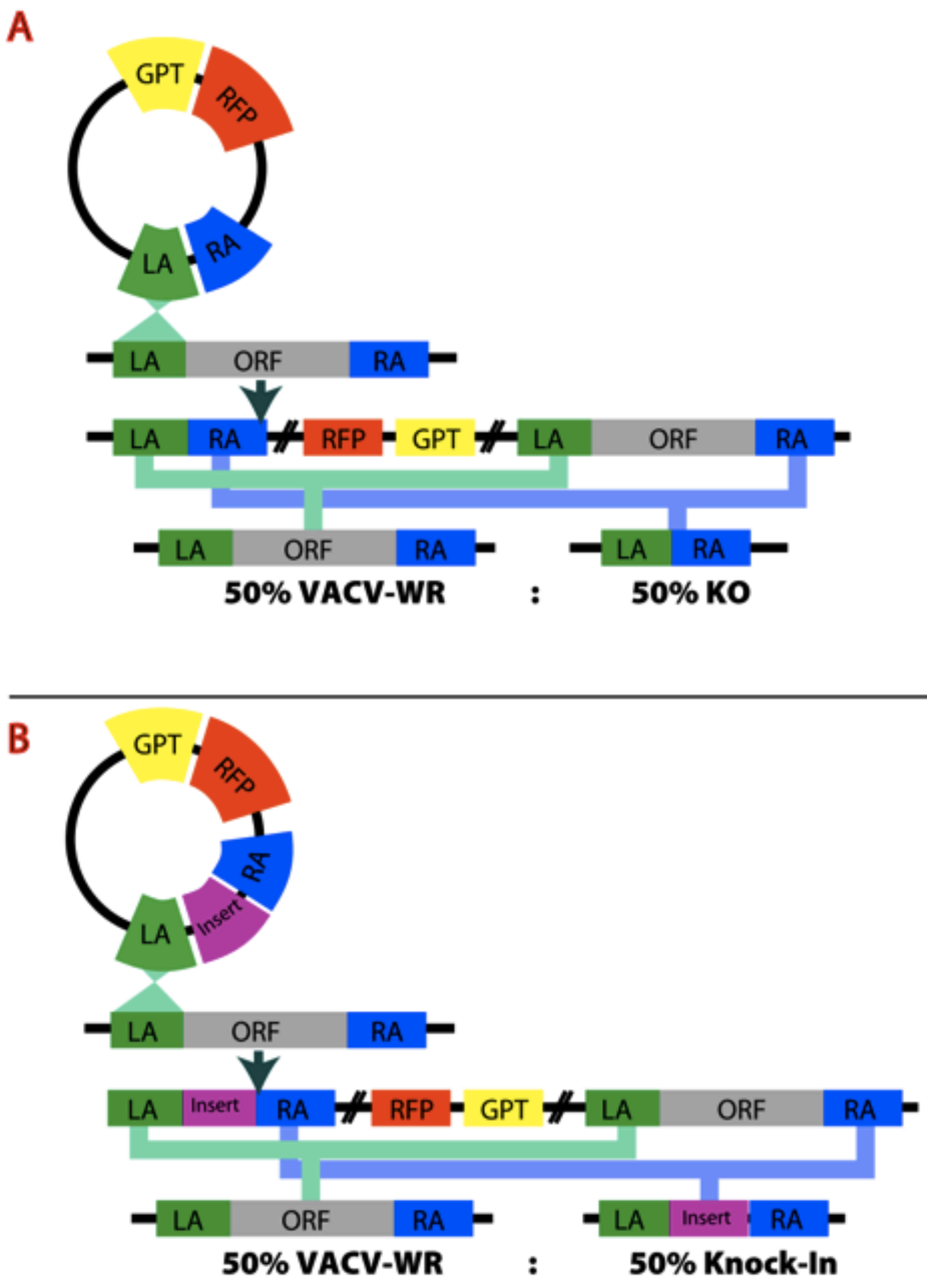

Figure 2.2: Transient dominant selection overview
For Knock out **(A)** upstream (LA) and downstream (RA) DNA of the gene of interest are cloned or synthesised side-by-side into a vector containing pE/L GPT and pE/L mRFP. For Knock-in **(B)**, upstream (LA) and downstream (RA) DNA of the location for the intended gene insertion are cloned/synthesised either side of the intended insert/gene fusion along with pE/L GPT and pE/L mCherry. After an initial crossover event, the entire construct is introduced into the genome. This insert is unstable, and is only retained under selection. Once selection is removed, internal homologous recombination will occur, leading to progeny that have either the parental genome or the intended genetic alteration (KO or knock-in).

2.5 IMMUNOFLUORESENCE

2.5.1 General buffers and solutions

Cytoskeletal buffer (CB), pH 6.1

10 mM 2-(N-morpholino) ethanesulfonic acid (MES) buffer

0.15 M NaCl

5 mM ethylene glycol tetraacetic acid (EGTA)

5 mM $MgCl_2$

50 mM glucose

Mowiol mounting media

10% (w/v) Polyvinyl Alcohol 4-88 (Sigma-Aldrich)

25% (w/v) glycerol

0.1M Tris, pH 8.5

Blocking buffer

1% BSA

2% FBS

Made up in CB

2.5.2 Fixation methods

Cells were grown on glass coverslips, infected with appropriate viruses and fixed with 3% paraformaldehyde (PFA) in cytoskeletal buffer (CB) for 10 min at room temperature before being washed 3 times in PBS and stored at 4°C.

2.5.3 Antibodies and fluorescent chemicals

Antibodies and fluorescent chemicals were mostly commercial, unless otherwise noted according to **Tables 2.7-2.9.** One antibody, α-A36-Y112, was not commercial or previously published, and was generated by Niki Scapelhorn at Cancer Research UK. It was raised against the phosphorylated peptide corresponding to residues 105-119 of VACV A36 (APSTEHIpYDSVAGST) and purified as described previously [296], but affinity is not influenced by phosphorylation of tyrosine 112 of A36.

Table 2.7. Primary antibodies used for IFA

ANTIBODY	SPECIES	DILUTION	ORIGIN
α-A36	Rabbit	1 in 250	[191]
α-A36-Y112	Rabbit	1 in 250	N. Scapelhorn
α-A27	Mouse	1 in 2000	[327]
α-B5	Rat	1 in 300	[264]
α-β-actin (AC-74)	Mouse	1 in 300	Sigma-Aldrich
α-cortactin (4F11)	Mouse	1 in 300	Merck-Millipore
α-GFP (3E1)	Mouse	1 in 300	Cancer Research UK
α-KHC (H-50)	Rabbit	1 in 200	Santa Cruz Biotechnology
α-phosphotyrosine (4G10)	Mouse	1 in 1000	Chemicon

Table 2.8. Secondary antibodies used for IFA

ANTIGEN	LABEL	SPECIES	DILUTION	ORIGIN
α-mouse	Alexa Fluor 350	Goat	1 in 200	Invitrogen
α-mouse	Alexa Fluor 488	Goat	1 in 200	Invitrogen
α-mouse	Alexa Fluor 568	Goat	1 in 200	Invitrogen
α-rat	Alexa Fluor 350	Goat	1 in 200	Invitrogen
α-rat	Alexa Fluor 488	Goat	1 in 200	Invitrogen
α-rat	Alexa Fluor 568	Goat	1 in 200	Invitrogen
α-rabbit	Alexa Fluor 488	Goat	1 in 200	Invitrogen
α-rabbit	Alexa Fluor 568	Goat	1 in 200	Invitrogen

Table 2.9. Fluorescent chemicals

CHEMICAL	LABEL	STRUCTURE SPECIFICITY	DILUTION	ORIGIN
Phalloidin	Alexa Fluor 488	Actin	1 in 300	Invitrogen
Phalloidin	Alexa Fluor 568	Actin	1 in 300	Invitrogen
DAPI	N/A	dsDNA	1 µg/mL	Sigma-Aldrich

2.5.4 Staining and mounting

Before staining, cells were either permeabilised with 0.1% Triton X-100 in CB for 5 min or not permeabilised, as specified. After washing three times in PBS, cells were blocked in blocking buffer for 20 min then incubated for 40 min with suitable primary antibodies, unless stated otherwise, diluted in blocking buffer. After an additional three washes with PBS, secondary antibodies diluted in blocking buffer were applied to cells for 20 min. When appropriate, Alexa Phalloidin conjugates were also added to blocking buffer to incubate with secondary antibodies. If dsDNA staining was required, coverslips were again washed three times in PBS and incubated with 1μg/mL 4',6-diamidino-2-phenylindole (DAPI) for 3 min. Coverslips were then washed in MQ and excess water drained before being mounted on a glass slide with 0.3-1% (w/v) P-phenylenediamine (Sigma-Aldrich) in mowiol mounting media [**Section 2.5.1**]. Slides were incubated at 37^{o}C for 30 min until the mowiol mounting media solidified prior to imaging.

2.5.5 Wide field microscopy

For imaging of IFAs, slides were analysed by phase-contrast and fluorescent microscopy using Olympus BX51 Microscope with Reflection Fluorescence System, Mercury Burner (U-RFL-T), F-view monochrome fluorescence camera and DAPI (347 nm/442 nm [#31013v2]), eCFP (436 nm/480 nm [#49001]), FITC (495 nm/515 nm [#31001]) and TxRed (584 nm/610 nm [#31004]) Chroma filters. Micrographs were captured using AnalySIS LS Starter (Olympus Soft Imaging Systems, ver. 2.8), and edited using Photoshop CS5.1 (Adobe, ver. 12.1) and ImageJ (NIH, ver. 1.4.4).

2.5.5.1 Measuring actin tails

As actin tails are not straight, to measure the length of tails, a freehand line was drawn with the line tool on an overlay of the micrograph in ImageJ (NIH, ver. 1.4.4). This length of line was then measured in pixels with the Measure function. This was converted to metric measurements with the scale bar.

2.6 CONFOCAL MICROSCOPY

2.6.1 Fibronectin coating

Fibronectin from bovine plasma (Sigma-Aldrich) was diluted in 1.5ml of PBS to 5 μg/cm^2 and rocked in a 3cm No. 1.5 glass μ-Dishes (Ibidi) for 1h. Remaining liquid was aspirated and the dishes were allowed to dry in a sterile environment. Dry plates were stored at 4^{o}C ready for cell seeding.

2.6.2 Photoactivation and tracking

HeLa seeded onto fibronectin coated No. 1.5 glass μ-Dishes (Ibidi) were infected with the appropriate virus and then imaged on an Olympus FV1000 confocal microscope at the Australian Centre for Microscopy and Microanalysis (ACMM, Sydney). Laser lines on the microscope that were utilised in this study are listed below [**Table 2.10**].

Infected cells were imaged sequentially with a UPLSAPO 60X oil objective lens with 405 nm diode laser and 488 nm multi-line argon laser (PSCFP2) or 488 nm multi-line argon laser and 559 nm diode laser (Dendra2) with 4.0 pixel/sec scan speed to obtain pre-activation images. In viruses with a CFP tag, a 458 nm multi-line argon laser was also used. A 40 x 40 pixel region of interest (ROI), the region of the cell with the brightest 405 nm (PSCFP2) or 488 nm (Dendra2) emission, was selected for photoconversion. The ROI was activated with 3% of the 405 nm SIM laser under "Tornado" setting for 100ms at a scan speed of 100μs/pixel. After activation, either a time course or Z-stack from the basal to apical surface was collected (step size was detemined by automated optimisation). See Chapter 3 Results for more details.

Table 2.10. Laser lines used

WAVELENGTH	LASER TYPE	POWER
405 nm	Diode	50 mW
458 nm	Multi-line argon (458, 488, 515 nm)	Total 30 mW
488 nm	Multi-line argon (458, 488, 515 nm)	Total 30 mW
559 nm	Diode	15 mW

2.6.3 Imaging live actin tails

35 mm glass bottom dishes (MatTek) were coated in 5 μg/cm^2 fibronectin (Sigma-Aldrich) for 2 h before HeLa cells were seeded and grown to 70% confluency. Cells were infected and recovered with fresh growth medium 1hpi before being transfected with pE/L Lifeact-GFP 6 h prior to

imaging (standard protocol, Lipofectamine 2000, Invitrogen). Either 8-10 hpi (VACV) or 24-26 hpi (ECTV), images of cells were acquired with Olympus Fluoview (Ver. 3.1) on an Olympus FV1000 confocal microscope using with a 488nm laser line. Resulting movies were processed with a Manual Tracking plugin in Image J (Ver. 1.44o). See Chapter 5 Results for more details.

2.7 MOUSE WORK AND IMMUNOLOGY

2.7.1 Ethics Statement

This study was performed in strict accordance with the recommendations in the Australian code of practice for the care and use of animals for scientific purposes and the Australian National Health and Medical Research Council Guidelines and Policies on Animal Ethics. The protocol was approved by the Animal Ethics and Experimentation Committee of the Australian National University (Permit Number: J.IG.75.09).

2.7.2 Mouse experiments

Inbred, specific-pathogen-free female BALB/cAnNCrl (BALB/c), C57BL/6J wild-type mice and Rag-1-deficient B6.129S7-Rag1^{tm1Mom}/J (B6.Rag-1$^{-/-}$) [328] mice on a C57BL/6J background at 6-8 weeks of age were obtained from the Australian National University Bioscience Services (Canberra ACT, Australia). Groups of female BALB/c mice were infected subcutaneously in the left hind leg with 10^2, 10^3, or 10^4 pfu ECTV or ECTV ΔA36R and monitored for survival and clinical signs of disease for 33 days. Separate groups of infected mice were euthanized at 5 and 8 dpi. Rag-1$^{-/-}$ mice were inoculated with 10^3 PFU virus and also sacrificed at days 5 and 8 dpi for determination of viral titers in organs. Viral load in livers, spleens and lymph nodes were quantified by viral plaque assay on BSC-1 cell monolayers as described previously [329] and are expressed as $\log_{10}$ PFU/gram tissue or per lymph node. On day 28 p.i., all surviving BALB/c mice infected with ECTV ΔA36R from the first group were bled and then challenged with a lethal dose by a subcutaneous route of 10^4 PFU ECTV on day 33. Eight days later, mice were sacrificed and anti-ECTV antibody in serum and virus in spleen, liver and lymph nodes were measured.

2.7.3 Enzyme-linked immunosorbent assay (ELISA)

Serum samples were assayed by ELISA for total ECTV-specific IgG as described earlier [330]. Briefly, U-bottom 96-well plates (Immulon 2, Dynatech Lab Inc., Alexandria, VA, USA) were coated with purified ECTV. Sera were assayed at 1:200 dilution and ECTV-specific antibody detected using horseradish peroxidase-conjugated goat anti-mouse IgG (Southern Biotechnology Associates, Birmingham, AL, USA) and color developed with TMB One-Step substrate (Dako Cytomation, Carpinteria, CA, USA).

2.7.4 Plaque reduction neutralisation test

The plaque reduction neutralisation test, used to determine the neutralising activity of the antibody present in serum samples to ECTV-WT has been described [330]. Serial dilutions of sera, starting at a 1: 50 dilution were used. The neutralization titer was taken as the reciprocal of the dilution of sera that caused a 50% reduction in the number of virus plaques.

2.7.5 Cytotoxic T lymphocyte (CTL) and natural killer (NK) cell assays

CTL and NK cell assays were performed as described elsewhere [329, 331]. To measure *ex vivo* CTL responses, spleen cells from infected animals were assessed for the ability to kill ^{51}Cr-labelled virus-infected or uninfected syngeneic P815 target cells over a 6 h culture period. To assess NK cell activity *ex vivo*, spleen cells from infected or uninfected BALB/c and C57BL/6 mice were cultured with ^{51}Cr-labelled YAC-1 target cells for 4 h and the radioactivity in the supernatant measured in a TopCount NXT™ scintillation counter.

CHAPTER 3: Optimising Phototracking of Vaccinia Virus Transport

3.1 INTRODUCTION

Some of the work detailed in this chapter (the method of generation of F13L-Dendra2 and F13L-GFP viruses) has been published: NB Marzook*, DJ Procter***,** **H Lynn**, Y Yamamoto, J Horsington, TP Newsome [2013]. *Methodology for the efficient generation of fluorescently tagged vaccinia virus proteins.* **Journal of Visualised Experiments**. 17(83), e51151. All viruses utilised in this chapter were constructed and purified by H. Lynn with the exception of previously published viruses as noted in Table 2.6. All of the represented data was generated and analysed by H. Lynn.

3.1.1 Imaging viral subcellular transport

Fluorescent protein technology has been instrumental in gaining insights into the subcellular transport mechanisms of VACV. However, the various morphological forms of VACV and the sheer number of viruses being transported at any one time in a single infected cell presents a considerable challenge to addressing many aspects of the replication cycle. We propose that utilising recent advances in fluorescent protein technology, specifically the development of photoswitchable fluorescent proteins, may allow us to probe further into the characterisation and regulation of virus dissemination.

3.1.2 Fluorescent proteins

Fluorescent proteins contain chromophores that absorb light of certain wavelengths and emit longer, less energetic wavelengths of light. They are described by the predominant colour of the wavelength of light they emit, for example, green fluorescent protein (GFP) emits green light (~500 nm) [332]. Each of these visible emissions or fluorescence consists of a wide spectrum of wavelengths at different intensities that can be described by an emission spectrum [**Figure 3.2C**]. Likewise, a range of wavelengths can excite/be absorbed by the chromophore and this can be represented by an excitation spectrum [**Figure 3.2C**]. The peak in the excitation spectrum is where the most efficient stimulation of the chromophore occurs.

Fluorescent proteins can be excited by different light sources, either incoherent lightsources such as short-arc lamps commonly used on both widefield and confocal microscopy systems that emit a wide spectrum of light (which can then narrowed by use of interference filters) or otherwise high intensity monochromatic lightsources; for example laser lines that are a single wavelength and are more often associated with confocal microscopy systems [333]. Laser lines closer to the excitation peak of the fluorophore will cause brighter emission, although excitation of the fluorophore anywhere along the excitation spectrum will cause a signal to be generated.

A large toolbox of fluorescent proteins covering the visual light spectrum from near ultraviolet blues to near infrared reds have been created, optimised and characterised [**Figure 3.1**] [310, 334-337]. These engineered and enhanced proteins allow for the coupling of two to three fluorescent tags in the same sample, enabling the simultaneous imaging of multiple proteins (without requiring optical demixing).

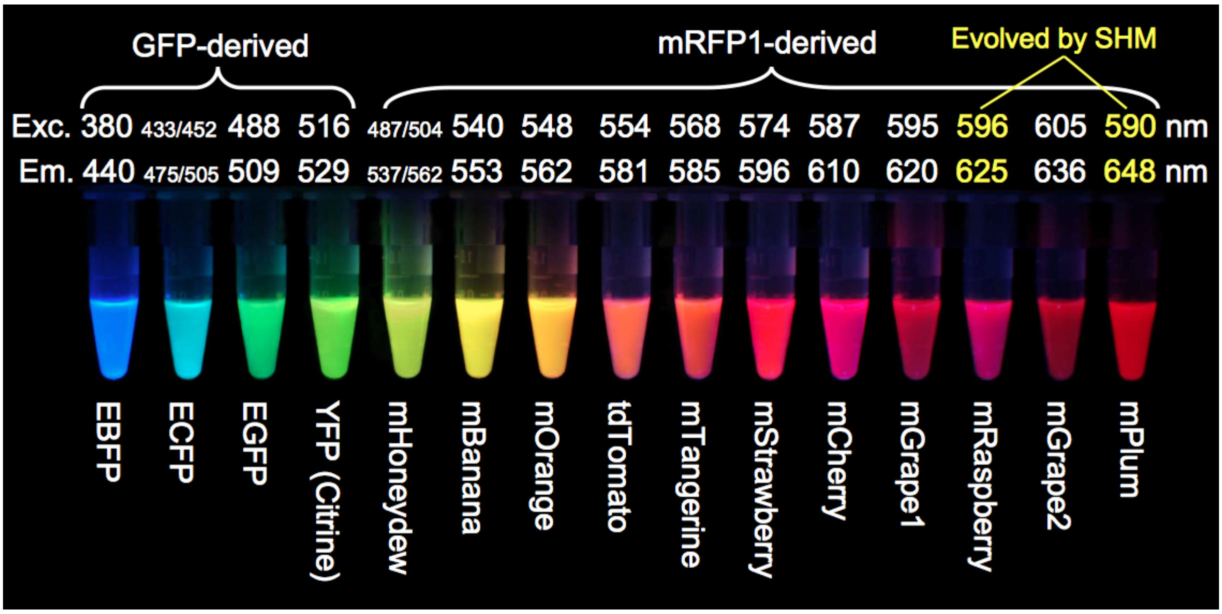

Figure 3.1: Range of non-oligomerising fluorescent proteins available
Representatives of fluorescent proteins derived from *Aequorea* GFP or *Discosoma* RFP through directed mutagenesis or by somatic hypermutation (SHM) that cover the entire visible light spectrum, expressed in bacteria and purified. E represents enhanced versions of GFP-derived fluorescent proteins all of which are monomeric (although some will dimerise at high concentrations), m represents other monomeric proteins, and tdTomato is a head-to-tail dimer. From [336].

3.1.2.2 Green Fluorescent Protein (GFP) and other traditional protein tags for fluorescent imaging

GFP from the jellyfish *Aequorea victoria* was the first fluorescent protein to be adopted widely as a genetically encoded in situ fluorescent tag. The particular utility of GFP is that all functions for chromophore formation and maturation are present within its coding sequence and no additional substrates or coenzymes are required for fluorescence [338, 339]. This enabled it to be readily cloned and expressed in multiple organisms with fluorescence functionality intact [340].

Wild-type GFP (wt-GFP) has an excitation spectrum that peaks at 395 nm, with a secondary peak at 470 nm and an emission spectrum that peaks at 508 nm [**Figure 3.2C**] [341]. This fluorescence is emitted from an 4-(p-hydroxybenzylidene)imidazolidin-5-one structure that is that is formed by the autocatalytic covalent modification of three adjacent amino acids (Ser65-Tyr66-Gly67) in a process called chromophore maturation [338, 340, 342, 343] [**Figure 3.2A**]. This chromophore is situated in the middle of a α-helix bridge that runs through the centre of a β-barrel formed from 11 β-sheets in the folded GFP structure [343, 344] [**Figure 3.2B**].

The hydrogen bonding and other electrostatic interactions between the chromophore and sidechains on the inside of the β-barrel influence the maturation, colour, brightness and photostability of the chromophore [345]. They have therefore been subject to multiple mutagenesis studies to improve GFP in all these aspects. Additionally, mutagenesis studies have aimed to increase the utility of GFP in standard *in vitro* contexts (carried out in mammalian animal or cell culture models at 37^{o}C).

The expression of wt-GFP was improved by optimising codons to mammalian expression while several additional mutations were found to facilitate folding at 37°C and prevent GFP dimerisation [340, 346, 347]. The speed of chromophore maturation was improved by almost four fold (to approximately 27 min) with the substitution of Thr65 for Ser65 (S65T) [332]. Finally, the 395 nm and secondary 470 nm excitation/absorbance peaks were converted into a single peak at 489 nm, leading to brighter fluorescence upon imaging while retaining a very similar emission profile [**Figure 3.2C**] [348, 349]. A GFP variant known as enhanced GFP (EGFP) includes all of these improvements [350].

Other mutants from GFP have resulted in a series of fluorescent proteins with shifted excitation/emission spectra, either towards shorter wavelengths like blue fluorescent protein (BFP) and cyan fluorescent protein (CFP) or towards longer wavelengths like yellow fluorescent protein (YFP) [**Figure 3.1**] [351, 352]. Further longer wavelength shifted fluorescent proteins are also available, including those with red or infrared emission profiles, although these do not originate from *A. victoria* GFP mutants. Instead, they are mostly derived from a monomeric red fluorescent protein (mRFP), which originates from modification of multimeric DsRed protein from *Discosoma* coral [**Figure 3.1**] [310, 353].

The obligate tetramerisation of wild type DsRed severely limits the study of subcellular localisation, with fusion proteins forming intracellular aggregates, thus impeding its widespread utility and use. A total of 33 mutations were required to create a monomeric protein (mRFP) with comparable brightness to DsRed in living cells [310].

The brightness of a fluorescent protein is a combination of factors including the molar extinction coefficient (the amount of light absorbed by the fluorescent protein), the fluorescence quantum yield (the efficiency of light emitted per photon of light absorbed), amount of protein expression, rate of maturation and the photostability of the protein (the rate of bleaching/decrease in emission over time excited) [354]. As such, improvements in certain values can compensate for decreases in others. This is true for mRFP, which compensates for a lower extinction coefficient, quantum yield and photostability than DsRed with fast chromophore maturation (~1 h compared to 10 h for DsRed) [310, 334]. Many of the later generation excitation/emission shifted mRFP derivatives improved on these various characteristics, creating a spectrum of fluorescent proteins with comparable experimental utility as EGFP, a benchmark for fluorescent protein technology [335].

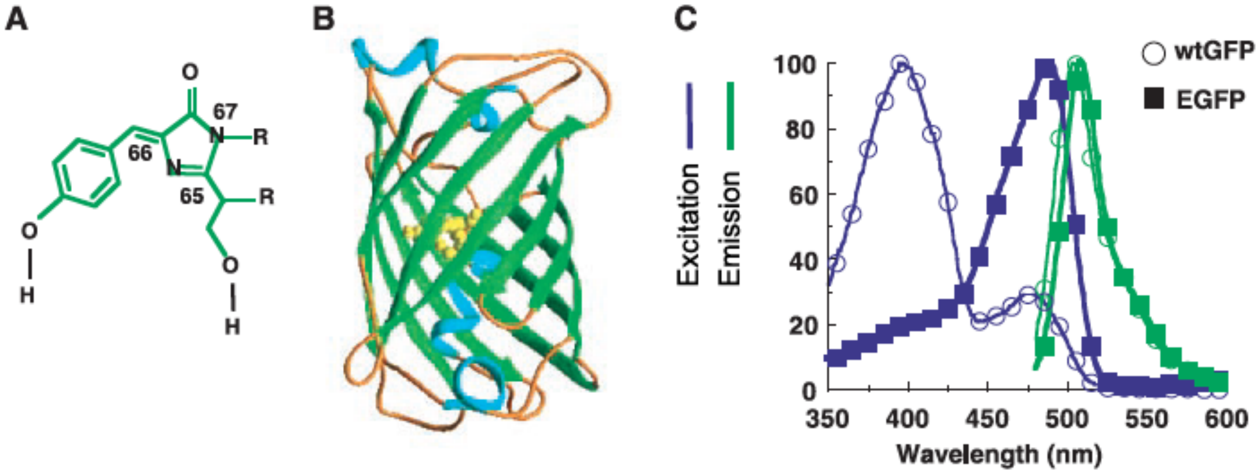

Figure 3.2: The structure and spectral properties of GFP
(A) A schematic of the wtGFP chromophore which forms from the autocatalytic cyclisation of Ser65, Tyr66, and Gly67 into 4-(p-hydroxybenzylidene)imidazolidin-5-one. (B) The protein structure of wtGFP with a α-helix bridge (blue) holding the chromophore (yellow) in the centre of an 11-sheet β-barrel (green). (C) The excitation (blue) and emission (green) spectra of wtGFP (open circles) and EGFP (closed squares). In generating EGFP, the two absorbance peaks of wtGFP were converted into a single peak without substatial alteration of the fluorescence emission peak. From [350].

3.1.2.3 Photoactivatable FPs

Even though the suite of traditional fluorescent proteins makes it possible to carry out sophisticated imaging of multiple targets or structures with high resolution spatially and temporally, there are still many questions that cannot be answered. For instance, as encoded fluorescent protein fusions are continuously being synthesised and degraded in cells, proteins of all ages are imaged simultaneously. Analysis of protein and protein complex turnover and temporal expression patterns is therefore extremely difficult [350]. The complexity of cellular processes, where many objects are constantly moving and interacting with others further clouds analyses of biological processes with traditional fluorescent tags.

One solution to this problem is distinguishing a specific subset of the fluorescent population from the bulk of the fluorescence signal. This can be achieved by purposefully photobleaching the fluorescence in selected areas of the cell and monitoring recovery of fluorescence in a process called fluorescence recovery after photobleaching (FRAP) [355]. FRAP can be performed with traditional fluorescent protein tags and can reveal information on protein turnover and diffusion kinetics. A complementary method called fluorescence loss in photobleaching (FLIP) can also be performed with traditional protein tags and involves the bleaching of a region of interest while monitoring the decline in fluorescence in a surrounding region or selected compartment to reveal information on protein mobility [355].

Alternatively, a selected area of the cell can be highlighted by region selective increase in fluorescence brightness (photoactivation) or alteration of excitation/emission spectra characteristics (photoswitching, although this process is also referred to as photoactivation) [**Figure 3.3**]. As photoconverted molecules display a distinguishably different fluorescence, their behaviour can be studied independently to subpopulations/areas that are not of interest [350]. This process cannot be performed with traditional fluorescent protein tags but requires newer generation photoconvertible fluorescent proteins [**Figure 3.3**]. These include photoactivatable green fluorescent protein (PA-GFP), Kaede, Eos, Dendra and photoswitchable cyan fluorescent protein (PS-CFP) [356-359].

PA-GFP was developed through the improvement of the native photoconversion of the wtGFP chromophore from a neutral/protonated state to an anionic species. The neutral state has a major absorption peak (at 395 nm), while the anionic species predominantly absorbs at the minor absorption peak (at 475 nm) [**Figure 3.2C**]. Intense irradiation with UV or near 400 nm light shifts the equilibrium towards the anionic state, thereby shifting the absorbance profile [360]. The T203H mutation in PA-GFP leads to the almost total absence of a minor absorption peak prior to photoconversion, providing maximum contrast between pre- and post- activated chromophores (with a 100-fold difference) [356].

A second photoactivatable fluorescent protein type includes Anthozoa-derived green- to-red convertible proteins and their enhanced variants. In the dark, these proteins mature (fold and form their chromophore) to the green fluorescent state, while irradiation with UV-violet light results in their irreversible transition into a red fluorescent state. The first member of this group was named Kaede [357], then EosFP and mEosFP [358] and KikGR [361]. The mechanism of photoactivation of these proteins involves intense irradiation by near-400 nm light causing the cleavage of a carboxyamide group containing peptide from the chromophore, which changes the absorbance and emission of the aromatic rings to a red fluorescence profile [358, 362].

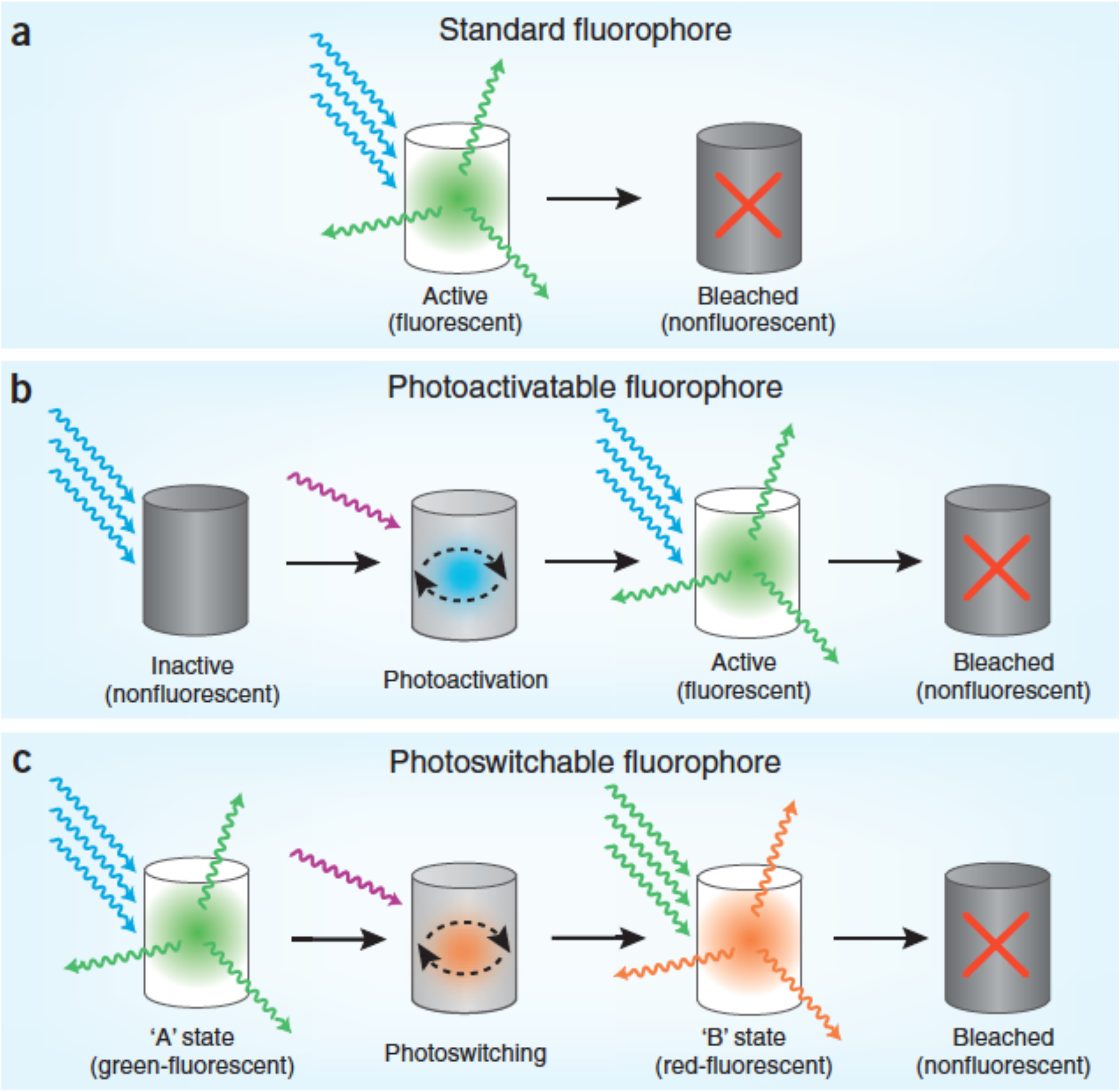

Figure 3.3: **Photoconvertible fluorescent proteins**

Schematic representation of traditional fluorescent protein tags compared to photoconvertible fluorescent proteins. (A) When a standard fluorophore is excited with light of the appropriate wavelength (blue), it emits light of a longer wavelength (green), the process of exciting the fluorophore will bleach it, causing a non-fluorescent state. (B) Photoactivatable fluorophores will be non-fluorescent at first and are not able to be excited. Upon the stimulation of the fluorophore with an activating wavelength of light (purple), the fluorphore will become fluorescent and act similarly to standard fluorophores. (C) A similar process occurs with photoswitchable fluorophores, but rather than being non-fluorescent at first, they have an "A" fluorescent state (blue absorbing and green emitting), and upon the stimulation by activating light, will convert to longer wavelength shifted "B" state (green absorbing and red emitting). Figure from [363].

3.1.2.4 Photoswitchable Cyan Fluorescent Protein 2 (PSCFP2) and Dendra2

Two of the newest available photoactivatable fluorescent proteins are PSCFP2 and Dendra2. As well as having some of highest reported contrast between pre- and post-activated fluorescence states (over 2000-fold for PSCFP2 and 4000-fold for Dendra2), they are bright in both states (relative to other photoactivatable fluorescent proteins), monomeric and mature at 37^{o}C [312].

PSCFP2 is derived from mutagenesis of acEGFP (which is itself a mutant from a colourless *Aequorea coerulescens* protein) [364]. It has a preactivation cyan profile with an excitation maximum of 400 nm and emission maximum of 468 nm [**Figure 3.4A**]. The mechanism for photoconversion is similar to that of PA-GFP, with irradiation of high intensity near 400 nm light causing PSCFP2 to undergo an irreversible chromophore deprotonation that leads to a longer wavelength shift of the emission profile. After activation, PSCFP2 has a green profile with an excitation maximum of 490 nm and emission maximum of 511 nm [**Figure 3.4B**] [312]. The cyan to green shift of PSCFP2 is a unique characteristic among photoactivatable proteins and may have utility in multichannel imaging in various contexts.

Dendra2 is derived from the mutagenesis of a fluorescent protein present in the coral *Dendranephthya spp.* (in the class Anthozoa) [365]. It has a pre-activation green profile with excitation maximum of 490 nm and emission maximum of 507 nm [**Figure 3.4C**]. The mode of photoactivation is similar to other Anthozoa-derived photoactivatable fluorescent proteins with intense ~400 nm light causing the irreversible cleavage of a peptide from the chromophore and shift into a red emission profile [312]. The post-activation excitation and emission maximum is 553 nm and 573 nm, respectively [**Figure 3.4D**]. A characteristic unique to Dendra2 is that as blue excitation light (such as 488 nm lasers) can be used for photoactivation, this may provide advantages over near 400 nm light exposure, as intense ultra violet light is damaging to cells and can induce an apoptotic response [312, 366].

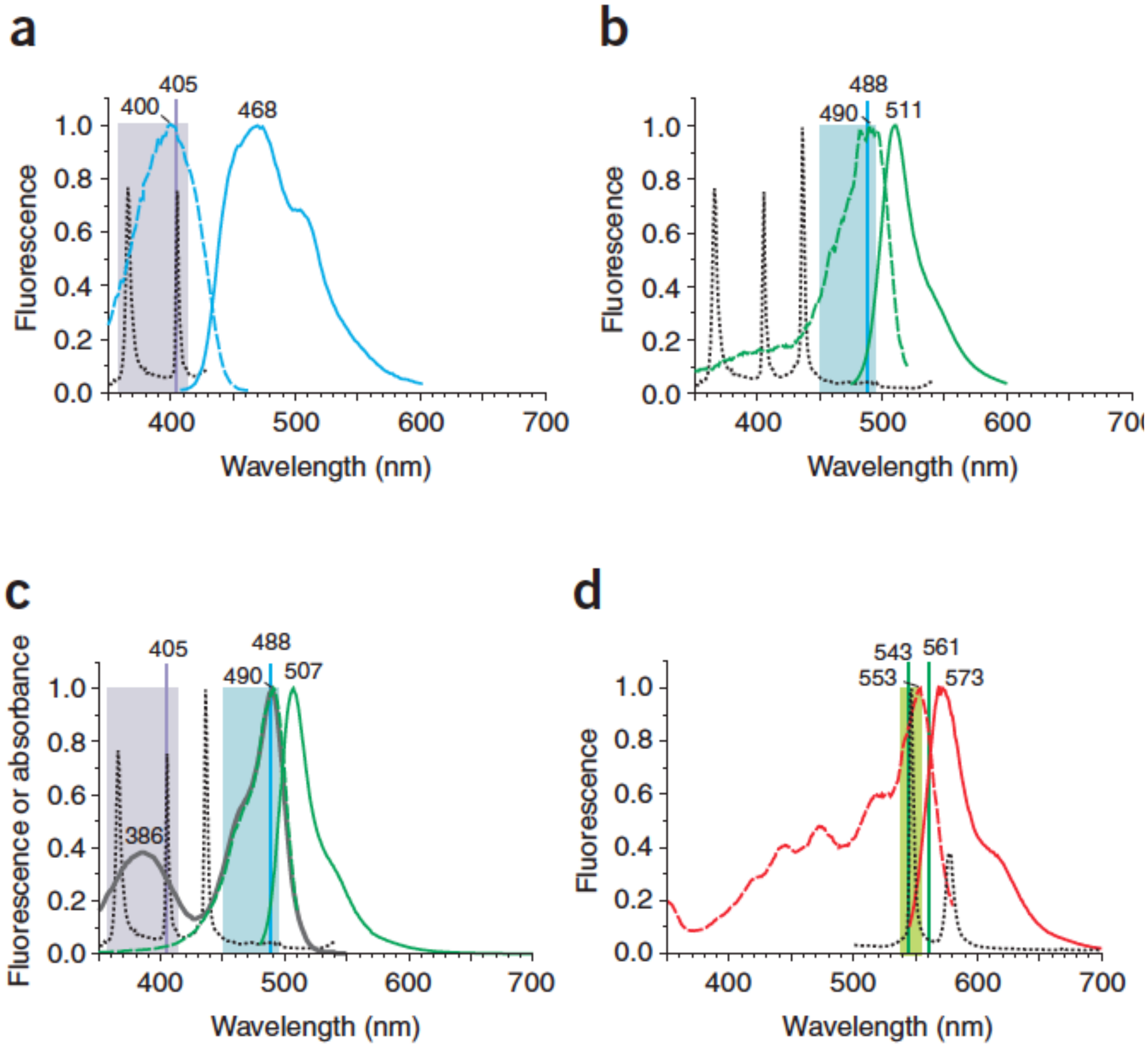

Figure 3.4: Spectral properties of PS-CFP2 and Dendra2

The excitation spectra (dashed lines) and emission spectra (solid lines) of PSCFP2 and Dendra2 are represented. PSCFP2 before **(A)** and after **(B)** photoconversion, with cyan and green profiles respectively. Dendra2 before **(C)** and after (**D**) photoconversion, with green and red profile respectively. Dotted black lines represent the emission spectrum of standard mercury lamp filters for widefield imaging and laser lines are represented with vertical lines. From [312].

3.1.3 Viral fusion proteins for effective imaging

Vaccinia virus has a complex replicative cycle [**Introduction 1.3.1**] and involves a series of distinct morphological forms with multiple transport steps [307]. The various morphological forms are composed of overlapping but different viral protein profiles. Selective tagging of viral proteins with fluorescent proteins, either alone or in combination, affords us a degree of discernment between the various morphological forms [**Figure 3.5**]. Three such viral proteins are A3 encoded by A3L, B5 encoded by B5R and F13 encoded by F13L. In this chapter, we aimed to develop a system of imaging and tracking specific subsets of viruses in the complex morphological cycle of VACV by generating recombinant viruses with fusions of the following proteins with the photoconvertible fluorescent proteins PSCFP2 and Dendra2.

3.1.3.1 A3L

A3 is a 62kDA viral core protein with a high degree of conservation across the poxvirus family [367]. It is processed from a 74kDa precursor protein and effective processing is linked to virion assembly and maturation; when proteolytic processing is inhibited, IMV do not form [368-370]. A3 is highly expressed in mature virions, constituting 11% of the virion by mass [370, 371]. The essentiality of the protein to the formation of the viral core precludes the analysis of ΔA3L recombinant viruses as they are unviable. A3 is however amenable to tagging and fluorescent protein fusions exhibit high levels of fluorescence without significant attenuation [295, 313]. As A3 is a core protein, particles positive for A3 represent both IMV and wrapped morphological forms of the virus (IEV, CEV and EEV).

3.1.3.2 B5R

B5 is a 42kDa integral membrane protein that is recruited to virus particles upon IEV morphogenesis at the TGN [372, 373]. It is one of 5 integral membrane proteins that are present in both the inner and outer membrane (along with A56, F13, A33 and A34) [163]. B5 functions in various processes during virus replication, most importantly in IEV morphogenesis and ΔB5R mutants display highly attenuated small plaque phenotypes [272, 273, 325]. Although expressed in far lower levels than A3, B5 is nonetheless a highly expressed, virus particle localised viral protein and is amenable to tagging. Recombinant viruses expressing B5 fluorescent fusion proteins exhibit bright fluorescence without significant attenuation [374]. As B5 is an integral membrane protein, virus particles positive for B5 represent only wrapped morphological forms of the virus (IEV, CEV and EEV) and not IMV. When combined with an A3 tagged with a second, complementary fluorescent protein tag, IMV can be distinguished from the wrapped morphological forms in live cells.

3.1.3.3 F13L

F13 is a 37kDa protein that associates with both the inner and outer membrane of IEV through palmitylated cysteines [375-377]. It localises to the TGN and is the most abundant protein in EEV [260]. It has similar functions as B5, with ΔF13L producing a small plaque phenotype with defects in membrane wrapping and IEV morphogenesis [378-380]. F13, like B5, is amenable to tagging and fusions with fluorescent proteins yield bright particles for imaging that represent the wrapped morphological forms of VACV [313, 377]. Direct comparisons between F13 and B5 indicate that F13 may be a superior tag for monitoring wrapped morphological forms of the virus with B5 fusions displaying an additional diffuse localisation not seen in untagged B5 [284]. This additional diffuse localisation was not detected in the F13L-GFP virus infections.

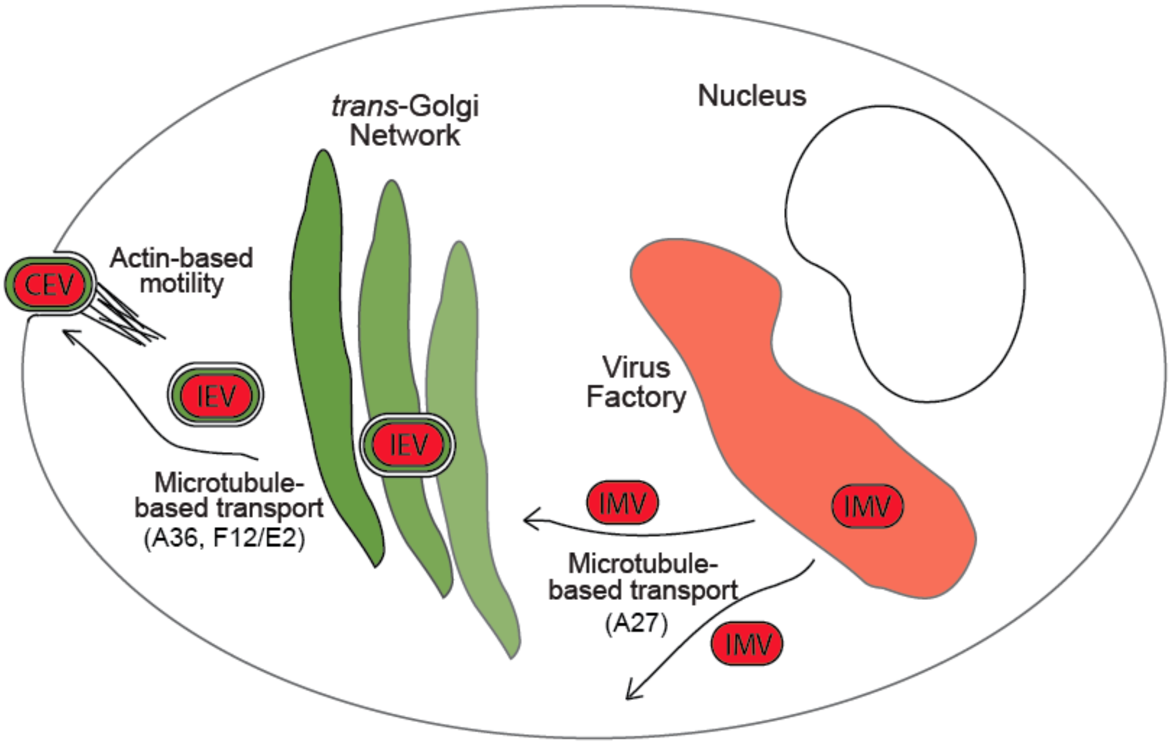

Figure 3.5: Discerning viral morphological forms with multiple fluorescent tags
The fluorescence profile of a doubly labelled virus (in this instance where an IMV protein such as A3 has been labelled with a red fluorescent protein and an IEV protein such as B5 or F13 has been labelled with a green fluorescent protein) allows for the differentiation of viral compartments and morphological forms. IMV particles, and the virus factory where there is a high density of IMV particles, will have a red fluorescent profile. IEV particles and other enveloped forms of the virus will be postitive for both IMV and IEV fusion proteins and the resultant colocalisation of red and green signals will lead to a yellow fluorescent profile. The membranes of the TGN will have a strong green signal due to the presence of the IEV fusion protein, but will also have a strong red signal due to the accumulation of IMV in the compartment undergoing the wrapping process. This differentiation of morphological forms can still be achieved in viruses with only a single fluorescent protein fusion by using an antibody raised against the complementary viral protein (such as α-B5). The viral proteins involved in the microtubule transport steps are shown in brackets underneath the microtubule transport stages.

3.2 RESULTS

3.2.1 B5R-PSCFP2 and PSCFP2-A3L both display unperturbed subcellular localisation and functional microtubule-based egress

To study IEV and IMV dynamics in VACV, we generated recombinant viruses expressing the IEV protein B5 and core protein A3 fused to PSCFP2 [**Section 2.4.1.2**]. For B5R-PSCFP2, a plasmid construct containing regions upstream and downstream of B5R flanking a genetic fusion of B5R with PSCFP2 was cloned. PSCFP2 was fused C-terminally to B5R as it has been previously demonstrated that C-terminus fusions of fluorescent proteins to B5 do not effect subcellular targeting of B5 and yield recombinant viruses with similar plaque phenotypes to parental strain WR [374, 381]. We then recombined this construct to rescue VACV ΔB5R that produces a small plaque phenotype and selected for recombinant viruses with restored WR-like large plaque sizes and exhibited faint blue fluorescence. Three rounds of purification were carried out to clonal, purified virus [**Section 2.3.3**].

As functional N-terminal fusions of fluorescent proteins to A3L have previous been published [317], we generated a plasmid construct with the sequence upstream of A3L cloned as a left arm to a genetic fusion of PSCFP2 to the first 500 bp of the A3L sequence [**Section 2.1.2.1**]. As deletion strains for A3L cannot be generated, selection of recombinant viruses by restoration of plaque size was not possible for the PSCFP2-A3L virus. Instead, the recombination sequence was shuttled into a vector containing both selectable marker *gpt*, an *E. coli* gene that encodes xanthine-guanine phosphoribosyltransferase to allow growth on GPT selection media, and screenable marker monomeric red fluorescent protein (mRFP) expressed from an artificial synthetic early/late promoter [**Section 2.1.2.1**]. We recombined this construct with WR and using TDS [**Section 2.4.1.3**], selected for recombinant virus able to replicate in the presence of GPT selection media with visible red fluorescent plaques. Following three rounds of purification, selection was removed to allow intragenomic recombination and removal of *gpt* and mRFP. Successful secondary recombinants were selected by picking plaques with faint blue fluorescence for an additional three rounds of purification.

We tested the integrity of B5R-PSCFP2 and PSCFP2-A3L with PCR analysis from genomic DNA. For B5R-PSCFP2, a primer pair consisting of a forward and reverse primer complementary to the end of the B5R ORF and 300 bp downstream of the stop codon of the ORF respectively was used (*B5R(end).for/B5R.RA.rev* [**Table 2.1**]). While an amplicon of approximately 300 bp was produced from the WR control, the B5R-PSCFP2 amplicon was 1000 bp; encompassing to PSCFP2 (717 bp) and the RA of B5R [**Figure 3.6A**]. When a second PCR was carried out with the same forward primer and a reverse primer complementary to the last 20 bp of PSCFP2

(*B5R(end).for/PSCFP4*), the WR virus genomic DNA did not produce a visible band, while B5R-PSCFP2 produced an amplicon of approximately 700 bp [**Figure 3.6A**], further validating the successful insertion of a B5R-PSCFP2 genomic fusion.

To validate PSCFP2-A3L, a primer pair consisting of a forward primer complementary to a region approximately 500 bp upstream of the start codon and a reverse primer complementary to a region 500 bp into the A3L ORF was used (*A3L.LA.CFPsew1/A3L2*). A product of approximately 1700 bp, encompassing the left arm (500 bp) and PSCFP2 (717 bp) fused to the beginning of A3L (500 bp) was amplified from the PSCFP2-A3L genome, compared to a 1000 bp amplicon from WR [**Figure 3.6B**]. When a second PCR was carried out with a forward primer complementary to the first 20 bp of PSCFP2 with the same reverse primer (*PSCFP1/A3L2)*, the WR genomic DNA did not produce a visible band compared to the 1200 bp amplicon from PSCFP2-A3L [**Figure 3.6B**].

We confirmed the expression of fusion proteins by immunoblot analysis. As PSCFP2 is derived from a variant of GFP, the amino acid sequences of EGFP and PSCFP2 have 89% consensus. We therefore tested α-GFP in immunofluoresence assays (IFA) of PSCFP2 transfected cells and observed colocalisation between the two signals, indicating that α-GFP binds to and is able to detect PSCFP2 [data not shown]. When VACV-infected lysates were probed with α-GFP, bands were detected in B5R-PSCFP2 and PSCFP2-A3L lysates at approximately 65 kDa and 85 kDa, respectively [**Figure 3.6C**]. This is consistent with successful fusions between PSCPF2 (27 kDa), and B5 (~42 kDa) [272] and A3 (~74 kDa, processed into a ~62 kDa protein) [371]. Reprobing the blot with α-B5 validated the B5R-PSCFP2 fusion, with the same 65 kDa band also being α-B5 immunoreactive.

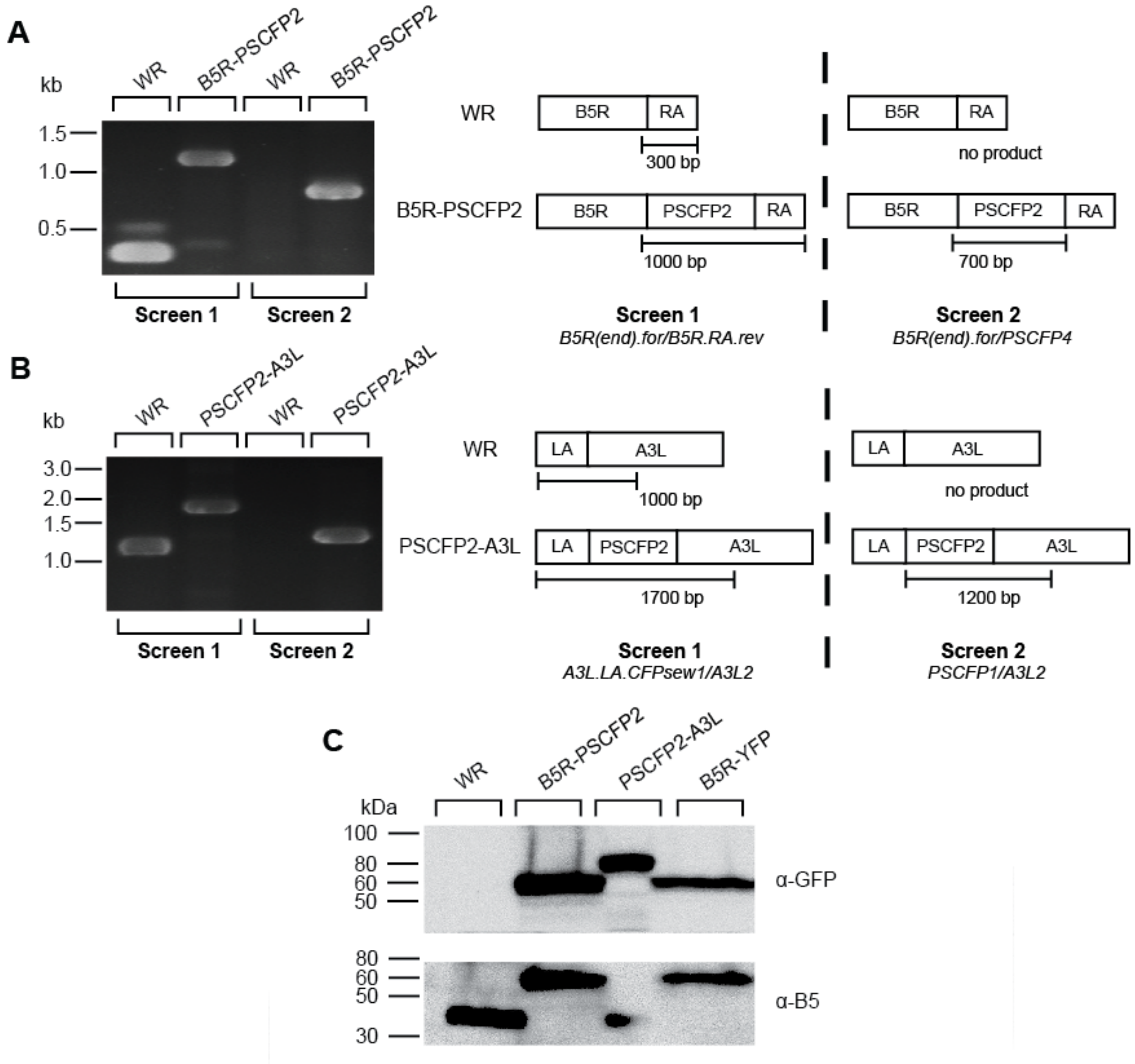

Figure 3.6: Construction and verification of PSCFP-2 tagged viruses

BSC-1 cells were infected with WR, B5R-PSCFP2 **(A)** and PSCFP2-A3L **(B)** and cell lysates collected at 24 hpi. PCR was conducted on proteinase K treated samples with indicated primer pairs to confirm correct insertion of the PSCFP2 gene into the virus. Molecular size markers are indicated on the left. **(C)** BSC-1 cells were infected with WR, B5R-YFP, B5R-PSCFP2 and PSCFP2-A3L at MOI 1 and cell lysates collected at 24 hpi. Cell lysates were separated with SDS-PAGE and transferred to nitrocellulose membranes for immunoblotting with α-GFP (able to detect YFP and PSCFP2) and α-B5R as an infection control. Molecular size markers are indicated on the left.

Upon verifying the construction of PSCFP2 fusion viruses, we proceeded to analyse replication dynamics and subcellular localisation to assess the impact of PSCFP2 fusions. Both B5 and A3 fusions with GFP and close GFP derivatives (such as YFP) have been widely utilised in analysis of VACV subcellular trafficking, with minimal to no reported impacts on protein localisation or viral replication [317, 374, 381]. As previously mentioned, PSCFP2 is also derived from GFP and maintains many of the same beneficial physical and chemical attributes of GFP including those that are most likely to affect virus structure and function when fused to dense virus proteins such as B5 and A3, such as size (they are both the same size at 27kDa) [382]). We therefore predicted that PSCFP2 fusions would have a similarly minimal impact on viral function.

We first performed plaque assays and unexpectedly observed that both viruses produced significantly smaller plaques than parental WR. B5R-PSCFP2 showed a substantial effect on plaque size, with PSCPF2-A3L displaying a relatively minor reduction in size [**Figure 3.7A, B**]. Both however produced significantly larger plaques than the widely utilised and published B5R-YFP. Due to this, we proceeded to perform immunofluoresence assays (IFA) to examine subcellular localisation of tagged proteins and to confirm functional microtubule-based egress of virus particles. While both viruses displayed effective egress to the cell periphery and the ability to produce actin tails, we were unable to image the PSCFP2 signal, as excitation with the appropriate wide field led to the rapid photoconversion of PSCFP2 and subsequent abrogation of the blue signal [**Figure 3.7C, D**].

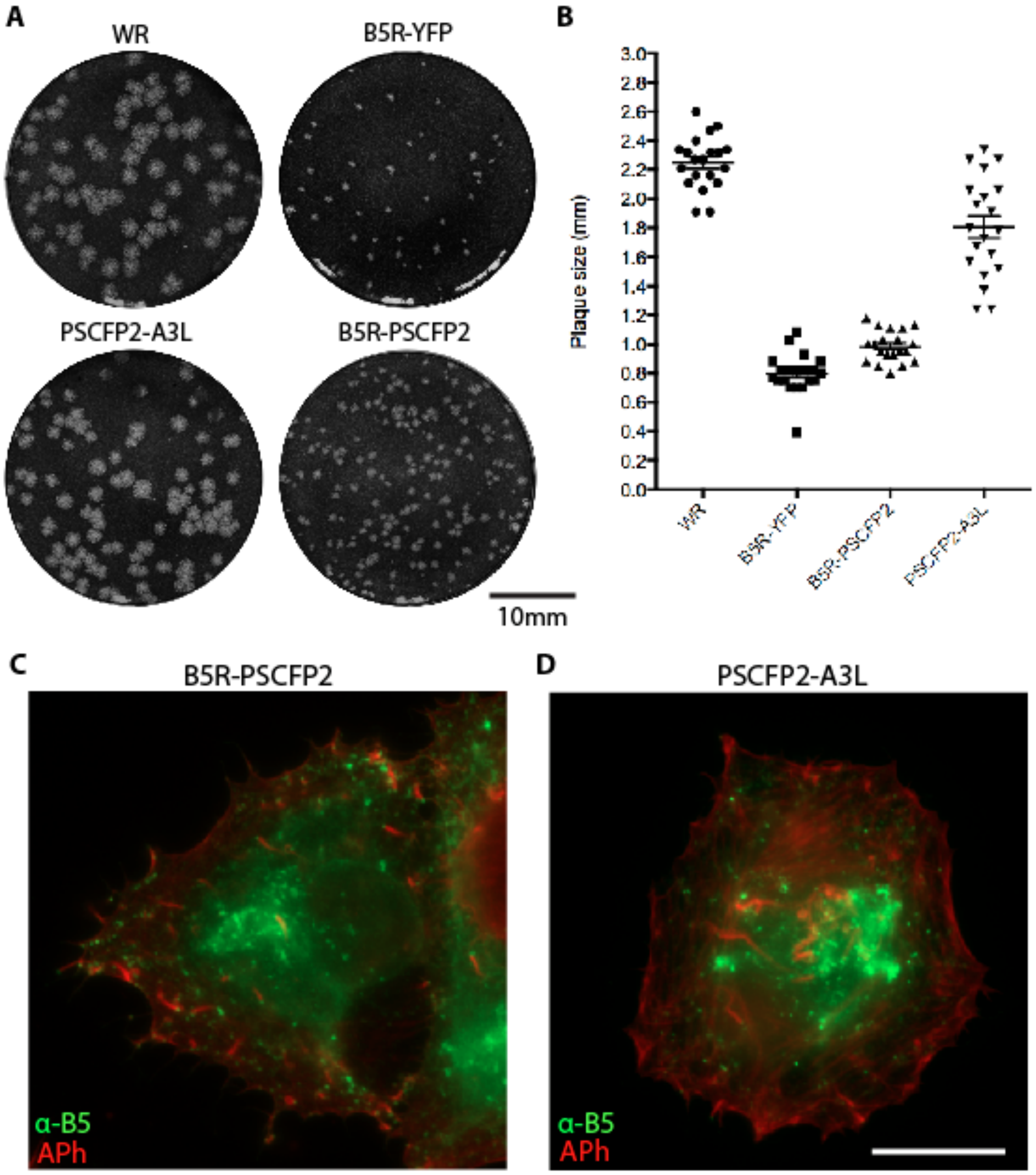

Figure 3.7: **Plaque phenotypes of PSCFP2 tagged viruses**
(A) BSC-1 cell monolayers were infected with WR, B5R-YFP, B5R-PSCFP2 and PSCFP2-A3L and overlayed with 1.5% CMC/DMEM. Four days post infection cell monolayers were washed and stained with crystal violet to observe plaques before being scanned with a Typhoon FLA9000 4 laser scanner. **(B)** The diameter of plaques was measured in ImageJ as the widest horizontal zone of clearing observed (n = 30). All viruses produced statistically different plaque sizes ($p<0.0001$, Unpaired *t*-test). For immunofluoesence assays, HeLa cells were infected with **(C)** B5R-PSCFP2 and **(D)** PSCFP2-A3L, then fixed and stained for immunofluorescence assays with α-B5R (green) and phalloidin (red). Scale bar represents 10 μm.

3.2.2 B5R-PSCFP2 has a low signal-to-noise ratio and does not undergo efficient photoconversion

Having validated the construction of both fusion viruses, we went on to image B5R-PSCFP2 in a live cell system. HeLa seeded onto fibronectin coated No. 1.5 glass μ-Dishes (Ibidi, Martinsried, Germany) were infected with the B5R-PSCFP2 for a minimum of 7h and then imaged on an Olympus FV1000 confocal microscope (Olympus, Notting Hill, VIC, Aus) at 600x to 1200x magnification (600x optical magnification and up to 2x digital magnification).

Infected cells were located and imaged with a 405 nm laser at 1% power (corresponding to 0.5 mW) and 488 nm laser at 0.1% power (corresponding to <0.03 mW) to obtain "pre-activation" images [**Figure 3.8A**]. One of the main concerns with imaging of any fluorescent fluorophore is bleaching, which occurs when fluorophores are exposed to excitation light [383, 384]. There is an additional concern with photoconvertible fluorophores such as PSCFP2; that excitation light can also lead to inadvertent photoconversion of the fluorophore before the intended timeframe of imaging [312]. As such, the power of the excitation lasers is optimally set to as low a setting as possible while still generating a clear signal. For B5R-PSCFP2, while 1% 405 nm laser excitation allowed for a signal bright enough to distinguish the subcellular localisation of B5R-PSCFP2, the signal is faint with significant noise (produced by the emission signal sensor in low light conditions [384]) and distinct virus particles are not readily resolved [**Figure 3.7A**]. Higher levels led to rapid photoconversion [data not shown] and 1% was selected as a compromise between resolving virus particles and inadvertent photoconversion.

Images were acquired with a 4.0 pixel/sec scan speed, this is the pixel dwell speed and indicates the amount of time the laser excites each pixel of the imaging field of view. Short pixel dwell times lead to less bleaching and unintended photoconversion, but as fluorophores are being excited for a shorter duration, the emission signal will not be as bright as a longer pixel dwell times, leading to noisier images with reduced resolution. So again, like laser power, a 4.0 pixel/sec dwell was selected as an optimal compromise between these factors.

The 488 nm excitation channel is required "pre-activation" to indicate what baseline green signal is present in the cell, possibly owing to photoconversion that has occurred in the process of locating infected cells. The two channels (405 nm and 488 nm) were collected sequentially, rather than simultaneously. Simultaneous acquisition involves the excitation of the same pixel of the imaging field of view with both lasers simultaneously. Collection of the emission signal of the excited fluorophores by two separate photo multiplier tubes (PMTs) of the microscope also occurs simultaneously. Simultaneous acquisition allows for faster imaging of the field of view (if using two lasers, simultaneous acquisition requires half the time of the same sequential acquisition).

However, if two fluorophores have overlapping emission spectra, as is the case with the pre-activation blue state and post-activation green state of PSCFP2 that both have a substantial 500-600 nm emission tail [**Figure 3.4**], the emission of the shorter wavelength fluorophore (blue) will also be detected by the PMT assigned to detect the emission of the longer wavelength fluorophore (green). It is therefore necessary to image the two channels sequentially for optimal signal separation.

A 40 x 40 pixel region of interest (ROI), the region of the cell with the brightest 405 nm emission (the trans-Golgi Network), was selected for photoconversion. For all imaging experiments, activation was optimised and conducted with a 40 x 40 pixel region of interest. This size was chosen as it was large enough to encompass both of the subcellular compartments of interest (the trans-Golgi network and the virus factory) 1200x magnification. The consistency of size was important as activation can be controlled mainly by altering three separate variables; laser power, time and scan speed. The same combination of these three variables will lead to different photoactivation efficiencies with different size ROIs as the number of iterations of the laser over each fluorophore will change.

The ROI was activated with 3% of the same 405 nm laser (1.5 mW) used for obtaining "pre-activation" images (the visible [VIS] laser, the microscope is also equipped with a second 405nm laser, called the SIM laser, which is described below [**Section 3.2.3**]), for 100 ms at a scan speed of 100 µs/pixel (the slowest scan speed). 1%, 2%, 4% and 5% laser were also attempted, with lower powers leading to a lack of visible photoconversion and higher powers leading to photobleaching [data not shown].

In the representative cell, at optimised activation settings, photoactivation led to an approximately 67% decrease in the blue signal with a concurrent approximately 39% increase in the photoactivated green signal [**Figure 3.8B**]. While this is consistent with photoconversion, the green signal is low both relative to the loss of the blue signal and also low in absolute terms. Experimentally useful photoconversion requires a high contrast between pre-activated and post-activated states, which was not achieved [356]. For our experimental requirements to determine the turnover of virus particles in compartments and track their trajectories, we require the ability to clearly resolve and distinguish photoactivated virus particles. This was not attainable with the achieved level of photoconversion using this experimental set-up.

It is important to note that the depicted cell [**Figure 3.8**] was selected as it effectively represents the pattern of conversion achieved in many other cells photoactivated with the described settings. However, the exact efficiency of the photoactivation differs between cells due to a combination of factors, including but not limited to; the infection level, cell morphology, density of fluorescent signal and any background fluorescence. This way of representing data was selected because the averaging of photoconversion data over multiple cells artificially obscured the efficiency of photoconversion. As such, although percentage increase/decrease is given to easily compare tags, these readings are informative as qualitative indications of the effectiveness of photoactivation, rather than as absolute quantitative measurements. This is similarly the case for cells in following photoconversion images [**Figure 3.9-3.10, 3.14-3.16**].

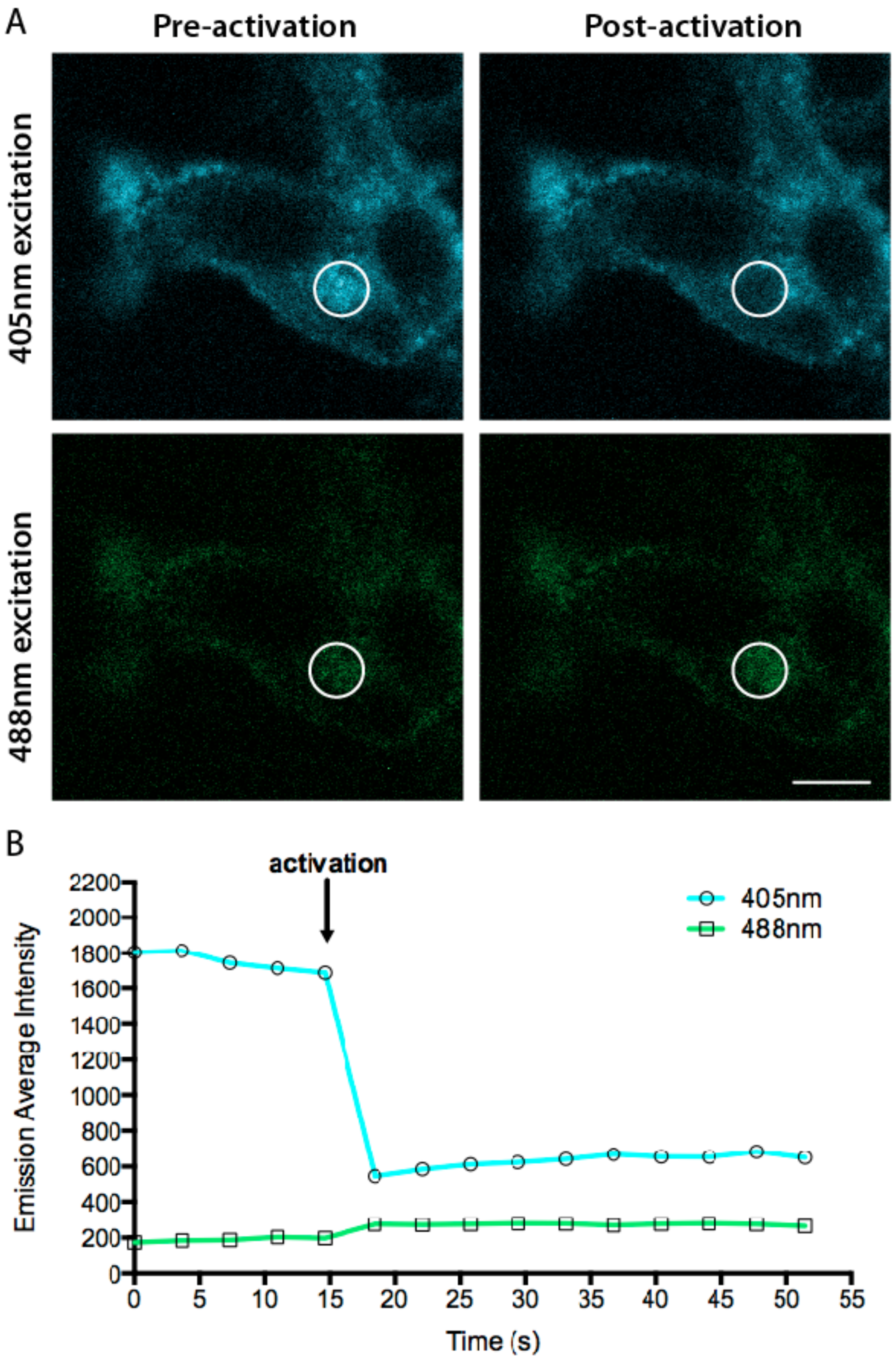

Figure 3.8: B5R-PSCFP2 does not undergo efficient photoconversion

(**A**) HeLa cells seeded onto fibronectin coated Ibidi dishes were infected with B5R-PSCFP2. The trans-Golgi network, the brightest signal in the cell, was located by the visualisation of the PSCFP2 signal with 1% intensity 405 nm laser excitation on an Olympus FV1000 confocal microscope and activated at the indicated region of interest (circle) with 3% intensity 405 nm laser. Excitation with 488 nm was also collected during imaging to monitor photoconversion of PSCFP2's pre-activation blue signal to post-activation green signal. Scale bar is 10 µm. **(B)** The average intensity of signal emitted by 405 nm and 488 nm laser lines in the activation region of interest was plotted over the course of imaging, with the point of photoactivation indicated with an arrow.

3.2.3 PSCFP2-A3L undergoes efficient photoconversion

Non-photoactivatable blue and cyan fluorescent derivatives of GFP often have poor relative brightness to EGFP. Enhanced Blue Fluorescent Protein (EBFP) for instance is 27% of EGFP, while Enhanced Cyan Fluorescent Protein (ECFP) is 39% of EGFP [349, 385, 386]. Similarly, the blue state of PSCFP2 has a brightness of 8.6 (a product of quantum yield of 0.2 multiplied by extinction coefficient of 43000 $M^{-1}cm^{-1}$) and the green state has a brightness of 10.8 (quantum yield 0.23, extinction coefficient 47000 $M^{-1}cm^{-1}$), compared to EGFP which has a brightness of 34, meaning the blue and green state are 25% and 31% as bright as EGFP respectively [312, 354].

The relative low brightness of CFP can be compensated for by creating fusions with highly abundant viral proteins, creating viruses with denser (and therefore brighter) fluorescent signals. A3 is one of the most abundant proteins in the IMV, making up over 5% of total IMV weight [268, 371]. Our previous experiences with imaging B5R-CFP and CFP-A3L virus infections have demonstrated that while B5R-CFP infections prove difficult to image, the high abundance and density of A3 in virus particles leads to bright fluorescent signals enabling good resolution of virus particles. We predicted a similar consequence with PSCFP2-A3L and therefore proceeded with imaging PSCFP2-A3L to determine if we could achieve more effective photoactivation.

HeLa seeded onto fibronectin coated No. 1.5 glass μ-Dishes (Ibidi) were infected with the PSCFP2-A3L and then imaged on an Olympus FV1000 confocal microscope. Infected cells were imaged with the same optimised acquisition settings as used for B5R-PSCFP2; sequentially with a 405 nm and 488 nm laser with 4.0 pixel/sec scan speed to obtain pre-activation images [**Figure 3.9A**]. As predicted, the PSCFP2-A3L signal is much brighter than B5R-PSCFP2 [**Figure 3.8A**], with no distinguishable background noise and clear resolution of virus particles.

Activation was performed with the optimised settings described above, with the exception of the activating laser line used; a 40 x 40 pixel region of interest (ROI), the region of the cell with the brightest 405 nm emission (this time the virus factory), was selected for photoconversion. The ROI was activated with 3% of the 405 nm laser SIM (simultaneous) scanner (instead of the 405 nm laser VIS scanner) under "Tornado" setting for 100 ms at a scan speed of 100 μs/pixel. As can be seen in post-activation images [**Figure 3.9A**], the blue signal is completely abrogated in the ROI after activation, with a dramatic increase in the brightness of the green signal.

The 405 nm SIM scanner used for activation does not, contrary to its name, allow the simultaneous collection of the 405 nm PSCFP2 emission. The course of activation can therefore only be monitored with 488 nm emission [**Figure 3.9B**]. The initial photoactivation led to an approximately 3-foldincrease in the green signal (from an emission average intensity of 550 to

1800 when stabilised). As the activation series was performed without a concurrent imaging in 405 nm, the activation was repeated a second time in the same series to ensure that maximal photoconversion had occurred. Although the second activation led to a slight increase in the green signal (from an emission average intensity of 1800 to 1900 when stabilised), the large bulk of photoconversion occurred with the initial photoactivation.

The SIM (simultaneous) laser scanner is a unit separate from the main laser scanning unit of the FV1000 confocal microscope specifically for stimulation (photoactivation or photobleaching) of the sample while simultaneously acquiring images, to allow for the monitoring of the ROI during the moment of stimulation [387]. The SIM scanner however is equipped with a 405 nm laser and the set up of the FV1000 microscope (at the Australian Centre of Microscopy and Microanalysis, ACMM) does not allow simultaneous stimulation and acquisition using a 405 nm laser, as use of the 405 nm SIM laser scanner blocks the light path of the 405 nm visualising laser (the visualising laser is the 405 nm laser of the main laser scanning unit, which I shall refer to as the abbreviation VIS to differentiate it from the SIM scanning unit).

An advantage the SIM scanner does have for our purposes is that the “Tornado” scanning function, which instead of using raster scanning in parallel lines over the ROI, spirals the laser from edge of the ROI into the centre and then back. This minimises superfluous scanning, leading to more efficient activation or bleaching and is therefore suitable for our purposes [387].

The technical difficulty resulting from the aforementioned inability to use both 405 VIS and 405 SIM lasers concurrently is that when working with the SIM laser for stimulation of a fluorophore that is also imaged with a 405 nm laser, pre-activation images need to be collected before the 405 nm laser is switched off for the activation series and then switched on again for post-activation images. These technical difficulties also make quantitative measurements of the effectiveness of the activation difficult, as we cannot observe the concurrent relative decrease of the blue signal and increase of the green signal at the moment of activation. Nevertheless, as PSCFP2 is activated by the same laser used to image it, minimising the amount of time the sample is exposed to 405 nm light to prevent off-target non-ROI activation is preferable, and together with the other advantages of the 405 nm SIM scanning unit, we decided to switch activation systems.

Even with the absolute minimum exposure to 405 nm light over the course of imaging and photoactivation, there is substantial off-target photoconversion as can be seen by the green fluorescence outside the ROI. The extent of off-target photoconversion can be measured by comparing two cells that have been transfected with constitutively expressed PSCFP2 [**Figure 3.10**]. While the cell selected for photoactivation by higher intensity excitation with the 405 nm

VIS laser has a 22% increase in green signal immediately post activation, the second cell has a 29% increase in the green signal by the end of the time course (25 frames) without any intended high intensity photoactivation. This off-target photoconversion effectively makes the clear distinguishing of a specific subset of virus particles (such as IMV in the VF) over time highly problematic. Thus while PSCFP2-A3L produced bright, easily resolved particles that photoconverted effectively, PSCFP2 was unsuitable to monitor virus transport of a cohort of virus particles.

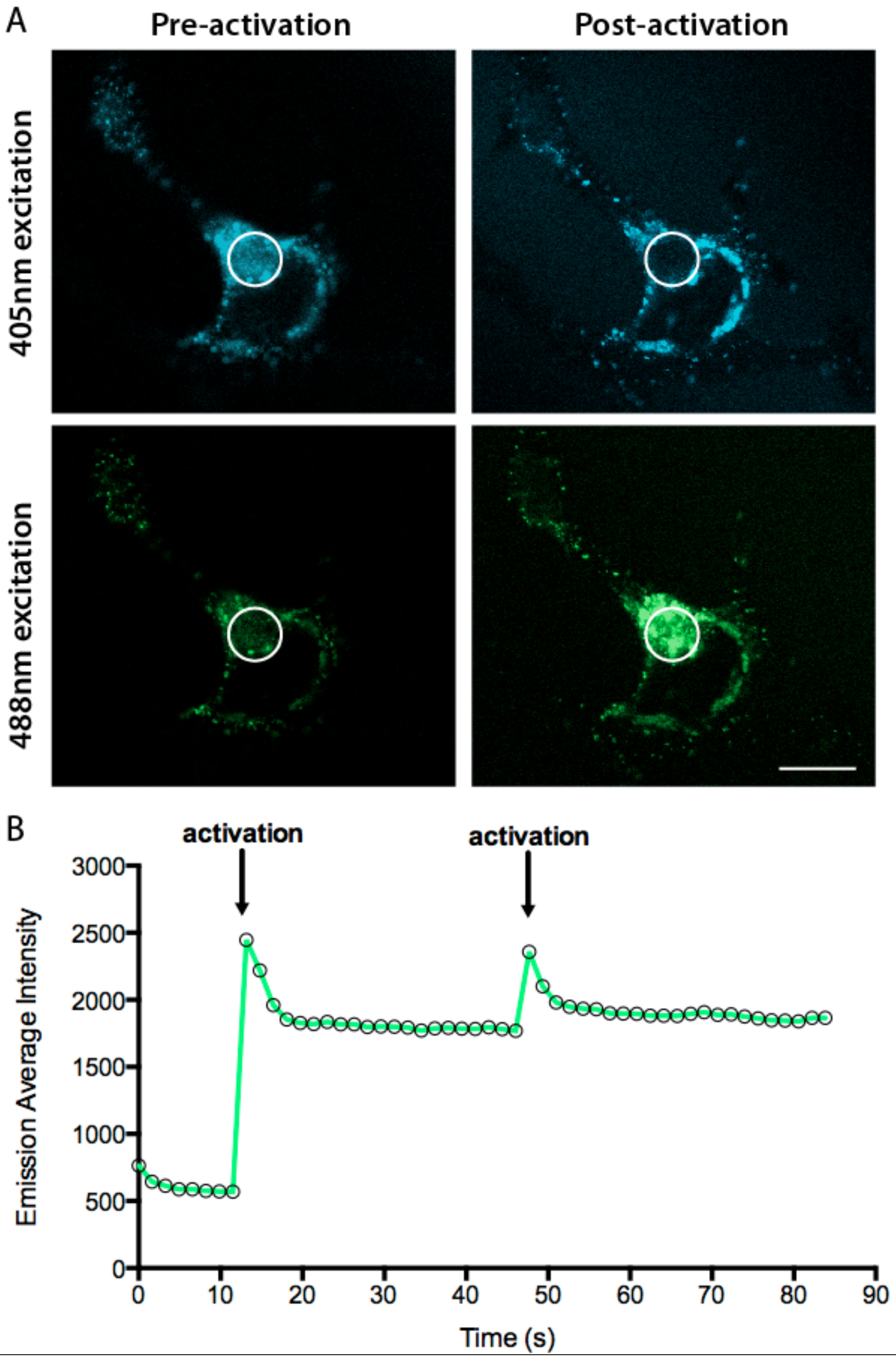

Figure 3.9: PSCFP2-A3L undergoes efficient photoconversion

(**A**) HeLa cells seeded onto fibronectin coated Ibidi dishes were infected with PSCFP2-A3L. The virus factory, the brightest signal in the cell, was located by the visualisation of the region of brightest PSCFP2 signal with 1% intensity 405 nm laser excitation on an Olympus FV1000 confocal microscope and activated at the indicated region of interest (circle) with 3% intensity 405 nm SIM laser. To ensure that complete conversion was achieved, the region of interest was activated a second time. Post-activation images were collected 120 s after the initial activation. Scale bar is 10 µm. **(B)** Excitation with 488 nm was collected during imaging to monitor photoconversion of the pre-activation blue signal to post-activation green signal. The average intensity of signal emitted by 488 nm laser lines in the activation region of interest was plotted over the course of imaging, with the two points of photoactivation indicated with an arrow.

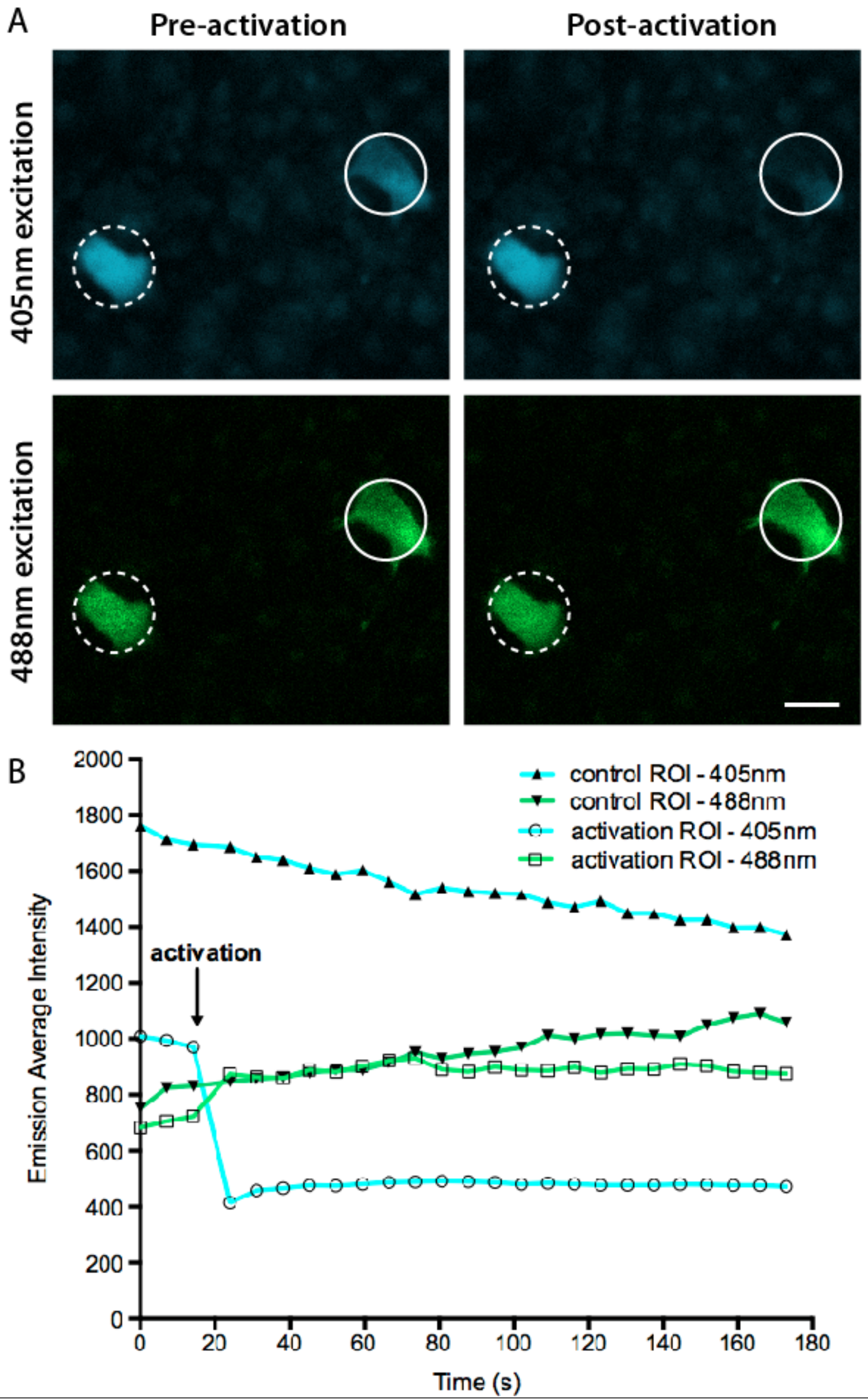

Figure 3.10: PSCFP2 photoactivates with low intensity 405 nm laser imaging
(A) HeLa cells seeded onto fibronectin coated Ibidi dishes were transfected with CB6 PSCFP2. Two cells with robust PSCPF2 expression were imaged with 1% intensity 405 nm laser excitation on an Olympus FV1000 confocal microscope and one of the cells indicated by a circle (bold line), was activated with 3% intensity 405 nm laser. Excitation with 488 nm was also collected during imaging to monitor photoconversion of PSCFP2's pre-activation blue signal to post-activation green signal. Scale bar is 20 µm. **(B)** The average intensity of signal emitted by 405 nm and 488 nm laser lines in the photoactivated cell and in the "unactivated" cell was plotted over the course of imaging, with the point of photoactivation indicated with an arrow.

3.2.4 Dendra2 fusion viruses display unperturbed subcellular localisation and microtubule-based egress dynamics

Following the challenges encountered with utilising PSCFP2, we moved on to another photoconvertible fluorescent tag, the monomeric green-to-red switcher Dendra2. The preactivation and postactivation forms were 2.6 and 1.8 times brighter than PSCFP2, respectively, and we predicted this improved brightness would enable effective imaging of lower density IEV-membrane protein fusions like B5 [312]. Furthermore, the preactivation excitation maximum of Dendra2 is 490 nm, while photoconversion is achieved with high intensity 405 nm light, enabling visualisation of cells without inadvertent photoactivation. Although 488 nm light can also cause photoconversion of the fluorophore, this requires longer periods of irradiation and can be avoided with low pixel dwell times [312].

B5R-Dendra2 and Dendra2-A3L were generated with the same strategies as outlined for B5R-PSCFP2 and PSCFP2-A3L above. As we observed a significant but mild attenuation of B5R-PSCFP2 plaque sizes, we also investigated F13L-Dendra2 as a fusion virus for IEV, as F13L-GFP has been reported to produce plaques very similar in size to WR [377]. To generate F13L-Dendra2, 150 bp long flanking regions of homology, at the end of F13L (LA) and downstream of F13L (RA), were synthesised into a plasmid with restriction sites between them to allow for the insertion of Dendra2 as a C-terminal fusion [**Section 2.1.2.1**]. Once the fluorescent protein gene was inserted, restriction sites flanking the entire stretch (LA-fluorescent protein gene-RA) were used to clone it into a TDS vector (containing pE/L gpt and pE/L mCherry). We recombined this construct with WR and using TDS [**Methods 2.4.1.3**], selected for recombinant virus able to replicate in the presence of GPT selection media with visible red fluorescent plaques [313]. After three rounds of purification, we removed selection to allow the intragenomic recombination and removal of *gpt* and mCherry. We screened for successful recombinants by identifying plaques with green fluorescence following three additional rounds of plaque purification.

We tested the integrity of all three recombinant viruses with PCR analysis from extracted genomic DNA. For B5R-Dendra2, a primer pair consisting of a forward and reverse primer complementary to the end of the B5R ORF and 300 bp downstream of the stop codon of the ORF respectively was used (*B5R(end).for/B5R.RA.rev*). While an amplicon of approximately 300 bp was produced from the WR control, the B5R-Dendra2 amplicon was 1000 bp; encompassing to Dendra2 (693 bp) and the 300 bp RA of B5R [**Figure 3.11A**]. When a second PCR was carried out with the same forward primer and a reverse primer complementary to the last 20 bp of Dendra2 (*B5R(end).for/Dendra2*), the WR virus genomic DNA did not produce a visible band, while B5R-

Dendra2 produced an amplicon of approximately 700 bp [**Figure 3.11A**], further validating the successful insertion of a B5R-Dendra2 genomic fusion.

For F13L-Dendra2, primers complementary the start and end of the F13L ORF were used (*F13L.for/F13L.rev*). Both the WR control and the F13L-Dendra2 amplicon was approximately 1400 bp, encompassing the F13L ORF [**Figure 3.11A**]. When a second PCR was carried out with the same forward primer and a reverse primer complementary to the last 20 bp of Dendra2 (*F13L.for/Dendra2*), the WR virus genomic DNA did not produce a visible band, while F13L-Dendra2 produced an amplicon of approximately 2100 bp [**Figure 3.11A**], confirming the successful insertion of a F13L-Dendra2 genomic fusion.

To validate Dendra2-A3L, a primer pair consisting of a forward primer complementary to a region approximately 500 bp upstream of the start codon and a reverse primer complementary to a region 500 bp into the A3L ORF was used (*A3L.LA.CFPsew1/A3L2*). A product of approximately 1700 bp, encompassing the left arm (500 bp) and Dendra2 (693 bp) fused to the beginning of A3L (500 bp) was amplified from the Dendra2-A3L genome, compared to a 1000 bp amplicon from WR [**Figure 3.11A**]. When a second PCR was carried out with a forward primer complementary to the first 20 bp of Dendra2 with the same reverse primer (*Dendra1/A3L2)*, the WR genomic DNA did not produce a visible band compared to the 1200 bp amplicon from Dendra2-A3L [**Figure 3.11A**].

We next carried out immunoblots to confirm the expression of fusion proteins. When VACV-infected lysates were probed with α-Dendra2, bands were detected in B5R-Dendra2, F13L-Dendra2 and Dendra2-A3L lysates at approximately 70 kDa, 60 kDa and 85 kDa, respectively [**Figure 3.11B**]. This is consistent with successful fusions between Dendra2 (26 kDa), and B5 (~42 kDa) [272], F13 (~42 kDa, with a 37 kDa mobility on SDS-PAGE) [377] and A3 (~74 kDa, processed into a ~62 kDa protein) [371]. Reprobing the blot with α-B5 validated the B5R-Dendra2 fusion, with the same 70kDa band also being α-B5 immunoreactive. Although comparable levels of viral replication have occurred in each of the recombinant viruses as seen through similar levels of B5 expression, the relative abundance of B5, F13 and A3 can be seen by the varying strength of bands in the α-Dendra2 blot.

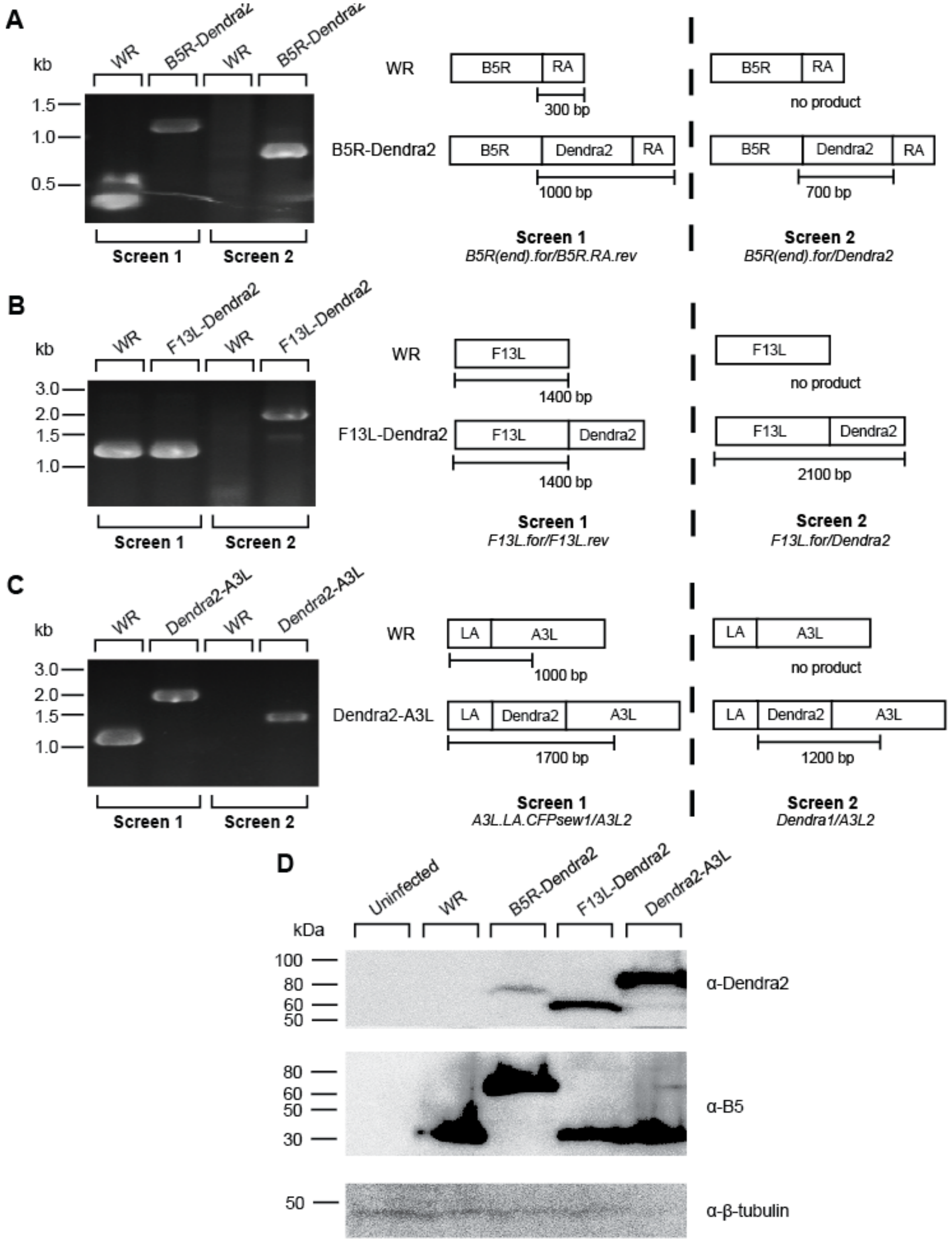

Figure 3.11: Construction and verification of Dendra2 tagged viruses

BSC-1 cells were infected with WR, B5R-Dendra2 **(A)** F13L-Dendra2 **(B)** and PSCFP2-A3L **(C)** and cell lysates were collected at 24 hpi. PCR was conducted on proteinase K treated samples with indicated primer pairs to confirm correct insertion of the Dendra2 gene into the virus. Molecular size markers are indicated on the left. **(D)** BSC-1 cells were infected with WR, B5R-YFP, B5R-Dendra2, F13L-GFP, F13L-Dendra2, YFP-A3L and Dendra2-A3L at MOI 1 and cell lysates collected at 24 hpi. Cell lysates were separated with SDS-PAGE and transferred to nitrocellulose membranes for immunoblotting with α-Dendra2, α-B5R and α-ß-tubulin as a loading control. Molecular size markers are indicated on the left.

We next performed plaque assays and determined that, like PSCFP2 fusion viruses, both B5R-Dendra2 and Dendra2-A3L viruses produced significantly smaller plaques than parental WR. B5R-Dendra2 displayed a substantial effect on plaque size, while Dendra2-A3L displayed a relatively minor reduction [**Figure 3.12A, B**]. Both however produced significantly larger plaques than the widely utilised and published B5R-YFP. F13L-Dendra2 produced plaques not significantly different in size to WR, confirming that F13L is a superior tag for labelling enveloped from of VACV [284, 377]. Interestingly, F13L-GFP plaques were significantly smaller than both WR plaques and F13L-Dendra2 plaques, possibly indicating that Dendra2 fusions have less effect on viral morphogenesis and/or egress than GFP.

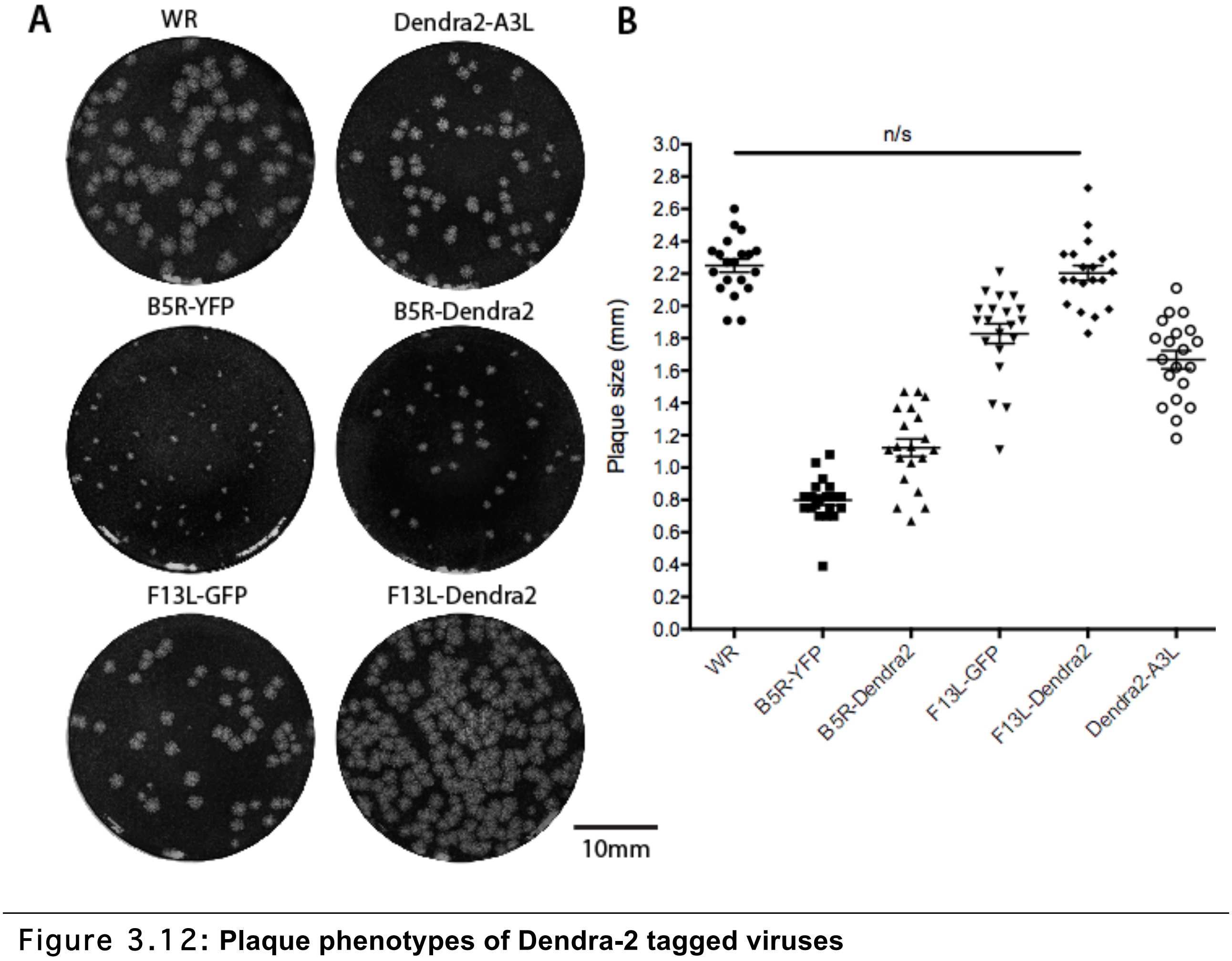

Figure 3.12: Plaque phenotypes of Dendra-2 tagged viruses

(A) BSC-1 cell monolayers were infected with WR, B5R-YFP, B5R-Dendra2, F13L-GFP, F13L-Dendra2 and Dendra2-A3L and overlayed with 1.5% CMC/DMEM. Four days post infection cell monolayers were washed and stained with crystal violet to observe plaques before being scanned with a Typhoon FLA9000 4 laser scanner. **(B)** The diameter of plaques was measured in ImageJ as the widest horizontal zone of clearing observed (n = 30). Unless otherwise indicated, all viruses produced statistically different plaque sizes ($p<0.0001$, Unpaired *t*-test).

To further validate construction of B5R-Dendra2, F13L-Dendra2 and Dendra2-A3L, we performed IFA on infected cells. Unlike PSCFP2 fusion viruses, excitation with the appropriate wide-field filter did not lead to the rapid photoconversion of the Dendra2 and we were able to examine subcellular localisation of tagged proteins [**Figure 3.13**]. We observed a cyan signal throughout the cell indicating complete colocalisation between the Dendra2 signal in B5R-Dendra2 infected cells in green with a monoclonal antibody raised against B5 in blue, verifying the tagging of B5 with Dendra2 [**Figure 3.13A**]. Performing the same B5 antibody label on F13L-Dendra2-infected cells showed colocalisation between the two signals, verifying the construction of F13L-Dendra2 [**Figure 3.13B**]. Unlike B5R-Dendra2, F13L-Dendra2 infected cells showed regions where the green Dendra2 signal is stronger and other regions where the blue B5 antibody signal is stronger. This is consistent with the fact that although B5 and F13 are both IEV proteins that localise to the TGN, they differ in relative abundance. Both B5R-Dendra2 and F13L-Dendra2 displayed effective egress to the cell periphery and efficiently induced virus-associated F-actin comets [**Figure 3.13A-B**].

Performing the a B5 antibody label on Dendra2-A3L infected cells showed some areas of colocalisation between the two signals (individual virus particles disseminated through the cytoplasm and in a region of the cell with a strong B5 signal, the TGN), and other regions of the cell that were positive for Dendra2 with no B5 signal [**Figure 3.13C**]. This is consistent with the successful tagging of A3, which localises to the virus factory where IMV are generated before addition of B5/IEV membranes, with Dendra2.

While generation of Dendra2-A3L was successful, fusions with A3 label all morphological forms of the virus (both IMV and all enveloped forms) and do not allow easy differentiation between the virus factory/IMV and the TGN/IEV in Dendra2-A3L infected cells without antibody labels (as demonstrated in **Figure 3.13C**). To enable the differentiation of these two compartments/different morphological forms with live cell microscopy that does not allow for antibody labelling, we introduced a second fluorescent tag, CFP, fused to B5. This was accomplished through coinfections of cells with Dendra2-A3L and B5R-CFP, allowing for intergenomic recombination and selection and purification of plaques displaying both Dendra2 and CFP fluorescent signals yielding a Dendra2-A3L/B5R-CFP virus [**Section 2.4.1.4**].

Successful construction of this virus was confirmed by imaging fixed cells under the Olympus BX51 wide-field microscope and demonstrated the clear differentiation between the VF with a strong green fluorescence and the TGN with a strong blue fluorescence with green particles [**Figure 3.13D**]. It was not necessary to confirm construction of this virus with PCR as the integration of the two fluorescent proteins into the correct viral locus through plasmid-based recombination cassettes had previously been verified. In the process of homologous recombination between two viruses, it is unlikely that a recombination event would occur that affected the locus of the fluorescent protein without also severely disrupting viral replication.

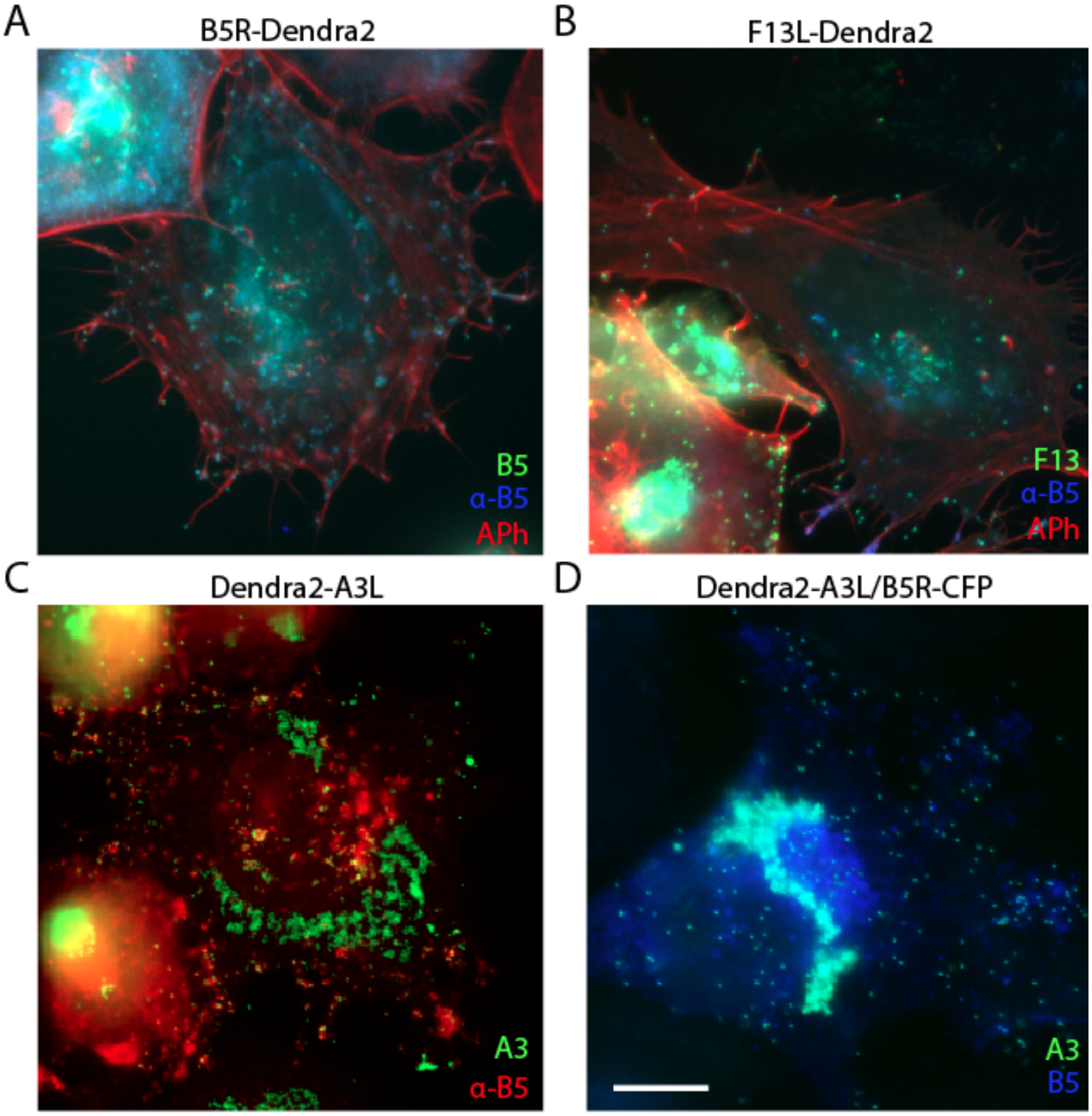

Figure 3.13: IFA images of viruses

HeLa cells on coverslips were infected, fixed and stained for immunofluorescence assays. **(A)** B5R-Dendra2 (green) was stained with α-B5R (blue) and phalloidin (red). **(B)** F13L-Dendra2 was stained with α-B5R (blue) and phalloidin (red). **(C)** Dendra2-A3L was stained with α-B5R (red). **(D)** Cells infected with Dendra2-A3L/B5R-CFP (green/blue) were imaged without staining. Scale bar represents 10 μm.

3.2.5 Dendra2 fusion viruses display bright fluorescence and photoconvert efficiently

Having validated the construction of our fusion viruses, we went on to image B5R-Dendra2, F13L-Dendra2 and Dendra2-A3L in our live cell system. HeLa seeded onto fibronectin coated No. 1.5 glass µ-Dishes were infected with the B5R-Dendra2 for a minimum of 7h (B5R-Dendra2 and F13L-Dendra2) or 5h (Dendra2-A3L) and then imaged on an Olympus FV1000 confocal microscope at 600x to 1200x magnification (600x optical magnification and up to 2x digital magnification). Infection times were chosen based on the approximate appearance of the mature Dendra2 fluorophore of expressed fusion proteins. The time chosen for IEV tags (B5 and F13) is later than the IMV tag (A3) due to their differing temporal expression profiles.

Infected cells were located and imaged with a 488 nm laser at 0.1% power (<0.03 mW) and 559 nm laser at 0.2% power (0.03 mW) to obtain “pre-activation” images [**Figure 3.14-3.16**]. Images were acquired with a 4.0 pixel/sec scan speed, the longest pixel dwell possible without unintended photoactivation [312]. The two channels (488 nm and 559 nm) were collected sequentially, as the pre- and post-activation fluorophores have overlapping excitation/emission spectra, with the 488 nm laser capable of exciting the post-activation fluorophore and the PMT assigned to detect the emission of the post-activation fluorophore detecting the tail of the pre-activation emission spectra from 565 nm onwards [**Figure 3.4**].

A 40 x 40 pixel region of interest (ROI), the region of the cell with the brightest 488 nm emission (the TGN in B5R-Dendra2 and F13L-Dendra2 and the virus factory in Dendra2-A3L), was selected for photoconversion. The ROI was activated with 3% 405 nm laser (1.5 mW), for 100 ms at a scan speed of 100 µs/pixel (the slowest scan speed). All three viruses photoactivated efficiently. In B5R-Dendra2, photoactivation led to an approximately 82% decrease in the green signal (a 5.5-fold change) with a concurrent 338% increase in the photoactivated red signal (a 4.4-fold change) [**Figure 3.14**]. This indicates a high contrast photoconversion with a 24-fold total change (the product of the fold changes in the green and red channels) in the fluorescent signal between non-photoactivated and photoactivated forms of the fusion protein. This is a substantial improvement on the experimentally achieved fold change of 4.3-fold for B5R-PSCFP2 [**Figure 3.8**].

While lower fold changes were achieved for F13L-Dendra2 and Dendra2-A3L at 13.9-fold and 11.4-fold respectively, these were not indicative of less efficient photoconversion than B5R-Dendra2, but are rather the result of lower initial green fluorescent signals due to compartments with less densely packed fluorophores [**Figure 3.15-3.16**]. While complete conversion of fluorescent signal did not lead to high fold changes in the green channel, the achieved change in the red channel was 4.2-fold for F13L-Dendra2 and 6.1-fold for Dendra2-A3L. These fold changes allow clear imaging and resolution of photoactivated red virus particles, allowing us to effectively track the trajectory of a selected cohort of virus particles in all three viruses.

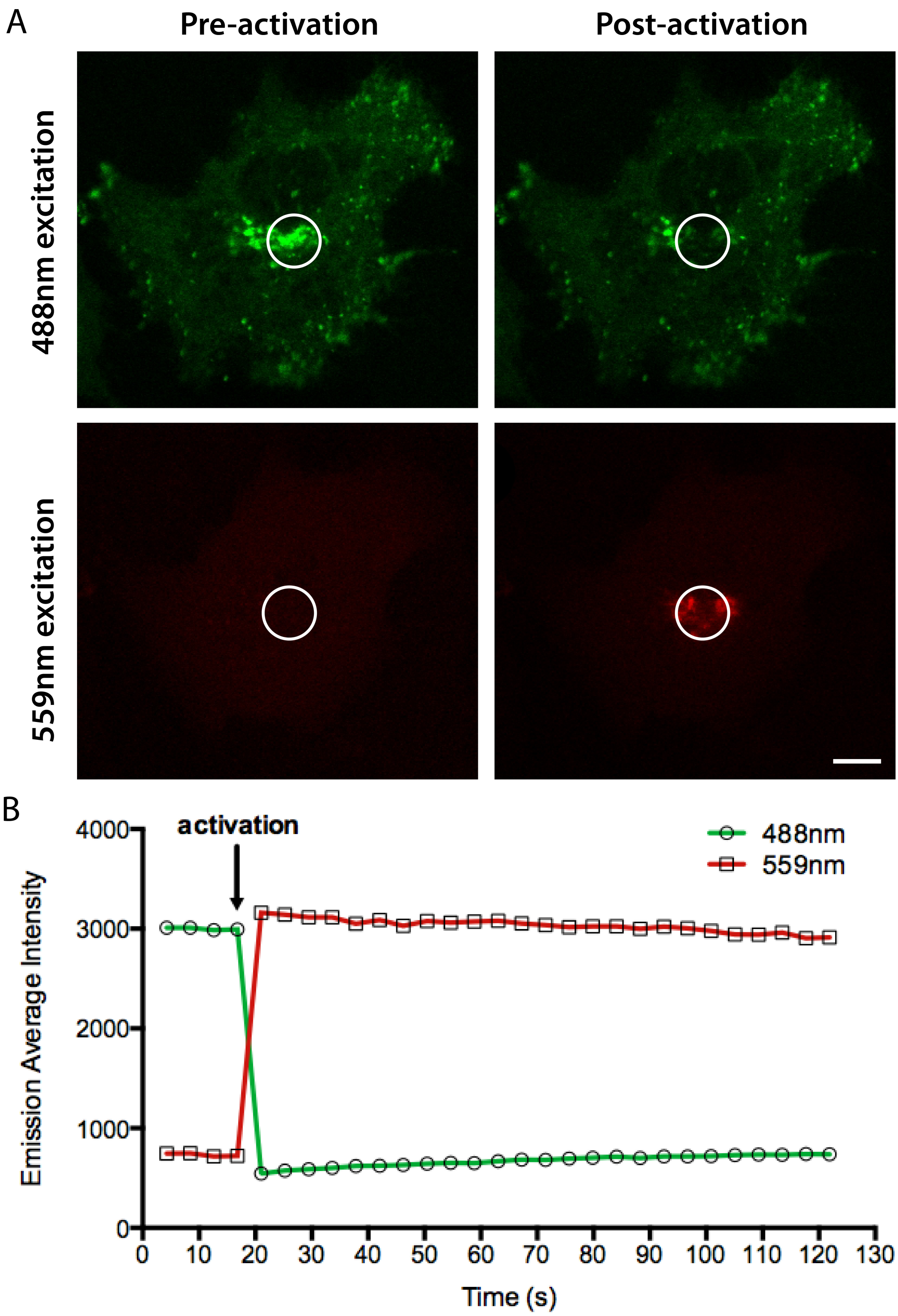

Figure 3.14: B5R-Dendra2 undergoes efficient photoconversion

(A) HeLa cells seeded onto fibronectin coated Ibidi dishes were infected with B5R-Dendra2. The trans-Golgi network, the brightest region in the cell, was located by the visualisation of Dendra2 signal with 0.1% intensity 488 nm laser excitation on an Olympus FV1000 confocal microscope and activated at the indicated region of interest (circle) with 3% 405 nm SIM laser. Excitation with 0.2% 559 nm was also collected during imaging to monitor photoconversion of the pre-activation green signal to post-activation red signal. Scale bar is 10 µm. **(B)** The average intensity of signal emitted by 488 nm and 559 nm laser lines in the activation region of interest was plotted over the course of imaging, with the point of photoactivation indicated with an arrow.

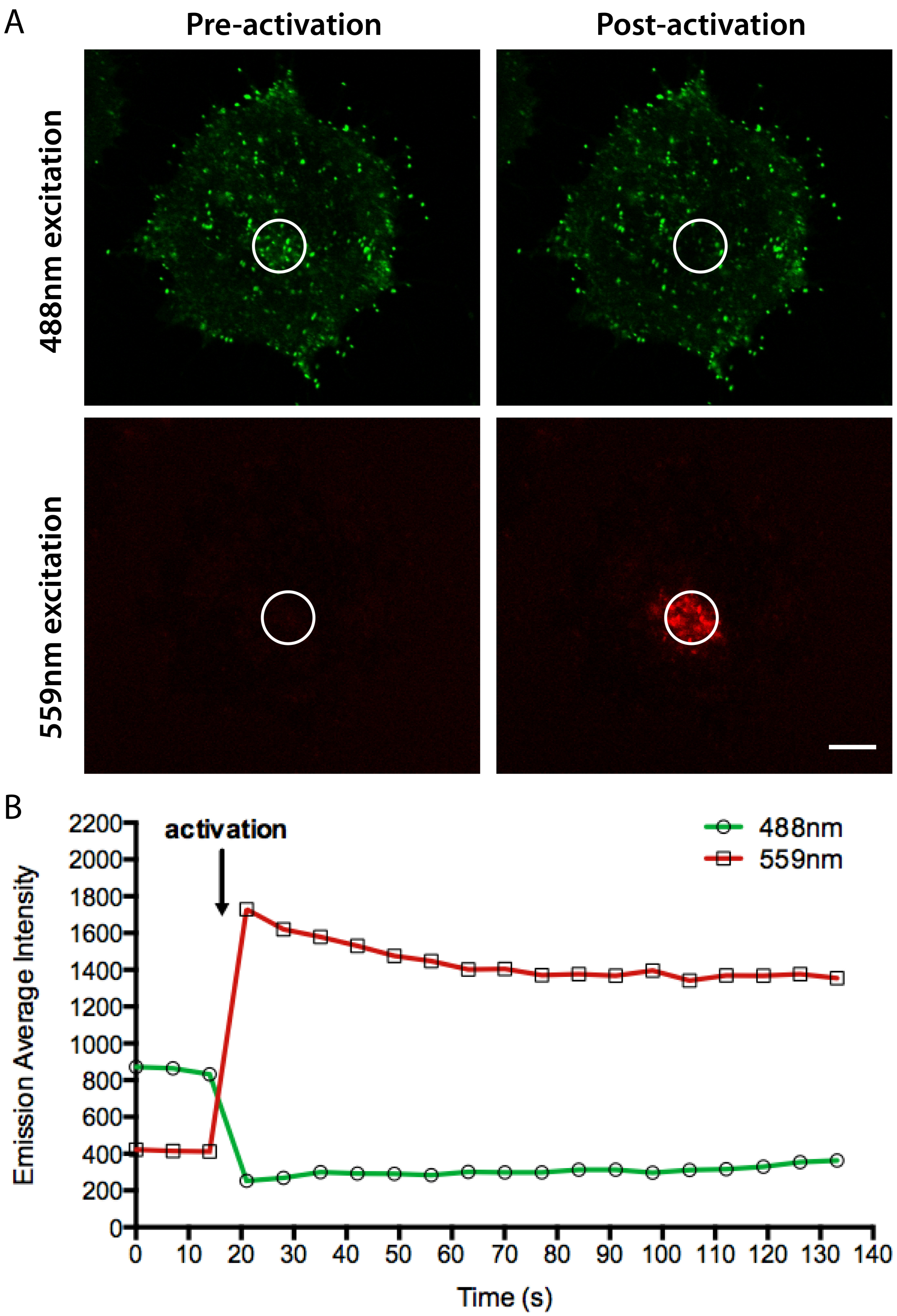

Figure 3.15: F13L-Dendra2 undergoes efficient photoconversion

(A) HeLa cells seeded onto fibronectin coated Ibidi dishes were infected with F13L-Dendra2. The virus factory, the brightest region in the cell, was located by the visualisation of Dendra2 signal with 0.1% intensity 488 nm laser excitation on an Olympus FV1000 confocal microscope and activated at the indicated region of interest (circle) with 3% intensity 405 nm SIM laser. Excitation with 0.2% 559 nm was also collected during imaging to monitor photoconversion of the pre-activation green signal to post-activation red signal. Scale bar is 10 µm. **(B)** The average intensity of signal emitted by 488 nm and 559 nm laser lines in the activation region of interest was plotted over the course of imaging, with the point of photoactivation indicated with an arrow.

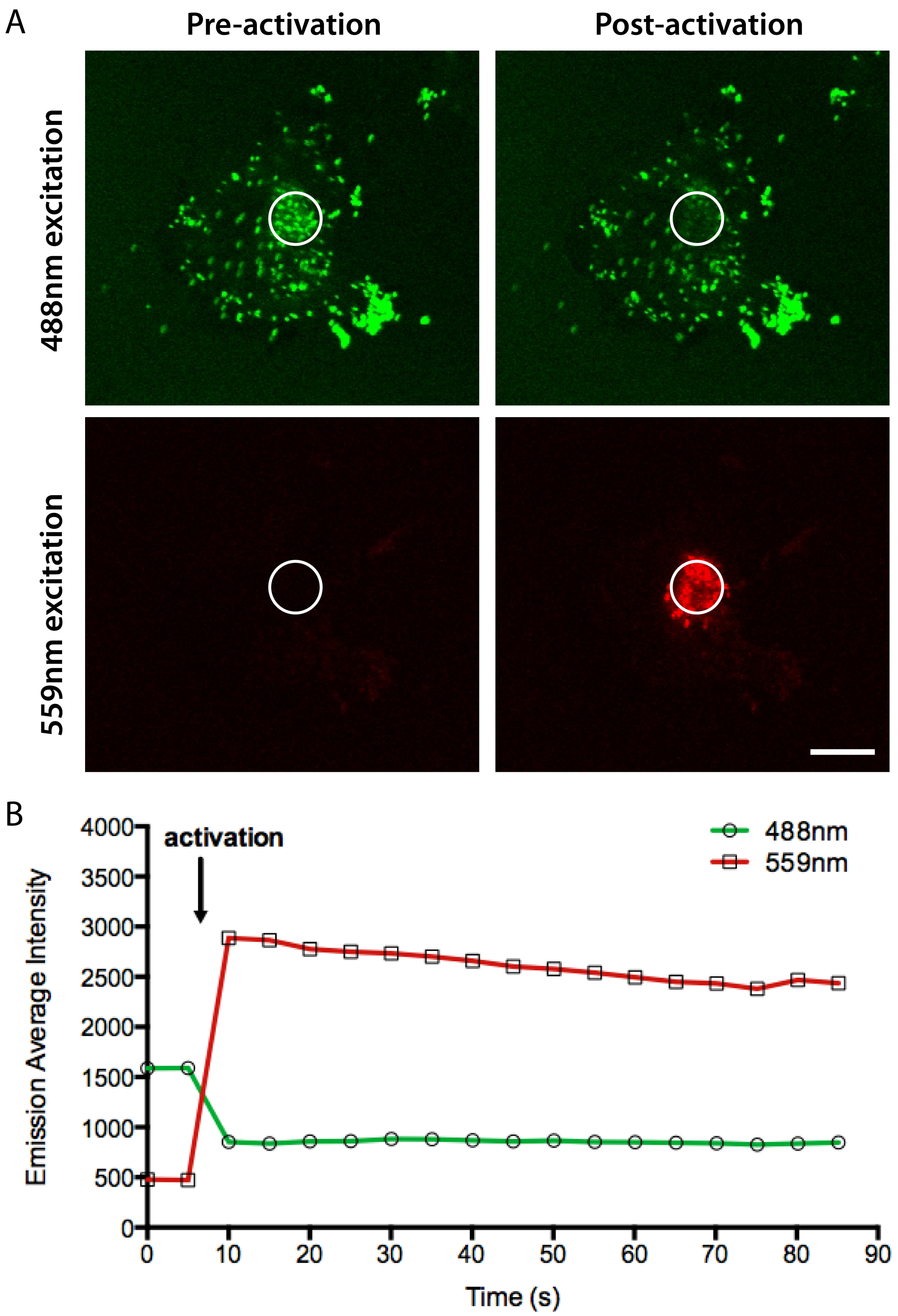

Figure 3.16: **Dendra2-A3L undergoes efficient photoconversion**

(A) HeLa cells seeded onto fibronectin coated Ibidi dishes were infected with Dendra2-A3L. The virus factory, the brightest region in the cell, was located by the visualisation of Dendra2 signal with 0.1% intensity 488 nm laser excitation on an Olympus FV1000 confocal microscope and activated at the indicated region of interest (circle) with 3% intensity 405 nm SIM laser. Excitation with 0.2% 559 nm laser was also collected during imaging to monitor photoconversion of the pre-activation green signal to post-activation red signal. Scale bar is 10 μm. **(B)** The average intensity of signal emitted by 488 nm and 559 nm laser lines in the activation region of interest was plotted over the course of imaging, with the point of photoactivation indicated with an arrow.

3.2.6 Photoconversion of Dendra2 tagged virus allows trajectory tracking of single virus particles

Single virus tracking in a complex system such as VACV infection is difficult for a number of reasons. Microtubule-based motility is very rapid and particles move at up to 3 μm/sec. There are also large numbers of particles within an infected cell, often in the hundreds. To be able to track a single particle over extended time periods, due to the speed and quantity of other particles, imaging would require a very high frame rate. As previously mentioned, higher frame rates result in a large amount of exposure of the fluorophore to exciting light, which potentially rapidly bleaches particles. These issues can be large overcome with a photoactivatable fluorescent protein tagged virus that allows us to highlight a single virus particle and distinguish it from other virus particles when the infected cell is imaged at a later time point.

To be able to identify single activated particles, efficient photoconversion is required so that there is high contrast between unactivated and activated particles and Dendra2-A3L satisfies these requirements. Having demonstrated that particles are extremely bright and the virus factory undergoes efficient photoconversion with optimised photoactivation settings, we went on to activate single virus particles to attempt longer time frame virus trajectory mapping.

HeLa seeded onto fibronectin coated No. 1.5 glass μ-Dishes (Ibidi) were infected with the Dendra-A3L and then imaged on an Olympus FV1000 confocal microscope. Infected cells were imaged sequentially with a 488 nm laser and 559 nm laser with 4.0 pixel/sec scan speed to obtain pre-activation images [**Figure 3.17**]. A 40 x 40 pixel region of interest (ROI), over an isolated virus particle separated from the virus factory, was selected for photoconversion. The ROI was activated with 3% of the 405 nm SIM laser under “Tornado” setting for 100 ms at a scan speed of 100 μs/pixel. 15 min after activation, a Z-stack from the basal to apical surface was collected (step size was determined by automated optimisation).

Photoactivation was successful, inducing a bright red photoconverted particle with concurrent decrease in the green signal [**Figure 3.17**]. Another virus particle outside but at the edge of the selected 40 x 40 pixel region of interest was also activated, but to a lower degree than the targeted particle, with only slight effects on the decrease of the green signal. Due to the differences in the green/red contrast between the two particles, the targeted particle can still be clearly differentiated. All the slices from the 15 min postactivation Z-stack was condensed into a projection (all slices through the volume of the cell overlayed into a singular image) and the photoactivated particle can be located as particle with the brightest 559 nm emission and lowest 488 nm emission ratio.

We have demonstrated that recombinant viruses with highly abundant viral proteins such as A3 fused to bright photoactivatable fluorescent proteins such as Dendra2, are able to be located over relatively long timeframes and imaged without substantial bleaching of fluorophores. Given the potential speed of microtubule movement of virus particles (3 µm/s), tracking of non-photoactivatible fluorescent protein-tagged viruses would have limited tracking timeframes to a maximum of a few minutes (one frame every 5 s would be able to be imaged for approximately 30 frames before fluorophores were substantially bleached). Single virus tracking has the potential to reveal detailed information about IMV and IEV trajectories over the course of infection.

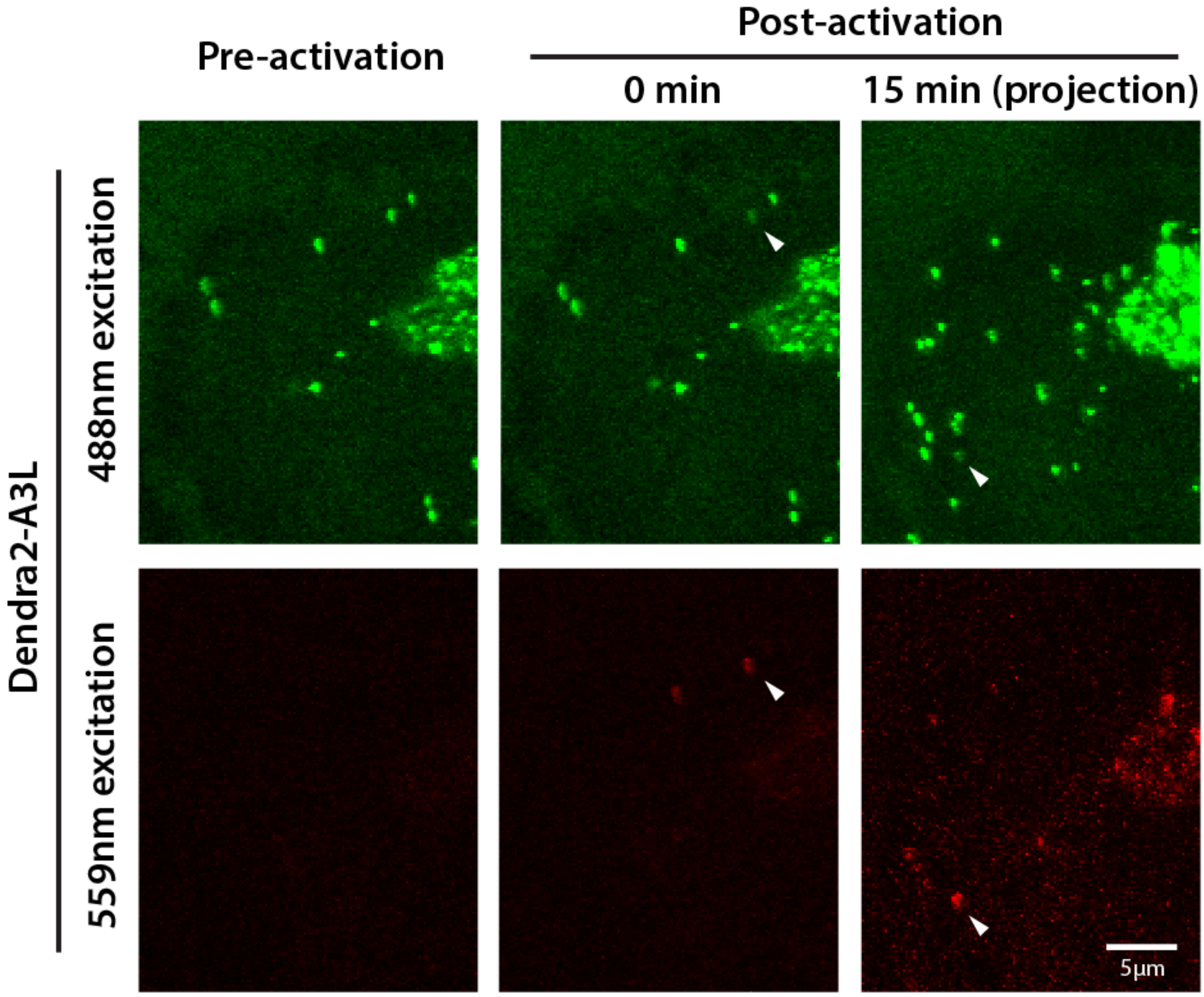

Figure 3.17: Dendra2-A3L is an effective tag for monitoring single virus trajectory
HeLa cells seeded onto fibronectin coated Ibidi dishes were infected with Dendra2-A3L. Well-isolated single virus particles (indicated with an arrow) were located by the visualisation of Dendra2 signal with 0.1% 488 nm laser excitation. 0.2% 559 nm laser excitation was collected preactivation to confirm the lack of photoconversion prior to the intended activation. The particle was activated with 3% intensity 405 nm SIM laser for 100 µs/pixel for 100 ms. 15 min post activation, the emission with 488 nm and 559 nm laser lines was collected to track post-activation trajectory. The 15 min timepoint is a projection of all the slices from a Z-stack taken from the apical to basal surface of the cell. Scale bar is 5 µm.

3.3 DISCUSSION

Originally, our intention in using PSCFP2 as a photoactivatable tag for VACV intracellular transport was that utilisation of blue and green channels would allow multichannel imaging with another complementary viral tag in red (mRFP or mCherry). A PSCFP2-A3L virus recombined with B5R-mRFP for instance would allow us to highlight a specific subset of virus particles, while differentiating between IMV (that would be positive for PSCFP2) and enveloped forms of the virus (positive for both PSCFP2 and mRFP). We have substantial experience imaging mRFP fusions of both B5 and A3, and envisaged that imaging a photoconverted population of PSCFP2 viruses in green simultaneously with a reference red fluorescence tag would allow the greatest flexibility and optical resolution for imaging virus dynamics.

Unfortunately we encountered various difficulties imaging PSCFP2 fusion viruses. Firstly, B5R-PSCFP2 did not generate sufficiently bright virus particles to resolve with a usable signal-to-noise ratio. To maximise the brightness of imaging, the pinhole of the confocal microscope was opened to the largest setting that did not allow laser reflection on the glass surface to enter the PMT, generally 400 µm. The pinhole functions to remove out of focus light from the image, which enables the imaging of thick samples with large amount of fluorescent signal on other focal planes [388]. As our samples are relatively thin at 10 µm, a relatively large pinhole allows us to capture the entirety of the signal in a single frame without compromising image quality with substantial out of focus light. Although dramatically improving the brightness of virus particles and compartments, we could still not achieve a usable signal-to-noise ratio.

Other groups have reported functional difficulties in utilising PSCFP2. In direct comparisons of photoconvertible proteins (PA-GFP, PSCFP2, Kaede and KikGR) for utility in cell labelling for mouse embryonic development analysis, PSCFP2 is reported as having dim pre-activation, inefficient photoconversion and considerable overlap between pre- and post-activation spectral profiles requiring spectral unmixing [389]. This group, however, imaged preactivation PSCFP2 using a 458 nm laser at 45% power [389]. This is the laser typically used to excite eCFP and Cerulean which have excitation maxima at 425 nm and 433 nm, respectively [390]. PSCFP2 on the other hand, is significantly short wavelength shifted, with only the slightest tail of its emission spectra at 458 nm [312]. The imaging settings used were therefore not reflective of the ideal achievable brightness of PSCFP2.

The low brightness and interrelated inefficient photoactivation we encountered with B5R-PSCFP2 were overcome with use of PSCFP2 fused to A3. As A3 is one of the most abundant proteins in the virus particle [371], PSCFP2-A3L produced substantially brighter particles that could be readily resolved. Nonetheless, the spectral properties of PSCFP2 presented further technical difficulties we were unable to overcome. With an excitation maximum of 400 nm, "pre-activation" imaging with the lowest 405 nm laser power that clearly resolved virus particles (1%/0.5 mW) led to unintended photoactivation of the fluorophore [312]. Attempts to minimise inadvertant photoactivation, including use of the fastest scan speed to locate appropriate cells (infected and also displaying a distinct virus factory) and monitoring the photoactivation series with the 488 nm laser only, did not completely eliminate inadvertant photoactivation. We therefore could not achieve experimental "highlighting" of a subset of virus particles with targeted photoactivation.

PSCFP2 has been effectively used in embryonic development studies utilising 3D imaging of organogenesis [391]. PSCFP2-labelled H2B was expressed from an electroporated plasmid construct in early embryos. Targeted nuclei expressing H2B-PSCFP2 were efficiently photoactivated with a 405 nm laser at 10% power and the photoactivated signal remained stable over the course of imaging, allowing cells to be tracked over time [391]. The authors did not report that imaging with 2% 405 nm laser caused any unintended photoactivation, perhaps due to the impeded penetration of light through the early embryos that are hundreds of cells thick, leading to lower intensities of light below the photoactivation threshold [392, 393].

However, in an earlier study by the same group comparing different photoactivatable proteins in a neural tube model, with the same imaging and activation settings, there is evidence of unintended photoactivation due to imaging with the 405 nm laser [394]. While photoactivation led to an inversion of the fluorescence intensity ratio of blue signal to green signal, "pre-activation" images indicated that there is a non-trivial amount of green fluorescence, with the ratio of blue-to-green approximately 1.5:1 prior to the photoactivation [394].

PSCPF2 can also be imaged by arc lamp excitation in widefield systems with select filters designed to image blue fluorophores such as DAPI [312]. As the intensity of excitation light cannot be controlled to the same degree as lasers in confocal systems, photoactivation upon imaging is likely inevitable. Surprisingly, it has been reported that long-term exposure (300 sec) of PSCFP2 to unfiltered 175W xenon light or 50W mercury lamp illumination led to no photoactivation [395]. In these photostability assays, a decrease in brightness of the non-photoconverted PSCFP2 signal (Semrock DAPI 5060B, excitation; 350-405 nm, emission; 415-480 nm) occurred with no detectable increase in the channel used to detect photoconverted PSCFP2 [395]. The authors attribute this change to photobleaching, and while a portion of the signal decrease is likely due to photobleaching, the filter cube used to detect photoconverted PSCFP2 (Semrock CFP-2432A, excitation; 425-455 nm, emission; 460-505 nm) misses both the excitation and emission maxima at 490 nm and 511 nm respectively, suggesting that photoactivation may have been occurring without detection in the assay.

An earlier form of PSCFP2, PSCFP, has been utilised successfully in the monitoring of diffusible glucokinase translocation in response to glucose and mannoheptulose stimulation [364, 396]. Regions of PSCFP-tagged glucokinase were photoactivated and the diffusion of photoconverted PSCFP out of the region of interest was tracked with a 488 nm laser. The monitoring of the return of activated signal in the ROI to baseline levels can be assessed independently of the rest of the cytoplasmic pool of glucokinase. Provided that complete photoactivation of all PSCFP in the ROI occurs, the apparent unintended photoactivation of PSCFP outside the ROI caused by imaging scans prior to the intended photoactivation does not affect the assay. A similar analysis approach does not have full utility in our VACV system, as we aimed to address hypotheses involving trajectory and destination of activated particles as well as rate of turnover through the ROI/compartment.

As well as having less of an effect on plaque size (and therefore viral replication and transport), compared to PSCFP2-fusion viruses, Dendra2-fusion viruses were also bright and easily imaged. Photoactivated Dendra2-fusion viruses were bright enough to clearly resolve and track in all three recombinant viruses generated. We did not always achieve full photoconversion of the fluorophore as the density of signal at the compartment changed based on the fusion virus used as well as the shape/organisation of the compartments in individual cells. However, even in instances with incomplete photoconversion, a high contrast between photoactivated virus particles and the background red channel signal was sufficient to clearly resolve virus particles. An extremely low power of laser was used to image both pre- and post-activation forms of Dendra2 (0.1% of 488 nm laser for the preactivation green form and 0.2% of the 559 nm laser for the post-activation red form, corresponding to approximately 0.03 mW of energy in both cases) which is indicative of the density of fluorescent protein packing in virus particles as well as the 2.6-fold improvement of relative brightness of Dendra2 compared to PSCFP2 [312].

Like PSCFP2, Dendra2 can be photoactivated by the same wavelength of light used to visualise the fluorophore at the excitation maximum (488 nm), as well as with the 405 nm laser line [312]. Photoactivation of Dendra2 with 488 nm light however requires that each fluorophore is exposed to a relatively long continuous beam of light [397]. The continuity of light can be controlled by the selected pixel dwell time, which determines the amount of time the laser line irradiates each point. Using a 4.0 pixel/sec dwell time (with 0.1% laser power) allowed us to clearly resolve Dendra2-fusion virus particles without eliciting discernible photoactivation, as can be seen by the stable fluorescence signal of both pre- and post-activation forms of the protein prior to the moment of photoactivation [**Figure 3.14-3.16**]. This lack of inadvertant photoconversion of the fluorophore by visualisation scans allowed us to successfully achieve targeted photoactivation at a defined ROI with the 405 nm laser that was not possible with PSCFP2-fusions.

Furthermore, as we were able to use the 405 nm SIM laser line for more efficient photoconversion of the ROI without blocking the visualising 488 nm light path, we could acquire images in both 488 nm and 559 nm channels simultaneously to photoactivation. The ability to image both pre- and post-activation channels at the moment of photoactivation allows us to assess the efficiency of photoconversion with brightness fold changes, measured as the fold decrease in one channel multiplied by fold increase in the other. We achieved fold changes between 10- and 25-fold compared to the reported theoretical achievable fold-change for Dendra2 of 4000 [312]. Other studies have demonstrated experimental fold-changes with Dendra2 similar to ours, including a study tracking the movement of Dendra2-tagged transcription factors through the *Arabidopsis* root (10-fold, [398]) and the original study describing the improved Dendra2 mutant (10-fold, [397]).

While observed experimental fold-changes are much lower than the theoretical capabilities of Dendra2, it is important to note that fold-changes in arbitrary fluorescent units are not solely indicative of the effectiveness of the photoconversion, but are also highly dependent on the concentration of fluorescent signal in ROI, as well as the baseline/background signal (which can be altered by changing the sensitivity of the photon detection system of a confocal microscope, called the gain). As an example, in a ROI with a pre-activation reading of 101 arbitrary fluorescence units and a post-activation reading of 501, photoactivation would have achieved a 5-fold change in fluorescence. A lower gain that reduced the arbitary fluorescence units by 100 would have resulted in pre- and post-activation readings of 1 and 401, respectively, leading to a 400-fold change, even though the effectiveness of the photoactivation is the same in both instances. Ultimately, although fold-changes give an indication of the contrast of pre- and post-activation forms of a photoactivatable protein, it is fairly arbitrary and optimising settings for maximal fold-change ratios have minimal utility experimentally when there is a clear, assayable differentiation of the chosen population, as was observed for all three Dendra2-fusion viruses.

The overall brightness and high achievable contrast of pre- and post-activated forms, combined with the fact that it is monomeric with a low tendency to aggregate, has meant that Dendra2 has been widely utilised since the original characterisation of Dendra [365] and subsequent optimisation [397]. It has been used to successfully differentiate the generation of newly formed centrioles from older photoconverted centrioles to elucidate the role of DNA damage-induced centrosome amplification in tumorigenesis [399]. While Dendra2 can be utilised to mark and differentiate subsets of fairly static structures such as centrioles, it is also ideal for tracking experiments of fast moving molecules and is regularly used in such studies, including the investigation of the intracellular transport of molecules via the plasmodesmata of moss [400], the aforementioned analysis of transcription factor transport through the *Arabidopsis* root [398] and the dynamic movement of protein transport machinery in the mitochondrial membrane [401]. It is in this second context that we aimed to answer questions of VACV intracellular transport [**Chapter 4**].

A substantial limitation to live cell imaging of fluorescent fusion proteins is the rate of maturation of the chromophore. The maturation of the chromophore occurs after protein folding and involves the cyclisation of three adjacent amino acid side chains [see **Section 3.1.2.2** for more details]; it is the chromophore maturation and not the protein folding of fluorescent protein that is the slow, rate-limiting step of fluorescent protein maturation [402]. As the fluorescent protein will not produce a fluorescent signal until chromophore maturation [340], biological events close to protein translation cannot be monitored with fluorescence microscopy and slower chromophore maturation times extend the window where viral transport dynamics cannot be monitored. While one of the improvements in Dendra2 over Dendra was the chromophore maturation, the maturation half-time of Dendra2 is still 90 min at 37^{o}C [312, 365, 403], compared to 65 min for EGFP [404].

A3 is an IMV protein and is expressed earlier than IEV proteins B5 and F13, with substantial expression of the 74kDa precusor protein (4b) at 4 hpi [368]. We were able to detect a fluorescent signal with live cell microscopy of Dendra2-A3L at 5 hpi, with a strong signal at 6 hpi. Although B5 can be detected earlier in infection at 4 hpi, it is expressed at highest levels in infected cells at 6-7 hpi [372]. F13 has a similar temporal expression pattern to B5, with detectable expression from 4-6 hpi [376]. We were able to detect bright, imageable fluorescent signals in both B5R-Dendra2 and F13L-Dendra2 at 7 hpi. Although we had concerns that the slower Dendra2 maturation rate (compared to EGFP) would limit our analysis of IEV egress, active wrapping is occurring after 6 hpi [405, 406] and 7-9 hpi is therefore an appropriate time frame to monitor IEV wrapping and egress. Consistent with this, studies reporting on movements of IEV utilising F13L-GFP and B5R-GFP fusion viruses have also performed imaging at 7-8 hpi, although imaging has also been performed much later in infection (~24h) [263, 282, 284, 374].

Other uses of photoactivatable fluorescent proteins in viral contexts have included tracking HIV-1 Pr55-Gag, the precusor for all structural determinants for HIV-1 particle formation, tagged with PA-GFP [407] and tracking NS5A, a key protein in the replication of Hepatitis C RNA replication, also tagged with PA-GFP [408]. These studies have aimed to monitor the motility of proteins over the course of viral assembly/replication, rather than using the photoactivatable fluorescent protein fusions as markers of individual virus particles, to analyse the subcellular transport mechanisms/egress of particles as we have done.

Lastly, as a combination of viral infection and imaging places a large amount of strain on cells, it is important to mention that a large amount of optimisation of the photoactivation protocol detailed in this thesis was to create optimal conditions where cells could be imaged for substantial periods of time without cell death.

Phototoxicity is a significant concern in live cell confocal imaging and is largely due to light-induced generation of reactive oxygen species (ROS) leading to oxidative damage of DNA, lipids and proteins [409-411]. While UV light (290-380 nm) is the most lethal, exposure of cultured cells to visible light in the violet range (400-450 nm), such as the wavelength of light used to photoactivate both PSCFP2 and Dendra2, has also been shown to induce mutations and cause cell death [410, 412, 413]. The damage of high intensity 405 nm light would be exponentially higher if utilised for visualisation of the fluorescent signal in addition to photoactivation (where only a small portion of the cell is exposed for 405 nm light for 100 ms). The lower amount of phototoxicity-related damage generated in the cells being imaged is therefore another advantage of tracking Dendra2 fusion viruses over PSCFP2 fusion viruses.

VACV infections, even of non-fluorescent viruses, induces an apoptotic response in cells [414-416], and combined with exposure to high intensity 405 nm light during photoactivation, the infected cells can exhibit rounding-up and detachment from the surface, obfuscating imaging analysis. To prevent this, cells must be well maintained (with regular passaging and discarding after reaching high passage numbers) and allowed to settle on the glass of the Ibidi μ-dish for 24 h before they are infected. Fibronectin coating of Ibidi dishes also proved critical to the successful imaging of Dendra2 tagged viruses. Fibronectin is a ~440 kDa glycoprotein of the extracellular matrix that binds to integral membrane proteins called integrins as well as extracellular matrix components such as collagen, fibrin, and heparan sulfate proteoglycans [417, 418]. In cell culture contexts, it aids in the adherence of cells to non-biological surfaces such as glass [417, 418].

CHAPTER 4: Characterising the Transport Dynamics of Various Morphological Forms of Vaccinia Virus

4.1 INTRODUCTION

All of the data represented in this chapter was generated and analysed by H. Lynn.

4.1.1 Key viral mediators of intracellular transport

VACV replication is a complex process involving two intracellular compartments, the VF where IMV are generated and the TGN where a subset of IMVs are wrapped by two lipid membranes to become IEV. The transport of particles from the VF to the IMV is microtubule-based transport step and is believed to be regulated by viral protein A27 [163], although this has been disputed [280].

A second microtubule-based egress step occurs to transport IEV to the cell periphery, where the outer most membrane fuses with the plasma membrane to CEV. These may stimulate actin-based motility that generates a propulsive force to push CEV into the extracellular space, where they become extracellular (EEV). Two mechanisms, one involving the viral protein A36 [282-286], and another involving a complex of the viral proteins F12 and E2 [283, 303] have been demonstrated to play critical roles in the egress and/or release of membrane wrapped forms of VACV [**Section 1.3.1.3-1.3.1.4**].

We use the novel viral imaging system optimised in Chapter 3 to analyse the transport dynamics of Dendra2-fusion viruses in different mutant backgrounds to dissect the relative contribution of A36 and F12 to the process of IEV egress.

4.2 RESULTS

4.2.1 B5R-Dendra2/ΔF12L and F13L-Dendra2/ΔA36R display small plaque phenotypes consistent with transport defects

Having validated the correct expression and photoconversion of IEV-protein tagged viruses B5R-Dendra2 and F13L-Dendra2, we introduced deletions of virus transport proteins F12 and A36 to analyse the contribution of these proteins to the dynamics of IEV wrapping and egress. Co-infections with B5R-Dendra2 and ΔF12L [303], and F13L-Dendra2 and ΔA36R [215] were performed [**Section 2.3.1.4**]. As recombinant viruses with A36R and F12L deletions have described defects in subcellular transport and a parallel reduction in plaque size [215, 316], resulting double recombinants were expected to produce small plaques with Dendra2 fluorescence. Appropriate plaques with expected fluorescence properties were selected from doubly infected cell lysates and purified by three rounds of plaque purification.

To confirm that the small plaque phenotype was due to the incorporation of the deletion mutant allele rather than another mutation, we examined B5R-Dendra2/ΔF12L and F13L-Dendra2/ΔA36R by immunofluorescence for the hallmarks of microtubule- and actin-based transport [**Figure 4.1**]. Both B5R-Dendra2/ΔF12L and F13L-Dendra2/ΔA36R viruses had a reduction in the appearance of EEV, and those that reached the cell surface were confined to central regions of the cell where the trans-Golgi network lies in close proximity to the plasma membrane [**Figure 4.1**]. Furthermore, we observed that while virus particles that did reach the cell surface in B5R-Dendra2/ΔF12L were able to produce actin tails, this was not the case for F13L-Dendra2/ΔA36R [**Figure 4.1**]. These results are consistent with ΔF12L and ΔA36R, indicating that the B5R-Dendra2/ΔF12L and F13L-Dendra2/ΔA36R plaque phenotypes during purification were due to the successful recombination of these deletions.

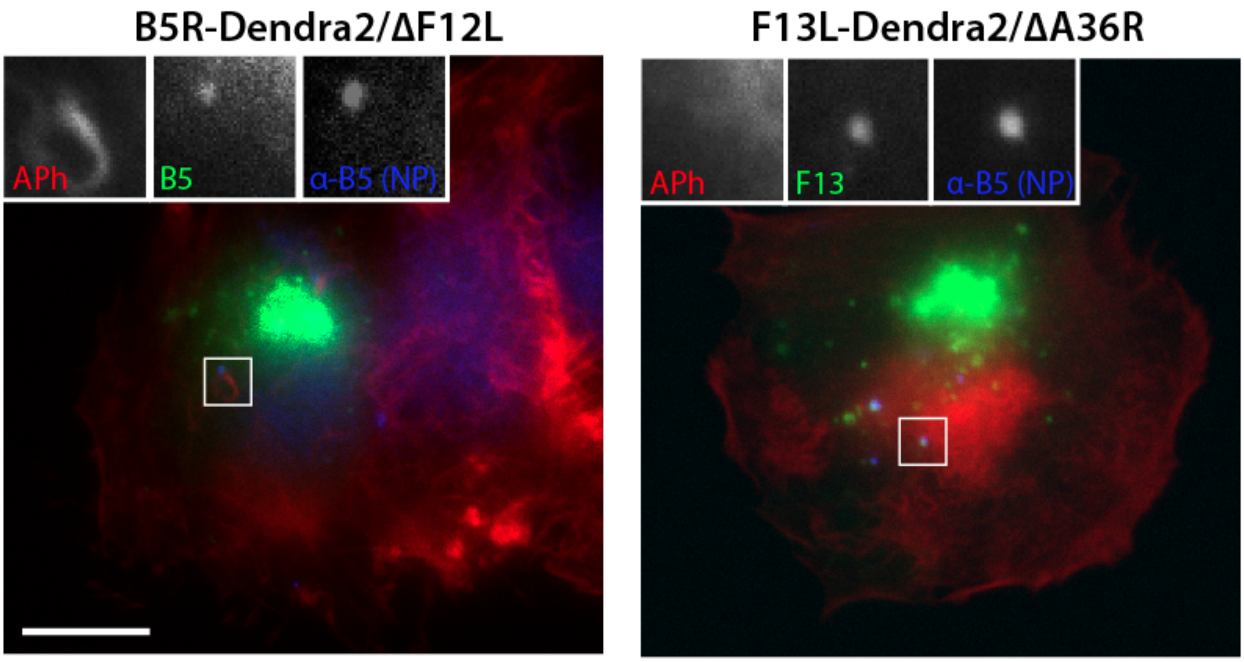

Figure 4.1: Subcellular localisation of mutant viruses

HeLa cells were infected with B5R-Dendra2/ΔF12L and F13L-Dendra2/ΔA36R before being fixed and stained for immunofluorescence assays. Non-permeablised cells (NP) were stained with α-B5 (blue) (which will indicate CEV that have reached the surface of the cell) before being permeablised and stained with AlexaPhalloidin (red); Dendra2 fusions are seen in green. Insets are of a CEV with colocalisation of Dendra2 signal and the α-B5 antibody. B5R-Dendra2/ΔF12L retains actin-based motility and an actin tail can be seen associated with the CEV. Scale bar represents 10μm.

4.2.2 B5R-Dendra2/ΔF12L and F13L-Dendra2/ΔA36R disperse from the TGN at a reduced rate and are not transported as far as parental strains

To characterise the dynamics of IEV transport out of the TGN, a series of live cell imaging experiments were carried out with B5R-Dendra2, B5R-Dendra2/ΔF12L, F13L-Dendra2 and F13L-Dendra2/ΔA36R. HeLa seeded onto fibronectin coated No. 1.5 glass μ-Dishes (Ibidi) were infected with the appropriate virus and then imaged on an Olympus FV1000 confocal microscope at 7 to 9.5 hours post infection. Infected cells were imaged sequentially with a 488 nm laser and 559 nm laser with 4.0 pixel/sec scan speed to obtain pre-activation images. A 40 x 40 pixel ROI over the region of the cell with the brightest 488 nm (Dendra2) emission was selected for photoconversion. The ROI was activated with 3% of the 405 nm SIM laser under "Tornado" setting for 100 ms at a scan speed of 100 μs/pixel.

At 15 min and 30 min post activation, a Z-stack of the photoactivated cell (with step size determined by automated optimisation) from the basal to apical surface was collected with 488 nm and 559 nm lasers to image both non-photoconverted and photoconverted signal. Z-stacks had between 7-14 slices, depending on the thickness of the cell being imaged. A digital projection of all Z-slices was created to allow the visualisation of the entirety of the fluorescent signal in an infected cell with a single 2D image [**Figure 4.2**].

Individual virus particles clearly resolved in the Z-projection as dispersed from the TGN were marked in ImageJ and counted manually. As each frame of the Z-stack took approximately 2 seconds to image, it is possible that particles were being transported on microtubules or actin tails between different z slices over the course of imaging. Therefore, particles that were present in <2 μm distance from each other in a linear trajectory over 3 slices were determined to be particles being transported or drifting across the z-axis (through movement of the cell etc.) and were only marked/counted once. Data from 17 to 26 cells per virus from three replicates (using the same viral stock to infect a new well of cells) carried out over three separate days were pooled and analysed [**Figure 4.3A**].

A mean of 31.1 ± 3.92 particles were transported out of the TGN at 15 min post-activation for cells infected with B5R-Dendra2, 15.1 ± 1.47 for B5R-Dendra2/ΔF12L, 33.0 ± 2.70 for F13L-Dendra2 and 13.0 ± 1.44 for F13L-Dendra2/ΔA36R [**Figure 4.3A**]. For all viruses, the large bulk of virus dispersal from the TGN occurs in the first 15 min post photoactivation, although there is a slight increase in the mean number of virus particles dispersed from the TGN at the 30 min time point compared to the 15 min timepoint. This increase was 8.17 particles for B5R-Dendra2, 0.612 for B5R-Dendra2/ΔF12L, 0.810 for F13L-Dendra2 and 3.73 for F13L-Dendra2/ΔA36R. This indicates that more transport out of the TGN is occurring between 15-30 min post-activation and while this increase is apparently substantial for B5R-Dendra2 and F13L-Dendra2/ΔA36R, none of the increases were statistically significant.

Comparisons in the number of particles dispersed in different virus infections showed that as expected, both mutations led to dramatic reductions relative to their parental strains. B5R-Dendra2/ΔF12L showed a mean reduction of 16.0 virus particles from B5R-Dendra2 at 15 min post-activation ($p < 0.0001$) and 23.6 at 30 min post-activation ($p < 0.0001$). A similar reduction was seen between F13L-Dendra2/ΔA36R and F13L-Dendra2, with a 20.0 difference at 15 min ($p < 0.0001$) and 17.0 difference at 30 min post-activation ($p < 0.0001$).

A qualitative indication of the longer-term effects of this restricted dispersal can be seen in the density of Dendra2 signal in the TGN even prior to photoactivation [**Figure 4.4**]. Both mutants have a higher density signal in the TGN than their parental strain, although the difference is particularly apparent between F13L-Dendra2 and F13L-Dendra2/ΔA36R. This higher density of signal is likely due to the accumulation of virus particles unable to be transported out of the compartment. It is important to note that although these trends in signal density were generally observed and imaging settings were consistent between viruses and cells, we were unable to quantify this observation from our collected data. Our imaging settings were determined by clear resolution of individual virus particles and due to the extremely high relative intensity of signal at the TGN, the dynamic range of pixels of the image was saturated at the TGN.

To further elucidate differences between our parental and mutant strains, we performed a second set of analyses on these same image series measuring the distance travelled by virus particles. The distance between the virus particle and the TGN was measured in ImageJ as the linear distance in the X-Y axis from the closest edge of the TGN. We did not account for distance travelled in the Z-axis for two reasons; firstly, the Z-axis stretching/distortion typical of imaging on confocal systems makes accurate measurements along the Z-axis extremely difficult, secondly, the HeLa cells used in these experiments are thin, with cells approximately 10 μm deep while they span between 50 – 100 μm at their widest point, restricting dispersal predominantly to the X-Y axis. The distance travelled by all virus particles (between 5 – 48 particles per cell) in six cells of each virus infection (two cells chosen randomly from each of the three replicates) were pooled [**Figure 4.3B**].

B5R-Dendra2 particles were transported a mean distance of 15.3 ± 0.775 μm from the TGN at 15min post-activation, B5R-Dendra2/ΔF12L were transported 4.68 ± 0.378 μm, F13L-Dendra2 were transported 11.7 ± 0.647 μm and F13L-Dendra2/ΔA36R were transported 6.02 ± 0.412 μm

[**Figure 4.3B**]. Similarly to the result observed for number of particles dispersed out of the TGN, the majority of the assayed measurement had already occurred by the 15 min post-activation time point, although there is a slight increase in the mean of distance dispersed at the 30 min time point compared to the 15 min timepoint. This increase was 1.44 µm for B5R-Dendra2, 0.561 µm for B5R-Dendra2/ΔF12L, 1.07 µm for F13L-Dendra2 and 0.747 µm for F13L-Dendra2/ΔA36R. This indicates that particles were transported further in the cytoplasm during the 15-30 min post-activation timeframe than had occured in the first 15 min. While this increase is consistent over all viruses, none of the increases were statistically significant.

Comparisons in the distances particles were transported in different virus infections showed that as expected, both mutations led to dramatic reductions relative to their parental strains, mirroring the trends observed in the number of particles dispersed [**Figure 4.3A**]. B5R-Dendra2/ΔF12L was transported a mean distance of 10.7 µm less than B5R-Dendra2 at 15 min post-activation ($p < 0.0001$) and 11.5 µm less at 30 min post-activation ($p < 0.0001$). A similar result is seen when comparing F13L-Dendra2/ΔA36R and F13L-Dendra2, with F13L-Dendra2/ΔA36R being transported a mean distance of 5.68 µm less than F13L-Dendra2 at 15 min post-activation ($p < 0.0001$) and 5.99 µm less at 30 min post-activation ($p < 0.0001$) [**Figure 4.3B**].

Comparisons between number of particles dispersed in different virus infections showed no significant difference between B5R-Dendra2 and F13L-Dendra2 at either time point ($p = 0.6865$ and $p = 0.2897$) [**Figure 4.3A**], indicating that defects as seen in the plaque size attenuation of the B5R-Dendra2 fusion [**Figure 3.12**] may not be clearly apparent in the first round of replication as measured at this timeframe (7-9.5h post-infection). However, there was a significant difference between the distance travelled by B5R-Dendra2 and F13L-Dendra2 particles at both 15 min ($p = 0.0004$) and 30 min ($p = 0.0001$), with B5R-Dendra2 particles being transported further from the edge of the TGN than F13L-Dendra2 particles [**Figure 4.3B**].

This difference also allows us to contextualise a comparison between the distance travelled by particles of B5R-Dendra2/ΔF12L and F13L-Dendra2/ΔA36R even though they have different parental backgrounds. While the parental strain F13L-Dendra particles were transported less far than B5R-Dendra, F13L-Dendra2/ΔA36R particles are transported further than B5R-Dendra2/ΔF12L, with a mean difference of 1.34 µm at 15 min post-activation ($p = 0.0195$) and 1.53 µm at 30 min post-activation ($p = 0.0163$) [**Figure 4.3B**]. This indicates that the deletions are having an affect on transport beyond the transport impacts of the Dendra2 fusions.

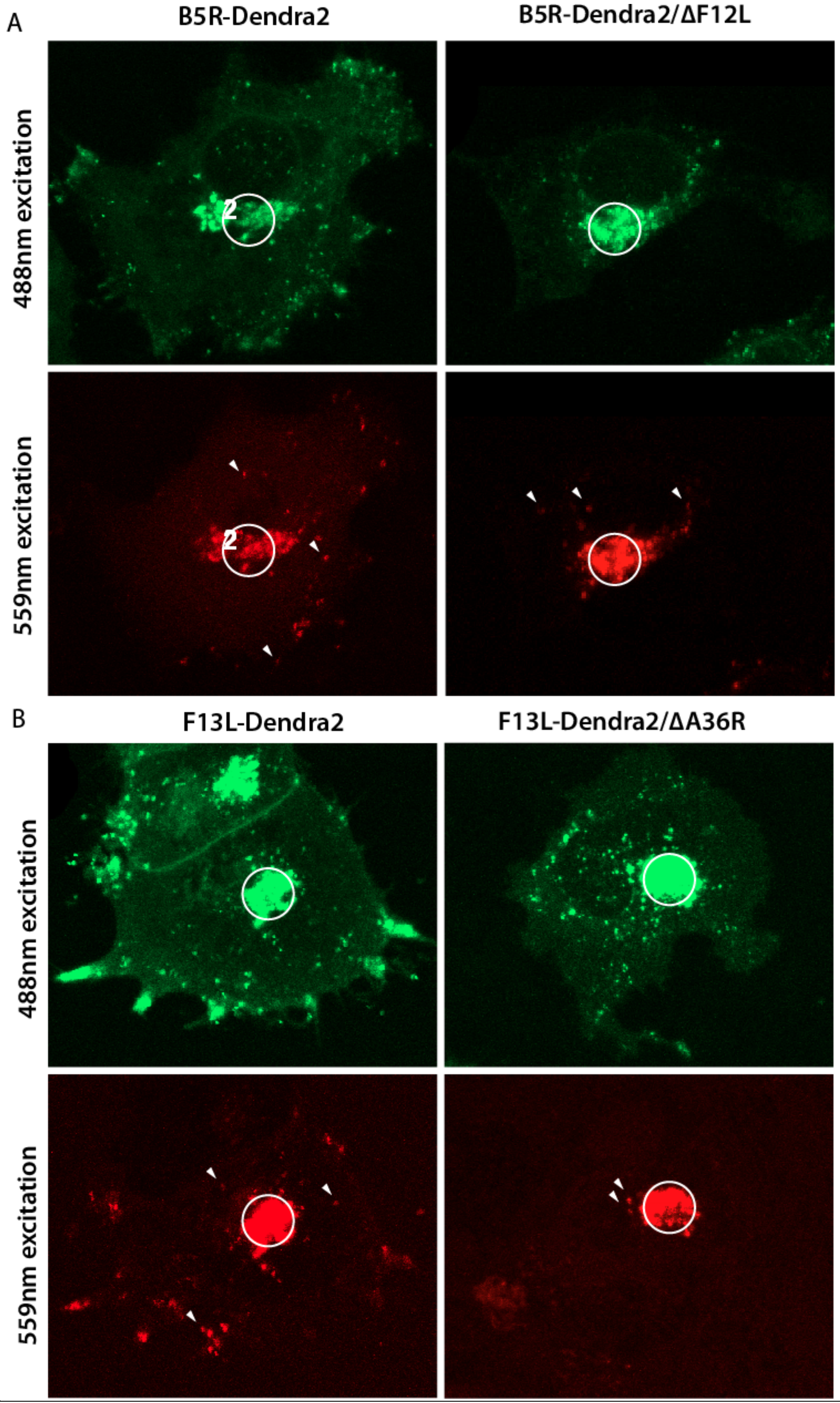

Figure 4.2: Transport of IEV out of the trans-Golgi network
HeLa cells seeded onto fibronectin coated Ibidi dishes were infected with **(A)** B5R-Dendra2 and B5R-Dendra2/ΔF12L, **(B)** F13L-Dendra2 and F13L-Dendra2/ΔA36R. The trans-Golgi network was located by the visualisation of the Dendra2 signal with 488 nm laser excitation on an Olympus FV1000 confocal microscope and activated at the indicated region of interest (circle). At 30min post activation, a z-stack was collected with 488 nm and 559 nm laser lines and the projection of all slices generated. Examples of particles migrated out of the region of interest are indicated with arrows.

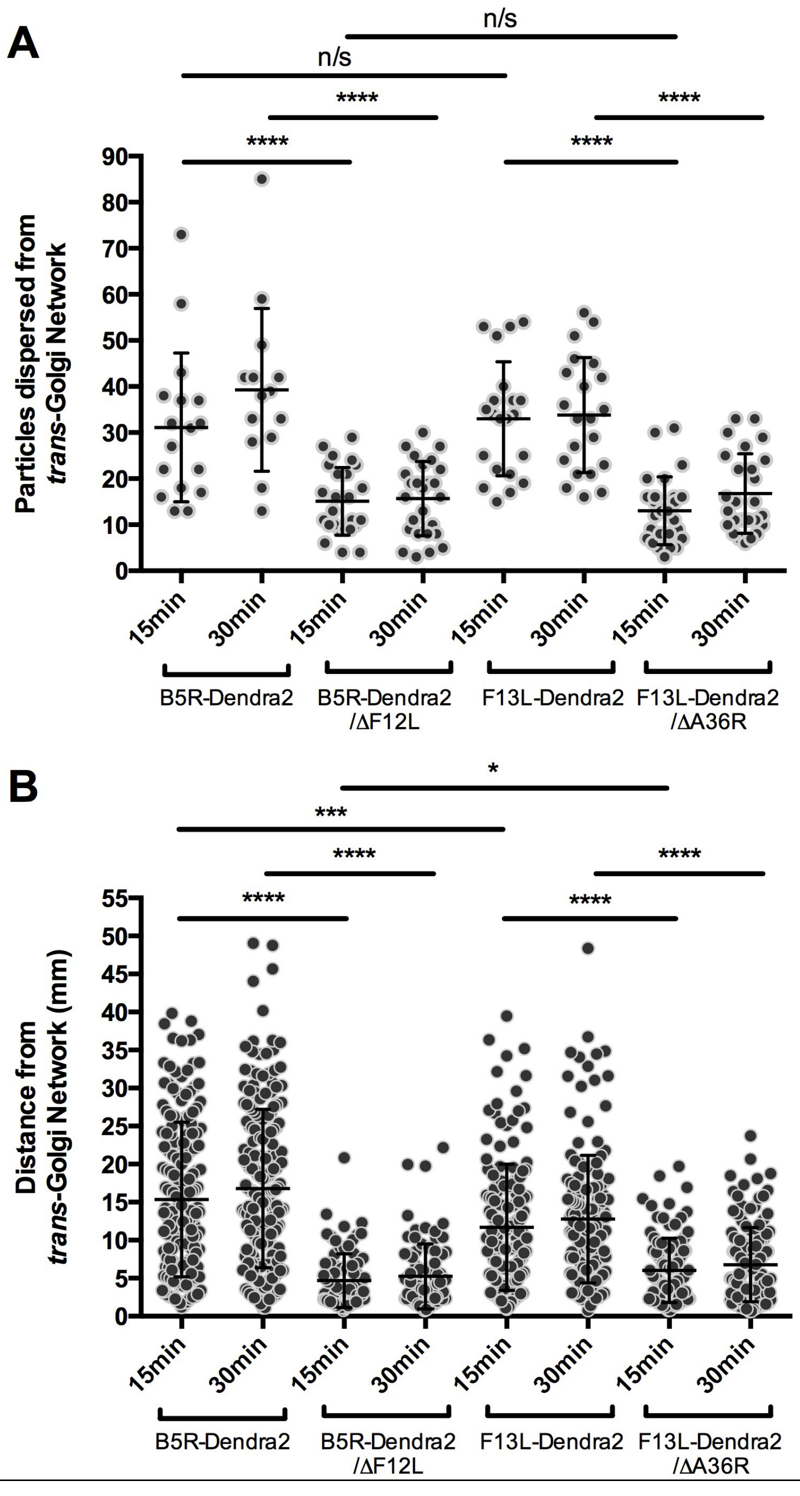

Figure 4.3: **Dynamics and characteristics of IEV transport**

HeLa cells seeded onto fibronectin coated Ibidi dishes were infected with B5R-Dendra2, B5R-Dendra2/ΔF12L, F13L-Dendra2 and F13L-Dendra2/ΔA36R. The trans-Golgi network was activated and a z-stack was collected with 488 nm and 559 nm laser lines at 15 and 30 min post activation. **(A)** Particles migrated out of the TGN were counted (n=18 cells, pooled from at least 3 replicates performed with the same stock in different wells) or **(B)** the distance migrated from the edge of photoactivated region was measured for all virus particles in cells analysed in **(A)** (6 cells for each condition, two randomly selected in each of the three replicates). Virus particles per cell ranged from n=5 to n=48, depending on the virus. ns: P > 0.05, *: P ≤ 0.05, **: P ≤ 0.01, ***: P ≤ 0.001, ****: P ≤ 0.0001.

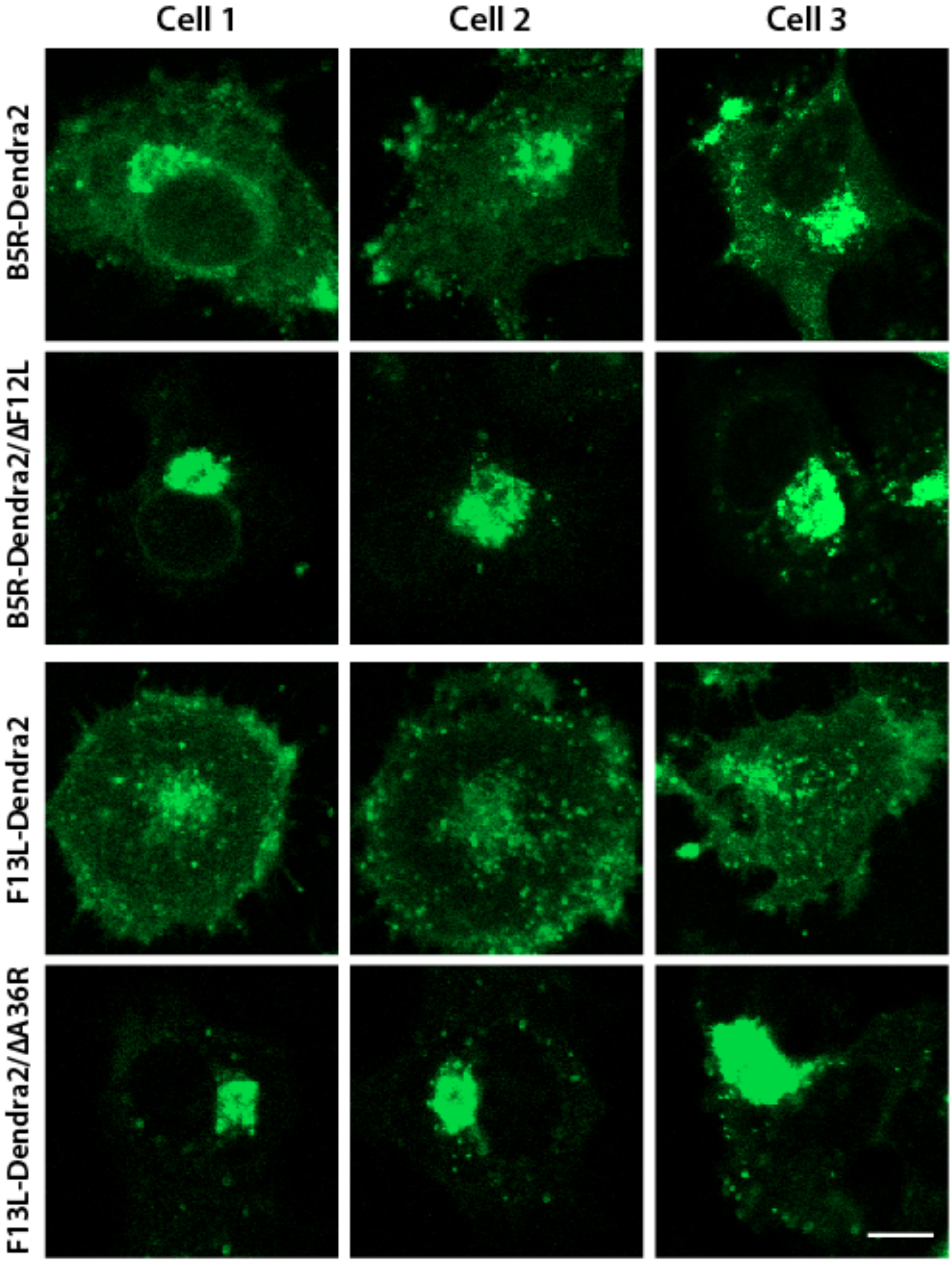

Figure 4.4: Density of Dendra2 signal at *trans*-Golgi Network

HeLa cells seeded onto fibronectin coated Ibidi dishes were infected with B5R-Dendra2, B5R-Dendra2/∆F12L, F13L-Dendra2 and F13L-Dendra2/∆A36R. Cells were imaged with a 488 nm laser line. Three replicate cells are depicted horizontally. Scale bar is 10 µm.

4.2.3 IEV do not undergo substantial intracompartment transport in the TGN

Having addressed questions of the wrapping and dispersal of IEV from the TGN, we went on to investigate the internal organisation of the compartment. HeLa seeded onto fibronectin coated No. 1.5 glass μ-Dishes (Ibidi) were infected with F13L-Dendra2 and then imaged on an Olympus FV1000 confocal microscope at 7 to 9.5 hours post infection. Infected cells were imaged sequentially with a 488 nm laser and 559 nm laser with 4.0 pixel/sec scan speed to obtain pre-activation images. A 40 x 40 pixel region of interest (ROI) over approximately half of the TGN was selected for photoconversion. The ROI was activated with 3% of the 405 nm SIM laser under "Tornado" setting for 100 ms at a scan speed of 100 μs/pixel.

At 15 min and 30 min post activation, a Z-stack of the photoactivated cell (with step size determined by automated optimisation) from the basal to apical surface was collected with 488 nm and 559 nm lasers to image both non-photoconverted and photoconverted signal. A digital projection of all Z-slices was created to allow the visualisation of the entirety of the fluorescent signal in an infected cell with a single 2D image [**Figure 4.5A**].

In 32% of cells, attempted activation of half of the TGN was unsuccessful and resulted in activation of more than two thirds of the compartment [data not shown]. We believed this was due to the orientation of the TGN in the 3D space of the cell. Half-compartment ROI selection and photoactivation was performed with XY scanning, as Z-stacks are too time consuming to allow effective monitoring of the moment of photoconversion. The TGN however spans multiple depths/Z-slices of the cell and photoactivation occurs in a tube of light through all depths of the sample and photoactivation performed in XY scanning only can therefore potentially activate substantially more of the TGN than intended.

Of the cells where close to 50% of the compartment was successfully activated, we measured the angle of dispersed particles relative to the center of the TGN. Particles that dispersed to the cytoplasm on the same side of the cell as the activated half of the TGN had readings from 0^o to 180^o and particles dispersed to the opposite side had readings from 0^o to -180^o. A schematic of 7 randomly chosen particles in 3 cells is depicted in **Figure 4.5B.** The angle of dispersal was measured for all photoactivated virus particles in 12 cells (4 cells each from 3 replicates) and revealed that 78% of virus particles disperse to the same side of the cell as the photoactivated half of the TGN [**Figure 4.5C**]. This indicates that the relative position to MTOC strongly affects the directionality of trafficking of IEV. We also observed that there was no substantial intra-compartmental movement of photoactivated signal between the two halves of the TGN at either the 15min or 30min time frames.

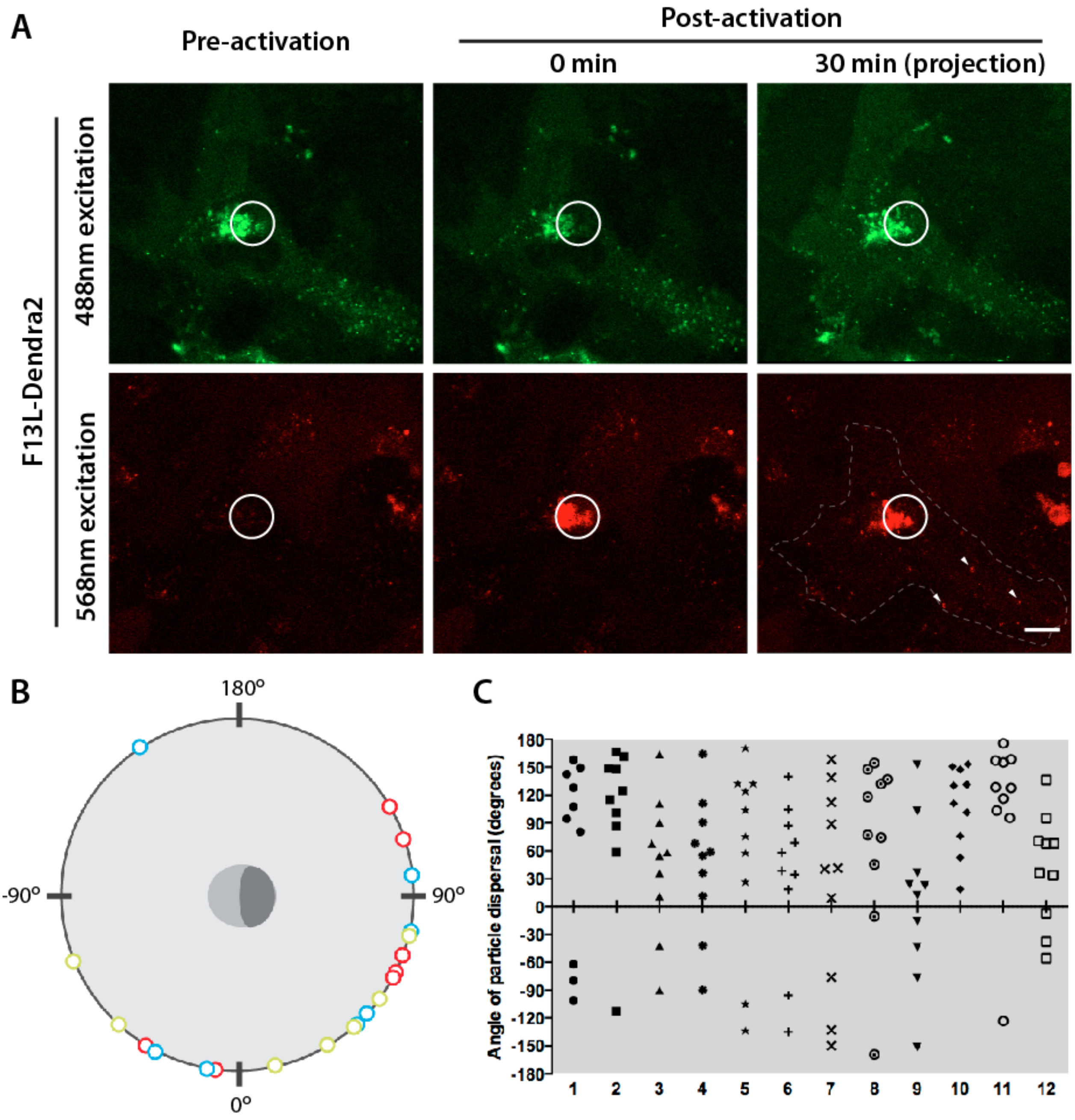

Figure 4.5: Directionality of photoactivated virus particles from half of the TGN
HeLa cells seeded onto fibronectin coated Ibidi dishes were infected with F13L-Dendra2. **(A)** The trans-Golgi network was located by the visualisation of the Dendra2 signal with 488 nm laser excitation on an Olympus FV1000 confocal microscope and then approximately half of the compartment was activated at the indicated region of interest (circle). At 30 min post activation, a z-stack was collected with 488 nm and 559 nm laser lines and the projection of all slices generated. Examples of particles migrated out of the region of interest are indicated with arrows. **(B)** A schematic representation of the resultant egress of particles from the activated half of the trans-Golgi network (represented in dark grey) from three cells (n=7 particles per cell) at 30min post activation with particles from each individual cell coloured green, blue and red. **(C)** The directionality of egressed particles from the region of interest was measured (n=12 cells with n=10 particles pooled from at least 3 replicates). Scale bar is 10 μm.

4.2.4 Dendra2-A3L/B5R-CFP allows differentiation between the VF and TGN

As previously mentioned, as a core protein, Dendra2-A3L fusions will label all morphological forms of the virus and both the VF and TGN will have a strong fluorescent signal. To differentiate between the VF and TGN, a second fluorescent tag (ECFP) was introduced to recombinant viruses as a fusion with IEV protein B5 [**Figure 3.12D**]. This would lead to VF exhibiting Dendra2 fluorescence, while the TGN would be positive for both Dendra2 and ECFP fluorescence. To confirm that the two compartments could be clearly differentiated, we performed live-cell imaging of the virus. HeLa seeded onto fibronectin coated No. 1.5 glass μ-Dishes (Ibidi) were infected with Dendra2-A3L/B5R-CFP and then imaged on an Olympus FV1000 confocal microscope at 7-9 hpi. Infected cells were imaged with a 458 nm laser to detect ECFP fluorescence and a 488 nm laser to detect Dendra2 fluorescence [**Figure 4.6**].

In most cells observed, both compartments were visible in both the 458 and 488 nm channels, although the ratio of fluorescent signal of the two channels enabled us to differentiate the VF indicated with the asterisk (lower 458 nm signal to a higher 488 nm signal) from the TGN indicated with the hash (higher 458 nm signal to lower 488 nm signal) [**Figure 4.6**]. The detection of both compartments in the 488 nm channel is a result of the replicative cycle of VACV; A3-positive IMV are transported from the VF to the TGN for wrapping where they accumulate to a degree before disseminating into the cytoplasm. The detection of both compartments in the 458 nm channel on the other hand is due to the substantial spectral overlap of ECFP and Dendra2. The excitation range for ECFP is approximately 350 to 500 nm, with a 430 nm peak that drops to a negligible excitation at 480 nm [419]. Dendra2 has a pre-activation excitation spectrum that extends from approximately 400 to 530 nm with a peak at 488 nm [**Figure 3.4C**]. Excitation of ECFP at 458 nm will therefore excite both fluorophores, leading to the detection of both compartments in the 458 nm channel (although Dendra2 is excited suboptimally and appears relatively less bright than ECFP). There is no similar cross stimulation with the 488 nm laser, as this is beyond the functional excitation spectrum of ECFP.

To confirm that we were able to clearly differentiate the two compartments even with the complicating factors, we performed imaging on the same infected cells with the 405 nm laser that excites ECFP with no excitation of Dendra2 [**Figure 4.6**]. As expected, a single compartment was detected with and verified our identification of the TGN as the compartment with a ratio of higher 458 nm fluorescence relative to 488 nm fluorescence (marked with an asterisk). It was impractical to differentiate the VF from the TGN by utilising the 405 nm laser in our tracking experiments as 405 nm excitation will lead to photoactivation of the Dendra2.

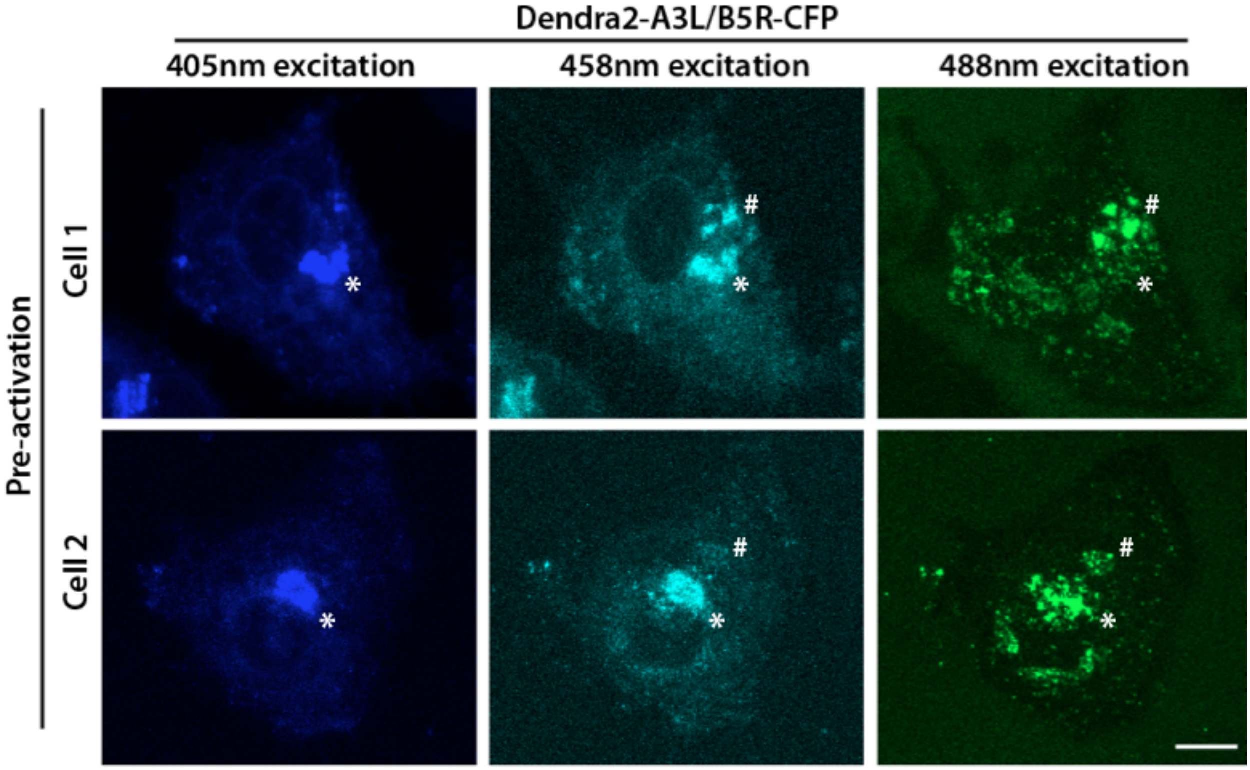

Figure 4.6: Virus factory and trans-Golgi Network are easily distinguishable
HeLa cells seeded onto fibronectin coated Ibidi dishes were infected with Dendra2-A3L/B5R-CFP. Z-stacks were collected with 405 nm, 458 nm and 488 nm laser excitation on an Olympus FV1000 confocal microscope from which projections were generated. Two representative cells are depicted vertically. The VF is marked with an adjacent asterisk and the TGN is marked with an adjacent hash. Scale bar is 10 μm.

Having verified our ability to differentiate the VF and TGN with 458 and 488 nm laser lines, we attempted to fate track IMV from the VF (either to the TGN for wrapping or directly into the cytoplasm). HeLa seeded onto fibronectin coated No. 1.5 glass μ-Dishes (Ibidi) were infected with Dendra2-A3L/B5R-CFP and then imaged on an Olympus FV1000 confocal microscope at 7-9 hpi. Infected cells were imaged with a 458 nm laser to detect ECFP fluorescence and then sequentially with a 488 nm laser and 559 nm laser with 4.0pixel/sec scan speed to obtain pre-activation images. A 40 x 40 pixel region of interest (ROI) over the VF was selected for photoconversion. The ROI was activated with 3% of the 405 nm SIM laser under "Tornado" setting for 100 ms at a scan speed of 100 μs/pixel.

At 60 min post activation, a Z-stack of the photoactivated cell (with step size determined by automated optimisation) from the basal to apical surface was collected with 458nm, 488 nm and 559 nm lasers to image the ECFP signal and both non-photoconverted and photoconverted Dendra2 signal. A digital projection of all Z-slices was created to allow the visualisation of the entirety of the fluorescent signal in an infected cell with a single 2D image [**Figure 4.7**]. Imaging at earlier time points (15 min and 30 min) post activation were also attempted, but did not reveal significant egress out of the VF, indicating that IMV morphogenesis occurs at a slower rate than wrapping to form IEV. We were able to track the transport of IMV to the TGN, with approximately 11 photoactivated particles present in the region of the representative cell with the TGN in the 60 min projection [**Figure 4.7**].

Quantifying this process in a statistically significant way in the imaging window of 7 to 9 hpi proved difficult due to the close juxtaposition of the two compartments (with the VF often wrapping around the TGN to a certain degree in three dimensional space), which led to the off-target photoactivation of particles in the TGN. Rare cells had distinctly isolated compartments, so while we did not achieve quantification in the scope of this thesis, it is possible with our photoactivation system. Similarly, it would also be possible to differentiate between the rate of transport into the TGN compared to the cytoplasm by scanning the 60 min postactivation projection with the 405 nm laser to differentiate which of the dispersed particles were IMV or IEV.

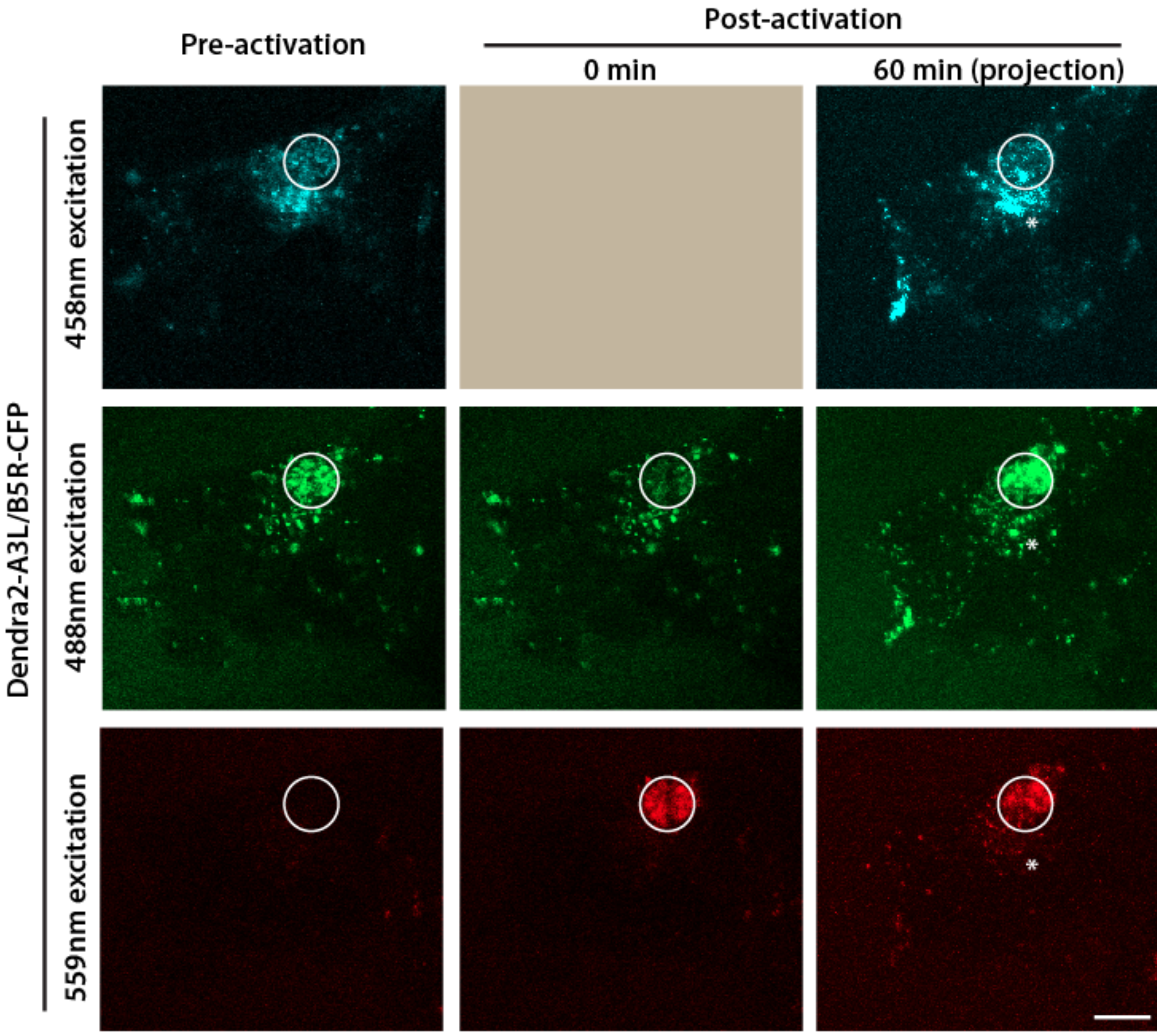

Figure 4.7: Egress of particles from virus factory

HeLa cells seeded onto fibronectin coated Ibidi dishes were infected with Dendra2-A3L/B5R-CFP. The virus factory was located by the visualisation of the Dendra2-A3L signal with 488 nm laser excitation and exclusion of the TGN-localised Dendra2 signal by concurrently visualising the B5R-CFP signal with 458 nm laser excitation. The virus factory was activated at the indicated region of interest (circle). The TGN is indicated with the asterisk. At 60 min post activation, a z-stack was collected with 458 nm, 488 nm and 559 nm laser lines and the projection of all slices generated. Scale bar is 10 µm.

4.3 DISCUSSION

B5R-Dendra2 and F13L-Dendra2 produced significantly different plaque sizes, with B5R-Dendra appearing to have some degree of attenuation compared to F13L-Dendra2 and WR [**Figure 3.11**], confirming previous reports that indicated F13L fusions are a more ideal IEV/WV tag than B5R fusions [284]. We made multiple attempts to generate a ΔF12L mutant in the parental F13L-Dendra2 strain. However, due to the attenuation of the ΔF12L strain combined with the fact that the two genes F12L and F13L are adjacent, relatively rapid methods of generating double recombinants through coinfections [**Section 2.4.1.3**] were not possible. Creation of this virus was therefore not achieved in the timeframe of this study. This being said, the differences between B5R-Dendra2 and F13L-Dendra2 were variable in our imaging experiments; there was no significant difference observed between the number of virus particles dispersed from the TGN in the course of imaging (at both 15min and 30min timepoints) [**Figure 4.3A**]. B5R-Dendra2 did display further dispersal from the TGN than F13L-Dendra2, 15.3 ± 0.775 μm and 11.7 ± 0.647 μm, respectively at 15 min ($p = 0.0088$) and 16.8 ± 0.733 μm and 12.8 ± 0.671 μm respectively at 30 min ($p = 0.0047$) [**Figure 4.3B**].

Altering the functioning of many diverse infection processes will affect the ability of the virus to undergo efficient cell-to-cell spread and therefore the plaque size of VACV. Deletion and mutation studies of proteins that play key roles in IMV production, wrapping [272, 280, 325, 379], microtubule-based egress [215, 289], actin-based propulsion into neighboring cells [292], and the repulsion of super infecting virions [215, 299] all cause small plaque phenotypes.

In many cases, a single viral protein may have multiple functions in the replicative cycle and determining the cause of plaque size defects is difficult. B5 for instance plays roles in the wrapping of IEV, their subsequent egress and formation of EEV [272, 325], EEV release [420, 421] and in the repulsion of super infecting virions [422]. Immunogold labeling electron microscopy of B5R-GFP fusion viruses indicate that C-terminal fusions of fluorescent proteins do not cause aberrant wrapping [374]. Although not a direct assay on wrapping, our observed egress of a similar number of IEV into the cytoplasm in both B5R-Dendra2 and F13L-Dendra2 suggest that potentially aberrant wrapping is not the most likely cause of the plaque defect in B5R-Dendra2 [**Figure 4.3A**]. Furthermore, the longer average distance B5R-Dendra2 was transported through the cytoplasm indicates that the fusion does not cause deleterious effects to microtubule-based egress of IEV particles.

It is possible that B5R-Dendra2 fusions are causing defects in cell-to-cell spread due to effects later in the replicative cycle such as in EEV release. Formation of CEV in VACV involves the fusion of the outer of two IEV membranes to the plasma membrane. B5 is believed to play roles in the tethering of CEV to the cell surface through protein interactions in its substantial luminal domain, as a P189S mutation has been shown to lead to dramatic increases in EEV release [420, 421]. Although the mechanisms behind release of attachment of CEV to produce free EEV is incompletely understood, it has been hypothesised that the B5^{P189S} mutation leads to weak luminal interactions that lead to decreased tethering of CEV to the cell [302]. Perhaps counterintuitively, increased EEV release in some cases led to smaller plaque sizes [421]. However, as Dendra2 is fused to the C-terminus of B5 rather than in the N-terminal luminal region, it is unlikely that there would be altered luminal interactions that would lead to plaque size defects.

Repulsion of super infecting virions involves the blocking of viral entry into already infected cells through cell signalling pathways which enables super infecting virions to be directed toward neighboring uninfected cells and allows viral spread to occur beyond the rate of replication [299]. Similarly to the involvement of B5 in EEV release, the demonstrated role of B5 in the repulsion of superinfecting virions has also been shown to involve the luminal domain of B5, relying on the presence of the short consensus repeat (SCR) 4 [422]. Therefore, again, it is unclear that a C-terminal fusion would affect this process, although the mechanism for repulsion of superinfecting virions is as of yet incompletely characterised.

As mentioned, we did detect a significant difference in the distance virus particles were transported out of the IEV, however B5R-Dendra2 dispersed further than F13L-Dendra2, a transport phenotype that is inconsistent with the demonstrated smaller plaque size. Ultimately, the cause of the attenuation of cell-to-cell spread of the B5R-Dendra2 fusion virus remains unclear, although it is possible that the defect occurs later in the replication cycle or it is relatively mild and requires multiple cycles of replication and spread to present clearly.

For all viruses, the large bulk of virus dispersal from the TGN occurs in the first 15min post photoactivation, with a slight increase in the mean of virus particle number dispersed from the TGN at the 30 min time point compared to the 15 min timepoint. While it may seem that this could be due to the rate of wrapping slowing over the course of infection, this is not what is represented in our data, which is a pooled aggregate from cells between 7 and 9 hpi. A potential explanation is that at any one point there is a pool of completely enveloped IEV ready to be transported out of the TGN into the cytoplasm, while a more gradual rate of wrapping of IEV occurs in the background. The movement out of the TGN captured in the 15 min series would therefore encompass the rate of transport of IEV out of the TGN with the slight increase of particles seen between 15 and 30 min time points indicating the more gradual rate caused by wrapping of IEV additional to the transport into the cytoplasm. It must also be considered that while IEV are transported out of the TGN, EEV will also be lost to the extracellular space and no longer be detected in our post-activation Z-stacks, causing reductions in assayed number of particles transported out of the TGN. Imaging more time points sooner after postactivation, at 1, 5, 10min would allow us to clarify and quantify these various contributing factors.

For all viruses, there is still a strong photoconverted signal in the TGN at the end of imaging [**Figure 4.4**], indicating that there is a pool of matured Dendra2 fusion protein either in the membranes of the TGN in the process of wrapping the viruses or on wrapped viruses yet to be transported out. Although it is possible that there would never be complete turnover of the photoconverted signal out of the compartment, carrying the experiment at longer time frames would also provide us with important information on the virus life cycle. For instance, it might allow us to monitor the rate of complete wrapping and transport out of the compartment, and more clearly distinguish the effect of mutations on these processes. Such measurements would not be possible in FRAP experiments, which are clouded by the translation of new fusion protein and maturation of the already present fluorophore.

As previously outlined [**Section 1.3.1.3-1.3.1.4**] both A36 and F12 (and E2, which complexes with F12) have been implicated it microtubule based transport, with deletion mutants displaying defective egress of IEV [282, 283, 285]. This deficiency in ΔA36 has been mapped to WD/WE motifs in A36 that bind to the TPR domains in the N-terminus of KLC2 and mediate interactions between IEV and kinesin-1 [286]. Unlike A36, F12/E2 are not intergral membrane proteins and have been shown to associate with A36, which may mediate their association with the virus [291, 303, 304]. If however F12/E2 is acting through A36, perhaps in a regulatory role that stabilises the interaction between kinesin-1 and A36, that loss of F12/E2 leads to a stronger phenotype than loss of A36 cannot be explained.

In an attempt to resolve this paradox, we quantified the number of virus particles egressing from the TGN, as well as the distance egressed particles travelled. Due to the mild attenuation of B5R-Dendra2, comparisons between B5R-Dendra2/ΔF12L and F13L-Dendra2/ΔA36R must be analysed in the context of the slight differences between their parental strains. We demonstrated that the number of particles transported out of the TGN over a 15 or 30 min time point is not significantly different between the two parental strains B5R-Dendra2 and F13L-Dendra2 ($p = 0.6865$ and $p = 0.2897$, respectively) and likewise that there were not significant differences between the two mutant viruses at either time point ($p = 0.3264$ and $p = 0.6441$) [**Figure 4.3A**].

On the other hand, the distance IEV particles egressed into the cytoplasm was significantly different, with average distance dispersed 4.68 µm for B5R-Dendra2/ΔF12L and 6.02 µm for

F13L-Dendra2/ΔA36R at 15 min ($p = 0.0195$) [**Figure 4.3B**]. As a direct comparison between their two parental strains shows that B5R-Dendra2 particles disperse a significantly further distance from the edge of the TGN than F13L-Dendra2 particles, that B5R-Dendra2/ΔF12L particles do not disperse as far as F13L-Dendra2/ΔA36R virus particles appears to indicate that the two proteins have a different strength of effect in the run length of microtubule-based transport.

It has been previously demonstrated that fewer CEV are formed in a ΔF12L background than a ΔA36R background [283]. Our data reveals that this is due to IEV particles in a ΔF12L background having shorter run lengths in the cytoplasm than ΔA36, as opposed to having less IEV particles egressing from the TGN. This disparity is suggestive of a differential affinity/recruitment of ΔF12L and ΔA36R viral cargoes to microtubule motors. Many viruses, including PRV [124, 423], HSV [180, 424] and HIV-1 [144] have been visualised undergoing saltatory bidirectional movement, even in an overall anterograde egress out of the cells. This bidirectionality may play roles in important processes such as navigating around physical blockades along particular microtubule paths [131, 182]. In HSV, this process involves the simultaneous binding of motors with opposing directionalities (kinesin-1 and dynein) that are regulated to achieve effective transport [134]. While it is possible that there is a similar process occurring in VACV egress, kinesin-1 at least appears to play a dominant role in the egress of VACV IEV and subsequent attenuation of ΔF12L and ΔA36R deletion mutants.

It has been reported that ΔF12L and ΔE2 do not recruit kinesin-1 even in the presence of A36 [290], but also that a A36$^{WEWD/AAAA}$ mutant (a microtubule-based transport defective mutant of A36 that does not effect actin-based motility) does not recruit kinesin-1 in the presence of F12 [286]. These results were determined with cryoimmuno-electron microscopy (cryo-EM) and immunofluorescence microscopy (IFA) respectively, with antibodies raised against KLC2. The apparently contradictory results can be explained by the limitations of the techniques used; cryo-EM gold labelling only sparsely labels epitopes on the viral surface and immunofluorescence-based assays rely on targeted fluorescent signals exceeding baseline fluorescent noise. In either instance, it is possible that the respective deletions/mutation led to reductions of KLC recruitment and subsequently to the KLC signal falling below an assayable threshold, without total abrogation of viral interaction with kinesin-1.

That both ΔF12L and ΔA36R mutants are able to egress into the cytoplasm indicates that both have the ability to undergo some degree of microtubule-based motility, indicating some functional redundancy between the two proteins. That either deletion mutant is able to undergo some microtubule-based motility is a finding that has been reported individually by other groups [283, 285]; with a focus on defining a single viral protein (either F12 or A36) as being the critical mediator of microtubule-based egress without significant acknowledgement of the complexity of viral interaction with kinesin-1. Until recently, A36 was the only viral protein demonstrated to directly interact with kinesin-1, as assayed by multiple means including Y2H, FRET and GST-pulldowns [181, 286, 288]. However, it has now been established that there is also a direct interaction between the F12/E2 complex and kinesin-1, with HA-tagged F12 co-precipitating with KLC2 only in the presence of E2 [425].

As both viral proteins are able to interact with kinesin-1, the variable run length of deletion viruses may be due to the differential recruitment of KLC isoforms to the virus. While A36 displayed no preferential association with KLC1 or KLC2 [286], F12/E2 prefentially co-precipitated with KLC2 over KLC1 [425]. Furthermore, it has been reported that siRNA mediated knockdown of KLC1 led to slight increases in the efficiency of IEV transport and the resultant plaque size, with no such effect observed with KLC2 knockdown [425]. This implies that the specific KLC isoform that mediates the association of viral cargo to kinesin-1 has impacts on the dynamics of viral transport. In infections with a ΔF12L virus, A36 is still present to interact with both KLC1 and KLC2 isoforms. In the reverse situation with a ΔA36R infection, only F12 is available to interact with kinesin-1 through KLC2; the lack of viral recruitment of KLC1 may increase the speed of transport dynamics and lead to longer run lengths [**Figure 4.3B**].

The N-terminal domain of KLC associates with KHC, while the C-terminal domain contains a six tetratricopeptide repeat (TPR) motifs to mediate cargo binding [426]. The association of cargos through WD/WE motifs can induce conformational changes in the KLC TPR domain [60, 427]. Cargo-induced conformational changes may subsequently influence kinesin-1 motor activation, through relief of motor autoinhibition [62, 428].

The current model of IEV egress is as follows: A36 associates with KLC with the TPR groove located at the N-terminal half of the TPR domain of KLC [286]. F12 has been demonstrated to bind to both A36 [429] and E2 [285], with E2 itself able to associate with the C-terminal TPR tail of KLC [425]. Deletion of either A36 or F12 (thereby preventing viral association of E2 bound KLC) limits viral association with the kinesin-1 motor, leading to strong attenuation, although IEV egress is not totally abrogated. The differential preferences for KLC isoforms might explain the changed dynamics and subsequent run lengths of the limited microtubule-based transport of ΔA36R and ΔF12L.

CHAPTER 5: Subcellular Transport of Ectromelia Virus

5.1 INTRODUCTION

The work detailed in this chapter has been published: H Lynn, J Horsington, LK Ter, S Han, YL Chew, RJ Diefenbach, M Way, G Chaudhri, G Karupiah, TP Newsome [2012]. *Loss of Cytoskeletal Transport during Egress Critically Attenuates Ectromelia Virus Infection In Vivo.* **Journal of Virology**. 86(13), 7427-7443. The deletion virus was generated by S. Han. Figure 5.6 panels A and B were generated by J. Horsington. H. Lynn carried out all other data generation and analysis.

5.1.1 Ectromelia virus

Ectromelia virus (ECTV), a member of the *orthopoxvirus* genus of Poxviridae, is the causative agent of mousepox. It was first isolated from infected laboratory mice in 1930 and this strain subsequently named the Hampstead strain [430]. Although the virus is predominantly identified in laboratory mouse populations, ECTV is also able to infect wild mice [431]. While some poxviruses such as VACV and monkeypox have a broad host range and can cause disease in many animal species, others including VARV and ECTV are very host specific [432]. ECTV is only able to cause disease in mice, with very large doses of virus required to cause subclinical infections in other animals including rats and rabbits [433].

After the initial isolation of the Hampstead strain, a variety of others were isolated and characterised, including Moscow (Mos), Naval, Ishibashi and NIH-79. Of these, Mos is the most commonly used laboratory strain, being both highly virulent and infectious [433, 434]. Depending on the route of inoculation and the mouse strain inoculated [**Section 6.1.2.2**], an extremely small amount of virus, between 0.3 – 4 plaque forming units (pfu) per ml are required to cause mortality in 50% of the infected population (referred to as the median lethal dose, LD50) within approximately 10 days [433, 435]. This high infectivity and virulence (as well as making mouse infection with ECTV Mos a pertinent disease model for smallpox [435] [**Section 6.1.3**]) has many experimental benefits, including the ease of inoculations and the ability to monitor disease progression to mortality within relatively short time frames.

The ECTV Mos genome has been sequenced and collated at The Viral Bioinformatics Resource Centre (http://athena.bioc.uvic.ca/). It is approximately 208 kb and encodes for 177 genes ([436], http://www.poxvirus.org/). There is very little genetic variance between different strains of ECTV, with ECTV Mos and ECTV Nav sharing 99.5% sequence identity [436]. Broadly, species across the orthopoxvirus genus share a large degree of genetic similarity, with the highly conserved central 100 kb of orthopoxvirus genomes displaying 90% sequence identity between all species [230]. At the more variable terminal regions of the genome, 12 out of 100 genes (including previously mentioned IEV proteins A56R and B5R) are present in all species. Phylogenetic analyses of these genes show low genetic distances of 0.0150–0.0354, with readings closer to 0 indicating more genetic similarity [230].

There is a wealth of knowledge on the pathogenesis of ECTV and the murine immune response to infection [**Section 6.1.2.3**]. Despite this, there is surprisingly little known regarding the cell biology of infection, with research until now focusing primarily on viral subversion of the immune system [437-439], the ubiquitin proteosome system [440, 441] and viral mediated syncytia formation [442].

While the replication cycle of ECTV has not yet been characterised, as with other orthopoxviruses, it has been presumed to follow that of the prototypal poxvirus VACV, due to aforementioned genomic similarity, as well as structural similarities between members of the genus. Structurally, ECTV virions are indistinguishable from other poxviruses by electron microscopy [433].

Preliminary studies on ECTV interaction with the actin cytoskeleton have been carried out [443, 444] [442] primarily in an attempt to identify actin-based motility as seen in other poxviruses VACV, MPXV and VARV [192, 264]. While it appears that actin-based motility is occurring, this has not been demonstrated definitively, nor has the mechanism and responsible ORF(s) been identified. Microtubule-based transport on the other hand has not been investigated, even phenotypically. We therefore aimed to elucidate mechanisms of viral mediation of subcellular transport, including interactions with the microtubule and actin cytoskeleton. This knowledge also provides us with a foundational framework to dissect the role of subcellular transport in animal model, which is investigated and discussed in Chapter 6.

5.2 RESULTS

5.2.1 Virus particles undergo microtubule-based transport during ECTV infection

Orthopoxvirus infection results in the formation of highly compartmentalised replication centres during productive infection. These replication centres can be identified using a combination of histological markers and stains. For example, the virus factory is positive for DNA stains such as DAPI and viral markers including p14 (A27) [163] but negative for IEV/EEV/CEV markers A36, A33, A34 and B5, which localise to the trans-Golgi network where IMV are wrapped to form IEV [191, 281].

Using a combination of stains and antibodies specific to VACV proteins found to cross-react with their ECTV homologues, we analysed BSC-1 cells infected with ECTV Mos at various time points post-infection. We looked for early hallmarks of viral replication, specifically the generation of the virus factory. The virus factory in poxviruses initially appears as a series of punctate sites in the perinuclear region that exclude host proteins and are surrounded by rough endoplasmic reticulum (RER). As viral crescents begin to form, the RER dissociates and a large compartment of low electron density (by electron microscopy) forms with the concurrent accumulation of viral DNA [249, 250, 445].

Using DAPI staining, we identified DNA positive virus replication sites with a characteristic punctate appearance and distribution through the cytoplasm early in infection that coalesced into a singular, more diffusely stained structure identified approximately 4-8 hours post infection (hpi). This was delayed comparatively to cells infected with VACV WR, where virus factories had formed in 20% of cells at 2 hpi [**Figure 5.1A**]. B5 expression was initiated at approximately the same time and was generally concentrated to a structure localised adjacent to the nucleus that may be a collapsed trans-Golgi network or early endosome [**data not shown and Figure 5.3B**]. Overall, ECTV infection closely resembles VACV infection, albeit slower by approximately 1.5-fold.

The perinuclear localisation of B5 expression indicates that ECTV IEV face a similar transport step for their delivery to the cell periphery. In VACV, this transport step is dependent on microtubule-based transport and we therefore tested whether the appearance of CEV/EEV required an intact microtubule cytoskeleton. With the exception of a few key proteins A33, A34 and A56 [**Figure 1.10**], CEV/EEV have identical viral markers as IEV, including B5. As previously mentioned, CEV/EEV are differentiated from IEV in immunofluorescence assays by applying α-B5 antibodies to cells that have not been permeabilised. As antibodies are too large to diffuse through intact cell membranes, only IEV that have reached the cell periphery and fused with the cell membrane to become CEV/EEV will be detected.

HeLa cells infected with ECTV produce large numbers of CEV/EEV 24 hpi [**Figure 5.1B**]. Treatment of cells with nocodazole, an agent that interferes with microtubule polymerisation and therefore disrupts microtubule-based transport, drastically reduced the appearance of CEV/EEV at the cell surface [**Figure 5.1B**]. Nocodazole was applied to infected cells at 8 hpi, chosen to correlate to our approximate observed IEV formation time frame. This nocodazole treatment therefore would not disrupt post-entry transport of incoming virus particles and formation of the virus factory that in VACV is also microtubule dependent [248], while preceding transport of IEV to the cell periphery. Washout of nocodazole allows microtubules to repolymerise thus restoring microtubule-based transport. Following washout of nocodazole, the appearance of CEV/EEV was restored [**Figure 5.1B**]. This confirms that similar to VACV replication, ECTV requires microtubule transport [263, 284, 287, 374].

In VACV, the molecular motor that mediates this microtubule-dependant transport is kinesin-1 [**Section 1.1.3.2, 1.3.1**] [181, 282, 286]. We therefore conducted immunofluorescence assays with a α-KHC antibody and colocalised the kinesin-1 heavy chain of the kinesin-1 motor complex to α-B5 labelled IEV particles [**Figure 5.1C**]. These B5-positive particles are IEV rather than non-virus vesicular B5 expression as they colocalise with a DAPI signal. IMV that stain positive for the DNA genome with DAPI while lacking a B5-positive membrane do not colocalise with the α-KHC signal, suggesting that it is an IEV specific protein or proteins recruiting kinesin-1. This suggests that the mechanism of microtubule transport is also conserved between ECTV and VACV [181, 282, 286, 290].

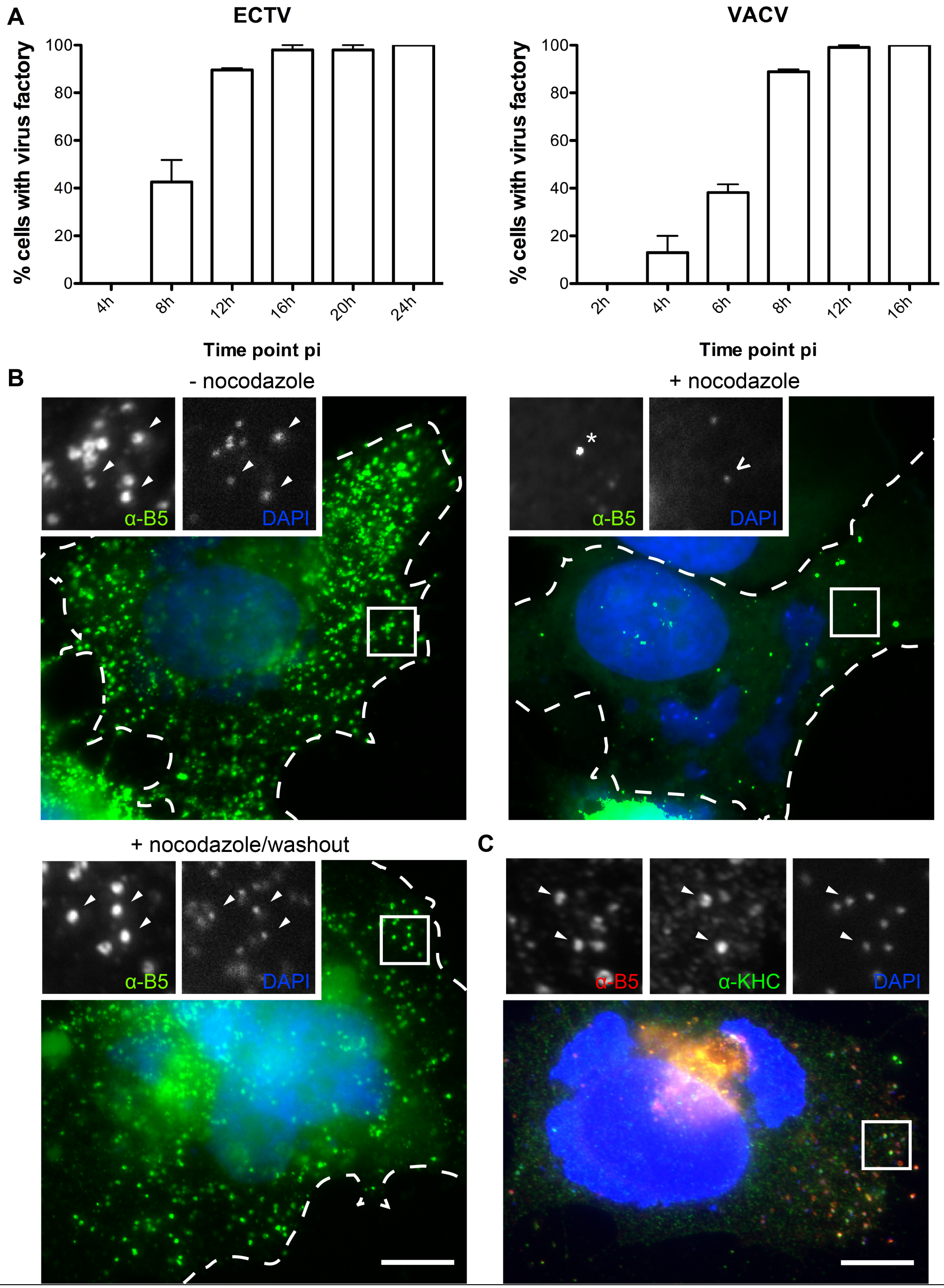

Figure 5.1: ECTV utilises microtubules for egress

(A) BSC-1 cells were infected with ECTV or VACV at MOI 1 and fixed at the indicated time points. Cells were stained with DAPI and assessed for the presence of a virus factory (n=50 per timepoint, in duplicate). The percentage of virus factory containing cells was calculated. Error bars indicate standard error. (B) HeLa cells were infected with ECTV and at 8 hpi 33 μM nocodazole was added to wells and either fixed 16 h later or washed three times in cell growth medium as a nocodazole wash-out control. Wash-out controls were allowed to incubate for an additional 24 h post wash-out before being fixed. Non-permeabilised cells (NPC) were stained for immunofluorescence assays with α-B5 (green) and DAPI (blue). The dotted line indicates the cell periphery, as determined by phase contrast microscopy. (C) HeLa cells infected ECTV, fixed and probed with α-B5 (red), KHC antisera (green) and DAPI (blue). Arrowheads indicate CEV. Asterisk indicates a B5-positive, DNA-negative particle, likely to be non-viral localisation of B5. Scale bars represent 10 μm.

5.2.2 Actin-based transport is active during ECTV infection

Having determined that an intact microtubule network is required during ECTV infection, we next investigated actin-based motility. Although it has been previously reported that ECTV stimulates actin polymerisation under virus particles [443], the mechanism involved in this process has not been well characterised.

Our first step towards this goal was to carry out immunofluorescence assays (IFA) of ECTV-infected cells of a variety of cell lines, including two murine lines; NIH3T3 and Mouse Embryonic Fibroblasts (MEFs). Virus-induced actin tails can be visualised by simultaneously labelling the virus particle and F-actin; they can be distinguished from other cellular F-actin structures as virus particles colocalise with the top of the actin tail and the tails characteristically taper at their tail end as F-actin depolymerises.

CEV were labelled with α-B5 in non-permeablised cells, followed by permeablisation and staining with either phalloidin, a phallotoxin that binds to F-actin, or an antibody targeted against cortactin a cellular protein that has weak actin nucleating activity in vitro but is best described as an actin bundling protein [446, 447]. No requirement for cortactin has been identified in VACV, but it has established roles in many processes including cell migration, invasion and endocytosis [448]. It is present in the cortical actin cytoskeleton but also localises to regions of active Arp2/3 complex F-actin nucleation.

We observed robust induction of typical orthopoxvirus-induced actin-based motility in all cell types examined with multiple visualisation techniques [**Figure 5.2**]. While we noticed distinct morphological differences between ECTV and VACV tails, we initially analysed the onset of actin tail formation in ECTV compared to VACV. A time course of actin tail formation revealed that tails were present in approximately 65% of ECTV-infected BSC-1 cells at 16 hpi and 100% at 24 hpi [**Figure 5.3A**]. In comparison, 50% of cells infected with VACV showed actin tails at 8 hpi, with 100% at 16 hpi. This approximately 1.5-fold delay in actin tail formation is consistent with the slower ECTV replication cycle as previously observed [**Section 5.3.1**].

Actin-based motility of VACV is dependent on recruitment of N-WASP to phosphorylated tyrosines on A36 (via the adaptor proteins Nck, Grb2 and WIP), which then locally stimulates activity of the Arp2/3 complex [292-298]. We first observed through immunofluorescence analysis of ECTV-infected cells that phosphorylated tyrosine localised to virus particles (as visualised by dsDNA stain DAPI) and the tip of actin tails [**Figure 5.3C**].

Based on the VACV actin nucleation cascade, we tested whether N-WASP was also required for ECTV induced actin-based motility. Infection of N-WASP knockout MEFs resulted in cells bereft of virus-associated actin tails, a phenotype that was rescued by transient expression of GFP-tagged N-WASP [**Figure 5.3D**]. Taken together, these results demonstrate that in addition to a high conservation at the genomic level, the replication of ECTV is highly conserved to that of VACV at the cellular level, although consistently slower. Like VACV, replication of ECTV includes transport of IEV that appears to be dependent on kinesin-1-mediated microtubule transport and N-WASP-Arp2/3 complex-dependent actin-based motility.

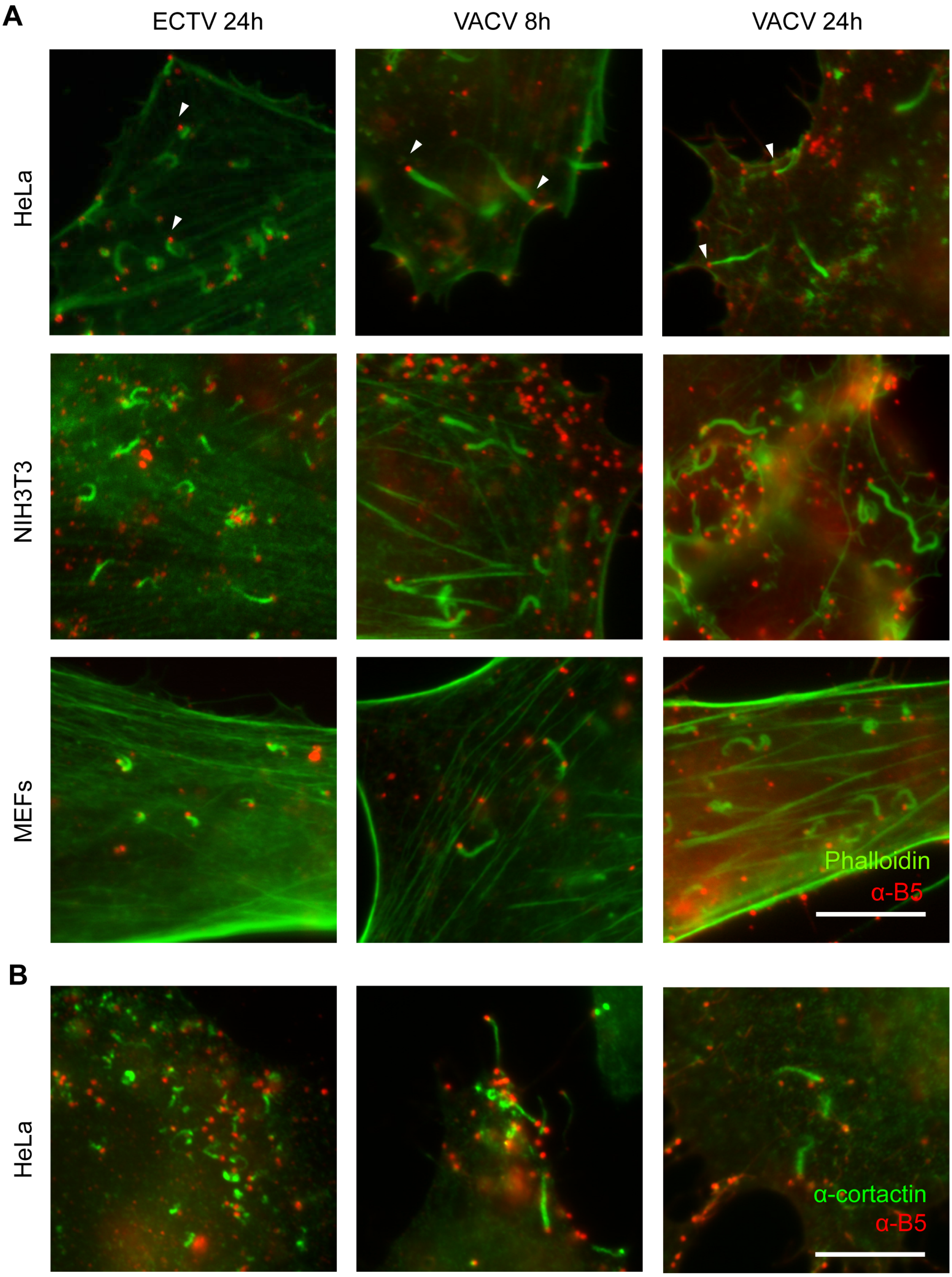

Figure 5.2: Actin-based motility of ECTV and VACV in various cell types.
(A) HeLa, NIH3T3 or MEFs were infected with ECTV or VACV, fixed and stained for immunofluorescence assays with α-B5 (NPC) (red), phalloidin (green) or (B) α-B5 (NPC) (red) and α-cortactin (green). Arrowheads indicate a CEV associated with an actin tail. Scale bars represent 10 μm.

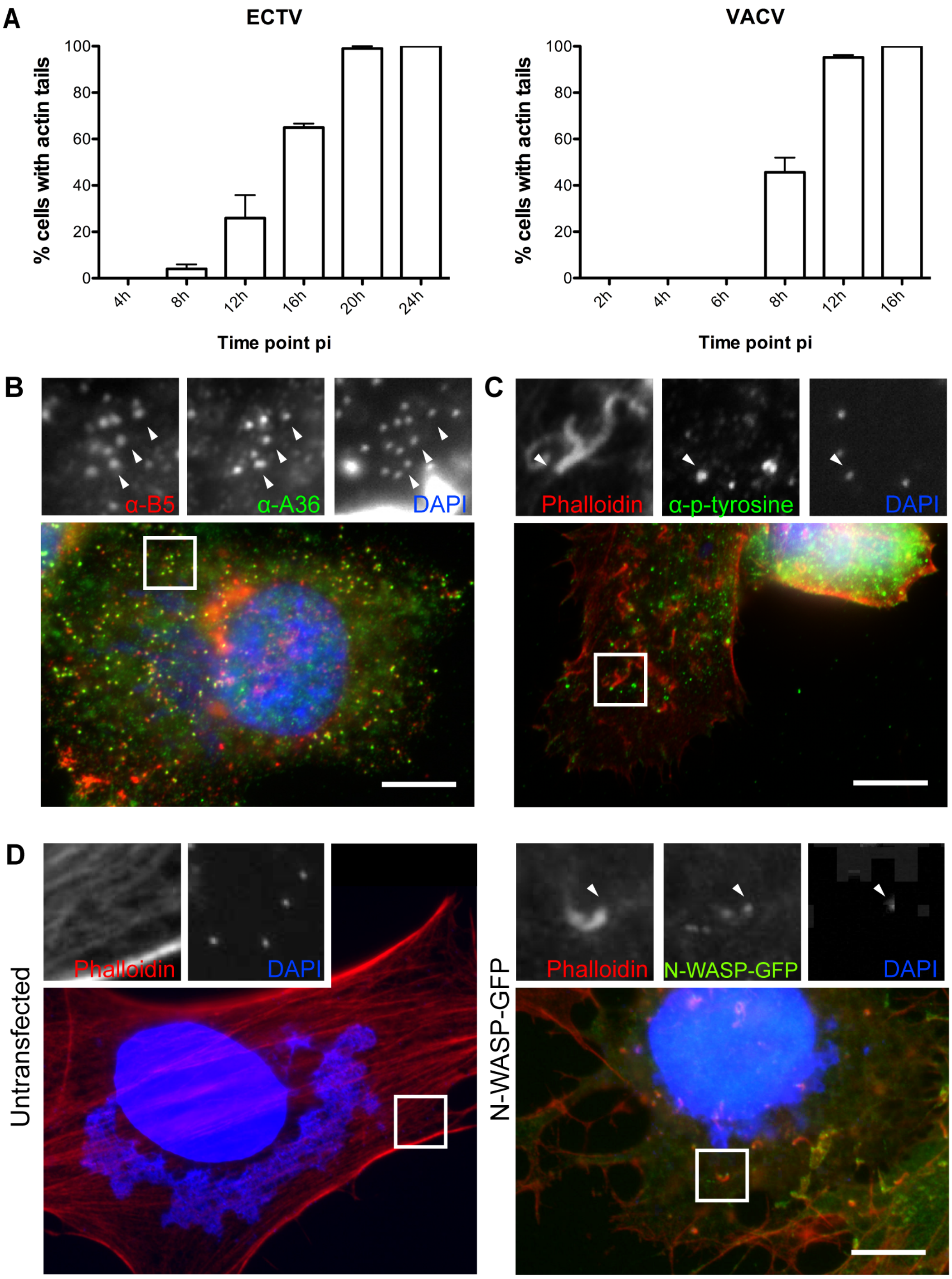

Figure 5.3: Actin-based motility of ECTV is via a N-WASP dependent pathway
(A) BSC-1 cells were infected with ECTV or VACV at MOI 1 and fixed at the indicated time points. Cells were stained with phalloidin and assessed for the presence of actin tails (n=50 per timepoint, in duplicate). The percentage of actin tail containing cells was calculated. Error bars indicate standard error. (B) ECTV-infected cells were also probed with α-A36-Y112 (green), α-B5R (red) and DAPI (blue) or (C) phalloidin (red), an anti-phosphotyrosine antibody (4G10, green) and DAPI (blue). (D) N-WASP$^{(-/-)}$ MEFs were mock-transfected or transfected with a N-WASP-GFP expression vector (green). Twenty-four h post-transfection, cells were infected with ECTV and fixed. For immunofluorescence assays, fixed cells were stained with phalloidin (red) and DAPI (blue). Arrowheads indicate IEV (B) or IEV associated with an actin tail (C, D). Scale bars represent 10 μm.

5.2.3 ECTV encodes a homologue of VACV protein A36

The IEV-specific viral transmembrane protein A36 is a critical mediator of both actin- [301] and microtubule-based transport of VACV [181, 282, 286] [**Section 1.3.1.3**]. We searched the ECTV (Moscow) genome for a homologue of A36 that might be responsible for subcellular transport of IEV during ECTV replication. We identified the ECTV open reading frame 137.5f as a candidate A36R homologue (which shall be referred to as ECTV A36R henceforth), consistent with previous findings [436]

ECTV A36R resides at a conserved genomic locus and encodes a hypothetical protein of 160 residues with 92% amino acid identity with the first 157 residues of VACV A36 [**Figure 5.4A**]. A 1 bp deletion in the nucleotide sequence leads to the formation of a premature stop codon and subsequent loss of homology from position 155 of ECTV A36 onwards and truncation of the C-terminus. Despite this predicted C-terminal truncation, the regions critical for actin-based motility (Tyr 112) [301] and the dominant interaction with kinesin-1 (WD 97-98) were conserved [181, 286]. While the ancillary interaction for kinesin-1 at residues 64-65 is WE motif in VACV A36, an amino acid substitution has resulted in a second WD motif in ECTV A36 that is unlikely to have an effect on kinesin-1 binding capabilities [286]. The ancillary site for actin-based motility (Tyr 132) was missing from ECTV A36.

Using antiserum raised against a peptide corresponding to residues 105-119 of VACV A36 (α-A36-Y112) we tested expression of ECTV A36 during ECTV infection in BSC-1 cells. Expression begins between 4-8 hpi, compared to 2-4 hpi for VACV A36, which displayed a faint band in the 4 hpi lysate. Migration on an SDS-PAGE gel indicated that ECTV A36 had an approximate size of 32 kDa, smaller than VACV A36, which migrates indicating a 43-50 kDa size [215] [**Figure 5.4B**]. Although both proteins migrated considerably above their predicted molecular weight, the discrepancy is consistent with the deletion in the 3’ of ECTV A36R ORF.

In DNA viruses, early and late gene expression refers to the expression of genes from the parental genome or expression that requires de novo mRNA synthesis, respectively [**Section 1.3.1**]. Poxviruses have further regulation resulting in an additional post-replicative phase preceding late gene expression called the intermediate phase [256]. Among other functions, early gene expression is essential for the establishment of replicative machinery responsible for DNA replication in the cell [257]. VACV A36 has an early component to its expression; it contains an early RNA start and termination sequence surrounding the ORF, and northern blotting of RNA extracted early in infection confirmed early transcription [215].

To test if the expression profile of ECTV A36 also had an early component, we performed VACV and ECTV infections in the presence of cytosine arabinoside (AraC), an inhibitor of DNA replication and late gene expression. A visible band was produced in both time points assayed; indicating that expression of ECTV was also under regulation by an early promoter [**Figure 5.4B**]. Using the same antibody as the immunoblot, immunofluorescence analysis of ECTV-infected cells was carried out. We observed that A36 localised to a perinuclear structure presumed to be the trans-Golgi network, due to the colocalisation of a strong, compartmental B5 signal. A36 also colocalised with B5 and DAPI at single virus particles, consistent with IMV-labelling [**Figure 5.3B**].

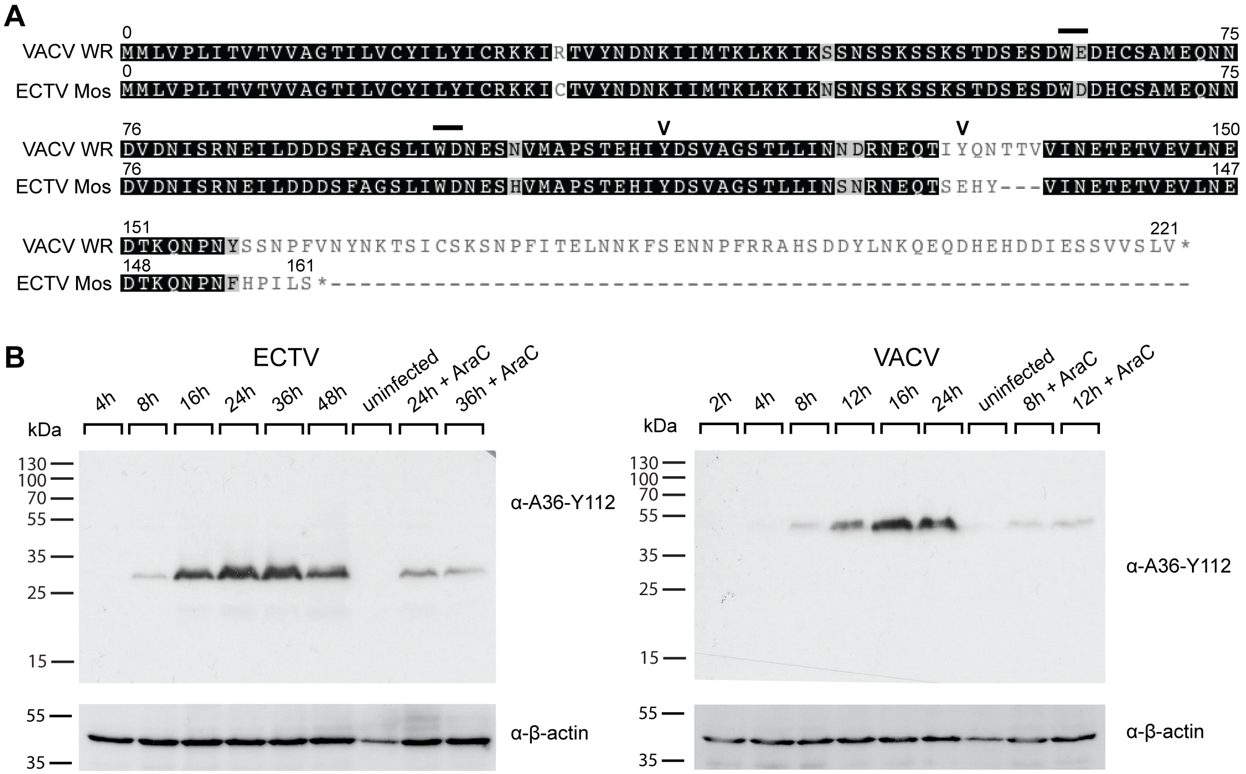

Figure 5.4: ECTV encodes a highly conserved homolgue of A36R

(A) Translations of open reading frames A36R in ECTV Mos (NCBI Genome Accession: AF012825) and A36R in VACV WR (NCBI Genome Accession: AY243312) obtained from www.poxvirus.org and aligned in Geneious 5.4.4 (Biomatters Ltd). Bars represent bipartite tryptophan domains for binding of kinesin-1 and microtubule-based motility. Chevrons represent tyrosine phosphorylation sites for actin-based motility. (B) BSC-1 cells were infected with ECTV or VACV at MOI 1 in the absence or presence of 40μg/ml AraC (Sigma) at the time points indicated. Cell lysates were separated with SDS-PAGE and transferred to nitrocellulose membranes for immunoblotting with α-A36-Y112, detecting ECTV or VACV A36. Immunoblots were also probed with α-β-actin as a loading control. Molecular size markers are indicated on the left.

5.2.4 Deletion of A36R results in defective subcellular transport

As ECTV A36R appeared to be a homologue of VACV A36 based on sequence conservation, expression and localisation, we sought to demonstrate that ECTV A36R was also required for actin- and microtubule-based motility. We generated a vector construct designed to replace the A36R ORF with selectable marker *gpt*, an *E. coli* gene that encodes xanthine-guanine phosphoribosyltransferase to allow growth on GPT selection media, and screenable marker monomeric red fluorescent protein (mRFP) from an artificial synthetic early/late promoter [308] [**Section 2.1.2.2**]. We recombined this construct with ECTV and selected for recombinant virus able to replicate in the presence of GPT selection media with visible red fluorescent plaques [**Section 2.4.2**].

After three rounds of purification, we tested the integrity of the ΔA36R recombinant virus with PCR analysis from extracted genomic DNA [**Figure 5.5A**]. A primer pair consisting of a forward and reverse primer complementary to a region approximately 900 bp upstream of the start codon and 900 bp downstream of the stop codon of the ORF respectively amplified a product of approximately 2300 bp, encompassing the ORF (486 bp) in the ECTV genome (a36r.rafor/a36r.larev, **Table 2.1**). In the ΔA36R recombinant virus, this product was approximately 3000 bp, consistent with the deletion of the ORF and insertion of the recombination cassette including *gpt* (152 bp) and mRFP (678 bp). When a second PCR was carried out with a forward primer complementary to the first 24 bp of the ORF with the same reverse primer (a36r.for/a36r.larev, **Table 2.1**), the ΔA36R virus genomic DNA did not produce a visible band, consistent with the predicted deletion of the ORF.

We next carried out immunoblots to confirm that A36 protein expression was abrogated in the ECTV ΔA36R virus. While a band was detectable in the ECTV-infected lysates probed with α-A36-Y112, no equivalent band was visible in ECTV ΔA36R-infected lysates [**Figure 5.5B**]. Reprobing this immunoblot with α-mRFP demonstrated robust expression of the screenable marker in ECTV ΔA36R-infected lysates, further validating the construction of the deletion virus. Of interest, when lysates were probed with antisera raised against the C terminus of VACV A36 (α-A36), the lack of a detectable band in ECTV-infected lysates is consistent with the absence of this region in the ECTV A36R ORF. This A36 protein abrogation was also reflected in immunofluorescence assays of ECTV ΔA36R-infected cells, where a A36 signal could no longer be detected [**Figure 5.5C**]. This is further confirmation that the predicted C-terminal truncation is present in the ECTV Moscow stock used in this study.

With the construction of ECTV ΔA36R verified, we went on to analyse replication dynamics and spread. We performed an EEV release assay in which we measured virus particles released by infected cells into supernatant at 32 hpi. Compared to the 3.93×10^3 infectious EEV produced by ECTV, ECTV ΔA36R demonstrated an approximately 50-fold reduction in release, with 8.53×10^1 infectious EEV produced [**Figure 5.6A**]. This was despite the total production of infectious virus (in both cells and supernatant) being unaffected by the A36R deletion [**Figure 5.6B**]. These results indicated that although normal levels of virus were being produced, IEV in ECTV ΔA36R were not reaching the surface of the cell to become EEV.

When we carried out plaque assays, ECTV ΔA36R were observed to produce small plaques with mRFP fluorescence [**Figure 5.6C**]. When measured, their average size was approximately half the diameter of those produced by the parental strain [**Figure 5.6D**]. Reduction in plaque size is consistent with compromised subcellular transport, as deficient viral transport to the cell periphery leads to retarded infection of neighbouring cells in the monolayer and subsequent inhibition of plaque formation. For example, in a VACV, recombinant viruses with A36R, A34L, B5R and F12L deletions have described defects in subcellular transport and a parallel reduction in plaque size [215, 303, 325, 449].

We next examined ECTV ΔA36R-infected cells by immunofluorescence for the hallmarks of microtubule- and actin-based transport. Loss of A36R resulted in a reduction in the appearance of EEV, and those that reached the cell surface were confined to central regions of the cell where the trans-Golgi network lies in close proximity to the plasma membrane [**Figure 5.7A**]. This phenotype was reminiscent of the defects seen in nocodazole-treated cells, consistent with disrupted microtubule-based transport [**Figure 5.1B**]. This was further confirmed by the lack of ECTV ΔA36R virus particle colocalisation with KHC compared to ECTV [**Figure 5.7B**]. Furthermore, we found that any virus particles that did reach the cell surface were unable to produce actin tails, demonstrating that actin-based motility was also abrogated [**Figure 5.7C**].

To confirm that these phenotypes were due specifically to the loss of A36 expression, we tested if transient expression of GFP-tagged ECTV A36R and A36R-Y112F could rescue any aspects of virus transport. While both constructs were able to rescue transport of IEV to the cell surface [**Figure 5.8A**], only A36R-GFP and not A36R-Y112F-GFP was able to rescue actin-based motility [**Figure 5.8B**]. This is consistent with previous findings made with VACV, where mutation of the critical Tyr 112 to Phe abrogates actin-based motility [292]. In summary, ECTV A36 is a functional homologue of VACV A36 and is required for efficient IEV intracellular transport and actin-based motility during ECTV infection.

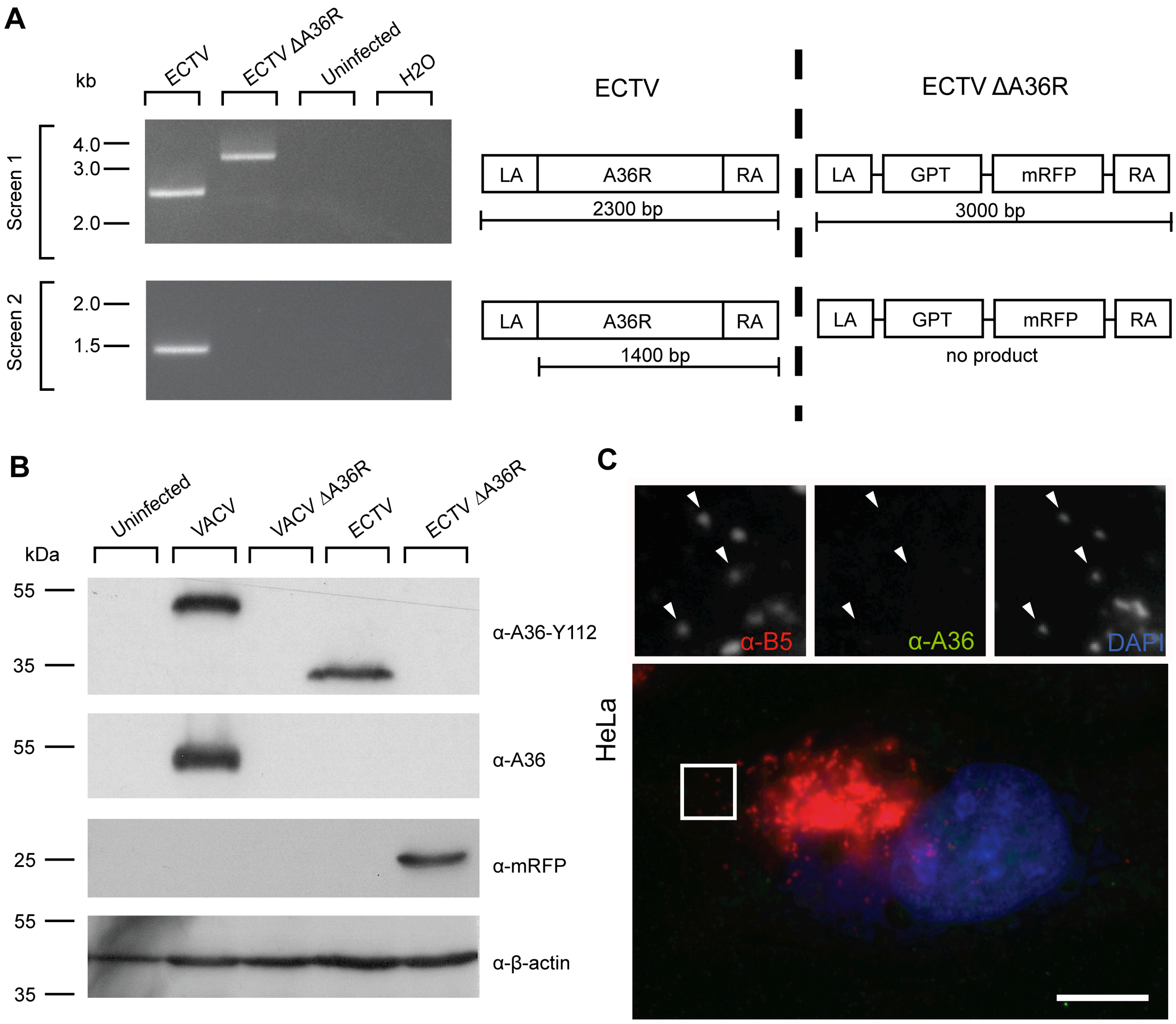

Figure 5.5: Construction and verification of ECTV ΔA36R.

(A) BSC-1 cells were infected with ECTV or recombinant ECTV ΔA36R and cell lysates collected at 48 hpi Genomic DNA was extracted and PCR was conducted with two primer pairs a36r.lafor/a36r.rarev and a36r.for/a36r.rev to confirm deletion of A36R and insertion of selection cassette. Uninfected cell lysate genomic DNA and no template control were run simultaneously as negative controls. Molecular size markers are indicated on the left. Schematic of the PCRs performed is represented on the right. (B) BSC-1 cells were infected with VACV, VACV ΔA36R, ECTV or ECTV ΔA36R at MOI 1 and cell lysates collected at 16 hpi (VACV) or 48 hpi (ECTV). Cell lysates were separated with SDS-PAGE and transferred to nitrocellulose membranes for immunoblotting with α-A36 (raised against the C terminus of VACV A36 that is absent in ECTV A36), α-A36-Y112, α-mRFP and α-ß-actin as a loading control. Molecular size markers are indicated on the left. (C) HeLa cells were infected with ECTV ΔA36R, fixed and stained for immunofluorescence assays with α-A36-Y112 (green), α-B5 (red) and DAPI (blue). mRFP expressed by ECTV ΔA36R was bleached by the addition of a high concentration of P-phenylenediamine [1% (w/v)] into mounting solution. Arrowheads indicate IEV. Scale bar represents 10 μm.

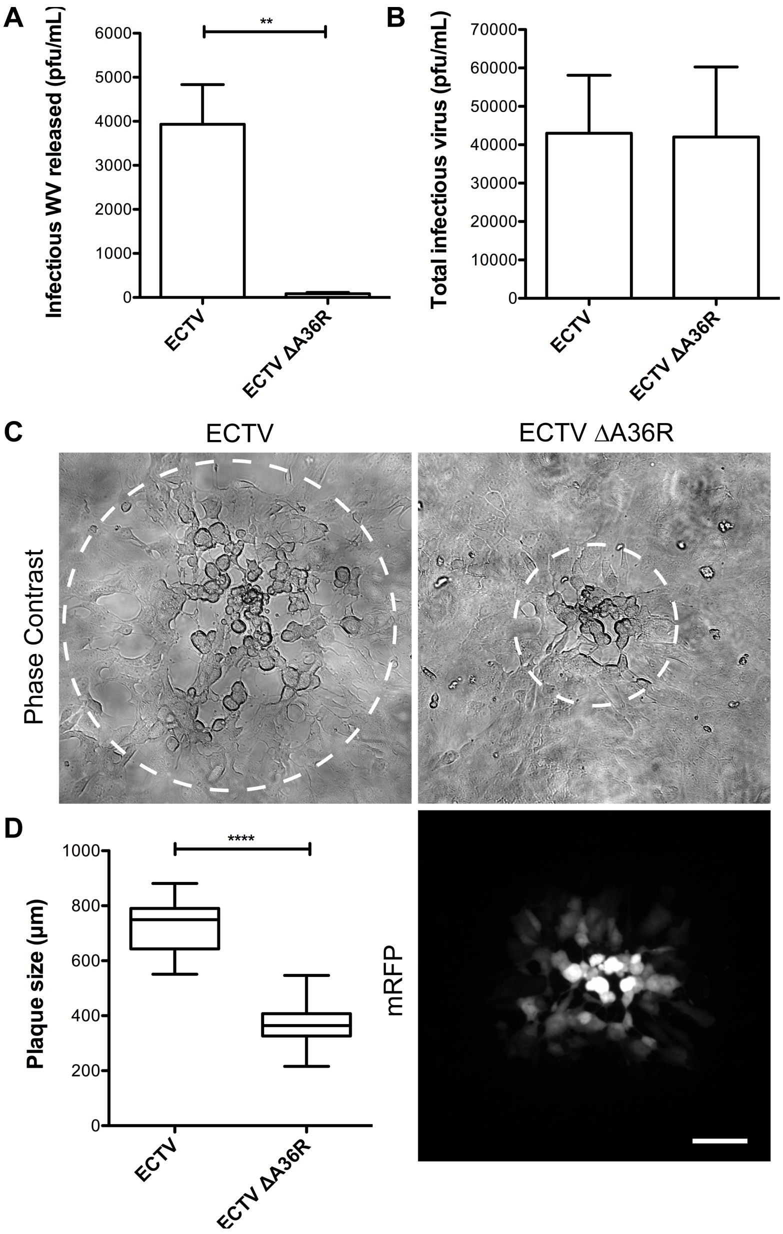

Figure 5.6: **ECTV ΔA36R results in reduced EEV release and virus spread.**
BSC-1 cells were infected with ECTV or ECTV ΔA36R at MOI 0.1 and (A) supernatants were collected at 32 hpi and centrifuged at 3350 rcf for 10 min to remove cells and cellular debris or (B) all cells were scraped into supernatants at 16 hpi before undergoing three freeze/thaw cycles to release viruses. Plaque assays were performed with BSC-1 monolayers overlayed with 1.5% CMC/DMEM and stained 5 dpi with crystal violet to quantify plaques. Differences between ECTV and ECTV ΔA36R were statistically different (p=0.0018, Unpaired *t*-test) for infectious EEV released, but not for total infectious virus. (C) BSC-1 cell monolayers were infected with ECTV or ECTV ΔA36R and overlayed with 1.5% CMC/DMEM. Four dpi, plaques were visualised with phase contrast microscopy (top panels) and fluorescent microscopy (bottom right panel). Scale bar represents 100µm. The diameter of plaques was determined in ImageJ as the widest point at which cytopathic effects were observed (circle). (D) Data from three replicates was pooled for n = 30. ECTV and ECTV ΔA36R were statistically different (p<0.0001, Unpaired *t*-test).

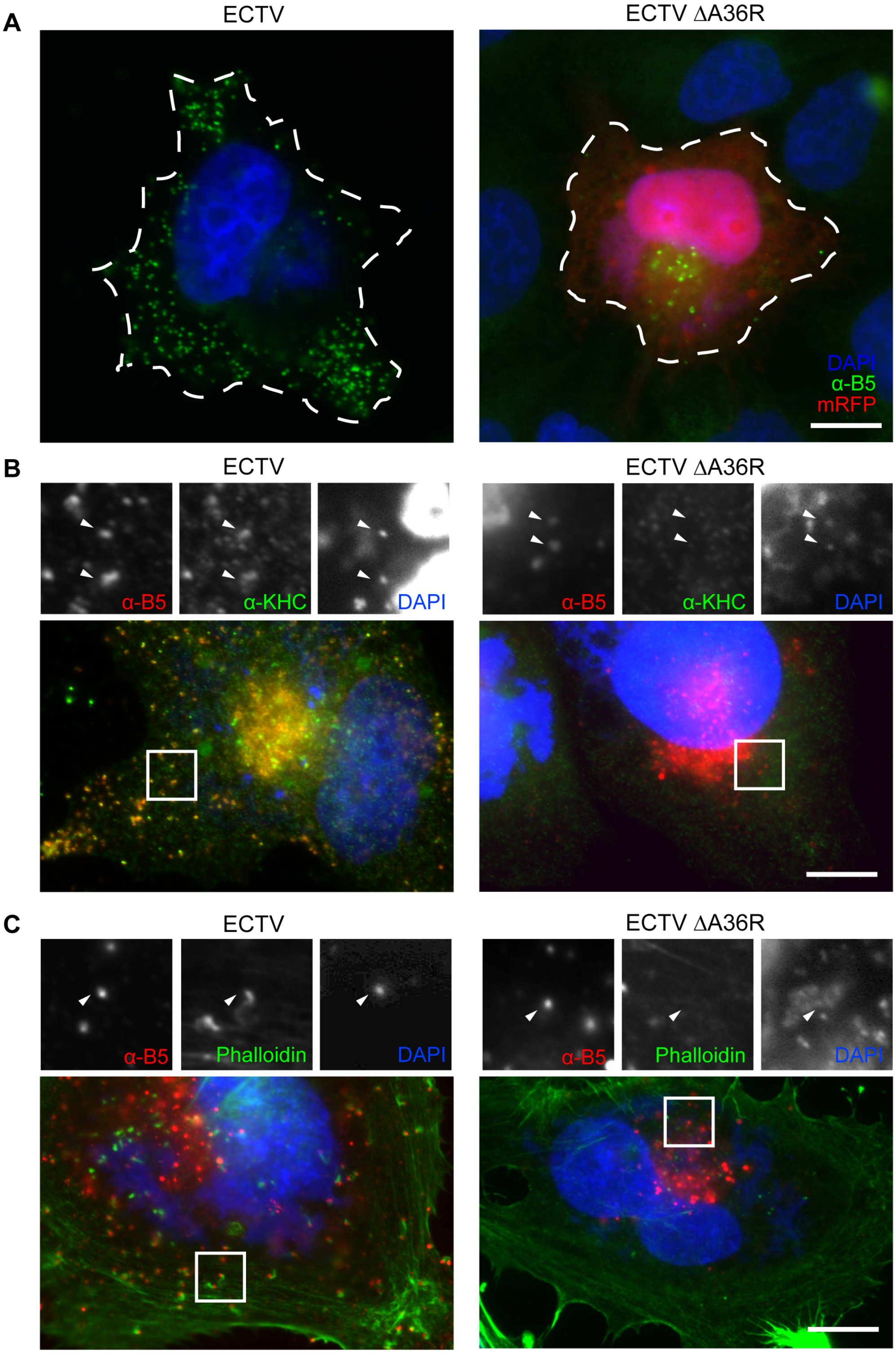

Figure 5.7: Deficient actin- and microtubule-based motility of ECTV ΔA36R.
(A) HeLa cells were infected with ECTV or ECTV ΔA36R, fixed and probed for immunofluorescence assays with α-B5 (NPC) (green) and DAPI (blue). The dotted line is the cell periphery, as determined by phase contrast microscopy. (B) Infected cells were also probed with α-B5 (red), KHC antisera (green) and DAPI (blue) or (C) α-B5 (NPC) (red), phalloidin (green) and DAPI (blue). mRFP expressed by ECTV ΔA36R was bleached by the addition of a high concentration of P-phenylenediamine [1% (w/v)] into mounting solution. Arrowheads indicate IEV. Scale bars represent 10 μm. The localisation in the cells depicted are representative of the large majority (99%) of infected cells.

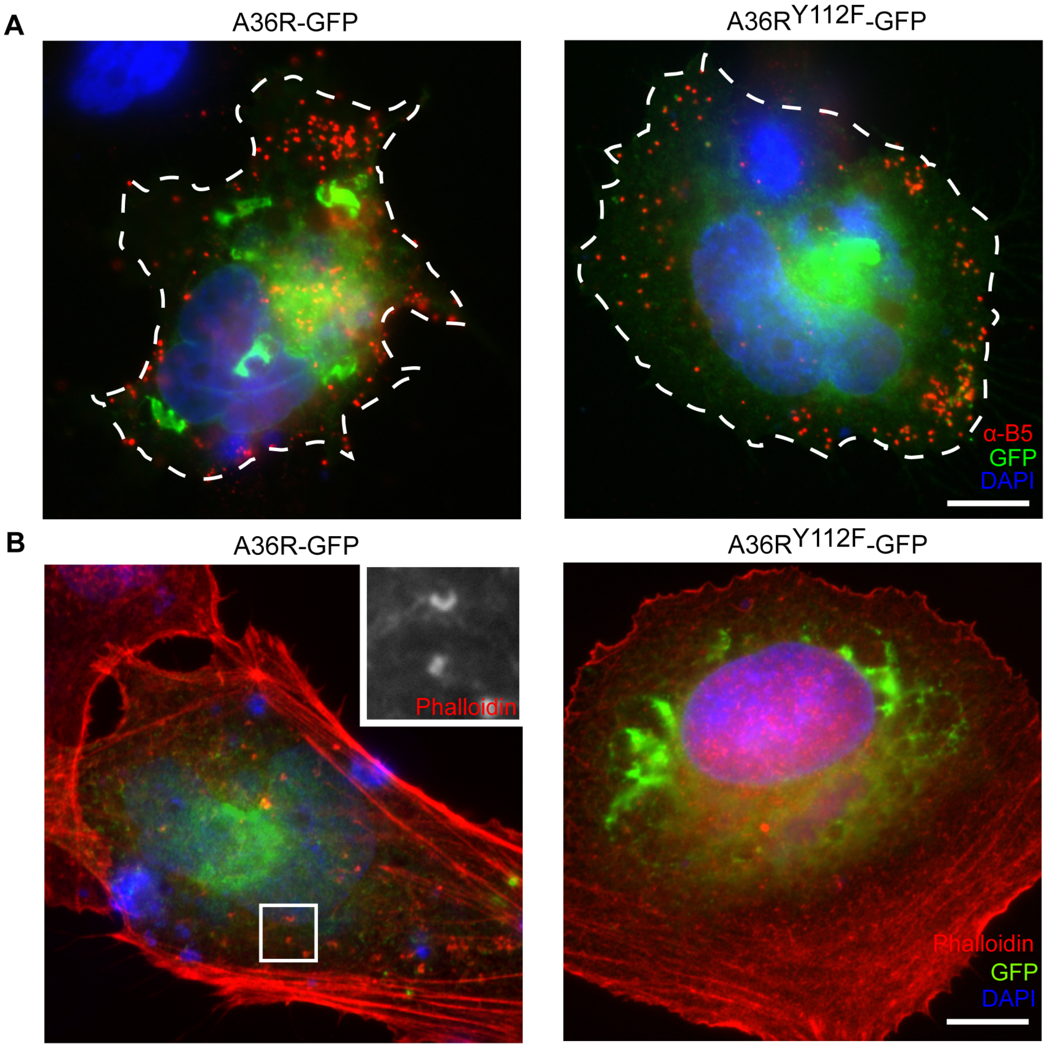

Figure 5.8: Transport defects of ECTV ΔA36R are restored by transient A36 expression.

(A) HeLa were infected with ECTV ΔA36R and transfected with vector constructs of A36R-GFP and A36Y112F-GFP (green) for transient expression under pE/L, fixed then stained for immunofluorescence assays with α-B5 (NPC) (red) and DAPI (blue). The dotted line indicates the cell periphery, as determined by phase contrast microscopy. (B) Infected and transfected cells were also probed with phalloidin (red) and DAPI (blue). Scale bars represent 10 μm.

5.2.5 ECTV actin tails display different morphology to VACV actin tails

As previously mentioned, we observed that actin tails that localised to EEV during ECTV infection had a divergent morphology to VACV tails being, on average, shorter in length (1.59 µm for ECTV and 2.88 µm for VACV, **Figure 5.10A**) and this difference was found to be statistically significant ($p<0.0001$, Unpaired t-test). The difference in actin tail morphology could be due to differences between the viral initiators (ECTV A36 and VACV A36) of actin polymerisation, in particular the C-terminal truncation, differences in other viral proteins or the time point at which actin-based motility was visualised due to the delayed ECTV replication cycle.

As VACV infected cells at 24 hpi retained the 'VACV-like' morphology [**Figure 5.2A**], we determined that the distinct morphologies of ECTV- and VACV-induced actin tails was not due to delayed replication dynamics. We therefore focused on testing the former hypotheses. We examined CEV-associated actin tails in VACV ΔA36R and ECTV ΔA36R infected cells transiently rescued with GFP-tagged VACV A36 and ECTV A36. Actin-based motility was rescued in all infection/transient expression combinations, with transiently expressed A36R-GFP colocalising to B5-positive CEV particles that formed actin tails [**Figure 5.9B-C**].

We went on to quantify the length of tails [**Section 2.5.5.1**] and found that VACV ΔA36R rescued with both GFP-tagged VACV A36 or ECTV A36 produced tails were not statistically different to VACV. This was not the case with ECTV ΔA36R; both construct rescues produced tails longer than ECTV, a difference that was statistically significant. While this was potentially due to overexpression of transient constructs, ECTV ΔA36R produced statistically shorter tails than VACV ΔA36R when rescued with either GFP-tagged VACV A36 or ECTV A36 (unpaired t-test, $p=0.0006$ and $p=0.0041$ respectively) [**Figure 5.10A**]. This verified that the difference in CEV-associated actin tail morphology is inherent to the background of the virus and not the identity of the viral initiator.

To further elucidate the phenotypic differences between VACV and ECTV actin-based motility, we carried out live cell imaging of infected cells and examined the speed and persistence of actin tails. This analysis revealed that differences in CEV-associated actin tail morphology did not lead to changes in the average speed of actin-based motility [**Figure 5.10B-C, Video. S1-2**]. We did however observe that there was more speed variation between individual actin tails produced by ECTV than VACV, with standard deviations of 0.050 µm/s and 0.018 µm/s, respectively. Furthermore, we found that ECTV-induced actin tails were visible for shorter periods of time compared to VACV; while 100% of VACV-induced actin tails visible at the start of imaging persisted for the duration of imaging (1 min 13 s), only 28% persisted over this time frame for ECTV [**Figure 5.10D**].

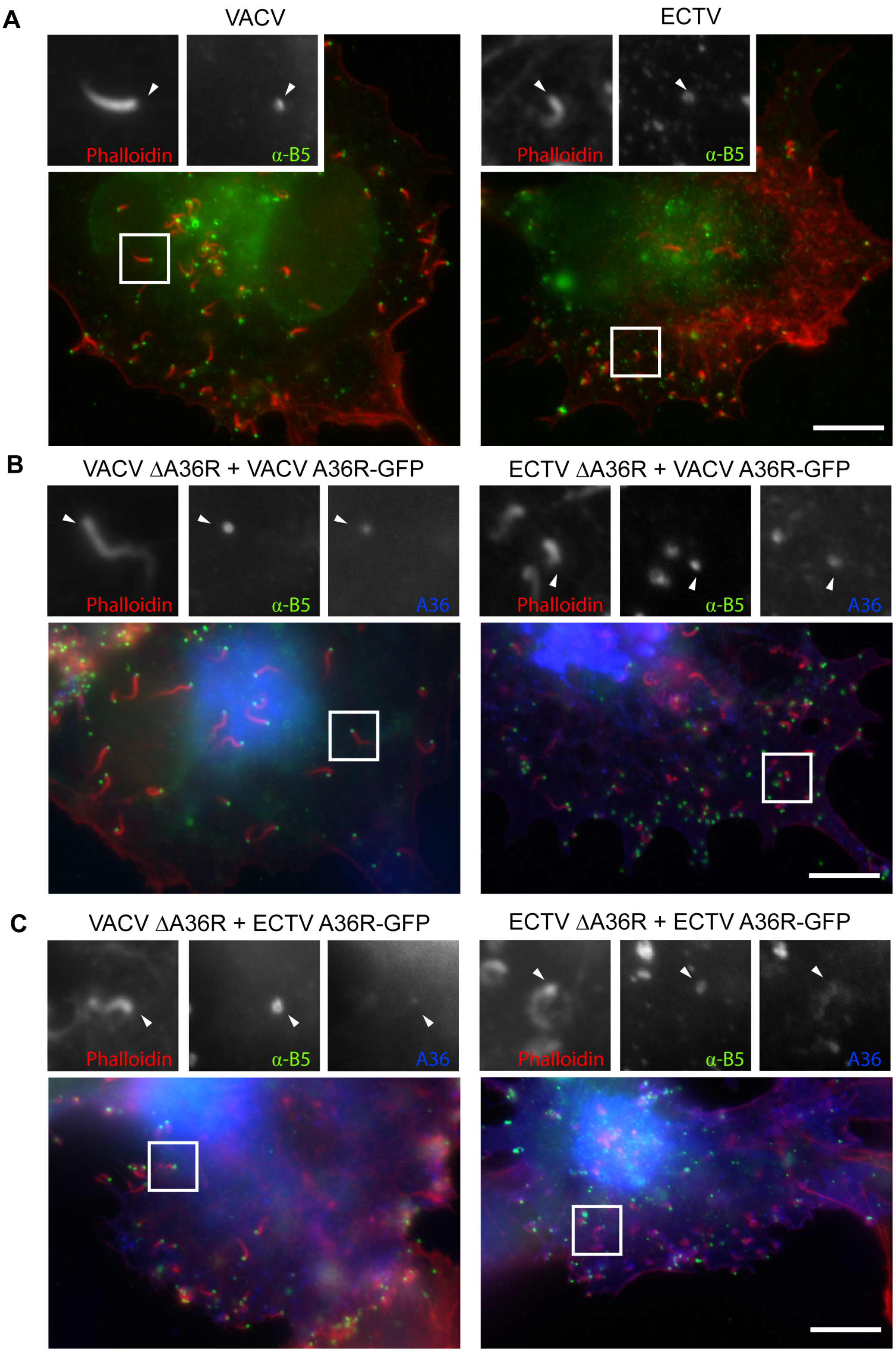

Figure 5.9: Actin-based motility rescued with transient VACV or ECTV A36R expression Representative cells of BSC-1 cells infected with VACV WR, VACV ΔA36R, ECTV Mos, ECTV ΔA36R and transfected with vector constructs containing VACV A36R-GFP (B) or ECTV A36R-GFP (C) for transient expression under pE/L. Cells were fixed and stained for immunofluorescence assays with α-B5 (NPC) (green) and phalloidin (red) to visualise actin tails. VACV A36R-GFP and ECTV A36R-GFP were visualised in the green channel, but have been represented in blue. Scale bars represent 10 µm.

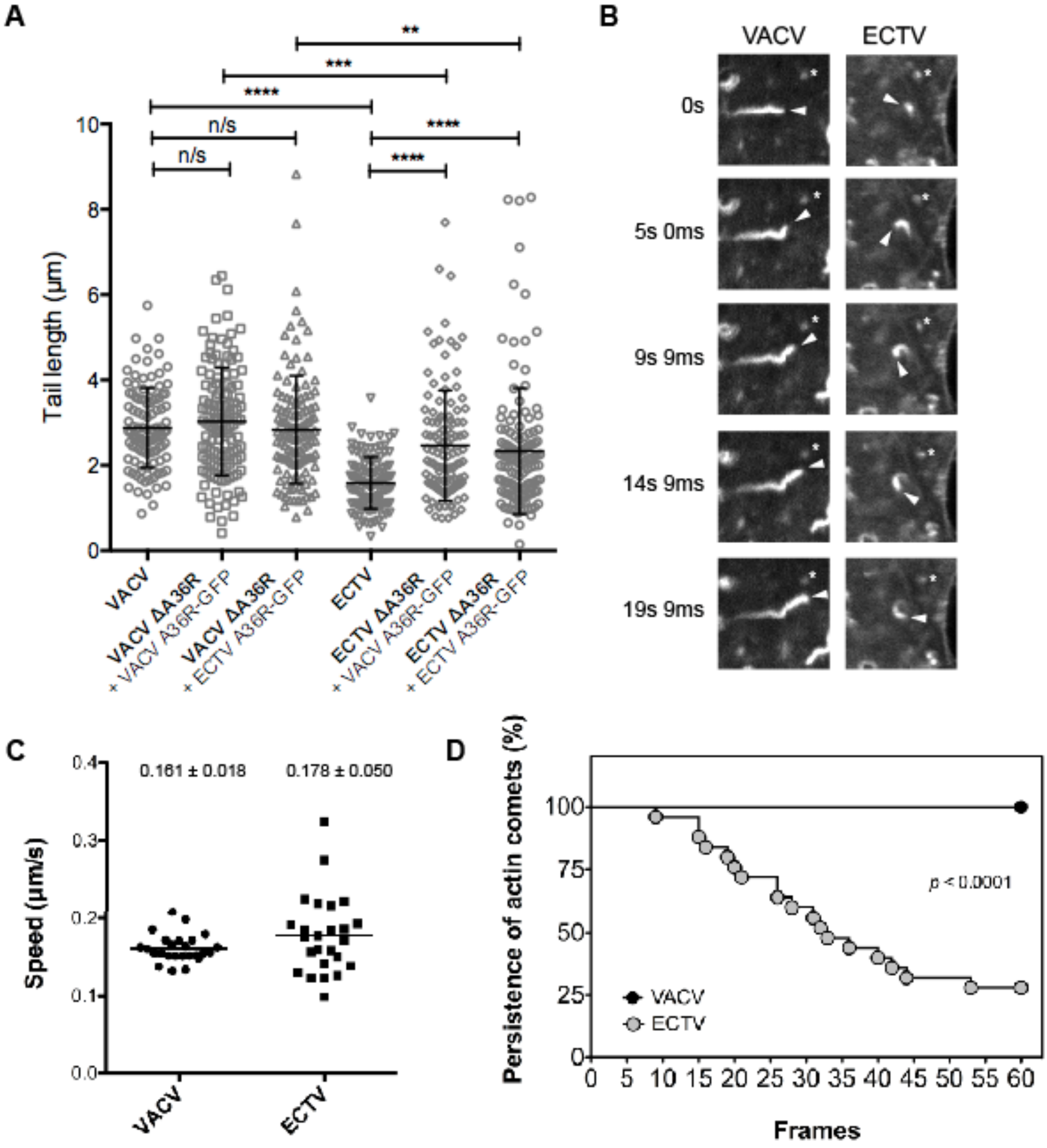

Figure 5.10: Characteristics of ECTV actin-based motility

(A) Tail lengths of 6 actin tails from at least 6 different cells (as shown in **Figure 5.9**) in three replicates (n=118) were measured in ImageJ and pooled. There were significant differences in tail lengths (n/s means not significant, **p<0.005, ***p<0.001 and ****p<0.0001, Unpaired *t*-test). (B) HeLa cells were infected with VACV or ECTV, transfected with pE/L Lifeact-GFP and imaged 8-10 hpi (VACV) or 24-26 hpi (ECTV). Arrowhead indicates tip of actin tail, asterisk indicates a stationary object. (C) Average speeds of actin tails in 5 different cells (n=25) calculated over 6 consecutive frames (3.7 s apart), with the Manual Tracker Plugin in ImageJ. (D) Percentage of actin tails in 5 different cells (n=25) that visibly persisted over 60 consecutive frames (1.2 s apart) of image acquistion, VACV and ECTV were statistically different (p<0.0001, Log-rank [Mantel-Cox] Test).

DISCUSSION

The ECTV Mos genome is highly conserved between related members of the orthopox genus, with approximately 90-99% identity at the amino acid level for IEV-specific proteins [436]. Our analysis of ECTV replication suggests the morphogenesis pathway that gives rise to IEV is also conserved. A subset of IMV generated at the virus factory acquires B5 and A36 immuno-reactivity and are transported to the cell periphery in a microtubule-dependent manner. We observed a delay in the replication of ECTV *in vitro* compared to VACV WR that was independent of cell type and origin of host cells. Although it might be expected that a virus of murine origin would replicate more efficiently, we were unable to find evidence to support this. At the minimum, other factors play a more significant role in the cells we analysed. The difference in replication dynamics may reflect adaptation by VACV to replication in cultured cells, as this delay is not apparent *in vivo* where infection of mice with either VACV or ECTV is lethal 6-8 days post-infection [215]. This interpretation is complicated by the absence of a known endemic host for VACV and differences in virus titer used to achieve a lethal dose.

Through immunoblot analyses, we observed that like VACV A36, ECTV A36 has an early component to its expression profile and alignments of the promoter region up to 100 nucleotides upstream of the open reading frames of the two genes showed 98% identity. The early expression of VACV A36 is believed to be important in repulsion of super infecting virions, a process which allows viral spread to occur at a rate beyond the speed of its replicative cycle [299]. Through cell surface signalling, viral entry into already infected cells is blocked and super infecting virions are directed toward uninfected cells [299]. Our results show that, as ECTV A36 is expressed early, it is possible that repulsion of super infecting virions also occurs in ECTV.

We have shown that the viral protein ECTV A36 plays a key role in mediating subcellular transport of ECTV, as has been shown previously for VACV A36 during VACV replication [181, 215, 263, 282, 286, 292, 300]. Divergent orthopoxviruses appear to encode functional homologues of A36 at conserved genomic loci and while these are highly conserved at the N-terminus they lack significant sequence conservation (8-15% amino acid identity) at the C-terminus [450]. ECTV A36 is consistent in displaying greater diversity at the C-terminus, in fact possessing the greatest extent of divergence amongst all available orthopoxvirus genomes with its predicted 63 residue C-terminus truncation.

Immunoblot analysis confirmed that ECTV A36R encoded a truncated protein. Nonetheless, it retains the essential transport functions of VACV A36 and possesses microtubule-based motility [**Figure 5.6-5.7**]. These observations are in agreement with a previous study in which microtubule transport of CEV is rescued in a VACV ΔA36R strain by the expression of the transmembrane domain of A36 fused to A36$^{71-100}$ suggesting that a KLC-binding site lies within this region [282]. This was further supported with yeast 2-hybrid assays demonstrating A36$^{81-100}$ was sufficient to mediate binding to KLC [181].

As previously mentioned, kinesin-1 recruitment (both KHC and KLC1 and KLC2) has been narrowed down to a bipartite tryptophan motif at residues 64/65 (WE) and 97/98 (WD) of VACV A36 [286], the second WD site which is within the A36$^{81-100}$ minimum binding domain established by Ward and Moss (2004). While ECTV A36 is conserved at the WD site, it has an amino acid substitution of another acidic residue at the WE site, creating a second WD site. Even though the sites are not absolutely conserved, a bipartite tryptophan domain is retained. In their study, Dodding and colleagues demonstrate that substitution of the WE/WD bipartite tryptophan motif with a WD/WD motif from Calsytenin retains kinesin-1 recruitment, and this substitution is unlikely to have any deleterious effects on microtubule-based motility. ECTV IEV particles were still found to partially colocalise with both components of the kinesin-1 motor complex, KHC and KLC [**Figure 5.7B** and data not shown] suggesting that microtubule transport of IEV is likely to operate via a conserved mechanism during ECTV replication [286].

Furthermore, although the exact role of the F12/E2 complex in microtubule motility of VACV remains to be clarified, as previously discussed, evidence suggests that it can interact directly with KLC2 and may have roles in modulating kinesin-1 motor activity [**Section 4.3**]. ECTV Mos possesses a highly conserved homolog to both VACV WR F12 (EVM035, Genbank accession: AAM92339.1) and E2 (EVM042, Genbank accession: AAM92346.1) that have 96.69% and 97.69% identity with their VACV WR homolog respectively, which may further suggest a conserved mechanism of microtubule-based motility.

Actin-based motility has been observed across the orthopox genus in VACV [264], ECTV (this study and [442-444]), VARV and monkeypox [192], as well as in more distantly related poxviruses such as myxoma virus [451] and yabalike disease virus [451-453]. In the closely related orthopoxviruses the nucleation of actin filaments is likely to be mediated by homologues of VACV A36, as we have demonstrated is the case in ECTV. Significantly, ECTV A36 is also the only orthopoxvirus homologue to lack the second tyrosine (Tyr 132) [450], nonetheless, ECTV A36 is sufficient to promote actin-based motility in ECTV and VACV [**Figure 5.9C**]. Interestingly, although the more divergent poxviruses do not encode A36 orthologues, the genomic locus where functional actin nucleators are encoded is conserved [452]. This study is only the third report defining the loss of actin-based motility in a recombinant virus deleted for the viral nucleator, along with VACV and baculovirus [193, 454].

We observed that ECTV-induced actin tails were morphologically distinct from those present during VACV infection, being shorter in length, a difference that was independent of the time point examined. The obvious explanation for these findings was the absence of the Grb2 binding site (Tyr 132), which when mutated to Phe blocks phosphorylation and Grb2 recruitment and results in shorter actin tails, increased virus motility and higher N-WASP turnover [293, 295].

However, although shorter, ECTV-induced actin tails were not faster than VACV-induced actin tails. This inconsistency was clarified through cross-rescue experiments with GFP tagged VACV A36 and ECTV A36. Although ECTV ΔA36R rescued with either construct led to tails statistically longer than ECTV, this was likely an artefact of transient expression and still resulted in tails shorter than those produced by VACV ΔA36R rescued with the same constructs. This indicated that the identity of the infecting virus and not the nucleator is likely responsible for the distinct actin tail morphology.

Following tyrosine phosphorylation of A36, actin tail formation in VACV infection is largely dependent on host cell machinery. The core cellular cascade involves Nck (recruited by A36^{Y112}), Grb2 (recruited A36^{Y132}), WIP, N-WASP and the Arp2/3 complex [292-298]. Infection with orthopoxviruses leads to disruption of many host-signaling pathways that impact on actin dynamics within the cell. Beyond the core cascade, other host proteins are recruited to virus-induced actin tails including cortactin, lamellipodin, profilin and VASP [455-459]. While the effects of many of these host-factors has yet to be determined, some have demonstrated roles in enhancing actin-based motility; depletion of the formin FHOD1 and the GTPase Rac1 (part of the same cell-signalling cascade) for instance leads to a decrease in the number and length of actin tails formed [460]. It is possible that host factors that impact actin dynamics are differentially stimulated by VACV and ECTV infection, but elucidation of the mechanism that defines the different rates of actin nucleation between VACV and ECTV must await future studies.

CHAPTER 6: Disrupting Subcellular Transport in an Endemic Animal Model

6.1 INTRODUCTION

The work detailed in this chapter has been published: H. Lynn, J. Horsington, L.K. Ter, S. Han, Y.L. Chew, R.J. Diefenbach, M. Way, G. Chaudhri, G. Karupiah, T.P. Newsome [2012]. *Loss of Cytoskeletal Transport during Egress Critically Attenuates Ectromelia Virus Infection In Vivo.* **Journal of Virology**. 86(13), 7427-7443. Mouse work and associated data analysis was carried out by our collaborators L.K. Ter, G. Chaudhri and G. Karupiah. H. Lynn was involved in design, planning and interpretation of experiments and provision of viral stocks.

6.1.1 The immune response

Even the most simple of animals possess some form of an immune system, which has evolved as as a defence against the challenge of pathogens. The immune response is divided into two arms, the innate immune system and adaptive immune system, although much interplay exists between both [461]. The innate immune system encompasses the immune responses that are immediate and non-specific and includes physical barriers, the inflammatory response, phagocytotic leukocytes and natural killer (NK) cells [461]. The adaptive immune system, which is exclusive to vertebrates, is antigen specific and acquired during the lifetime of the animal. It is composed of antibody-mediated humoral immunity generated by B-lymphocytes and cell mediated processes involving T-lymphocytes [462]. Due to the fact that the lymphocytes of the adaptive immune system must expand and mature following exposure to novel antigens, upon first exposure/primary infection, the response is not as immediate as the innate immune response [462].

6.1.2 ECTV Disease Progression

The natural route of infection of susceptible mice with ECTV is through skin abrasions; with virus able to enter the lower layers of the epidermis or dermis from external sources such as other infected animals or the environment [431, 434] [**Figure 6.1**]. Infection at the primary site of inoculation will then spread to the draining lymph nodes where viruses can be detected as early as 8 hpi. Replication occurs at the draining lymph node before entering the bloodstream to cause primary viremia that leads to the spread to organs, with high viral loads in the spleen and liver at 3-4 days post infection (dpi) [434]. Replication will again occur here and death of infected cells near sinusoidal vasculature releases large amounts of virus into the blood stream [237]. This secondary viremia leads to infection of distal sites in the body and ultimately, the formation of papules on the skin characteristic of poxviral diseases. At 5-13 dpi, virus is detected in most tissues and susceptible animals will succumb to the tissue necrosis of major organs [463].

Multiple factors contribute to the disease progression and severity of ECTV-caused disease, with mild, self-limiting disease in some animals and severe ulceration and death in others. These factors include the viral strain, the dose of the virus, the route of infection and the genetic background of the mouse being inoculated. As previously mentioned, the ECTV Mos strain is a commonly used due to its high virulence and infectiousness [433-435]. However, only some mice strains, including BALB/c, A/J and DBA/2, are susceptible to infection. Wild mice populations have variable susceptibility [464] and other common laboratory strains such as C57BL/6 are resistant to infection. These differences in susceptibility are due to well-characterised differences in the immune functions of these various strains, a fact that has been utilised to dissect immune factors that contribute to the control of ECTV infection.

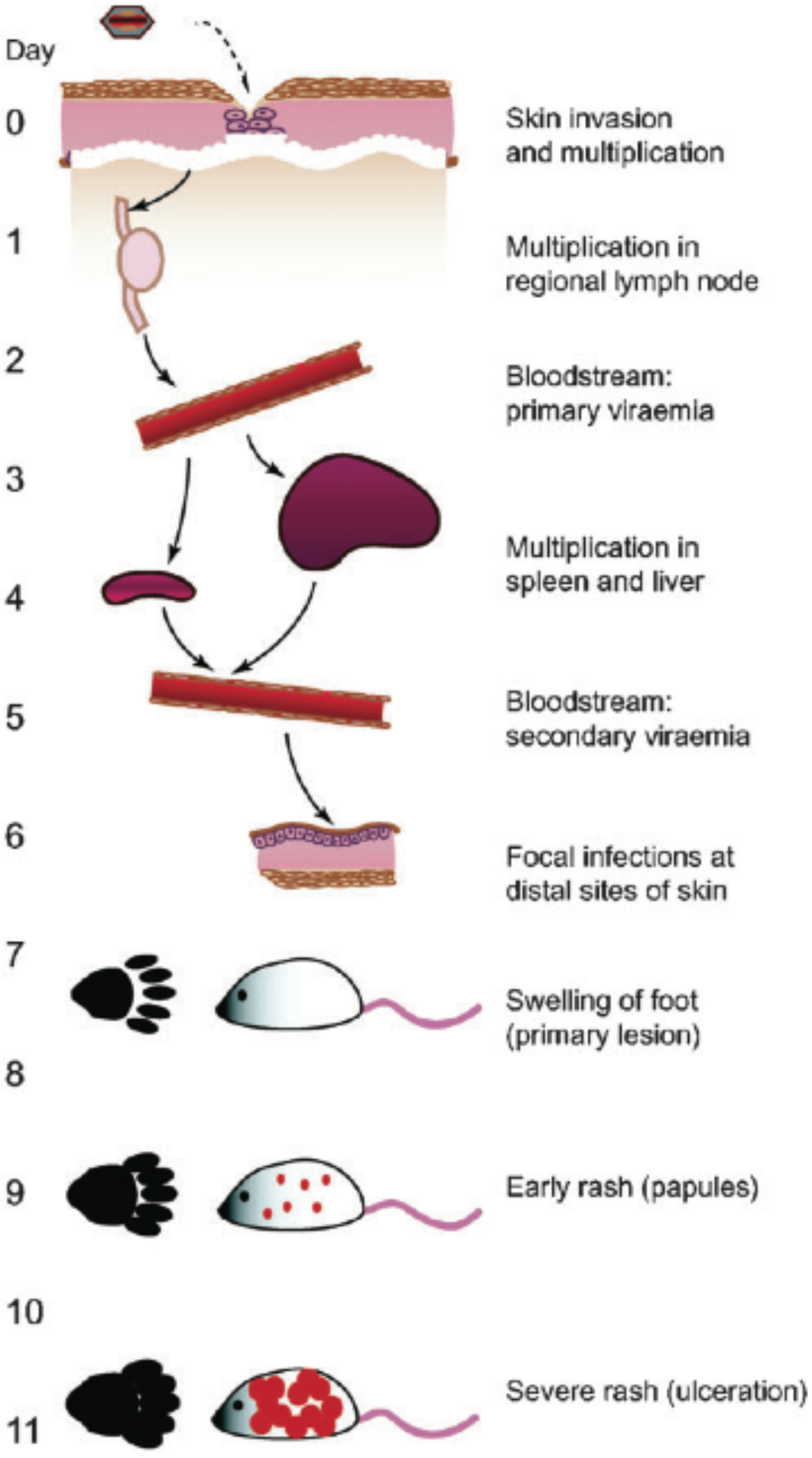

Figure 6.1: ECTV disease progression

ECTV disease progression in susceptible mice begins with viral entry through abrasions in the skin, viral dissemination then occurs through the lymph nodes, blood stream and major organs such as the liver and spleen. Secondary vireamia then leads to small pox like ulceration in its final stages, which is often fatal. Image from [434].

6.1.3 Immune response to ECTV infection

As ECTV infection occurs through abrasions in the skin, the initial immune response against ECTV involves specialised cell types present in the skin for responding to invading pathogens that include keratinocytes, melanocytes, Langerhans cells (LC) and dendritic epidermal T-Cells (DETCs) [434]. Keratinocytes will be activated by the inflammatory response generated in response to skin trauma and are then able to recognise viral components through Toll-like receptors (TLRs) and other pathogen-assocated molecular pattern recognition receptors. TLR signalling leads to the stimulation of the antiviral response including production of interferon (IFN) [465]. The production of these first waves of cytokines leads to signalling cascades that activate downstream effectors of both the innate and adaptive immune system that contribute to control of ECTV infection. For instance, cytokine activated LCs containing viral antigens migrate through the dermal layers to reach the lymph node where they can then present antigens to naïve T and B-lymphocytes [434].

While the B-lymphocyte generated humoral response to ECTV infection may contribute to complete recovery or protection upon reexposure, control of primary infection requires cell-mediated immunity, including a polarised type 1 response [329, 331]. Type 1 responses are defined by strong cellular immune responses, specifically helper type 1 (Th1) lympocytes secreting cytokines such as interleukin-2 (IL-2), IFN-α and IFN-γ that amplify phagocytic activity [466]. Type 2 responses on the other hand involve Th2 lymphocytes secreting a different suite of cytokines including IL-4, IL-5, IL-10 and IL-13 to stimulate the humoral response with an associated high antibody production [466]. A polarised type 1 response with associated cytotoxic T lymphocyte (CTL) response was observed in resistant C57BL/6 mice, while susceptible BALB/c and A/J mice displayed a type 2 response with limited CTL activation [329]. NK cells have also been demonstrated play important roles in the recovery from infection [467, 468]. As a part of cell-mediated immunity in the innate immune system, they are involved in the early control of ECTV and are activated rapidly following ECTV infection [329, 468, 469].

6.1.4 ECTV an effective model of infection processes in an endemic host

Due to the hazards and limited host range of working with VARV and the unknown host and origin of VACV, ECTV infection in mice has been used extensively as a model for smallpox infection [434, 435]. There are many similarities between infection and disease progression in both systems. Like VARV in humans, ECTV causes a characteristic exanthematous rash in the final stages of disease progression and although the progression of this stage to death occurs approximately 2-3 times faster in ECTV infection of mice, the high virulence of ECTV causes mortality rates that mimic the 40-90% seen in smallpox outbreaks [237, 470, 471].

Secondly, while ECTV is naturally transmitted by abrasions in the skin, intranasal models of infection can be used to model large droplet transmission of VARV in humans [435, 472, 473]. Like VARV, the lung is not involved in early infection and prior to the exanthematous rash in the pre-exanthem period, virus is detectable in respiratory gases [471, 474]. Futhermore, relatively small inoculums, often less than 1 pfu will cause an LD50 in susceptible animals, although it is unknown the exact inoculum of VARV required to cause similar disease in humans, it is believed to be low [433, 435, 470]. In comparison, intranasal infection of mice with CPXV requires inoculums of over 10^6 pfu to cause disease with an LD50 [475].

Beyond its effectiveness in modelling smallpox, the use of a model in mice provides many advantages. Conducting experiments with a small animal presents relative technical ease, and the restricted host range of ECTV limits biosafety concerns. Moreover, the mouse immune system has been extensively characterised, and the similarities and differences between the mouse and human immune system are well understood (reviewed in [476] and [477]. The various advantages of the mouse infection model therefore afford us the opportunity to address the contribution of subcellular transport pathways to virulence in an endemic host.

6.2 RESULTS

6.2.1 ECTV ΔA36R is attenuated *in vivo*

Having demonstrated that A36R plays a conserved role in directing the subcellular transport of ECTV, we examined the effects of disabling this motility on infection of the ECTV-susceptible BALB/c mouse strain using three different doses of virus. In the group that received the lowest dose of 10^2 pfu ECTV, 10 of 15 mice (66%) succumbed to mousepox and died by 18 days dpi [**Figure 6.2A**]. Mice that had survived past day 18 developed pox lesions on their tails that ulcerated with time and were therefore euthanised at 28 dpi for ethical reasons. Animals in the groups infected with 10^3 (n=7) or 10^4 pfu (n=6) of ECTV succumbed to mousepox with 100% mortality, with a mean time to death of 11.1 and 8.8 days, respectively. All mice infected with ECTV had unkempt hair coat and hunched posture from about day 6 pi and generally became moribund before they died. In contrast, mice infected with the 3 different doses of ECTV ΔA36R survived until at least 33 dpi with no overt clinical signs of disease [**Figure 6.2A**].

Organism-wide dissemination of virus was clearly affected by deletion of A36R. The viral load in the draining lymph nodes, spleen and liver at 5 dpi was 3 to 4 $\log_{10}$ pfu higher in mice infected with 10^2 pfu ECTV than in those infected with ECTV ΔA36R [**Figure 6.2B**]. This difference further increased to 5 $\log_{10}$ pfu at 8 dpi due to the increasing viral load in all organs of ECTV infected mice and decreasing viral load in all organs of ECTV ΔA36R infected mice [**Figure 6.2C**]. While ECTV infection is lethal in BALB/c mice, ECTV ΔA36R infection is readily controlled, showing strong attenuation *in vivo*. This attenuation was also evident in C57BL/6 wild type [data not shown] and C57BL/6 Rag-$1^{-/-}$ mice, which lack B or T cells, and therefore do not possess adaptive immunity [**Figure 6.2D**]. Titers of ECTV ΔA36R were between 1 to 4 $\log_{10}$ PFU lower than those of ECTV at 5 dpi. We were unable to determine viral load in organs of Rag$1^{-/-}$ mice at 8 dpi as all mice infected with ECTV had died by this time whereas those infected with ECTV ΔA36R were still alive with no clinical signs of disease.

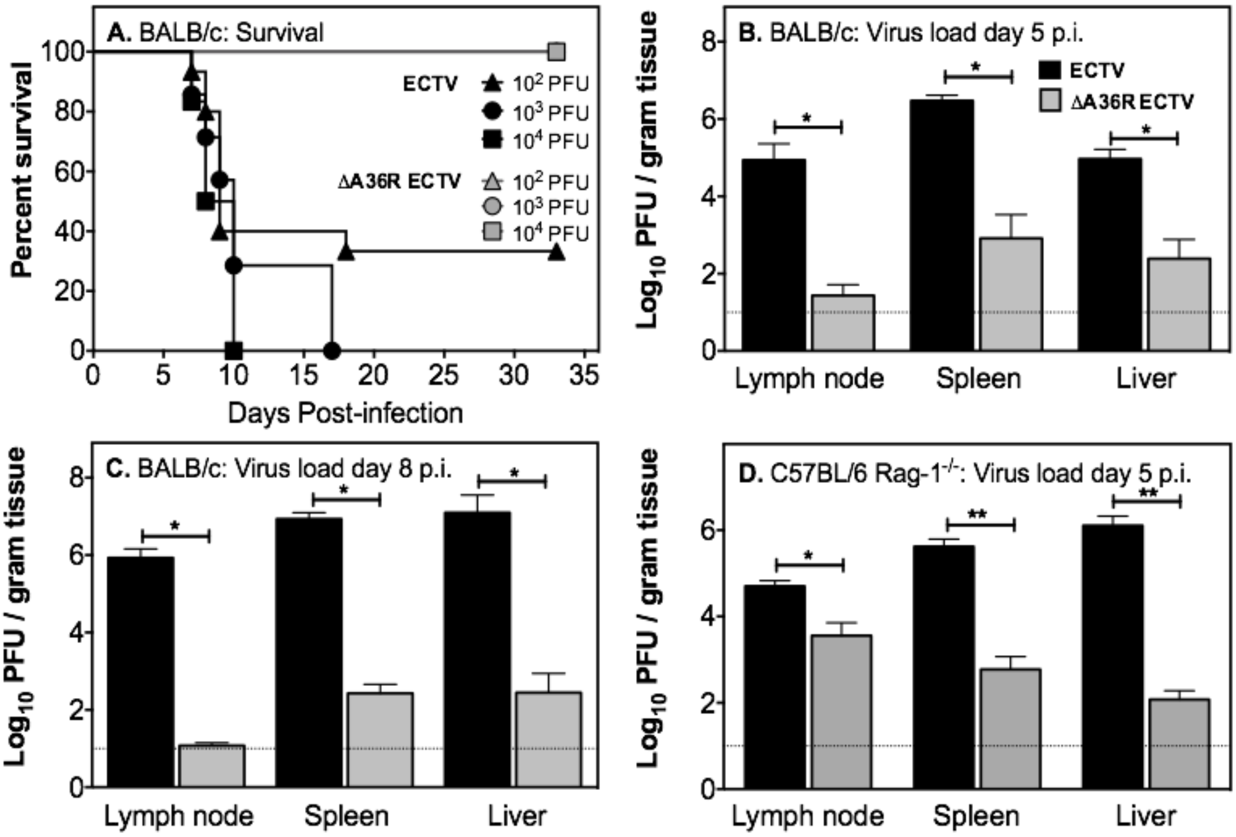

Figure 6.2: **Virulence of ECTV ΔA36R in mouse infections.**

Groups of 6-15 female BALB/c mice were infected subcutaneously in the left hind leg with 10^2, 10^3 or 10^4 pfu ECTV or ECTV ΔA36R. Mice were monitored for (A) survival over 33 days. Survival for 10^2 and 10^3 pfu ECTV ΔA36R were 100%. There were significant differences in survival of mice infected with ECTV or ECTV ΔA36R ($p<0.0001$ at 10^2 and 10^3 pfu and $p<0.001$ at 10^4 pfu, Log-rank [Mantel-Cox] Test). Data shown for the 10^2 dose of virus has been combined from 2 different experiments. Separate groups of mice were infected with 10^2 pfu virus and euthanised at (B) 5 or (C) 8 dpi and the viral load in lymph nodes, spleens and livers was quantified by viral plaque assays. Groups of 5 C57BL/6 Rag-$1^{-/-}$ female mice were infected with 10^3 pfu ECTV or ECTV ΔA36R and euthanized at (D) 5 dpi and the viral load in lymph nodes, spleens and livers was quantified by plaque assays. Titers of ECTV and ECTV ΔA36R in lymph nodes, livers and spleens were significantly different (*$p<0.05$, **$p<0.01$, Mann-Whitney test). Data shown in B, C and D are viral load ± SEM. The horizontal dotted lines indicate the limit of detection of the viral plaque assay, which is 1 $\log_{10}$ pfu.

6.2.2 NK response

The finding that ECTV ΔA36R titers were significantly lower compared to those of ECTV even in C57BL/6 Rag-1$^{-/-}$ mice early during the course of infection suggested that either the virus replicated poorly *in vivo* or that the innate immune system effectively controlled virus replication. As mentioned, since NK cells play a key role in controlling ECTV, we assessed the cytolytic activity of NK cells in virus-infected BALB/c and C57BL/6 wild type mice at 5 dpi, the peak of the NK cell response. The NK cell activity induced by ECTV ΔA36R was more than 3-fold lower in BALB/c mice and at least 27-fold lower in C57BL/6 mice than the activity that was generated by ECTV infection in both strains of mice [**Figure 6.3A-B**]. The data suggested that it is unlikely that NK cells contributed to the early control of mutant virus replication.

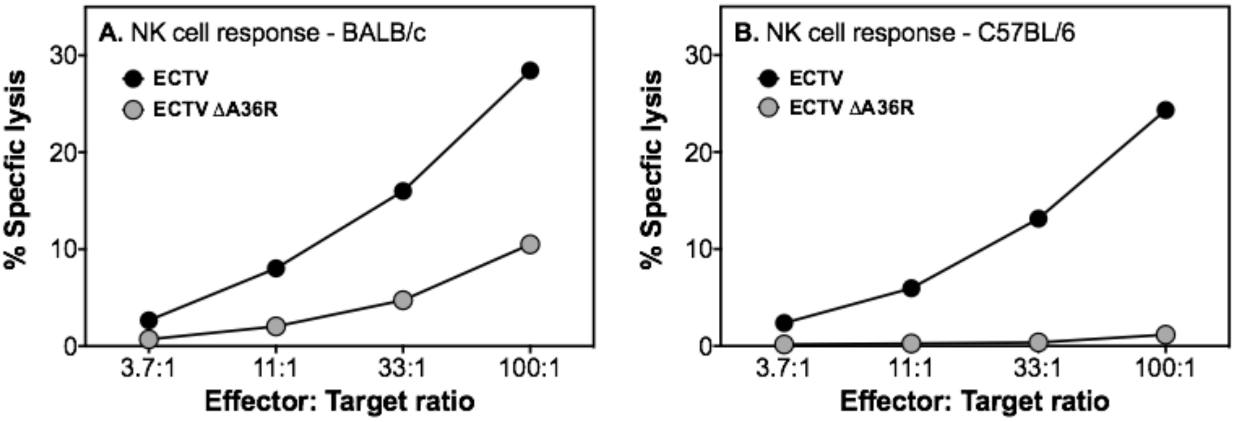

Figure 6.3: NK responses to ECTV and ECTV ΔA36R infection

Splenic NK cell responses were measured by the ^{51}chromium release assay. Groups of 3 (A) BALB/c and (B) C57BL/6 mice were infected with 10^{3} pfu of ECTV or ECTV ΔA36R virus. Spleen cells were extracted and cultured with ^{51}Cr-labelled YAC-1 target cells for 4 h and the radioactivity in the supernatant measured in a TopCount NXT™ scintillation counter to give a measure of lysis.

6.2.3 ECTV ΔA36R infection induces protective immunity

We determined whether ECTV ΔA36R, which replicated poorly in mice, induced any protective immunity to ECTV. All mice that had survived infection with either 10^2, 10^3 or 10^4 pfu ECTV ΔA36R were challenged with a lethal dose (10^4 pfu) of ECTV at 33 dpi. Eight days later, mice were sacrificed, their spleen, liver and lymph nodes collected for determination of viral load whereas the serum was used to measure anti-ECTV antibody titers. Splenocytes were used to measure the recall anti-ECTV-specific CTL response.

Virus was below the level of detection in spleen, liver and lymph nodes in mice challenged with a lethal dose of ECTV [data not shown], indicating that a primary infection with all 3 doses of ECTV ΔA36R induced protective immunity against a subsequent lethal virus challenge. Recall anti-ECTV CTL responses were generated in all groups at near comparable levels in magnitude [**Figure 6.4A**].

Since antibody plays a critical role in recovery and virus control during both primary and secondary ECTV infection [330, 478], we measured virus-specific antibodies in sera obtained from mice infected with ECTV ΔA36R during primary infection and subsequent secondary challenge. ECTV-specific IgG was clearly induced during primary (14 and 28 dpi) infection with ECTV ΔA36R and 8 days post-challenge with ECTV [**Figure 6.4B**]. Antibody titers were augmented as the virus inoculum dose was increased. It was also evident that as the antibody response matured over time (i.e. between 14 and 28 dpi), the anti-ECTV IgG titers also increased. In addition, IgG titers were boosted further in all groups following secondary virus challenge. ECTV ΔA36R generated neutralizing antibodies during a primary infection, and neutralising titers increased substantially after the secondary virus challenge [**Figure 6.4C**].

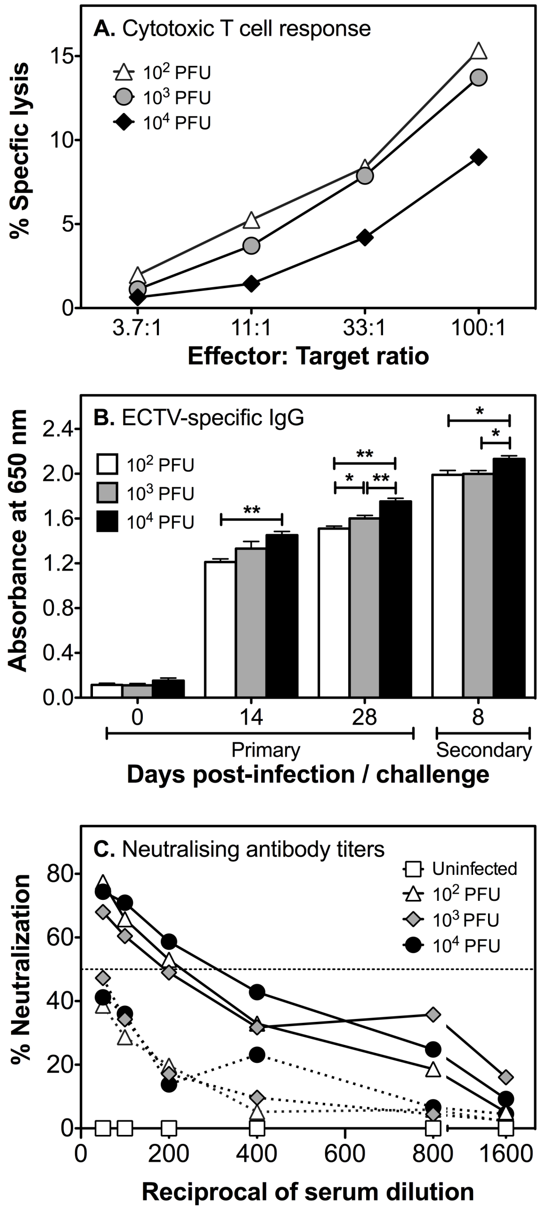

Figure 6.4: ECTV ΔA36R infection induces protective immunity

At 33 dpi, all BALB/c mice inoculated with 10^2, 10^3 or 10^4 pfu ECTV ΔA36R mice that survived were challenged with a lethal dose of ECTV by the subcutaneous route. Mice were sacrificed at day 8 post-challenge and sera, spleen, liver and lymph nodes were collected. The recall CTL response (A) in the spleen was similar in all groups. ECTV-specific IgG was measured by ELISA in sera (B) during primary (0, 14 and 28 dpi) and 8 days after secondary challenge. ECTV-specific IgG titers increased with increased doses of virus innoculum, over time post-infection and after secondary challenge (* $p<0.05$, ** $p< 0.01$, Mann Whitney test) Serial dilutions of sera, starting at a 1:50 dilution, obtained from mice during primary infection with varying doses of ECTV ΔA36R (broken lines) and after secondary challenge with ECTV (solid lines) were used to determine neutralising activity (C). ECTV ΔA36R induced neutralising antibody during primary infection, albeit, levels were below the 50% neutralising titer (horizontal dotted line). Virus was not detected in any of the organs following a secondary virus challenge (data not shown).

6.3 DISCUSSION

The reduced microtubule transport and loss of virus-associated actin tails due to disruption of A36R function in ECTV had a significantly attenuated phenotype *in vivo* in two susceptible strains of mice. First, the ECTV-susceptible BALB/c mouse strain did not exhibit any clinical signs of disease and survived doses that were otherwise fatal with ECTV. ECTV ΔA36R titers were several orders of magnitude lower in the draining lymph node, spleen and liver than titers of ECTV at 5 and 8 dpi. Second, ECTV ΔA36R was also attenuated in Rag-$1^{-/-}$ mice, which are devoid of an adaptive immune system. Viral load in organs of this strain were also orders of magnitude lower compared with titers of ECTV at 5 dpi. All Rag-$1^{-/-}$ mice infected with ECTV died from the infection at 8 dpi whereas those infected with ECTV ΔA36R were still alive with no clinical signs of disease [data not shown]. Although we envisage that Rag-$1^{-/-}$ mice would have eventually succumbed to infection with the mutant virus since adaptive immunity is essential for complete recovery [329, 479], this finding further attests to the importance of microtubule transport and actin-based motility for virus replication, spread and ability to cause disease.

The BALB/c strain normally generates poor immune response to ECTV infection and depending on the virus dose, succumbs to mousepox between 7-20 dpi [**Figure 6.2A**] [329, 480]. However, when infected with mutant viruses lacking thymidine kinase activity or immune evasion molecules that target interferon function, they are able to generate an antiviral immune response and recover [478, 480, 481]. Thus, reducing the level of virus replication can tip the balance in favour of the BALB/c mouse, allowing it sufficient time to mount CTL and antibody responses to overcome an infection that is otherwise lethal.

The NK cell response to ECTV infection generally peaks by 5 dpi and contributes to early virus control [329, 468, 469]. We reasoned that replication of the ECTV ΔA36R was possibly controlled by NK cells, as mutant virus titers were at least 1-4 $\log_{10}$ pfu lower than ECTV at 5 dpi. However, infection of the ECTV-susceptible BALB/c or ECTV-resistant C57BL/6 mice with the mutant virus induced very weak NK cell cytolytic activity that was several fold lower in magnitude than the activity generated by ECTV in both mouse strains.

The specific requirement for individual innate cell types in controlling ECTV is currently unknown. Although it is possible that other innate cell types such as dendritic cells are involved in rapidly reducing mutant virus titers, we believe that the attenuated phenotype of this virus, in contrast to some other ECTV mutants discussed above, is due to its inability to replicate efficiently as a consequence of defective subcellular transport.

Although we did not measure the primary CTL response in BALB/c mice infected with ECTV ΔA36R, it is very likely that cell-mediated immunity contributed to the recovery from primary infection [329]. Anti-ECTV antibody was clearly generated during primary infection and this response is vital for complete recovery from a primary infection [**Figure 6.4B**].

Despite the significant attenuation of ECTV ΔA36R, it nonetheless induced protective immunity. BALB/c mice that had recovered from infection with 3 different doses of ECTV ΔA36R were protected against challenge with a lethal dose of ECTV. At day 8 post-challenge, we were unable to demonstrate the presence of virus in all organs examined. Recall CTL and antibody responses were clearly generated, and are indicative of induction of T and B cell memory during primary infection [**Figure 6.4A-C**]. Although a role for cell-mediated immunity cannot be completely excluded, humoral immunity is known to be absolutely required for recovery from a secondary orthopoxvirus infection. We have previously shown that humoral immunity but not the function of CD4 or CD8 T lymphocyte subsets is required to control virus replication during the acute phase of a secondary ECTV infection [330, 478]. This requirement for antibody is not unique to ECTV as elimination of CD4 or CD8 T cells does not affect monkeypox virus clearance or the neutralising antibody response during the acute phase of a secondary infection in VACV vaccinated macaques [482].

As the vaccine responsible for the irradication of smallpox, VACV has been extensively investigated as a vaccine vector for infectious diseases and as a vector for therapeutic immunisation against cancer (reviewed in [483]). Being a large double stranded DNA virus that replicates entirely in the cytoplasm, VACV affords many advantages in use as a vaccine vector including the amenability to genetic modification and the ability to carry large genetic inserts with very minimal risk of intergration into the host genome [483]. However, the pathogenicity of many VACV strains present concerns in immunocompromised and immunonaive individuals. Highly attenuated, non-replicating MVA provides a substantially safer vaccine vector alternative with preclinical trials with animals for infectious diseases including HIV, malaria and and tuberculosis demonstrating efficacy [484, 485]. However, once progressed to clinical trials, in many cases, only moderate immunogenicity has been achieved, likely due to the extent of attenuation in MVA [483].

Single gene deletions that attenuate viruses can be adequately safe while retaining higher levels of immunogenicity [486]. The findings in the current study suggest that orthopoxvirus vectors with A36 deletions may be considered as safe vaccine candidates. A36 deletions generate virions expressing all envelope proteins, so while they have defective transmission and are severely attenuated, all neutralising epitopes are present in their natural state.

This is the first ECTV recombinant virus with a WV-specific open reading frame deleted. The significant reduction in the capacity of mutant virus to replicate locally and be transmitted to other tissues *in vivo* highlights the importance of WV and the specific roles played by A36 in subcellular transport. Deletion of genes encoding WV-specific proteins in VACV such as A36, B5 and A34 also led to highly attenuated infections in mice [215, 272, 487, 488]. However, intranasal infection of mice with VACV WR require large doses of between 10^4 – 10^6 pfu to achieve substantial mortality [215, 272, 487], which may not be reflective of doses of variola virus required to cause disease and death in humans. Using lower infectious doses (10^{-2} – 10^{-4} pfu), we have shown that deletion of A36R in ECTV attenuates the virus to the extent that even genetically susceptible mice are able to survive the infection and generate immunological memory. Our characterisation of the role and function of A36R with a combination of a host and its natural pathogen offers considerable advantages to elucidate its contribution to virulence.

CHAPTER 7: Conclusions

7.1 SUMMARY OF FINDINGS AND FUTURE DIRECTIONS

We have utilised recent advances in fluorescent protein technology, specifically the development of photoactivatable fluorescent protein Dendra2, to establish an imaging system to fate track the different morphological forms of VACV over relatively long timeframes. We constructed recombinant viruses expressing core protein A3 and envelope proteins B5 and F13 fused to Dendra2 in both parental and deletion strains of the WR strain. All Dendra2-fusion viruses were bright and photoconverted efficiently. We were able to target both compartments and single virus particles for photoactivation and tracking, a testament to the sophistication of our imaging system.

We examined the dynamics of envelopment at and egress from the TGN, including the effect on A36 and F12 on those processes. It has been previously suggested that the F12/E2 complex may associate with virus particles through A36 [429], but this is inconsistent with the observation that F12 deletions result in more severe attenuation of IEV egress resulting in the formation of less EEV and smaller plaque phenotypes [283, 303]. Over the time frames examined, we found that while a similar number of IEV egressed from the TGN, the distance virus particles of the ΔF12L mutant were transported from the TGN was significantly less than the ΔA36R mutant, which could account for the stronger attenuation observed in previous phenotypic assays.

As both mutants appear to be able to undergo some degree of microtubule-based motility (albeit much reduced compared to parental viruses), these reduced run lengths may be due to the differential recruitment of molecular motor kinesin-1 to the virus particle rather than the complete inability to recruit kinesin-1. Our findings therefore suggest a path to consolidation of apparently contradictory findings in the field that define either A36 or F12/E2 as the sole critical mediator of microtubule-based motility [283, 285]. Elucidating how F12/E2 associate with the virus may shed further light into the role F12/E2 plays in microtubule-based motility.

Although limited by time constraints, the viruses created and the imaging system established would easily allow us to extend our analyses to the transport dynamics of IMV from the VF. Similar to our analysis of deletion viruses of proteins important to IEV egress, we could image the subcellular transport of a ΔA27 mutant to clarify the role this protein plays on microtubule-based motility and the viral life cycle.

We have also characterised the subcellular transport mechanisms of ECTV, which allows us to investigate the contribution of subcellular transport in a well-characterised endemic host. We found that ECTV encodes an A36 homologue (ECTV-Mos-142) that is highly conserved despite a large truncation at the C terminus. Deleting the ECTV A36R gene leads to a reduction in the number of extracellular viruses formed and to a reduced plaque size, consistent with a role in microtubule transport. We also observed a complete loss of virus-associated actin tails, another phenotype dependent on A36 expression during VACV infection.

Infection of ECTV-susceptible BALB/c mice with ΔA36R resulted in drastically attenuated pathogenesis, including a strong reduction in the spread of virus from the site of inoculation and lower viral load in the major target organs. Virus spread and replication was also significantly curtailed in Rag-1-deficient mice, which lack a functional adaptive immune system. Taken together, these findings demonstrate the critical role that subcellular transport pathways play not only in orthopoxvirus infection in an *in vitro* context but also during orthopoxvirus pathogenesis in a natural host.

Despite the attenuation of ECTV ΔA36R, BALB/c mice that survived ΔA36R infection effectively generated protective antibody and cytotoxic T lymphocyte (CTL) responses and were able to overcome a subsequent lethal challenge with wild-type ECTV. This suggests that orthopoxvirus vectors with A36 deletions may be considered another safe vaccine alternative. Attentuating virus spread by disabling transport mechanisms maintains the integrity of virion epitopes and is an attractive generic approach to generate safe vaccines.

Deletion of A36, as a mediator of both microtubule and actin-based motility, does not allow us to distinguish between the contributions of each type of subcellular transport to pathogenesis. However, the critical residues involved in both processes have been identified in VACV and are both conserved in ECTV, with a WD/WD motif (WE/WD in VACV) mediating microtubule-based motility and a Y112 residue (the ancilliary Y132 site present in VACV is absent in ECTV) mediating actin-based motility. Future directions therefore could involve the construction of ECTV a A36^{Y112F} mutant virus to be used in the mouse model to dissect the specific contribution of actin-based motility in a host organism. As microtubule-based motility precedes actin-based motility, a A36$^{WDWD/AAAA}$ is unlikely to reveal substantial phenotypic differences to the ΔA36R strain due to microtubule-based motility alone. However, the impact of superrepulsion on organism-wide dissemination would be able to be examined.

Subcellular transport pathways are critical steps in the replication of many viruses, particularly large DNA viruses that are significantly hindered by the host cytoplasm environment [489]. Recruitment of cellular microtubule motors during virus egress is often complex, requiring multiple, redundant interactions with surface viral proteins. These surface viral proteins are often pleiotropic and possess key roles in other stages of morphogenesis, obfuscating straightforward genetic analysis of their function in transport. For example, egress of Herpes Simplex Virus-1 (HSV-1) requires kinesin-1 function and while HSV-1 tegument proteins pUL36 (VP1/2) and pUL37 are good candidate interaction partners [134], null mutants do not produce enveloped virions [490, 491]. The effect of these mutations on kinesin-1 recruitment therefore cannot be effectively analysed and in fact, no mutations in HSV-1 have been identified that mimic the loss of kinesin-1 function [492, 493]. Similarly, ablation of kinesin-2 function blocks Kaposi's Sarcoma-Associated Herpesvirus release and while viral protein ORF45 has been shown to interact with kinesin-2 through Y2H screens, again null mutants are morphologically defective [139, 494].

In contrast, the microtubule-dependent egress of VACV is mediated by interactions between A36 and F12 and the kinesin-1 complex, disruption of either producing a strong defect in virus transport. We have exploited this knowledge and translated it to the related ECTV to demonstrate movement on microtubules and polymerised actin is essential for virus propagation and transmission in its natural host. In an intact animal, cell-to-cell virus transmission occurs in a complex 3-dimensional environment of tissue. This is distinct from the predominantly 2-dimensional surface imposed by virus cell culture techniques such as plaque assays, where virus spread occurs within a cell monolayer and which may overstate the importance of cytoplasmic transport. Our results confirm that cytoplasmic transport is a fundamental barrier to orthopoxvirus transmission in an intact host and therefore an attractive target for inhibiting viral pathogenesis.

References

1. Berg, H.C., *The rotary motor of bacterial flagella.* Annual Review of Biochemistry, 2003. **72**: p. 19-54.

2. Mattick, J.S., *Type IV pili and twitching motility.* Annual Review of Microbiology, 2002. **56**: p. 289-314.

3. Nunnari, J. and A. Suomalainen, *Mitochondria: in sickness and in health.* Cell, 2012. **148**(6): p. 1145-59.

4. Schroder, M., *Endoplasmic reticulum stress responses.* Cellular and molecular life sciences : CMLS, 2008. **65**(6): p. 862-94.

5. Andreeva, A.V., et al., *The structure and function of the Golgi apparatus: a hundred years of questions.* Journal of Experimental Botany, 1998. **49**(325): p. 1281-1291.

6. Luzio, J.P., P.R. Pryor, and N.A. Bright, *Lysosomes: fusion and function.* Nature Reviews. Molecular Cell Biology, 2007. **8**(8): p. 622-32.

7. Diekmann, Y. and J.B. Pereira-Leal, *Evolution of intracellular compartmentalization.* The Biochemical journal, 2013. **449**(2): p. 319-31.

8. Kirschner, M. and J. Gerhart, *Evolvability.* Proceedings of the National Academy of Sciences of the United States of America, 1998. **95**(15): p. 8420-7.

9. Jones, D.L., *Organic acids in the rhizosphere - a critical review.* Plant and Soil, 1998. **205**(1): p. 25-44.

10. Luby-Phelps, K., *Cytoarchitecture and physical properties of cytoplasm: volume, viscosity, diffusion, intracellular surface area.* International review of cytology, 2000. **192**: p. 189-221.

11. Martoglio, B. and B. Dobberstein, *Signal sequences: more than just greasy peptides.* Trends in Cell Biology, 1998. **8**(10): p. 410-415.

12. Herrmann, H. and S.V. Strelkov, *History and phylogeny of intermediate filaments: now in insects.* BMC Biology, 2011. **9**: p. 16.

13. Herrmann, H. and U. Aebi, *Intermediate filaments: molecular structure, assembly mechanism, and integration into functionally distinct intracellular Scaffolds.* Annual Review of Biochemistry, 2004. **73**: p. 749-89.

14. Goldman, R.D., et al., *Inroads into the structure and function of intermediate filament networks.* Journal of Structural Biology, 2012. **177**(1): p. 14-23.

15. Teixido-Travesa, N., J. Roig, and J. Luders, *The where, when and how of microtubule nucleation - one ring to rule them all.* Journal of Cell Science, 2012. **125**(Pt 19): p. 4445-56.

16. Singla, V. and J.F. Reiter, *The primary cilium as the cell's antenna: signaling at a sensory organelle.* Science, 2006. **313**(5787): p. 629-33.

17. Azimzadeh, J. and M. Bornens, *Structure and duplication of the centrosome.* Journal of Cell Science, 2007. **120**(Pt 13): p. 2139-42.

18. Moritz, M., et al., *Microtubule nucleation by gamma-tubulin-containing rings in the centrosome.* Nature, 1995. **378**(6557): p. 638-40.

19. Zheng, Y., et al., *Nucleation of microtubule assembly by a gamma-tubulin-containing ring complex.* Nature, 1995. **378**(6557): p. 578-83.

20. Luders, J. and T. Stearns, *Microtubule-organizing centres: a re-evaluation.* Nature Reviews. Molecular Cell Biology, 2007. **8**(2): p. 161-7.

21. Spiegelman, B.M., S.M. Penningroth, and M.W. Kirschner, *Turnover of tubulin and the N site GTP in Chinese hamster ovary cells.* Cell, 1977. **12**(3): p. 587-600.

22. David-Pfeuty, T., H.P. Erickson, and D. Pantaloni, *Guanosinetriphosphatase activity of tubulin associated with microtubule assembly.* Proceedings of the National Academy of Sciences of the United States of America, 1977. **74**(12): p. 5372-6.

23. Mitchison, T. and M. Kirschner, *Dynamic instability of microtubule growth.* Nature, 1984. **312**(5991): p. 237-42.

24. Chretien, D., S.D. Fuller, and E. Karsenti, *Structure of Growing Microtubule Ends - 2-Dimensional Sheets Close into Tubes at Variable Rates.* Journal of Cell Biology, 1995. **129**(5): p. 1311-1328.

25. Evans, L., T. Mitchison, and M. Kirschner, *Influence of the centrosome on the structure of nucleated microtubules.* The Journal of cell biology, 1985. **100**(4): p. 1185-91.

26. Desai, A. and T.J. Mitchison, *Microtubule polymerization dynamics.* Annual Review of Cell and Developmental Biology, 1997. **13**: p. 83-117.

27. Seetapun, D., et al., *Estimating the microtubule GTP cap size in vivo.* Current biology : CB, 2012. **22**(18): p. 1681-7.

28. Kirschner, M. and T. Mitchison, *Beyond self-assembly: from microtubules to morphogenesis.* Cell, 1986. **45**(3): p. 329-42.

29. Roll-Mecak, A. and F.J. McNally, *Microtubule-severing enzymes.* Current Opinion in Cell Biology, 2010. **22**(1): p. 96-103.

30. Cassimeris, L., *The oncoprotein 18/stathmin family of microtubule destabilizers.* Current Opinion in Cell Biology, 2002. **14**(1): p. 18-24.

31. Thoma, C.R., et al., *Quantitative image analysis identifies pVHL as a key regulator of microtubule dynamic instability.* The Journal of cell biology, 2010. **190**(6): p. 991-1003.

32. Dehmelt, L. and S. Halpain, *The MAP2/Tau family of microtubule-associated proteins.* Genome Biology, 2005. **6**(1): p. 204.

33. Vitre, B., et al., *EB1 regulates microtubule dynamics and tubulin sheet closure in vitro.* Nature Cell Biology, 2008. **10**(4): p. 415-21.

34. Bieling, P., et al., *CLIP-170 tracks growing microtubule ends by dynamically recognizing composite EB1/tubulin-binding sites.* The Journal of cell biology, 2008. **183**(7): p. 1223-33.

35. Garnham, C.P. and A. Roll-Mecak, *The chemical complexity of cellular microtubules: tubulin post-translational modification enzymes and their roles in tuning microtubule functions.* Cytoskeleton, 2012. **69**(7): p. 442-63.

36. Dixit, R., et al., *Microtubule plus-end tracking by CLIP-170 requires EB1.* Proceedings of the National Academy of Sciences of the United States of America, 2009. **106**(2): p. 492-7.

37. Gupta, K.K., et al., *Probing interactions between CLIP-170, EB1, and microtubules.* Journal of Molecular Biology, 2010. **395**(5): p. 1049-62.

38. Wang, Z. and M.P. Sheetz, *The C-terminus of tubulin increases cytoplasmic dynein and kinesin processivity.* Biophysical Journal, 2000. **78**(4): p. 1955-64.

39. Reed, N.A., et al., *Microtubule acetylation promotes kinesin-1 binding and transport.* Current biology : CB, 2006. **16**(21): p. 2166-72.

40. Hammond, J.W., et al., *Posttranslational modifications of tubulin and the polarized transport of kinesin-1 in neurons.* Molecular Biology of the Cell, 2010. **21**(4): p. 572-83.

41. Ikegami, K., et al., *Loss of alpha-tubulin polyglutamylation in ROSA22 mice is associated with abnormal targeting of KIF1A and modulated synaptic function.* Proceedings of the National Academy of Sciences of the United States of America, 2007. **104**(9): p. 3213-8.

42. Conde, C. and A. Caceres, *Microtubule assembly, organization and dynamics in axons and dendrites.* Nature Reviews. Neuroscience, 2009. **10**(5): p. 319-32.

43. Akhmanova, A. and M.O. Steinmetz, *Tracking the ends: a dynamic protein network controls the fate of microtubule tips.* Nature Reviews. Molecular Cell Biology, 2008. **9**(4): p. 309-22.

44. Hirokawa, N. and Y. Noda, *Intracellular transport and kinesin superfamily proteins, KIFs: structure, function, and dynamics.* Physiological Reviews, 2008. **88**(3): p. 1089-118.

45. Hirokawa, N. and R. Takemura, *Molecular motors and mechanisms of directional transport in neurons.* Nature Reviews. Neuroscience, 2005. **6**(3): p. 201-14.

46. Hirokawa, N., et al., *Kinesin superfamily motor proteins and intracellular transport.* Nature Reviews. Molecular Cell Biology, 2009. **10**(10): p. 682-96.

47. Echard, A., *Interaction of a Golgi-Associated Kinesin-Like Protein with Rab6.* Science, 1998. **279**(5350): p. 580-585.

48. Xu, Y., et al., *Role of KIFC3 motor protein in Golgi positioning and integration.* The Journal of cell biology, 2002. **158**(2): p. 293-303.

49. Harada, A., et al., *Golgi vesiculation and lysosome dispersion in cells lacking cytoplasmic dynein.* Journal of Cell Biology, 1998. **141**(1): p. 51-59.

50. Kimura, T., et al., *Tubulin and CRMP-2 complex is transported via Kinesin-1.* Journal of Neurochemistry, 2005. **93**(6): p. 1371-82.

51. Tanaka, Y., et al., *Targeted disruption of mouse conventional kinesin heavy chain, kif5B, results in abnormal perinuclear clustering of mitochondria.* Cell, 1998. **93**(7): p. 1147-58.

52. Nakata, T. and N. Hirokawa, *Microtubules provide directional cues for polarized axonal transport through interaction with kinesin motor head.* The Journal of cell biology, 2003. **162**(6): p. 1045-55.

53. Byrd, D.T., et al., *UNC-16, a JNK-signaling scaffold protein, regulates vesicle transport in C. elegans.* Neuron, 2001. **32**(5): p. 787-800.

54. Diefenbach, R.J., et al., *The heavy chain of conventional kinesin interacts with the SNARE proteins SNAP25 and SNAP23.* Biochemistry, 2002. **41**(50): p. 14906-15.

55. Rahman, A., D.S. Friedman, and L.S. Goldstein, *Two kinesin light chain genes in mice. Identification and characterization of the encoded proteins.* The Journal of biological chemistry, 1998. **273**(25): p. 15395-403.

56. Junco, A., et al., *Kinesin light-chain KLC3 expression in testis is restricted to spermatids.* Biology of Reproduction, 2001. **64**(5): p. 1320-30.

57. DeLuca, J.G., et al., *Purification and characterization of native conventional kinesin, HSET, and CENP-E from mitotic hela cells.* The Journal of biological chemistry, 2001. **276**(30): p. 28014-21.

58. Sun, F., et al., *Sunday Driver/JIP3 binds kinesin heavy chain directly and enhances its motility.* The EMBO journal, 2011. **30**(16): p. 3416-29.

59. Wozniak, M.J. and V.J. Allan, *Cargo selection by specific kinesin light chain 1 isoforms.* EMBO Journal, 2006. **25**(23): p. 5457-5468.

60. Pernigo, S., et al., *Structural basis for kinesin-1:cargo recognition.* Science, 2013. **340**(6130): p. 356-9.

61. Verhey, K.J. and J.W. Hammond, *Traffic control: regulation of kinesin motors.* Nature Reviews. Molecular Cell Biology, 2009. **10**(11): p. 765-77.

62. Blasius, T.L., et al., *Two binding partners cooperate to activate the molecular motor Kinesin-1.* The Journal of cell biology, 2007. **176**(1): p. 11-7.

63. Sato-Yoshitake, R., et al., *The phosphorylation of kinesin regulates its binding to synaptic vesicles.* The Journal of biological chemistry, 1992. **267**(33): p. 23930-6.

64. Guillaud, L., R. Wong, and N. Hirokawa, *Disruption of KIF17-Mint1 interaction by CaMKII-dependent phosphorylation: a molecular model of kinesin-cargo release.* Nature Cell Biology, 2008. **10**(1): p. 19-29.

65. Cahu, J., et al., *Phosphorylation by Cdk1 increases the binding of Eg5 to microtubules in vitro and in Xenopus egg extract spindles.* PLoS ONE, 2008. **3**(12): p. e3936.

66. Stagi, M., et al., *Unloading kinesin transported cargoes from the tubulin track via the inflammatory c-Jun N-terminal kinase pathway.* FASEB journal : official publication of the Federation of American Societies for Experimental Biology, 2006. **20**(14): p. 2573-5.

67. Macaskill, A.F., et al., *Miro1 is a calcium sensor for glutamate receptor-dependent localization of mitochondria at synapses.* Neuron, 2009. **61**(4): p. 541-55.

68. Nielsen, E., et al., *Rab5 regulates motility of early endosomes on microtubules.* Nature Cell Biology, 1999. **1**(6): p. 376-82.

69. Niwa, S., Y. Tanaka, and N. Hirokawa, *KIF1Bbeta- and KIF1A-mediated axonal transport of presynaptic regulator Rab3 occurs in a GTP-dependent manner through DENN/MADD.* Nature Cell Biology, 2008. **10**(11): p. 1269-79.

70. Kardon, J.R. and R.D. Vale, *Regulators of the cytoplasmic dynein motor.* Nature Reviews. Molecular Cell Biology, 2009. **10**(12): p. 854-65.

71. Merino-Gracia, J., M.F. Garcia-Mayoral, and I. Rodriguez-Crespo, *The association of viral proteins with host cell dynein components during virus infection.* The FEBS journal, 2011. **278**(17): p. 2997-3011.

72. King, S.M., *AAA domains and organization of the dynein motor unit.* Journal of Cell Science, 2000. **113**(14): p. 2521-2526.

73. Schroer, T.A., *Dynactin.* Annual Review of Cell and Developmental Biology, 2004. **20**: p. 759-79.

74. Gill, S.R., et al., *Dynactin, a conserved, ubiquitously expressed component of an activator of vesicle motility mediated by cytoplasmic dynein.* The Journal of cell biology, 1991. **115**(6): p. 1639-50.

75. Schroer, T.A. and M.P. Sheetz, *Two activators of microtubule-based vesicle transport.* The Journal of cell biology, 1991. **115**(5): p. 1309-18.

76. Kardon, J.R., S.L. Reck-Peterson, and R.D. Vale, *Regulation of the processivity and intracellular localization of Saccharomyces cerevisiae dynein by dynactin.* Proceedings of the National Academy of Sciences of the United States of America, 2009. **106**(14): p. 5669-74.

77. Lai, C., et al., *The G59S mutation in p150(glued) causes dysfunction of dynactin in mice.* The Journal of neuroscience : the official journal of the Society for Neuroscience, 2007. **27**(51): p. 13982-90.

78. Moore, J.K., J. Li, and J.A. Cooper, *Dynactin function in mitotic spindle positioning.* Traffic, 2008. **9**(4): p. 510-27.

79. Pollard, T.D. and J.A. Cooper, *Actin, a central player in cell shape and movement.* Science, 2009. **326**(5957): p. 1208-12.

80. Mitchison, T.J. and L.P. Cramer, *Actin-based cell motility and cell locomotion.* Cell, 1996. **84**(3): p. 371-9.

81. Gouin, E., M.D. Welch, and P. Cossart, *Actin-based motility of intracellular pathogens.* Current Opinion in Microbiology, 2005. **8**(1): p. 35-45.

82. Vandekerckhove, J. and K. Weber, *At least six different actins are expressed in a higher mammal: an analysis based on the amino acid sequence of the amino-terminal tryptic peptide.* Journal of Molecular Biology, 1978. **126**(4): p. 783-802.

83. Perrin, B.J. and J.M. Ervasti, *The actin gene family: function follows isoform.* Cytoskeleton, 2010. **67**(10): p. 630-4.

84. Dominguez, R. and K.C. Holmes, *Actin structure and function.* Annual review of biophysics, 2011. **40**: p. 169-86.

85. Dugina, V., et al., *Beta and gamma-cytoplasmic actins display distinct distribution and functional diversity.* Journal of Cell Science, 2009. **122**(Pt 16): p. 2980-8.

86. Begg, D.A., R. Rodewald, and L.I. Rebhun, *The visualization of actin filament polarity in thin sections. Evidence for the uniform polarity of membrane-associated filaments.* The Journal of cell biology, 1978. **79**(3): p. 846-52.

87. Pollard, T.D., L. Blanchoin, and R.D. Mullins, *Molecular mechanisms controlling actin filament dynamics in nonmuscle cells.* Annual Review of Biophysics and Biomolecular Structure, 2000. **29**: p. 545-76.

88. Bindschadler, M., et al., *A mechanistic model of the actin cycle.* Biophysical Journal, 2004. **86**(5): p. 2720-39.

89. Le Clainche, C. and M.F. Carlier, *Regulation of actin assembly associated with protrusion and adhesion in cell migration.* Physiological Reviews, 2008. **88**(2): p. 489-513.

90. Bock-Marquette, I., et al., *Thymosin beta 4 activates integrin-linked kinase and promotes cardiac cell migration, survival and cardiac repair.* Nature, 2004. **432**(7016): p. 466-472.

91. Witke, W., *The role of profilin complexes in cell motility and other cellular processes.* Trends in Cell Biology, 2004. **14**(8): p. 461-469.

92. Goldberg, M.B., *Actin-based motility of intracellular microbial pathogens.* Microbiology and Molecular Biology Reviews, 2001. **65**(4): p. 595-626.

93. Campellone, K.G. and M.D. Welch, *A nucleator arms race: cellular control of actin assembly.* Nature Reviews. Molecular Cell Biology, 2010. **11**(4): p. 237-51.

94. Mullins, R.D., J.A. Heuser, and T.D. Pollard, *The interaction of Arp2/3 complex with actin: Nucleation, high affinity pointed end capping, and formation of branching networks of filaments.* Proceedings of the National Academy of Sciences of the United States of America, 1998. **95**(11): p. 6181-6186.

95. Takenawa, T. and S. Suetsugu, *The WASP-WAVE protein network: connecting the membrane to the cytoskeleton.* Nature Reviews Molecular Cell Biology, 2007. **8**(1): p. 37-48.

96. Dominguez, R., *The beta-thymosin/WH2 fold: multifunctionality and structure.* Annals of the New York Academy of Sciences, 2007. **1112**: p. 86-94.

97. Caldwell, J.E., et al., *Effects of Capz, an Actin Capping Protein of Muscle, on the Polymerization of Actin.* Biochemistry, 1989. **28**(21): p. 8506-8514.

98. Yamashiro, S., et al., *Tropomodulins: pointed-end capping proteins that regulate actin filament architecture in diverse cell types.* Cytoskeleton, 2012. **69**(6): p. 337-70.

99. Bernstein, B.W. and J.R. Bamburg, *ADF/cofilin: a functional node in cell biology.* Trends in Cell Biology, 2010. **20**(4): p. 187-95.

100. Silacci, P., et al., *Gelsolin superfamily proteins: key regulators of cellular functions.* Cellular and molecular life sciences : CMLS, 2004. **61**(19-20): p. 2614-23.

101. Edwards, R.A. and J. Bryan, *Fascins, a family of actin bundling proteins.* Cell Motility and the Cytoskeleton, 1995. **32**(1): p. 1-9.

102. Karlsson, R. and U. Lindberg, *Profilin, an Essential Control Element for Actin Polymerization*, in *Actin-Monomer-Binding Proteins*2007, Springer New York. p. 29-44.

103. Heasman, S.J. and A.J. Ridley, *Mammalian Rho GTPases: new insights into their functions from in vivo studies.* Nature Reviews Molecular Cell Biology, 2008. **9**(9): p. 690-701.

104. Sit, S.T. and E. Manser, *Rho GTPases and their role in organizing the actin cytoskeleton.* Journal of Cell Science, 2011. **124**(5): p. 679-683.

105. Pollard, T.D., *Regulation of actin filament assembly by Arp2/3 complex and formins.* Annual Review of Biophysics and Biomolecular Structure, 2007. **36**: p. 451-77.

106. Goley, E.D. and M.D. Welch, *The ARP2/3 complex: an actin nucleator comes of age.* Nature Reviews: Molecular Cell Biology, 2006. **7**(10): p. 713-26.

107. Sweeney, H.L. and A. Houdusse, *Structural and functional insights into the Myosin motor mechanism.* Annual review of biophysics, 2010. **39**: p. 539-57.

108. Vreugde, S., et al., *Nuclear myosin VI enhances RNA polymerase II-dependent transcription.* Molecular Cell, 2006. **23**(5): p. 749-755.

109. Holmes, K.C., *The swinging lever-arm hypothesis of muscle contraction.* Current biology : CB, 1997. **7**(2): p. R112-8.

110. Lymn, R.W. and E.W. Taylor, *Mechanism of Adenosine Triphosphate Hydrolysis by Actomyosin.* Biochemistry, 1971. **10**(25): p. 4617-&.

111. Mehta, A.D., et al., *Myosin-V is a processive actin-based motor.* Nature, 1999. **400**(6744): p. 590-593.

112. Igakura, T., et al., *Spread of HTLV-I between lymphocytes by virus-induced polarization of the cytoskeleton.[see comment].* Science, 2003. **299**(5613): p. 1713-6.

113. Nejmeddine, M., et al., *Human T-lymphotropic virus, type 1, tax protein triggers microtubule reorientation in the virological synapse.* The Journal of biological chemistry, 2005. **280**(33): p. 29653-60.

114. Ploubidou, A., et al., *Vaccinia virus infection disrupts microtubule organization and centrosome function.* EMBO Journal, 2000. **19**(15): p. 3932-44.

115. Jouvenet, N. and T. Wileman, *African swine fever virus infection disrupts centrosome assembly and function.* Journal of General Virology, 2005. **86**(Pt 3): p. 589-94.

116. Arakawa, Y., et al., *F11L-mediated inhibition of RhoA-mDia signaling stimulates microtubule dynamics during vaccinia virus infection.* Cell Host & Microbe, 2007. **1**(3): p. 213-226.

117. Wittmann, T. and C.M. Waterman-Storer, *Cell motility: can Rho GTPases and microtubules point the way?* Journal of Cell Science, 2001. **114**(Pt 21): p. 3795-803.

118. Hertle, R. and H. Schwarz, *Serratia marcescens internalization and replication in human bladder epithelial cells.* BMC Infectious Diseases, 2004. **4**.

119. Haglund, C.M. and M.D. Welch, *Pathogens and polymers: microbe-host interactions illuminate the cytoskeleton.* The Journal of cell biology, 2011. **195**(1): p. 7-17.

120. Suomalainen, M., et al., *Microtubule-dependent plus- and minus end-directed motilities are competing processes for nuclear targeting of adenovirus.* Journal of Cell Biology, 1999. **144**(4): p. 657-672.

121. Kelkar, S.A., et al., *Cytoplasmic dynein mediates adenovirus binding to microtubules.* Journal of Virology, 2004. **78**(18): p. 10122-10132.

122. Bremner, K.H., et al., *Adenovirus transport via direct interaction of cytoplasmic dynein with the viral capsid hexon subunit.* Cell Host and Microbe, 2009. **6**(6): p. 523-35.

123. Strunze, S., et al., *Kinesin-1-mediated capsid disassembly and disruption of the nuclear pore complex promote virus infection.* Cell Host and Microbe, 2011. **10**(3): p. 210-23.

124. Seisenberger, G., et al., *Real-time single-molecule imaging of the infection pathway of an adeno-associated virus.* Science, 2001. **294**(5548): p. 1929-1932.

125. Suikkanen, S., et al., *Release of canine parvovirus from endocytic vesicles.* Virology, 2003. **316**(2): p. 267-80.

126. Alonso, C., et al., *African swine fever virus protein p54 interacts with the microtubular motor complex through direct binding to light-chain dynein.* Journal of Virology, 2001. **75**(20): p. 9819-27.

127. Heath, C.M., M. Windsor, and T. Wileman, *Aggresomes resemble sites specialized for virus assembly.* The Journal of cell biology, 2001. **153**(3): p. 449-55.

128. Jouvenet, N., et al., *Transport of African swine fever virus from assembly sites to the plasma membrane is dependent on microtubules and conventional kinesin.* Journal of Virology, 2004. **78**(15): p. 7990-8001.

129. Sodeik, B., M.W. Ebersold, and A. Helenius, *Microtubule-mediated transport of incoming herpes simplex virus 1 capsids to the nucleus.* The Journal of cell biology, 1997. **136**(5): p. 1007-21.

130. Smith, G.A., et al., *Local modulation of plus-end transport targets herpesvirus entry and egress in sensory axons.* Proceedings of the National Academy of Sciences of the United States of America, 2004. **101**(45): p. 16034-16039.

131. Dohner, K., C.H. Nagel, and B. Sodeik, *Viral stop-and-go along microtubules: taking a ride with dynein and kinesins.* Trends in Microbiology, 2005. **13**(7): p. 320-7.

132. Diefenbach, R.J., et al., *Herpes simplex virus tegument protein US11 interacts with conventional kinesin heavy chain.* Journal of Virology, 2002. **76**(7): p. 3282-3291.

133. Koshizuka, T., Y. Kawaguchi, and Y. Nishiyama, *Herpes simplex virus type 2 membrane protein UL56 associates with the kinesin motor protein KIF1A.* The Journal of general virology, 2005. **86**(Pt 3): p. 527-33.

134. Radtke, K., et al., *Plus- and minus-end directed microtubule motors bind simultaneously to herpes simplex virus capsids using different inner tegument structures.* PLoS pathogens, 2010. **6**(7): p. e1000991.

135. Kaelin, K., et al., *The UL25 protein of pseudorabies virus associates with capsids and localizes to the nucleus and to microtubules.* Journal of Virology, 2000. **74**(1): p. 474-482.

136. Zaichick, S.V., et al., *The herpesvirus VP1/2 protein is an effector of dynein-mediated capsid transport and neuroinvasion.* Cell Host and Microbe, 2013. **13**(2): p. 193-203.

137. Kramer, T., et al., *Kinesin-3 mediates axonal sorting and directional transport of alphaherpesvirus particles in neurons.* Cell Host and Microbe, 2012. **12**(6): p. 806-14.

138. Ogawa-Goto, K., et al., *Microtubule network facilitates nuclear targeting of human cytomegalovirus capsid.* Journal of Virology, 2003. **77**(15): p. 8541-7.

139. Sathish, N., F.X. Zhu, and Y. Yuan, *Kaposi's sarcoma-associated herpesvirus ORF45 interacts with kinesin-2 transporting viral capsid-tegument complexes along microtubules.* PLoS Pathogens, 2009. **5**(3): p. e1000332.

140. Zhang, W., W. Greene, and S.J. Gao, *Microtubule- and dynein-dependent nuclear trafficking of rhesus rhadinovirus in rhesus fibroblasts.* Journal of Virology, 2012. **86**(1): p. 599-604.

141. Frampton, A.R., Jr., et al., *Equine herpesvirus type 1 (EHV-1) utilizes microtubules, dynein, and ROCK1 to productively infect cells.* Veterinary Microbiology, 2010. **141**(1-2): p. 12-21.

142. Jacob, Y., et al., *Cytoplasmic dynein LC8 interacts with lyssavirus phosphoprotein.* Journal of Virology, 2000. **74**(21): p. 10217-22.

143. Saib, A., et al., *Nuclear targeting of incoming human foamy virus Gag proteins involves a centriolar step.* Journal of Virology, 1997. **71**(2): p. 1155-61.

144. McDonald, D., et al., *Visualization of the intracellular behavior of HIV in living cells.* Journal of Cell Biology, 2002. **159**(3): p. 441-452.

145. Petit, F., et al., *Intrinsic and extrinsic pathways signaling during HIV-1 mediated cell death.* Biochimie, 2003. **85**(8): p. 795-811.

146. Martinez, N.W., et al., *Kinesin KIF4 regulates intracellular trafficking and stability of the human immunodeficiency virus type 1 Gag polyprotein.* Journal of Virology, 2008. **82**(20): p. 9937-50.

147. Gaudin, R., et al., *Critical role for the kinesin KIF3A in the HIV life cycle in primary human macrophages.* The Journal of cell biology, 2012. **199**(3): p. 467-79.

148. Tang, Y., et al., *Cellular motor protein KIF-4 associates with retroviral Gag.* Journal of Virology, 1999. **73**(12): p. 10508-13.

149. Su, Y., et al., *Microtubule-dependent retrograde transport of bovine immunodeficiency virus.* Cellular Microbiology, 2010. **12**(8): p. 1098-107.

150. Funk, A., et al., *Itinerary of hepatitis B viruses: delineation of restriction points critical for infectious entry.* Journal of Virology, 2004. **78**(15): p. 8289-300.

151. Boulant, S., et al., *Hepatitis C virus core protein induces lipid droplet redistribution in a microtubule- and dynein-dependent manner.* Traffic, 2008. **9**(8): p. 1268-82.

152. Florin, L., et al., *Identification of a dynein interacting domain in the papillomavirus minor capsid protein l2.* Journal of Virology, 2006. **80**(13): p. 6691-6.

153. Schneider, M.A., et al., *Identification of the dynein light chains required for human papillomavirus infection.* Cellular Microbiology, 2011. **13**(1): p. 32-46.

154. Pelkmans, L., J. Kartenbeck, and A. Helenius, *Caveolar endocytosis of simian virus 40 reveals a new two-step vesicular-transport pathway to the ER.* Nature Cell Biology, 2001. **3**(5): p. 473-83.

155. Leopold, P.L., et al., *Dynein- and microtubule-mediated translocation of adenovirus serotype 5 occurs after endosomal lysis.* Human Gene Therapy, 2000. **11**(1): p. 151-165.

156. Sanjuan, N., A. Porras, and J. Otero, *Microtubule-dependent intracellular transport of murine polyomavirus.* Virology, 2003. **313**(1): p. 105-16.

157. Georgi, A., et al., *Detection of individual fluorescently labeled reovirions in living cells.* Proceedings of the National Academy of Sciences of the United States of America, 1990. **87**(17): p. 6579-83.

158. Chambers, R. and T. Takimoto, *Trafficking of Sendai Virus Nucleocapsids Is Mediated by Intracellular Vesicles.* PLoS ONE, 2010. **5**(6).

159. Lakadamyali, M., et al., *Visualizing infection of individual influenza viruses.* Proceedings of the National Academy of Sciences of the United States of America, 2003. **100**(16): p. 9280-5.

160. Mueller, S. and E. Wimmer, *Recruitment of nectin-3 to cell-cell junctions through trans-heterophilic interaction with CD155, a vitronectin and poliovirus receptor that localizes to alpha(v)beta3 integrin-containing membrane microdomains.* The Journal of biological chemistry, 2003. **278**(33): p. 31251-60.

161. Fehling, S.K., et al., *The microtubule motor protein KIF13A is involved in intracellular trafficking of the Lassa virus matrix protein Z.* Cellular Microbiology, 2013. **15**(2): p. 315-34.

162. Kubota, T., et al., *Ebolavirus VP35 interacts with the cytoplasmic dynein light chain 8.* Journal of Virology, 2009. **83**(13): p. 6952-6.

163. Sanderson, C.M., M. Hollinshead, and G.L. Smith, *The vaccinia virus A27L protein is needed for the microtubule-dependent transport of intracellular mature virus particles.* Journal of General Virology, 2000. **81**(Pt 1): p. 47-58.

164. Brault, J.B., et al., *The interaction of flavivirus M protein with light chain Tctex-1 of human dynein plays a role in late stages of virus replication.* Virology, 2011. **417**(2): p. 369-78.

165. Ferree, P.M., et al., *Wolbachia utilizes host microtubules and Dynein for anterior localization in the Drosophila oocyte.* PLoS Pathogens, 2005. **1**(2): p. e14.

166. Serbus, L.R. and W. Sullivan, *A cellular basis for Wolbachia recruitment to the host germline.* PLoS Pathogens, 2007. **3**(12): p. e190.

167. Marsman, M., et al., *Dynein-mediated vesicle transport controls intracellular Salmonella replication.* Molecular Biology of the Cell, 2004. **15**(6): p. 2954-64.

168. Dumont, A., et al., *SKIP, the host target of the Salmonella virulence factor SifA, promotes kinesin-1-dependent vacuolar membrane exchanges.* Traffic, 2010. **11**(7): p. 899-911.

169. Grieshaber, S.S., N.A. Grieshaber, and T. Hackstadt, *Chlamydia trachomatis uses host cell dynein to traffic to the microtubule-organizing center in a p50 dynamitin-independent process.* Journal of Cell Science, 2003. **116**(Pt 18): p. 3793-802.

170. Hu, L. and D.J. Kopecko, *Campylobacter jejuni 81-176 associates with microtubules and dynein during invasion of human intestinal cells.* Infection and Immunity, 1999. **67**(8): p. 4171-82.

171. Kim, S.W., et al., *Microtubule- and dynein-mediated movement of Orientia tsutsugamushi to the microtubule organizing center.* Infection and Immunity, 2001. **69**(1): p. 494-500.

172. Kasamatsu, H. and A. Nakanishi, *How do animal DNA viruses get to the nucleus?* Annual Review of Microbiology, 1998. **52**: p. 627-686.

173. Schmid, M., et al., *DNA virus replication compartments.* Journal of Virology, 2014. **88**(3): p. 1404-20.

174. Wolfstein, A., et al., *The inner tegument promotes herpes simplex virus capsid motility along microtubules in vitro.* Traffic, 2006. **7**(2): p. 227-37.

175. Krautwald, M., et al., *Translocation of incoming pseudorabies virus capsids to the cell nucleus is delayed in the absence of tegument protein pUL37.* Journal of Virology, 2009. **83**(7): p. 3389-96.

176. Diefenbach, R., M. Miranda Saksena, and A. Cunningham, *Herpes simplex virus: Microtubule-dependent transport and egress from neurons*, in *Viral Transport, Assembly and Egress*, R.J.D.a.A.L. Cunningham, Editor 2011, Research Signpost: Kerala, India. p. 49-78.

177. Funk, A., et al., *Spread of hepatitis B viruses in vitro requires extracellular progeny and may be codetermined by polarized egress.* Journal of Virology, 2004. **78**(8): p. 3977-83.

178. Henry, T., et al., *The Salmonella effector protein PipB2 is a linker for kinesin-1.* Proceedings of the National Academy of Sciences of the United States of America, 2006. **103**(36): p. 13497-502.

179. Boucrot, E., et al., *The intracellular fate of Salmonella depends on the recruitment of kinesin.* Science, 2005. **308**(5725): p. 1174-8.

180. Willard, M., *Rapid directional Translocations in virus replication.* Journal of Virology, 2002. **76**(10): p. 5220-5232.

181. Ward, B.M. and B. Moss, *Vaccinia virus A36R membrane protein provides a direct link between intracellular enveloped virions and the microtubule motor kinesin.* Journal of Virology, 2004. **78**(5): p. 2486-93.

182. Welte, M.A., *Bidirectional transport along microtubules.* Current Biology, 2004. **14**(13): p. R525-R537.

183. Pelkmans, L., et al., *Caveolin-stabilized membrane domains as multifunctional transport and sorting devices in endocytic membrane traffic.* Cell, 2004. **118**(6): p. 767-80.

184. Chevalier, S.A., et al., *Gem-induced cytoskeleton remodeling increases cellular migration of HTLV-1-infected cells, formation of infected-to-target T-cell conjugates and viral transmission.* PLoS Pathogens, 2014. **10**(2): p. e1003917.

185. Lehmann, M.J., et al., *Actin- and myosin-driven movement of viruses along filopodia precedes their entry into cells.* The Journal of cell biology, 2005. **170**(2): p. 317-25.

186. Roberts, K.L. and J.D. Baines, *Myosin Va enhances secretion of herpes simplex virus 1 virions and cell surface expression of viral glycoproteins.* Journal of Virology, 2010. **84**(19): p. 9889-96.

187. Aggarwal, A., et al., *Mobilization of HIV spread by diaphanous 2 dependent filopodia in infected dendritic cells.* PLoS Pathogens, 2012. **8**(6): p. e1002762.

188. Knutton, S., et al., *Actin accumulation at sites of bacterial adhesion to tissue culture cells: basis of a new diagnostic test for enteropathogenic and enterohemorrhagic Escherichia coli.* Infection and Immunity, 1989. **57**(4): p. 1290-8.

189. Kenny, B., *Phosphorylation of tyrosine 474 of the enteropathogenic Escherichia coli (EPEC) Tir receptor molecule is essential for actin nucleating activity and is preceded by additional host modifications.* Molecular Microbiology, 1999. **31**(4): p. 1229-41.

190. Cudmore, S., et al., *A vaccinia virus core protein, p39, is membrane associated.* Journal of Virology, 1996. **70**(10): p. 6909-21.

191. Rottger, S., et al., *Interactions between vaccinia virus IEV membrane proteins and their roles in IEV assembly and actin tail formation.* Journal of Virology, 1999. **73**(4): p. 2863-75.

192. Reeves, P.M., et al., *Variola and monkeypox viruses utilize conserved mechanisms of virion motility and release that depend on abl and SRC family tyrosine kinases.* J Virol, 2011. **85**(1): p. 21-31.

193. Ohkawa, T., L.E. Volkman, and M.D. Welch, *Actin-based motility drives baculovirus transit to the nucleus and cell surface.* Journal of Cell Biology, 2010. **190**(2): p. 187-195.

194. Bishe, B., et al., *Role of phosphatidylinositol 4-phosphate (PI4P) and its binding protein GOLPH3 in hepatitis C virus secretion.* The Journal of biological chemistry, 2012. **287**(33): p. 27637-47.

195. Valiya Veettil, M., et al., *Interaction of c-Cbl with myosin IIA regulates Bleb associated macropinocytosis of Kaposi's sarcoma-associated herpesvirus.* PLoS Pathogens, 2010. **6**(12): p. e1001238.

196. Chakraborty, S., et al., *Kaposi's sarcoma-associated herpesvirus interacts with EphrinA2 receptor to amplify signaling essential for productive infection.* Proceedings of the National Academy of Sciences of the United States of America, 2012. **109**(19): p. E1163-72.

197. Kadiu, I. and H.E. Gendelman, *Human immunodeficiency virus type 1 endocytic trafficking through macrophage bridging conduits facilitates spread of infection.* Journal of neuroimmune pharmacology : the official journal of the Society on NeuroImmune Pharmacology, 2011. **6**(4): p. 658-75.

198. Tilney, L.G. and D.A. Portnoy, *Actin filaments and the growth, movement, and spread of the intracellular bacterial parasite, Listeria monocytogenes.* The Journal of cell biology, 1989. **109**(4 Pt 1): p. 1597-608.

199. Kocks, C., et al., *L. monocytogenes-induced actin assembly requires the actA gene product, a surface protein.* Cell, 1992. **68**(3): p. 521-31.

200. Welch, M.D., A. Iwamatsu, and T.J. Mitchison, *Actin polymerization is induced by Arp2/3 protein complex at the surface of Listeria monocytogenes.* Nature, 1997. **385**(6613): p. 265-9.

201. Welch, M.D., et al., *Interaction of human Arp2/3 complex and the Listeria monocytogenes ActA protein in actin filament nucleation.* Science, 1998. **281**(5373): p. 105-8.

202. Bernardini, M.L., et al., *Identification of icsA, a plasmid locus of Shigella flexneri that governs bacterial intra- and intercellular spread through interaction with F-actin.* Proceedings of the National Academy of Sciences of the United States of America, 1989. **86**(10): p. 3867-71.

203. Jeng, R.L., et al., *A Rickettsia WASP-like protein activates the Arp2/3 complex and mediates actin-based motility.* Cellular Microbiology, 2004. **6**(8): p. 761-9.

204. Stamm, L.M., et al., *Mycobacterium marinum escapes from phagosomes and is propelled by actin-based motility.* Journal of Experimental Medicine, 2003. **198**(9): p. 1361-8.

205. Stamm, L.M., et al., *Role of the WASP family proteins for Mycobacterium marinum actin tail formation.* Proceedings of the National Academy of Sciences of the United States of America, 2005. **102**(41): p. 14837-42.

206. Kespichayawattana, W., et al., *Burkholderia pseudomallei induces cell fusion and actin-associated membrane protrusion: a possible mechanism for cell-to-cell spreading.* Infection and Immunity, 2000. **68**(9): p. 5377-84.

207. Stevens, J.M., E.E. Galyov, and M.P. Stevens, *Actin-dependent movement of bacterial pathogens.* Nature Reviews. Microbiology, 2006. **4**(2): p. 91-101.

208. Machesky, L.M., et al., *Vaccinia virus expresses a novel profilin with a higher affinity for polyphosphoinositides than actin.* Biochemistry, 1994. **33**(35): p. 10815-24.

209. Goley, E.D., et al., *Critical conformational changes in the Arp2/3 complex are induced by nucleotide and nucleation promoting factor.* Molecular Cell, 2004. **16**(2): p. 269-79.

210. Rohatgi, R., et al., *The interaction between N-WASP and the Arp2/3 complex links Cdc42-dependent signals to actin assembly.* Cell, 1999. **97**(2): p. 221-31.

211. Lambrechts, A., et al., *Listeria comet tails: the actin-based motility machinery at work.* Trends in Cell Biology, 2008. **18**(5): p. 220-7.

212. Makino, S., et al., *A genetic determinant required for continuous reinfection of adjacent cells on large plasmid in S. flexneri 2a.* Cell, 1986. **46**(4): p. 551-5.

213. Sansonetti, P.J., et al., *OmpB (osmo-regulation) and icsA (cell-to-cell spread) mutants of Shigella flexneri: vaccine candidates and probes to study the pathogenesis of shigellosis.* Vaccine, 1991. **9**(6): p. 416-22.

214. Domann, E., et al., *A novel bacterial virulence gene in Listeria monocytogenes required for host cell microfilament interaction with homology to the proline-rich region of vinculin.* The EMBO journal, 1992. **11**(5): p. 1981-90.

215. Parkinson, J.E. and G.L. Smith, *Vaccinia virus gene A36R encodes a M(r) 43-50 K protein on the surface of extracellular enveloped virus.* Virology, 1994. **204**(1): p. 376-90.

216. Smith, G.A., J.A. Theriot, and D.A. Portnoy, *The tandem repeat domain in the Listeria monocytogenes ActA protein controls the rate of actin-based motility, the percentage of moving bacteria, and the localization of vasodilator-stimulated phosphoprotein and profilin.* The Journal of cell biology, 1996. **135**(3): p. 647-60.

217. Geese, M., et al., *Contribution of Ena/VASP proteins to intracellular motility of listeria requires phosphorylation and proline-rich core but not F-actin binding or multimerization.* Molecular Biology of the Cell, 2002. **13**(7): p. 2383-96.

218. Yoshikawa, Y., et al., *Listeria monocytogenes ActA-mediated escape from autophagic recognition.* Nature Cell Biology, 2009. **11**(10): p. 1233-40.

219. Travier, L., et al., *ActA promotes Listeria monocytogenes aggregation, intestinal colonization and carriage.* PLoS Pathogens, 2013. **9**(1): p. e1003131.

220. Egile, C., et al., *Activation of the CDC42 effector N-WASP by the Shigella flexneri IcsA protein promotes actin nucleation by Arp2/3 complex and bacterial actin-based motility.* The Journal of cell biology, 1999. **146**(6): p. 1319-32.

221. Breitbach, K., et al., *Actin-based motility of Burkholderia pseudomallei involves the Arp 2/3 complex, but not N-WASP and Ena/VASP proteins.* Cellular Microbiology, 2003. **5**(6): p. 385-93.

222. Stevens, M.P., et al., *Identification of a bacterial factor required for actin-based motility of Burkholderia pseudomallei.* Molecular Microbiology, 2005. **56**(1): p. 40-53.

223. Zhao, G., et al., *The genome of Yoka poxvirus.* Journal of Virology, 2011. **85**(19): p. 10230-8.

224. Afonso, P.P., et al., *Biological characterization and next-generation genome sequencing of the unclassified Cotia virus SPAn232 (Poxviridae).* Journal of Virology, 2012. **86**(9): p. 5039-54.

225. Griffiths, G., et al., *Structure and assembly of intracellular mature vaccinia virus: thin-section analyses.* Journal of Virology, 2001. **75**(22): p. 11056-70.

226. Griffiths, G., et al., *Structure and assembly of intracellular mature vaccinia virus: isolated-particle analysis.* Journal of Virology, 2001. **75**(22): p. 11034-55.

227. Cyrklaff, M., et al., *Cryo-electron tomography of vaccinia virus.* Proceedings of the National Academy of Sciences of the United States of America, 2005. **102**(8): p. 2772-7.

228. Condit, R.C., N. Moussatche, and P. Traktman, *In a nutshell: structure and assembly of the vaccinia virion.* Advances in Virus Research, 2006. **66**: p. 31-124.

229. Upton, C., et al., *Poxvirus Orthologous Clusters: toward Defining the Minimum Essential Poxvirus Genome.* Journal of Virology, 2003. **77**(13): p. 7590-7600.

230. Gubser, C., *Poxvirus genomes: a phylogenetic analysis.* Journal of General Virology, 2004. **85**(1): p. 105-117.

231. Iyer, L.M., et al., *Evolutionary genomics of nucleo-cytoplasmic large DNA viruses.* Virus Research, 2006. **117**(1): p. 156-84.

232. Behbehani, A.M., *The smallpox story: life and death of an old disease.* Microbiological Reviews, 1983. **47**(4): p. 455-509.

233. Henderson, D.A., et al., *Smallpox as a biological weapon: medical and public health management. Working Group on Civilian Biodefense.* JAMA, 1999. **281**(22): p. 2127-37.

234. Riedel, S., *Edward Jenner and the history of smallpox and vaccination.* Proceedings, 2005. **18**(1): p. 21-5.

235. Baxby, D., *The origins of vaccinia virus.* The Journal of infectious diseases, 1977. **136**(3): p. 453-5.

236. McFadden, G., *Poxvirus tropism.* Nature Reviews. Microbiology, 2005. **3**(3): p. 201-13.

237. Buller, R.M. and G.J. Palumbo, *Poxvirus pathogenesis.* Microbiol Rev, 1991. **55**(1): p. 80-122.

238. Huygelen, C., *[Jenner's cowpox vaccine in light of current vaccinology].* Verhandelingen - Koninklijke Academie voor Geneeskunde van Belgie, 1996. **58**(5): p. 479-536; discussion 537-8.

239. Goebel, S.J., et al., *The complete DNA sequence of vaccinia virus.* Virology, 1990. **179**(1): p. 247-66.

240. Meyer, H., G. Sutter, and A. Mayr, *Mapping of deletions in the genome of the highly attenuated vaccinia virus MVA and their influence on virulence.* The Journal of general virology, 1991. **72 (Pt 5)**: p. 1031-8.

241. DeFilippes, F.M., *Restriction enzyme mapping of vaccinia virus DNA.* Journal of Virology, 1982. **43**(1): p. 136-49.

242. Moss, B., *Poxvirus cell entry: how many proteins does it take?* Viruses, 2012. **4**(5): p. 688-707.

243. Townsley, A.C., et al., *Vaccinia virus entry into cells via a low-pH-dependent endosomal pathway.* Journal of Virology, 2006. **80**(18): p. 8899-908.

244. Carter, G.C., et al., *Entry of the vaccinia virus intracellular mature virion and its interactions with glycosaminoglycans.* The Journal of general virology, 2005. **86**(Pt 5): p. 1279-90.

245. Laliberte, J.P., A.S. Weisberg, and B. Moss, *The membrane fusion step of vaccinia virus entry is cooperatively mediated by multiple viral proteins and host cell components.* PLoS Pathogens, 2011. **7**(12): p. e1002446.

246. Senkevich, T.G. and B. Moss, *Vaccinia virus H2 protein is an essential component of a complex involved in virus entry and cell-cell fusion.* Journal of Virology, 2005. **79**(8): p. 4744-54.

247. Moss, B., *Poxvirus entry and membrane fusion.* Virology, 2006. **344**(1): p. 48-54.

248. Mallardo, M., S. Schleich, and J. Krijnse Locker, *Microtubule-dependent organization of vaccinia virus core-derived early mRNAs into distinct cytoplasmic structures.* Molecular Biology of the Cell, 2001. **12**(12): p. 3875-91.

249. Mallardo, M., et al., *Relationship between vaccinia virus intracellular cores, early mRNAs, and DNA replication sites.* Journal of Virology, 2002. **76**(10): p. 5167-83.

250. Tolonen, N., et al., *Vaccinia virus DNA replication occurs in endoplasmic reticulum-enclosed cytoplasmic mini-nuclei.* Molecular biology of the cell, 2001. **12**(7): p. 2031-46.

251. Munyon, W., E. Paoletti, and J.T. Grace, Jr., *RNA polymerase activity in purified infectious vaccinia virus.* Proceedings of the National Academy of Sciences of the United States of America, 1967. **58**(6): p. 2280-7.

252. Baldick, C.J., Jr. and B. Moss, *Characterization and temporal regulation of mRNAs encoded by vaccinia virus intermediate-stage genes.* Journal of Virology, 1993. **67**(6): p. 3515-27.

253. Davison, A.J. and B. Moss, *Structure of vaccinia virus late promoters.* Journal of Molecular Biology, 1989. **210**(4): p. 771-84.

254. Davison, A.J. and B. Moss, *Structure of vaccinia virus early promoters.* Journal of Molecular Biology, 1989. **210**(4): p. 749-69.

255. Baldick, C.J., Jr., J.G. Keck, and B. Moss, *Mutational analysis of the core, spacer, and initiator regions of vaccinia virus intermediate-class promoters.* Journal of Virology, 1992. **66**(8): p. 4710-9.

256. Yang, Z., et al., *Expression profiling of the intermediate and late stages of poxvirus replication.* Journal of Virology, 2011. **85**(19): p. 9899-908.

257. Broyles, S.S., *Vaccinia virus transcription.* Journal of General Virology, 2003. **84**(9): p. 2293-2303.

258. Condit, R.C., *Vaccinia, Inc.--probing the functional substructure of poxviral replication factories.* Cell Host and Microbe, 2007. **2**(4): p. 205-7.

259. Moss, B. and E.N. Rosenblum, *Protein cleavage and poxvirus morphogenesis: tryptic peptide analysis of core precursors accumulated by blocking assembly with rifampicin.* Journal of Molecular Biology, 1973. **81**(2): p. 267-9.

260. Schmelz, M., et al., *Assembly of vaccinia virus: the second wrapping cisterna is derived from the trans Golgi network.* Journal of Virology, 1994. **68**(1): p. 130-47.

261. Sodeik, B. and J. Krijnse-Locker, *Assembly of vaccinia virus revisited: de novo membrane synthesis or acquisition from the host?* Trends in Microbiology, 2002. **10**(1): p. 15-24.

262. Roberts, K.L. and G.L. Smith, *Vaccinia virus morphogenesis and dissemination.* Trends in Microbiology, 2008. **16**(10): p. 472-9.

263. Hollinshead, M., et al., *Vaccinia virus utilizes microtubules for movement to the cell surface.* Journal of Cell Biology, 2001. **154**(2): p. 389-402.

264. Cudmore, S., et al., *Actin-based motility of vaccinia virus.* Nature, 1995. **378**(6557): p. 636-8.

265. Payne, L.G., *Significance of extracellular enveloped virus in the in vitro and in vivo dissemination of vaccinia.* The Journal of general virology, 1980. **50**(1): p. 89-100.

266. Smith, G.L., A. Vanderplasschen, and M. Law, *The formation and function of extracellular enveloped vaccinia virus.* Journal of General Virology, 2002. **83**(Pt 12): p. 2915-31.

267. Vanderplasschen, A., et al., *Extracellular enveloped vaccinia virus is resistant to complement because of incorporation of host complement control proteins into its envelope.* Proceedings of the National Academy of Sciences of the United States of America, 1998. **95**(13): p. 7544-9.

268. Chung, C.S., et al., *Vaccinia virus proteome: identification of proteins in vaccinia virus intracellular mature virion particles.* Journal of Virology, 2006. **80**(5): p. 2127-40.

269. Perdiguero, B., M.M. Lorenzo, and R. Blasco, *Vaccinia virus A34 glycoprotein determines the protein composition of the extracellular virus envelope.* Journal of Virology, 2008. **82**(5): p. 2150-60.

270. Perdiguero, B. and R. Blasco, *Interaction between vaccinia virus extracellular virus envelope A33 and B5 glycoproteins.* Journal of Virology, 2006. **80**(17): p. 8763-8777.

271. Sanderson, C.M., et al., *Roles of vaccinia virus EEV-specific proteins in intracellular actin tail formation and low pH-induced cell-cell fusion.* Journal of General Virology, 1998. **79**(Pt 6): p. 1415-25.

272. Engelstad, M. and G.L. Smith, *The vaccinia virus 42-kDa envelope protein is required for the envelopment and egress of extracellular virus and for virus virulence.* Virology, 1993. **194**(2): p. 627-37.

273. Herrera, E., et al., *Functional analysis of vaccinia virus B5R protein: essential role in virus envelopment is independent of a large portion of the extracellular domain.* Journal of Virology, 1998. **72**(1): p. 294-302.

274. Vazquez, M.I., et al., *The vaccinia virus 14-kilodalton (A27L) fusion protein forms a triple coiled-coil structure and interacts with the 21-kilodalton (A17L) virus membrane protein through a C-terminal alpha-helix.* Journal of Virology, 1998. **72**(12): p. 10126-37.

275. Chung, C.S., et al., *A27L protein mediates vaccinia virus interaction with cell surface heparan sulfate.* Journal of Virology, 1998. **72**(2): p. 1577-85.

276. Howard, A.R., T.G. Senkevich, and B. Moss, *Vaccinia virus A26 and A27 proteins form a stable complex tethered to mature virions by association with the A17 transmembrane protein.* Journal of Virology, 2008. **82**(24): p. 12384-91.

277. Chang, T.H., et al., *Crystal structure of vaccinia viral A27 protein reveals a novel structure critical for its function and complex formation with A26 protein.* PLoS Pathogens, 2013. **9**(8): p. e1003563.

278. Rodriguez, J.F., E. Paez, and M. Esteban, *A 14,000-Mr envelope protein of vaccinia virus is involved in cell fusion and forms covalently linked trimers.* Journal of Virology, 1987. **61**(2): p. 395-404.

279. Kochan, G., et al., *Membrane cell fusion activity of the vaccinia virus A17-A27 protein complex.* Cellular Microbiology, 2008. **10**(1): p. 149-64.

280. Ward, B.M., *Visualization and characterization of the intracellular movement of vaccinia virus intracellular mature virions.* Journal of Virology, 2005. **79**(8): p. 4755-63.

281. van Eijl, H., M. Hollinshead, and G.L. Smith, *The vaccinia virus A36R protein is a type Ib membrane protein present on intracellular but not extracellular enveloped virus particles.* Virology, 2000. **271**(1): p. 26-36.

282. Rietdorf, J., et al., *Kinesin-dependent movement on microtubules precedes actin-based motility of vaccinia virus.[see comment].* Nature Cell Biology, 2001. **3**(11): p. 992-1000.

283. Herrero-Martinez, E., et al., *Vaccinia virus intracellular enveloped virions move to the cell periphery on microtubules in the absence of the A36R protein.* Journal of General Virology, 2005. **86**(Pt 11): p. 2961-8.

284. Geada, M.M., et al., *Movements of vaccinia virus intracellular enveloped virions with GFP tagged to the F13L envelope protein.* Journal of General Virology, 2001. **82**(Pt 11): p. 2747-60.

285. Dodding, M., et al., *An E2-F12 complex is required for IEV morphogenesis during vaccinia infection.* Cellular Microbiology, 2009. **11**(5): p. 808-824.

286. Dodding, M.P., et al., *A kinesin-1 binding motif in vaccinia virus that is widespread throughout the human genome.* The EMBO journal, 2011.

287. Schepis, A., T. Stauber, and J. Krijnse Locker, *Kinesin-1 plays multiple roles during the vaccinia virus life cycle.* Cellular Microbiology, 2007. **9**(8): p. 1960-73.

288. Jeshtadi, A., et al., *Interaction of poxvirus intracellular mature virion proteins with the TPR domain of kinesin light chain in live infected cells revealed by two-photon-induced fluorescence resonance energy transfer fluorescence lifetime imaging microscopy.* Journal of Virology, 2010. **84**(24): p. 12886-94.

289. van Eijl, H., et al., *The vaccinia virus F12L protein is associated with intracellular enveloped virus particles and is required for their egress to the cell surface.* Journal of General Virology, 2002. **83**(Pt 1): p. 195-207.

290. Morgan, G.W., et al., *Vaccinia protein F12 has structural similarity to kinesin light chain and contains a motor binding motif required for virion export.* PLoS Pathog, 2010. **6**(2): p. e1000785.

291. Johnston, S.C. and B.M. Ward, *The vaccinia virus protein F12 associates with IEV through an interaction with A36.* Journal of Virology, 2009. **83**(4): p. 1708-17.

292. Frischknecht, F., et al., *Actin-based motility of vaccinia virus mimics receptor tyrosine kinase signalling.* Nature, 1999. **401**(6756): p. 926-9.

293. Scaplehorn, N., et al., *Grb2 and Nck act cooperatively to promote actin-based motility of vaccinia virus.* Current Biology, 2002. **12**(9): p. 740-5.

294. Moreau, V., et al., *A complex of N-WASP and WIP integrates signalling cascades that lead to actin polymerization.* Nature Cell Biology, 2000. **2**(7): p. 441-8.

295. Weisswange, I., et al., *The rate of N-WASP exchange limits the extent of Arp2/3 complex dependent actin-based motility.* Nature, 2009. **458**(7234): p. 87-91.

296. Newsome, T.P., N. Scaplehorn, and M. Way, *SRC mediates a switch from microtubule- to actin-based motility of vaccinia virus.[see comment].* Science, 2004. **306**(5693): p. 124-9.

297. Newsome, T.P., et al., *Abl collaborates with Src family kinases to stimulate actin-based motility of vaccinia virus.* Cellular Microbiology, 2006. **8**(2): p. 233-41.

298. Reeves, P.M., et al., *Disabling poxvirus pathogenesis by inhibition of Abl-family tyrosine kinases.[see comment][erratum appears in Nat Med. 2005 Dec;11(12):1361].* Nature Medicine, 2005. **11**(7): p. 731-9.

299. Doceul, V., et al., *Repulsion of Superinfecting Virions: A Mechanism for Rapid Virus Spread.* Science, 2010. **327**: p. 873-876.

300. Ward, B.M. and B. Moss, *Vaccinia virus intracellular movement is associated with microtubules and independent of actin tails.* Journal of Virology, 2001. **75**(23): p. 11651-63.

301. Frischknecht, F., et al., *Tyrosine phosphorylation is required for actin-based motility of vaccinia but not Listeria or Shigella.* Current Biology, 1999. **9**(2): p. 89-92.

302. Horsington, J., et al., *A36-dependent actin filament nucleation promotes release of vaccinia virus.* PLoS Pathogens, 2013. **9**(3): p. e1003239.

303. Zhang, W.H., D. Wilcock, and G.L. Smith, *Vaccinia virus F12L protein is required for actin tail formation, normal plaque size, and virulence.* Journal of Virology, 2000. **74**(24): p. 11654-62.

304. Johnston, S.C. and B.M. Ward, *The vaccinia virus protein F12 associates with IEV through an interaction with A36.* Journal of Virology, 2009.

305. Domi, A., A.S. Weisberg, and B. Moss, *Vaccinia virus E2L null mutants exhibit a major reduction in extracellular virion formation and virus spread.* Journal of Virology, 2008. **82**(9): p. 4215-26.

306. Yutin, N., et al., *Chordopoxvirus protein F12 implicated in enveloped virion morphogenesis is an inactivated DNA polymerase.* Biology Direct, 2014. **9**(1): p. 22.

307. Newsome, T.P., et al., *Navigating the subcellular space: lessons from vaccinia virus*, in *Viral transport, assembly and egress*, R.J. Diefenbach and A.L. Cunningham, Editors. 2010, Research Signpost/Transworld Research Network: Kerala, India.

308. Chakrabarti, S., J.R. Sisler, and B. Moss, *Compact, synthetic, vaccinia virus early/late promoter for protein expression.* Biotechniques, 1997. **23**(6): p. 1094-7.

309. Holden, J.A., P.D. Harriman, and J.D. Wall, *Escherichia coli mutants deficient in guanine-xanthine phosphoribosyltransferase.* Journal of Bacteriology, 1976. **126**(3): p. 1141-8.

310. Campbell, R.E., et al., *A monomeric red fluorescent protein.* Proceedings of the National Academy of Sciences of the United States of America, 2002. **99**(12): p. 7877-82.

311. Falkner, F.G. and B. Moss, *Escherichia-Coli Gpt Gene Provides Dominant Selection for Vaccinia Virus Open Reading Frame Expression Vectors.* Journal of Virology, 1988. **62**(6): p. 1849-1854.

312. Chudakov, D.M., S. Lukyanov, and K.A. Lukyanov, *Tracking intracellular protein movements using photoswitchable fluorescent proteins PS-CFP2 and Dendra2.* Nature Protocols, 2007. **2**(8): p. 2024-2032.

313. Marzook, N.B., et al., *Methodology for the efficient generation of fluorescently tagged vaccinia virus proteins.* Journal of visualized experiments : JoVE, 2014(83): p. e51151.

314. Cordeiro, J.V., et al., *F11-Mediated Inhibition of RhoA Signalling Enhances the Spread of Vaccinia Virus In Vitro and In Vivo in an Intranasal Mouse Model of Infection.* Plos One, 2009. **4**(12).

315. Riedl, J., et al., *Lifeact: a versatile marker to visualize F-actin.* Nat Methods, 2008. **5**(7): p. 605-7.

316. Zhang, G., V. Gurtu, and S.R. Kain, *An enhanced green fluorescent protein allows sensitive detection of gene transfer in mammalian cells.* Biochemical and Biophysical Research Communications, 1996. **227**(3): p. 707-11.

317. Arakawa, Y., et al., *The release of vaccinia from infected cells requires RhoA-mDia modulation of cortical actin.* Cell Host & Microbe, 2007. **1**(3): p. 227-240.

318. Snapper, S.B., et al., *N-WASP deficiency reveals distinct pathways for cell surface projections and microbial actin-based motility.* Nature Cell Biology, 2001. **3**(10): p. 897-904.

319. Panicali, D. and E. Paoletti, *Construction of poxviruses as cloning vectors: insertion of the thymidine kinase gene from herpes simplex virus into the DNA of infectious vaccinia virus.* Proceedings of the National Academy of Sciences of the United States of America, 1982. **79**(16): p. 4927-31.

320. Mackett, M., G.L. Smith, and B. Moss, *General method for production and selection of infectious vaccinia virus recombinants expressing foreign genes.* Journal of Virology, 1984. **49**(3): p. 857-64.

321. Falkner, F.G. and B. Moss, *Transient dominant selection of recombinant vaccinia viruses.* Journal of Virology, 1990. **64**(6): p. 3108-11.

322. Fenner, F. and B.M. Comben, *Genetic studies with mammalian poxviruses. I. Demonstration of recombination between two strains of vaccina virus.* Virology, 1958. **5**(3): p. 530-48.

323. Willer, D.O., et al., *Vaccinia virus DNA polymerase promotes DNA pairing and strand-transfer reactions.* Virology, 1999. **257**(2): p. 511-23.

324. Yao, X.D. and D.H. Evans, *Characterization of the recombinant joints formed by single-strand annealing reactions in vaccinia virus-infected cells.* Virology, 2003. **308**(1): p. 147-56.

325. Wolffe, E.J., S.N. Isaacs, and B. Moss, *Deletion of the vaccinia virus B5R gene encoding a 42-kilodalton membrane glycoprotein inhibits extracellular virus envelope formation and dissemination.[erratum appears in J Virol 1993 Sep;67(9):5709-11].* Journal of Virology, 1993. **67**(8): p. 4732-41.

326. Yao, X.D. and D.H. Evans, *Effects of DNA structure and homology length on vaccinia virus recombination.* Journal of Virology, 2001. **75**(15): p. 6923-32.

327. Rodriguez, J.F., R. Janeczko, and M. Esteban, *Isolation and characterization of neutralizing monoclonal antibodies to vaccinia virus.* Journal of virology, 1985. **56**(2): p. 482-8.

328. Mombaerts, P., et al., *RAG-1-deficient mice have no mature B and T lymphocytes.* Cell, 1992. **68**(5): p. 869-77.

329. Chaudhri, G., et al., *Polarized type 1 cytokine response and cell-mediated immunity determine genetic resistance to mousepox.* Proceedings of the National Academy of Sciences of the United States of America, 2004. **101**(24): p. 9057-62.

330. Panchanathan, V., G. Chaudhri, and G. Karupiah, *Interferon function is not required for recovery from a secondary poxvirus infection.* Proceedings of the National Academy of Sciences of the United States of America, 2005. **102**(36): p. 12921-6.

331. Karupiah, G., et al., *Different roles for CD4+ and CD8+ T lymphocytes and macrophage subsets in the control of a generalized virus infection.* Journal of virology, 1996. **70**(12): p. 8301-9.

332. Heim, R., A.B. Cubitt, and R.Y. Tsien, *Improved green fluorescence.* Nature, 1995. **373**(6516): p. 663-4.

333. Nolte, A., J.B. Pawley, and L. Horing, *Non-laser light sources for three-dimensional microscopy*, in *Handbook of Biological Confocal Microscopy*, J.B. Pawley, Editor 2006, Springer: New York. p. 126-143.

334. Shaner, N.C., et al., *Improved monomeric red, orange and yellow fluorescent proteins derived from Discosoma sp. red fluorescent protein.* Nature Biotechnology, 2004. **22**(12): p. 1567-72.

335. Shaner, N.C., et al., *Improving the photostability of bright monomeric orange and red fluorescent proteins.* Nature Methods, 2008. **5**(6): p. 545-51.

336. Tsien, R.Y., *Constructing and exploiting the fluorescent protein paintbox (Nobel Lecture).* Angewandte Chemie, 2009. **48**(31): p. 5612-26.

337. Shcherbo, D., et al., *Near-infrared fluorescent proteins.* Nature Methods, 2010. **7**(10): p. 827-9.

338. Prasher, D.C., et al., *Primary structure of the Aequorea victoria green-fluorescent protein.* Gene, 1992. **111**(2): p. 229-33.

339. Chalfie, M., et al., *Green fluorescent protein as a marker for gene expression.* Science, 1994. **263**(5148): p. 802-5.

340. Tsien, R.Y., *The green fluorescent protein.* Annual Review of Biochemistry, 1998. **67**: p. 509-544.

341. Ward, W.W. and S.H. Bokman, *Reversible denaturation of Aequorea green-fluorescent protein: physical separation and characterization of the renatured protein.* Biochemistry, 1982. **21**(19): p. 4535-40.

342. Cody, C.W., et al., *Chemical structure of the hexapeptide chromophore of the Aequorea green-fluorescent protein.* Biochemistry, 1993. **32**(5): p. 1212-8.

343. Yang, T.T., L. Cheng, and S.R. Kain, *Optimized codon usage and chromophore mutations provide enhanced sensitivity with the green fluorescent protein.* Nucleic Acids Research, 1996. **24**(22): p. 4592-3.

344. Ormo, M., et al., *Crystal structure of the Aequorea victoria green fluorescent protein.* Science, 1996. **273**(5280): p. 1392-5.

345. Chudakov, D.M., et al., *Fluorescent proteins and their applications in imaging living cells and tissues.* Physiological Reviews, 2010. **90**(3): p. 1103-63.

346. Cormack, B.P., R.H. Valdivia, and S. Falkow, *FACS-optimized mutants of the green fluorescent protein (GFP).* Gene, 1996. **173**(1 Spec No): p. 33-8.

347. Zacharias, D.A., *Sticky caveats in an otherwise glowing report: oligomerizing fluorescent proteins and their use in cell biology.* Science's STKE : signal transduction knowledge environment, 2002. **2002**(131): p. pe23.

348. Delagrave, S., et al., *Red-shifted excitation mutants of the green fluorescent protein.* Bio/Technology, 1995. **13**(2): p. 151-4.

349. Cubitt, A.B., et al., *Understanding, improving and using green fluorescent proteins.* Trends in Biochemical Sciences, 1995. **20**(11): p. 448-55.

350. Lippincott-Schwartz, J. and G.H. Patterson, *Development and use of fluorescent protein markers in living cells.* Science, 2003. **300**(5616): p. 87-91.

351. Heim, R., D.C. Prasher, and R.Y. Tsien, *Wavelength mutations and posttranslational autoxidation of green fluorescent protein.* Proceedings of the National Academy of Sciences of the United States of America, 1994. **91**(26): p. 12501-4.

352. Nagai, T., et al., *A variant of yellow fluorescent protein with fast and efficient maturation for cell-biological applications.* Nature Biotechnology, 2002. **20**(1): p. 87-90.

353. Matz, M.V., et al., *Fluorescent proteins from nonbioluminescent Anthozoa species.* Nature Biotechnology, 1999. **17**(10): p. 969-73.

354. Shaner, N.C., P.A. Steinbach, and R.Y. Tsien, *A guide to choosing fluorescent proteins.* Nature Methods, 2005. **2**(12): p. 905-9.

355. Ishikawa-Ankerhold, H.C., R. Ankerhold, and G.P. Drummen, *Advanced fluorescence microscopy techniques--FRAP, FLIP, FLAP, FRET and FLIM.* Molecules, 2012. **17**(4): p. 4047-132.

356. Patterson, G.H. and J. Lippincott-Schwartz, *A photoactivatable GFP for selective photolabeling of proteins and cells.* Science, 2002. **297**(5588): p. 1873-7.

357. Ando, R., et al., *An optical marker based on the UV-induced green-to-red photoconversion of a fluorescent protein.* Proceedings of the National Academy of Sciences of the United States of America, 2002. **99**(20): p. 12651-6.

358. Wiedenmann, J., et al., *EosFP, a fluorescent marker protein with UV-inducible green-to-red fluorescence conversion.* Proceedings of the National Academy of Sciences of the United States of America, 2004. **101**(45): p. 15905-10.

359. McKinney, S.A., et al., *A bright and photostable photoconvertible fluorescent protein.* Nature Methods, 2009. **6**(2): p. 131-3.

360. Henderson, J.N., et al., *Structure and mechanism of the photoactivatable green fluorescent protein.* Journal of the American Chemical Society, 2009. **131**(12): p. 4176-7.

361. Tsutsui, H., et al., *Semi-rational engineering of a coral fluorescent protein into an efficient highlighter.* EMBO Reports, 2005. **6**(3): p. 233-8.

362. Mizuno, H., et al., *Photo-induced peptide cleavage in the green-to-red conversion of a fluorescent protein.* Molecular Cell, 2003. **12**(4): p. 1051-1058.

363. Hess, S.T., *Red lights, camera, photoactivation!* Nature Methods, 2009. **6**(2): p. 124-125.

364. Chudakov, D.M., et al., *Photoswitchable cyan fluorescent protein for protein tracking.* Nature Biotechnology, 2004. **22**(11): p. 1435-1439.

365. Gurskaya, N.G., et al., *Engineering of a monomeric green-to-red photoactivatable fluorescent protein induced by blue light.* Nature Biotechnology, 2006. **24**(4): p. 461-5.

366. Dunkern, T.R., G. Fritz, and B. Kaina, *Ultraviolet light-induced DNA damage triggers apoptosis in nucleotide excision repair-deficient cells via Bcl-2 decline and caspase-3/-8 activation.* Oncogene, 2001. **20**(42): p. 6026-6038.

367. Rosel, J. and B. Moss, *Transcriptional and translational mapping and nucleotide sequence analysis of a vaccinia virus gene encoding the precursor of the major core polypeptide 4b.* Journal of Virology, 1985. **56**(3): p. 830-8.

368. Vanslyke, J.K., C.A. Franke, and D.E. Hruby, *Proteolytic Maturation of Vaccinia Virus Core Proteins - Identification of a Conserved Motif at the N Termini of the 4b and 25k Virion Proteins.* Journal of General Virology, 1991. **72**: p. 411-416.

369. Lee, P. and D.E. Hruby, *Proteolytic cleavage of vaccinia virus virion proteins. Mutational analysis of the specificity determinants.* The Journal of biological chemistry, 1994. **269**(11): p. 8616-22.

370. Sarov, I. and W.K. Joklik, *Studies on the nature and location of the capsid polypeptides of vaccinia virions.* Virology, 1972. **50**(2): p. 579-92.

371. Resch, W., et al., *Protein composition of the vaccinia virus mature virion.* Virology, 2007. **358**(1): p. 233-47.

372. Engelstad, M., S.T. Howard, and G.L. Smith, *A constitutively expressed vaccinia gene encodes a 42-kDa glycoprotein related to complement control factors that forms part of the extracellular virus envelope.* Virology, 1992. **188**(2): p. 801-10.

373. Isaacs, S.N., et al., *Characterization of a vaccinia virus-encoded 42-kilodalton class I membrane glycoprotein component of the extracellular virus envelope.* Journal of Virology, 1992. **66**(12): p. 7217-24.

374. Ward, B.M. and B. Moss, *Visualization of intracellular movement of vaccinia virus virions containing a green fluorescent protein-B5R membrane protein chimera.* Journal of Virology, 2001. **75**(10): p. 4802-13.

375. Grosenbach, D.W., D.O. Ulaeto, and D.E. Hruby, *Palmitylation of the vaccinia virus 37-kDa major envelope antigen. Identification of a conserved acceptor motif and biological relevance.* The Journal of biological chemistry, 1997. **272**(3): p. 1956-64.

376. Grosenbach, D.W. and D.E. Hruby, *Analysis of a vaccinia virus mutant expressing a nonpalmitylated form of p37, a mediator of virion envelopment.* Journal of Virology, 1998. **72**(6): p. 5108-20.

377. Husain, M. and B. Moss, *Vaccinia virus F13L protein with a conserved phospholipase catalytic motif induces colocalization of the B5R envelope glycoprotein in post-Golgi vesicles.* Journal of Virology, 2001. **75**(16): p. 7528-42.

378. Hiller, G. and K. Weber, *Golgi-derived membranes that contain an acylated viral polypeptide are used for vaccinia virus envelopment.* Journal of Virology, 1985. **55**(3): p. 651-9.

379. Blasco, R. and B. Moss, *Extracellular vaccinia virus formation and cell-to-cell virus transmission are prevented by deletion of the gene encoding the 37,000-Dalton outer envelope protein.* Journal of Virology, 1991. **65**(11): p. 5910-20.

380. Vliegen, I., et al., *Deletion of the vaccinia virus F13L gene results in a highly attenuated virus that mounts a protective immune response against subsequent vaccinia virus challenge.* Antiviral Research, 2012. **93**(1): p. 160-6.

381. Ward, B.M. and B. Moss, *Golgi network targeting and plasma membrane internalization signals in vaccinia virus B5R envelope protein.* Journal of Virology, 2000. **74**(8): p. 3771-80.

382. Terpe, K., *Overview of tag protein fusions: from molecular and biochemical fundamentals to commercial systems.* Applied Microbiology and Biotechnology, 2003. **60**(5): p. 523-33.

383. Bernas, T., et al., *Loss of image quality in photobleaching during microscopic imaging of fluorescent probes bound to chromatin.* Journal of Biomedical Optics, 2005. **10**(6): p. 064015.

384. Sheppard, C.R., et al., *Signal-to-Noise Ratio in Confocal Microscopes*, in *Handbook Of Biological Confocal Microscopy*, J.B. Pawley, Editor 2006, Springer US. p. 442-452.

385. Patterson, G.H., et al., *Use of the green fluorescent protein and its mutants in quantitative fluorescence microscopy.* Biophysical Journal, 1997. **73**(5): p. 2782-90.

386. Olenych, S.G., et al., *The fluorescent protein color palette.* Current protocols in cell biology / editorial board, Juan S. Bonifacino ... [et al.], 2007. **Chapter 21**: p. Unit 21 5.

387. Olympus, *Fluoview - Always Evolving (Confocal Laser Scanning Biological Microscope FV1000 Fluoview)*, in *Internet.*

388. Webb, R.H., *Confocal optical microscopy.* Reports on Progress in Physics, 1996. **59**(3): p. 427.

389. Nowotschin, S. and A.K. Hadjantonakis, *Use of KikGR a photoconvertible green-to-red fluorescent protein for cell labeling and lineage analysis in ES cells and mouse embryos.* BMC Developmental Biology, 2009. **9**: p. 49.

390. Rizzo, M.A., et al., *An improved cyan fluorescent protein variant useful for FRET.* Nature Biotechnology, 2004. **22**(4): p. 445-9.

391. Kulesa, P.M., et al., *Watching the assembly of an organ a single cell at a time using confocal multi-position photoactivation and multi-time acquisition.* Organogenesis, 2009. **5**(4): p. 238-247.

392. Helmchen, F. and W. Denk, *Deep tissue two-photon microscopy.* Nature Methods, 2005. **2**(12): p. 932-40.

393. Chudakov, D.M., S. Lukyanov, and K.A. Lukyanov, *Fluorescent proteins as a toolkit for in vivo imaging.* Trends in Biotechnology, 2005. **23**(12): p. 605-13.

394. Stark, D.A. and P.M. Kulesa, *An in vivo comparison of photoactivatable fluorescent proteins in an avian embryo model.* Developmental dynamics : an official publication of the American Association of Anatomists, 2007. **236**(6): p. 1583-94.

395. Xia, J., et al., *Practical three color live cell imaging by widefield microscopy.* Biological procedures online, 2006. **8**: p. 63-8.

396. Baltrusch, S. and S. Lenzen, *Novel insights into the regulation of the bound and diffusible glucokinase in MIN6 beta-cells.* Diabetes, 2007. **56**(5): p. 1305-1315.

397. Chudakov, D.M., S. Lukyanov, and K.A. Lukyanov, *Using photoactivatable fluorescent protein Dendra2 to track protein movement.* Biotechniques, 2007. **42**(5): p. 553, 555, 557 passim.

398. Wu, S., et al., *Assessing the utility of photoswitchable fluorescent proteins for tracking intercellular protein movement in the Arabidopsis root.* PLoS ONE, 2011. **6**(11): p. e27536.

399. Loffler, H., et al., *DNA damage-induced centrosome amplification occurs via excessive formation of centriolar satellites.* Oncogene, 2013. **32**(24): p. 2963-72.

400. Kitagawa, M. and T. Fujita, *Quantitative imaging of directional transport through plasmodesmata in moss protonemata via single-cell photoconversion of Dendra2.* Journal of Plant Research, 2013. **126**(4): p. 577-85.

401. Kuzmenko, A., et al., *Single molecule tracking fluorescence microscopy in mitochondria reveals highly dynamic but confined movement of Tom40.* Scientific reports, 2011. **1**: p. 195.

402. Reid, B.G. and G.C. Flynn, *Chromophore formation in green fluorescent protein.* Biochemistry, 1997. **36**(22): p. 6786-91.

403. Zhang, L., et al., *Method for real-time monitoring of protein degradation at the single cell level.* Biotechniques, 2007. **42**(4): p. 446-450.

404. Evdokimov, A.G., et al., *Structural basis for the fast maturation of Arthropoda green fluorescent protein.* EMBO Reports, 2006. **7**(10): p. 1006-12.

405. Tooze, J., et al., *Progeny vaccinia and human cytomegalovirus particles utilize early endosomal cisternae for their envelopes.* European Journal of Cell Biology, 1993. **60**(1): p. 163-78.

406. Sodeik, B., et al., *Assembly of Vaccinia Virus - Role of the Intermediate Compartment between the Endoplasmic-Reticulum and the Golgi Stacks.* Journal of Cell Biology, 1993. **121**(3): p. 521-541.

407. Gomez, C.Y. and T.J. Hope, *Mobility of human immunodeficiency virus type 1 Pr55(Gag) in living cells.* Journal of Virology, 2006. **80**(17): p. 8796-8806.

408. Jones, D.M., et al., *Mobility analysis of an NS5A-GFP fusion protein in cells actively replicating hepatitis C virus subgenomic RNA.* Journal of General Virology, 2007. **88**(Pt 2): p. 470-5.

409. Peak, M.J. and J.G. Peak, *Solar-ultraviolet-induced damage to DNA.* Photo-Dermatology, 1989. **6**(1): p. 1-15.

410. Hockberger, P.E., et al., *Activation of flavin-containing oxidases underlies light-induced production of H2O2 in mammalian cells.* Proceedings of the National Academy of Sciences of the United States of America, 1999. **96**(11): p. 6255-60.

411. Wright, A., et al., *Singlet oxygen-mediated protein oxidation: evidence for the formation of reactive side chain peroxides on tyrosine residues.* Photochemistry and Photobiology, 2002. **76**(1): p. 35-46.

412. Bradley, M.O. and N.A. Sharkey, *Mutagenicity and toxicity of visible fluorescent light to cultured mammalian cells.* Nature, 1977. **266**(5604): p. 724-6.

413. Tyrrell, R.M., *Mutagenic action of monochromatic UV radiation in the solar range on human cells.* Mutation Research, 1984. **129**(1): p. 103-10.

414. Kibler, K.V., et al., *Double-stranded RNA is a trigger for apoptosis in vaccinia virus-infected cells.* Journal of Virology, 1997. **71**(3): p. 1992-2003.

415. Humlova, Z., et al., *Vaccinia virus induces apoptosis of infected macrophages.* The Journal of general virology, 2002. **83**(Pt 11): p. 2821-32.

416. Liskova, J., et al., *Apoptosis and necrosis in vaccinia virus-infected HeLa G and BSC-40 cells.* Virus Research, 2011. **160**(1-2): p. 40-50.

417. Yamamoto, A., et al., *Quantitative evaluation of cell attachment to glass, polystyrene, and fibronectin- or collagen-coated polystyrene by measurement of cell adhesive shear force and cell detachment energy.* Journal of Biomedical Materials Research, 2000. **50**(2): p. 114-24.

418. Pankov, R., *Fibronectin at a glance.* Journal of Cell Science, 2002. **115**(20): p. 3861-3863.

419. Patterson, G., R.N. Day, and D. Piston, *Fluorescent protein spectra.* Journal of Cell Science, 2001. **114**(Pt 5): p. 837-8.

420. Katz, E., E. Wolffe, and B. Moss, *Identification of second-site mutations that enhance release and spread of vaccinia virus.* Journal of Virology, 2002. **76**(22): p. 11637-44.

421. Katz, E., et al., *Mutations in the vaccinia virus A33R and B5R envelope proteins that enhance release of extracellular virions and eliminate formation of actin-containing microvilli without preventing tyrosine phosphorylation of the A36R protein.* Journal of Virology, 2003. **77**(22): p. 12266-75.

422. Doceul, V., et al., *Protein B5 is required on extracellular enveloped vaccinia virus for repulsion of superinfecting virions.* The Journal of general virology, 2012. **93**(Pt 9): p. 1876-86.

423. Smith, G.A., et al., *Local modulation of plus-end transport targets herpesvirus entry and egress in sensory axons.* Proceedings of the National Academy of Sciences of the United States of America, 2004. **101**(45): p. 16034-9.

424. Dohner, K., et al., *Function of dynein and dynactin in herpes simplex virus capsid transport.* Molecular Biology of the Cell, 2002. **13**(8): p. 2795-2809.

425. Carpentier, D.C., et al., *Vaccinia virus protein complex F12/E2 interacts with kinesin light chain isoform 2 to engage the kinesin-1 motor complex.* PLoS Pathogens, 2015. **11**(3): p. e1004723.

426. Gindhart, J.G., Jr. and L.S. Goldstein, *Tetratrico peptide repeats are present in the kinesin light chain.* Trends in Biochemical Sciences, 1996. **21**(2): p. 52-3.

427. Zhu, H., et al., *Crystal structures of the tetratricopeptide repeat domains of kinesin light chains: insight into cargo recognition mechanisms.* PLoS ONE, 2012. **7**(3): p. e33943.

428. Cai, D., et al., *Kinesin-1 structural organization and conformational changes revealed by FRET stoichiometry in live cells.* The Journal of cell biology, 2007. **176**(1): p. 51-63.

429. Johnston, S.C. and B.M. Ward, *Vaccinia virus protein F12 associates with intracellular enveloped virions through an interaction with A36.* Journal of Virology, 2009. **83**(4): p. 1708-17.

430. Marchal, J., *Infectious ectromelia. A hitherto undescribed virus disease of mice.* The Journal of Pathology and Bacteriology, 1930. **33**(3): p. 713-728.

431. Fenner, F., *Mousepox (infectious ectromelia): past, present, and future.* Laboratory Animal Science, 1981. **31**(5 Pt 2): p. 553-9.

432. Haller, S.L., et al., *Poxviruses and the evolution of host range and virulence.* Infection, genetics and evolution : journal of molecular epidemiology and evolutionary genetics in infectious diseases, 2014. **21**: p. 15-40.

433. Fenner, F., R. Wittek, and K.R. Dumbell, *Ectromelia virus*, in *The Orthopoxviruses*, F. Fenner, R. Wittek, and K.R. Dumbell, Editors. 1989, Academic Press, Inc.: San Diego, California. p. 269-298.

434. Esteban, D.J. and R.M. Buller, *Ectromelia virus: the causative agent of mousepox.* Journal of General Virology, 2005. **86**(Pt 10): p. 2645-59.

435. Buller, R.M., *Mousepox: a small animal model for biodefense research.* Applied Biosafety, 2004. **9**(1): p. 10-19.

436. Chen, N., et al., *The genomic sequence of ectromelia virus, the causative agent of mousepox.* Virology, 2003. **317**(1): p. 165-86.

437. Smith, G.L., et al., *Vaccinia virus immune evasion.* Immunological reviews, 1997. **159**: p. 137-54.

438. Moss, B. and J.L. Shisler, *Immunology 101 at poxvirus U: immune evasion genes.* Seminars in immunology, 2001. **13**(1): p. 59-66.

439. Seet, B.T., et al., *Poxviruses and immune evasion.* Annual review of immunology, 2003. **21**: p. 377-423.

440. Huang, J., et al., *The poxvirus p28 virulence factor is an E3 ubiquitin ligase.* The Journal of biological chemistry, 2004. **279**(52): p. 54110-6.

441. Wilton, B.A., et al., *Ectromelia virus BTB/kelch proteins, EVM150 and EVM167, interact with cullin-3-based ubiquitin ligases.* Virology, 2008. **374**(1): p. 82-99.

442. Erez, N., et al., *Induction of cell-cell fusion by ectromelia virus is not inhibited by its fusion inhibitory complex.* Virol J, 2009. **6**: p. 151.

443. Boratynska, A., et al., *Contribution of rearranged actin structures to the spread of Ectromelia virus infection in vitro.* Acta Virologica, 2010. **54**(1): p. 41-8.

444. Butler-Cole, C., et al., *An ectromelia virus profilin homolog interacts with cellular tropomyosin and viral A-type inclusion protein.* Virol J, 2007. **4**: p. 76.

445. Novoa, R.R., et al., *Virus factories: associations of cell organelles for viral replication and morphogenesis.* Biology of the Cell, 2005. **97**(2): p. 147-172.

446. Uruno, T., et al., *Activation of Arp2/3 complex-mediated actin polymerization by cortactin.* Nature Cell Biology, 2001. **3**(3): p. 259-66.

447. Weaver, A.M., et al., *Cortactin promotes and stabilizes Arp2/3-induced actin filament network formation.* Current biology : CB, 2001. **11**(5): p. 370-4.

448. Ammer, A.G. and S.A. Weed, *Cortactin branches out: roles in regulating protrusive actin dynamics.* Cell Motility and the Cytoskeleton, 2008. **65**(9): p. 687-707.

449. Earley, A.K., W.M. Chan, and B.M. Ward, *The Vaccinia Virus B5 Protein Requires A34 for Efficient Intracellular Trafficking from the Endoplasmic Reticulum to the Site of Wrapping and Incorporation into Progeny Virions.* Journal of Virology, 2007. **82**(5): p. 2161-2169.

450. Pulford, D.J., H. Meyer, and D. Ulaeto, *Orthologs of the vaccinia A13L and A36R virion membrane protein genes display diversity in species of the genus Orthopoxvirus.* Archives of Virology, 2002. **147**(5): p. 995-1015.

451. Duteyrat, J.L., J. Gelfi, and S. Bertagnoli, *Ultrastructural study of myxoma virus morphogenesis.* Archives of virology, 2006. **151**(11): p. 2161-80.

452. Dodding, M.P. and M. Way, *Nck- and N-WASP-dependent actin-based motility is conserved in divergent vertebrate poxviruses.* Cell Host Microbe, 2009. **6**(6): p. 536-50.

453. Law, M., et al., *Yaba-like disease virus protein Y144R, a member of the complement control protein family, is present on enveloped virions that are associated with virus-induced actin tails.* Journal of General Virology, 2004. **85**(Pt 5): p. 1279-90.

454. Goley, E.D., et al., *Dynamic nuclear actin assembly by Arp2/3 complex and a baculovirus WASP-like protein.* Science, 2006. **314**(5798): p. 464-7.

455. Zettl, M. and M. Way, *New tricks for an old dog?[comment].* Nature Cell Biology, 2001. **3**(3): p. E74-5.

456. Krause, M., et al., *Lamellipodin, an Ena/VASP ligand, is implicated in the regulation of lamellipodial dynamics.[see comment].* Developmental Cell, 2004. **7**(4): p. 571-83.

457. Zeile, W.L., et al., *Vaccinia locomotion in host cells: evidence for the universal involvement of actin-based motility sequences ABM-1 and ABM-2.* Proceedings of the National Academy of Sciences of the United States of America, 1998. **95**(23): p. 13917-22.

458. Li, Y., et al., *The profilin:actin complex localizes to sites of dynamic actin polymerization at the leading edge of migrating cells and pathogen-induced actin tails.* European Journal of Cell Biology, 2008. **87**(11): p. 893-904.

459. Grosse, R., et al., *A role for VASP in RhoA-Diaphanous signalling to actin dynamics and SRF activity.* EMBO Journal, 2003. **22**(12): p. 3050-61.

460. Alvarez, D.E. and H. Agaisse, *The formin FHOD1 and the small GTPase Rac1 promote vaccinia virus actin-based motility.* The Journal of cell biology, 2013. **202**(7): p. 1075-90.

461. Parkin, J. and B. Cohen, *An overview of the immune system.* The Lancet, 2001. **357**(9270): p. 1777-1789.

462. Bonilla, F.A. and H.C. Oettgen, *Adaptive immunity.* The Journal of allergy and clinical immunology, 2010. **125**(2 Suppl 2): p. S33-40.

463. Jacoby, R.O. and P.N. Bhatt, *Mousepox in inbred mice innately resistant or susceptible to lethal infection with ectromelia virus. II. Pathogenesis.* Laboratory Animal Science, 1987. **37**(1): p. 16-22.

464. Buller, R.M., M. Potter, and G.D. Wallace, *Variable resistance to ectromelia (mousepox) virus among genera of Mus.* Current Topics in Microbiology and Immunology, 1986. **127**: p. 319-22.

465. Doyle, S.E., et al., *Toll-like receptor 3 mediates a more potent antiviral response than Toll-like receptor 4.* Journal of Immunology, 2003. **170**(7): p. 3565-71.

466. Spellberg, B. and J.E. Edwards, Jr., *Type 1/Type 2 immunity in infectious diseases.* Clinical infectious diseases : an official publication of the Infectious Diseases Society of America, 2001. **32**(1): p. 76-102.

467. Jacoby, R.O., P.N. Bhatt, and D.G. Brownstein, *Evidence that NK cells and interferon are required for genetic resistance to lethal infection with ectromelia virus.* Archives of Virology, 1989. **108**(1-2): p. 49-58.

468. Parker, A.K., et al., *Induction of natural killer cell responses by ectromelia virus controls infection.* Journal of virology, 2007. **81**(8): p. 4070-9.

469. Fang, M., L.L. Lanier, and L.J. Sigal, *A role for NKG2D in NK cell-mediated resistance to poxvirus disease.* PLoS pathogens, 2008. **4**(2): p. e30.

470. Fenner, F., et al., *Smallpox and its eradication*1988, Geneva, Switzerland.: World Health Organisation.

471. Parker, S., et al., *Ectromelia virus infections of mice as a model to support the licensure of anti-orthopoxvirus therapeutics.* Viruses, 2010. **2**(9): p. 1918-32.

472. Parker, S., et al., *Mousepox in the C57BL/6 strain provides an improved model for evaluating anti-poxvirus therapies.* Virology, 2009. **385**(1): p. 11-21.

473. Panchanathan, V., G. Chaudhri, and G. Karupiah, *Correlates of protective immunity in poxvirus infection: where does antibody stand?* Immunology & Cell Biology, 2008. **86**(1): p. 80-6.

474. Roberts, J.A., *Histopathogenesis of mousepox. I. Respiratory infection.* British Journal of Experimental Pathology, 1962. **43**: p. 451-61.

475. Martinez, M.J., M.P. Bray, and J.W. Huggins, *A mouse model of aerosol-transmitted orthopoxviral disease: morphology of experimental aerosol-transmitted orthopoxviral disease in a cowpox virus-BALB/c mouse system.* Archives of Pathology and Laboratory Medicine, 2000. **124**(3): p. 362-77.

476. Haley, P.J., *Species differences in the structure and function of the immune system.* Toxicology, 2003. **188**(1): p. 49-71.

477. Mestas, J. and C.C.W. Hughes, *Of mice and not men: Differences between mouse and human immunology.* Journal of Immunology, 2004. **172**(5): p. 2731-2738.

478. Panchanathan, V., G. Chaudhri, and G. Karupiah, *Protective immunity against secondary poxvirus infection is dependent on antibody but not on CD4 or CD8 T-cell function.* Journal of virology, 2006. **80**(13): p. 6333-8.

479. Chaudhri, G., et al., *Obligatory requirement for antibody in recovery from a primary poxvirus infection.* Journal of virology, 2006. **80**(13): p. 6339-44.

480. Sakala, I.G., et al., *Poxvirus-encoded gamma interferon binding protein dampens the host immune response to infection.* Journal of Virology, 2007. **81**(7): p. 3346-53.

481. Xu, R.H., et al., *The orthopoxvirus type I IFN binding protein is essential for virulence and an effective target for vaccination.* Journal of Experimental Medicine, 2008. **205**(4): p. 981-92.

482. Edghill-Smith, Y., et al., *Smallpox vaccine-induced antibodies are necessary and sufficient for protection against monkeypox virus.* Nature Medicine, 2005. **11**(7): p. 740-7.

483. Walsh, S.R. and R. Dolin, *Vaccinia viruses: vaccines against smallpox and vectors against infectious diseases and tumors.* Expert Review of Vaccines, 2011. **10**(8): p. 1221-40.

484. Sutter, G. and B. Moss, *Nonreplicating vaccinia vector efficiently expresses recombinant genes.* Proceedings of the National Academy of Sciences of the United States of America, 1992. **89**(22): p. 10847-51.

485. Gomez, C.E., et al., *The poxvirus vectors MVA and NYVAC as gene delivery systems for vaccination against infectious diseases and cancer.* Current Gene Therapy, 2008. **8**(2): p. 97-120.

486. Jacobs, B.L., et al., *Vaccinia virus vaccines: past, present and future.* Antiviral Research, 2009. **84**(1): p. 1-13.

487. McIntosh, A.A. and G.L. Smith, *Vaccinia virus glycoprotein A34R is required for infectivity of extracellular enveloped virus.* Journal of Virology, 1996. **70**(1): p. 272-81.

488. Tscharke, D.C., P.C. Reading, and G.L. Smith, *Dermal infection with vaccinia virus reveals roles for virus proteins not seen using other inoculation routes.* Journal of General Virology, 2002. **83**(Pt 8): p. 1977-86.

489. Sodeik, B., *Mechanisms of viral transport in the cytoplasm.* Trends in Microbiology, 2000. **8**(10): p. 465-72.

490. Desai, P., et al., *A null mutation in the gene encoding the herpes simplex virus type 1 UL37 polypeptide abrogates virus maturation.* Journal of virology, 2001. **75**(21): p. 10259-71.

491. Desai, P.J., *A null mutation in the UL36 gene of herpes simplex virus type 1 results in accumulation of unenveloped DNA-filled capsids in the cytoplasm of infected cells.* Journal of virology, 2000. **74**(24): p. 11608-18.

492. Dodding, M.P. and M. Way, *Coupling viruses to dynein and kinesin-1.* The EMBO journal, 2011. **30**(17): p. 3527-39.

493. Diefenbach, R.J., et al., *Transport and egress of herpes simplex virus in neurons.* Reviews in medical virology, 2008. **18**(1): p. 35-51.

494. Zhu, F.X., et al., *Functional characterization of Kaposi's sarcoma-associated herpesvirus ORF45 by bacterial artificial chromosome-based mutagenesis.* Journal of virology, 2006. **80**(24): p. 12187-96.